TECHNISCHE UNIVERSITÄT MÜNCHEN

Fakultät für Physik
Lehrstuhl für Funktionelle Materialien

Polymer Templated Nanostructures for Application in Hybrid Photovoltaics and Li Ion Batteries

Mesoscale Structure Manipulation & Implications for Efficiency

Nuri Hohn, M. Sc.

Vollständiger Abdruck der von der Fakultät für Physik der Technischen Universität München zur Erlangung des akademischen Grades eines

Doktors der Naturwissenschaften (Dr. rer. nat.)

genehmigten Dissertation.

Vorsitzende:	Prof. Dr. Martin Zacharias
Prüfer der Dissertation:	1. Prof. Dr. Peter Müller-Buschbaum
	2. Prof. Dr. Aliaksandr Bandarenka

Die Dissertation wurde am 27.02.2019 bei der Technischen Universität München eingereicht und durch die Fakultät für Physik am 10.04.2019 angenommen.

Abstract

Novel approaches to nanostructure foam-like and high surface-to-volume ratio mesoporous thin films for application in hybrid photovoltaics and Li ion batteries are introduced. Within this scope, the controlled microphase separation of an amphiphilic diblock copolymer template is exploited and combined with sol-gel concepts in a good-poor solvent pair system to custom tailor respective nanomorphologies. Precise control over structures on a mesoscale < 40 nm is achieved. Compatibility of the introduced processing routines with large scale deposition techniques such as spraying is proven. Versatility in terms of different suitable precursors to form either Ti- or Ge-based nanostructures is furthermore demonstrated. Direct correlation of the mesoscale morphology of Ge-based thin films to the performance in Li ion battery applications is studied. Introduced novel processing routines are characterized primarily with focus on influences to control the inner morphology and surface. X-ray scattering techniques and scanning electron microscopy have been extensively used to extract respective structural information.

Zusammenfassung

Es werden neuartige Ansätze zur Nanostrukturierung von schwammartigen und mesoporösen Dünnschichten mit großem Oberflächen-zu-Volumen-Verhältnis eingeführt und mit Hinblick auf Anwendung im Bereich Hybridphotovoltaik und Li-Ionen-Batterien untersucht. Dabei wird die kontrollierte Mikrophasenseparation eines amphiphilen Diblock Copolymers mit Sol-Gel Konzepten in einem sogenannten gut-schlecht Lösungsmittelgemisch kombiniert, um entsprechende Nanomorphologien gezielt herzustellen. Dadurch wird die präzise Kontrolle über Strukturen auf einer Mesoskala < 40 nm erreicht. Eine Kompatibilität der eingeführten Strukturierungsmethoden mit großflächigen Beschichtungsprozessen wie Sprühen wird gezeigt. Besonderes Augenmerk liegt außerdem auf der demonstrierten Vielseitigkeit der Methode in Bezug auf verschiedene verfügbare Ausgangsstoffe zur Herstellung von Ti- oder Ge-basierten Dünnschichten. Ein direkter Zusammenhang zwischen der spezifischen mesoskopischen Morphologie von Ge-basierten Dünnschichten zur Leistungsfähigkeit in Li-Ionen-Batterien wird untersucht. Neuartige Nanostrukturierungsmethoden werden besonders im Hinblick auf ihre Oberfläche und innere Struktur untersucht. Rasterelektronenmikroskopie sowie Techniken, die auf Röntgenstreuung basieren, werden dabei verstärkt zur Strukturanalyse angewandt.

Contents

Contents iii

List of abbreviations vii

1 Introduction 1

2 Theoretical aspects 7

2.1 Synthesis of mesoporous materials . . . 7

2.1.1 Diblock copolymers . . . 7

2.1.2 Basic properties of titania and germanium . . . 10

2.1.3 Titania reaction scheme . . . 11

2.1.4 Diblock copolymer mediated structure control . . . 13

2.2 Applications . . . 14

2.2.1 Hybrid photovoltaics . . . 15

2.2.2 Li ion batteries . . . 18

2.3 X-ray scattering . . . 19

2.3.1 Basic principles . . . 20

2.3.2 X-ray diffraction . . . 23

2.3.3 Grazing incidence small angle X-ray scattering . . . 24

3 Methods 27

3.1 Structural characterization . . . 27

3.1.1 Profilometry . . . 28

3.1.2 Optical microscopy . . . 28

3.1.3 Scanning electron microscopy . . . 29

3.1.4 Atomic force microscopy . . . 32

3.1.5 X-ray diffraction . . . 33

3.1.6 Grazing incidence small angle X-ray scattering . . . 34

3.2 Spectroscopic characterization . . . 37

3.2.1 UV/Vis spectroscopy . . . 38

3.2.2 Fourier transform infrared spectroscopy . . . 40

3.2.3 X-ray photoelectron spectroscopy . . . 41

4 Sample preparation **45**
4.1 Materials . . . 45
4.2 Deposition techniques . . . 48
4.3 Fabrication of mesoporous thin films . . . 51
4.3.1 Blade coating of titania . . . 52
4.3.2 Spray deposition of titania . . . 53
4.3.3 Spin coating of germanium . . . 54
4.3.4 Drop casting of germanium . . . 55

5 Morphological tunability of mesoporous TiO_2 thin films **57**
5.1 Preface . . . 58
5.2 Experimental: Synthesis of mesoporous titania thin films via blade coating 59
5.2.1 Evaporation time studies . . . 60
5.2.2 Immersion bath composition studies . . . 61
5.3 Proof of principle: Influence of immersion bath . . . 61
5.4 Impact of evaporation time on phase separation behavior . . . 64
5.5 Impact of immersion bath composition on phase separation behavior . . . 69
5.6 Conclusion . . . 75

6 Influence of HCl on spray-deposited mesoporous TiO_2 thin films **77**
6.1 Preface . . . 78
6.2 Experimental: Synthesis of mesoporous titania thin films via spray deposition 79
6.3 Characterization of static samples . . . 80
6.4 *In situ* GISAXS investigation during spray deposition . . . 84
6.5 Conclusion . . . 92

7 Morphological tunability of mesoporous Ge-based thin films **93**
7.1 Preface . . . 94
7.2 Experimental: Synthesis of mesoporous Ge-based thin films via spin coating 96
7.3 Basic properties of mesoporous Ge-based thin films . . . 96
7.4 Control of pore sizes in mesoporous Ge-based thin films . . . 103
7.4.1 K_4Ge_9-unsaturated regime . . . 103
7.4.2 K_4Ge_9-saturated regime . . . 107
7.4.3 Summary . . . 109
7.5 Conclusion . . . 110

8 Mesoporous Ge-based films as anode material in Li ion batteries **111**
8.1 Preface . . . 112
8.2 Experimental: Synthesis of mesoporous Ge thin films via drop casting . . . 114

8.3 Influence of azeotrope solvent treatment 114
8.4 Influence of tempering atmosphere 122
8.5 Conclusion 130

9 Conclusion and outlook 131

Bibliography 135

List of publications 155

Acknowledgements 161

List of abbreviations

AFM:	atomic force microscopy
AFM-IR:	atomic force microscopy combined with local IR spectroscopy
cal.:	calcined
DMC:	dimethyl carbonate
DSSC:	dye-sensitized solar cell
DWBA:	Distorted Wave Born Approximation
EC:	ethylene carbonate
EIA:	Effective Interface Approximation
en:	ethylenediamine
FEC:	fluoroethylene carbonate
FFT:	fast Fourier transform
FTIR:	Fourier transformed infrared spectroscopy
FTO:	fluorine doped tin oxide
FWHM:	full width at half maximum
GISAXS:	grazing incidence small angle X-ray scattering
HCl:	hydrocloric acid
HOMO:	highest occupied molecular orbital
HPV:	hybrid photovoltaics
IR:	infrared
LIB:	lithium ion battery
LUMO:	lowest unoccupied molecular orbital
OM:	optical microscopy
OPV:	organic photovoltaics
NHCl:	samples without addition of HCl
PS-b-PEO:	polystyrene-block-polyethylene oxide
PSD:	power spectral density
PT:	post-treatment
PSC:	perovskite solar cell
PV:	photovoltaics

rms:	root mean square
SDD:	sample detector distance
SEM:	scanning electron microscopy
SLD:	scattering length density
ssDSSC:	solid-state dye-sensitized solar cell
TCO:	transparent conductive oxide
TTIP:	titanium (IV) isopropoxide
uncal.:	not calcined
UV/Vis:	ultraviolet/visible spectroscopy
WHCl:	samples with addition of HCl
XPS:	X-ray photoelectron spectroscopy
XRD:	X-ray diffraction

1 Introduction

Technological advances in the field of new energy generation devices are currently heavily focused due to an increasing world-wide demand of sustainable resources. Photovoltaics has emerged as a powerful candidate to provide renewable conversion of solar irradiation to electrical energy. Nowadays, the inorganic, semiconducting element silicon is most commonly employed in commercialized photovoltaic devices. Major disadvantages of theses commercialized inorganic devices are high production costs through energy-intensive manufacturing steps, mechanical stiffness and lack of transparency and tunable properties. Therefore, commercialized and rather expensive Si-based solar panels inherently come with long energy payback times and only limited fields of application. Research in the field of photovoltaics aims to especially tackle the above-mentioned limitations through the development of novel approaches such as organic photovoltaics (OPV), hybrid photovoltaics (HPC), dye-sensitized solar cells (DSSCs), solid-state dye-sensitized solar cells (ssDSSCs) and perovskite solar cells (PSCs).

The origins of the branch of organic semiconductor photovoltaics are closely related to the discovery of highly conductive polyacetylene. Through iodine doping an increase of conductivity by several orders of magnitude was achieved [1]. Steadily increasing performances of OPV devices have lead to power conversion efficiencies surpassing 17% in tandem cells [2]. Key advantages such as potential low-cost, large scale production through wet-chemical processing, tunable optoelectronic properties and mechanical flexibility allow for a broader field of application and design possibilities as compared to conventional Si-based inorganic devices. However, drawbacks in terms of structural stability and lifetimes commonly occur [3]. To overcome these downsides, hybrid photovoltaics (HPV) aims to combine high charge carrier mobility and structural stability of the inorganic part with the cost-effectiveness and flexibility of the organic part [4, 5]. A typical approach consists in the synthesis of an inorganic framework, which prevents structural degradation and which is backfilled with an organic material. Thereby, device lifetimes are expected to be significantly increased. Additionally, low-cost coating techniques like printing and spray deposition become accessible through application of wet-chemical, inorganic precursors [6, 7]. In contrast to DSSCs and ssDSSCs, the danger of liquid electrolyte leakage and dye degradation through photo-bleaching is negated in an HPV approach. The

above-described theoretical advantages represent an immense potential in terms of future benchmarks in PV technology. Nevertheless, fundamental research is still in the early stage and requires further attention.

For the case of an inverted solar cell architecture, which is typically employed for HPV devices, and under illumination, light initially passes the glass substrate and the layer of transparent conductive oxide, which acts as an electrode. Photons are commonly absorbed by the hole-conducting material, which is typically a semiconducting polymer. As generated excitons (bound electron-hole pairs) have higher binding energies in organic materials as compared to inorganic silicon, no thermally-induced charge separation occurs [8, 9]. For this purpose, an interface between organic and inorganic material with suitable energy band alignment is required. Only at such an interface the generated exciton can be split and extracted. Therefore, high surface-to-volume ratio inorganic frameworks with large potential interface area are desirable for good performance of final devices [10]. If no such interface is reached within the lifetime, the exciton simply decays and the contribution to the power generation is lost. Once charge separation took place, electrons are transported through the inorganic electron-conductor. Similarly, the hole is transported through the hole-conductor until the top gold electrode is reached. Due to the high absorption coefficients in the UV/Vis regime, only few hundreds nanometers of organic material are required to harvest most of the incoming light. This results in reduced percolation paths, correlated decreased recombination of charge carriers and less quantities of needed material in a HVP approach as compared to DSSCs. Note that in an HPV approach, backfilling of the inorganic matrix with an organic macromolecule represents one of the key challenges [11, 12]. Therefore, the pores of the inorganic framework need to be sufficiently large to ensure good backfilling efficiencies. However, larger pores inherently decrease the surface-to-volume ratio, which decreases the likeliness of an exciton reaching an interface. Note that typical exciton diffusion lengths are in the range < 20 nm in commonly employed macromolecular material [13]. Consequently, for each material system an ideal pore size / surface-to-volume ratio needs to be adjusted, which fulfills the conditions for both good backfilling and small recombination losses. Therefore, it is fundamentally essential for good power conversion efficiencies to be able to precisely control the pore size / surface-to-volume ration of the inorganic matrix.

Despite all evident advantages of HPV, photo conversion efficiencies cannot yet compete with conventional DSSCs. Apart from the challenge of efficient backfilling, major issues in ongoing research are imposed by the contact between inorganic and organic material, suitable energy band alignment between electron- and hole-conducting material, charge carrier mobility, light absorption and efficient routines to precisely control the nanomorphology. Through the investigation of novel materials with tunable properties

like band gab, electron- and hole-mobility and absorption behavior key challenges can be tackled. Through the development of new processing routines, improved control over the nanomorphology and the contact between the constituents of the active layer could be achieved. Related characterization of the inner morphology is aimed to provide fundamental knowledge and to pave the way towards an improved tailoring of future PV devices.

Closely related to the field of photovoltaic energy generation, the equally-hot topic of energy storage devices can be found. Among those, Li ion batteries have emerged as a promising candidate to be combined with PV devices for example in the field of automotive industry. Key factors to be taken into account are properties like specific power density, specific capacity and safety. Remarkably, similar processing routines as developed for HVP with high interfacial area have been found to be especially useful. For example the increased mechanical flexibility of nanostructured material could negate negative impacts due to high volume expansion upon lithiation/delithiation of commonly employed materials such as silicon or germanium [14, 15]. Li ion migration into a highly porous inorganic framework has been proven to yield high specific capacities [16]. Furthermore, novel materials with higher theoretical specific capacity bear the potential of replacing typical anode or cathode materials [17]. Due to the close proximity of energy storage to the field of hybrid photovoltaic energy generation, novel nanostructured materials are investigated with regard to possible application in both fields.

A promising candidate for application in HPV, DSSCs, ssDSSCs and PSCs is nanostructured and mesoporous titanium dioxide [18–21]. Devices can benefit from high electron mobility, possibility of a flexible design and unique properties coupled to being a wide bandgap semiconductor. However, most common processing techniques either lack precise control of nanostructures or are linked to tedious processing steps with no possibility for large scale deposition. The semiconductor germanium even surpasses titania in terms of bulk electron mobility and, therefore, also appears to be a promising candidate for application in nanostructured HPV devices [22]. Additionally, energy storage devices could potentially benefit from high specific capacities in nanostructured germanium films. However, facile ways of nanostructuring germanium are scarce mainly due to the limited variety of suitable, wet-chemical germanium precursors.

Within the present thesis, novel nanostructuring approaches on the basis of titania and germanium are investigated. A schematic overview of research topics treated within the frame of the present thesis is given in Figure 1.1. In all cases, nanostructure formation is aimed to be manipulated through controlled microphase separation of an amphiphilic diblock copolymer template in a sol-gel inspired process (Figure 1.1.I). In this process, the polymer template self-assembles in the energetically most favorable way. Through con-

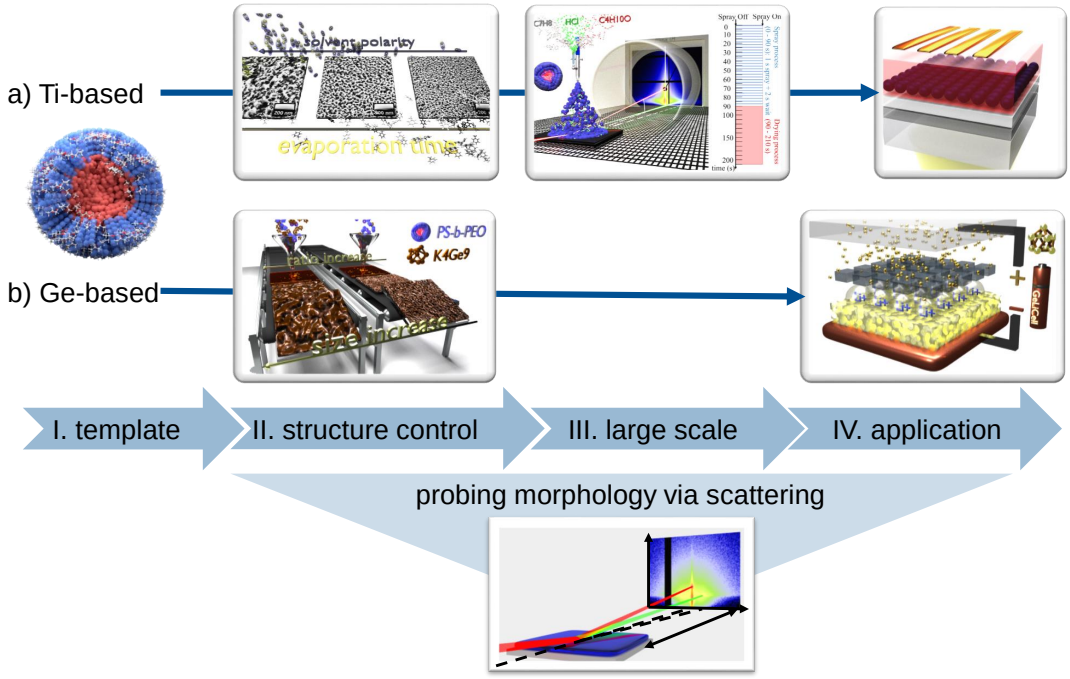

Figure 1.1: *Schematic overview of research topics treated within the frame of the present thesis. (I) A common diblock copolymer templating approach represented as micelle in the center is employed to fabricate either Ti- or Ge-based nanostructures in a sol-gel approach. (II) Tailoring structures via controlled change of processing conditions is investigated for both Ti- and Ge-based nanostructures. (III) Compatibility with large scale deposition techniques such as spray deposition is further focused for mesoporous Ti-based thin film synthesis. (IV) Implications for application in the field of photovoltaics is discussed for both Ti- and Ge-based nanostructures, while performance in the field of energy storage is directly measured for Ge-based films. Within this scope, core techniques to investigate the inner morphology rely on X-ray scattering.*

trolled and step-wise change of processing conditions, major fundamental influences on the phase separation behavior are investigated and tailored (Figure 1.1.II). Within this frame, scattering techniques are preferably applied to possibly extract quantitative information about the inner morphological and to correlate structural alteration to respective changes of processing conditions. Furthermore, all introduced novel approaches are wet-chemical processes, which are inherently assumed to enable large scale deposition (Figure 1.1.III). For the case of nanostructured Ti, *in situ* structure formation during spray deposition is particularly focused via scattering experiments. Changes of performance due to altered morphologies are discussed for the field of PV and Li ion batteries (Figure 1.1.IV).

One key advantage of diblock copolymer templated sol-gel approaches is the control of nanostructures via altered phase separation while simultaneously ensuring the potential of large scale deposition. However, readily available titania nanostructuring routines are

scarce. Chapter 5 is tackling the challenge of finding a facile diblock copolymer templated processing routine, which could be especially exploited for the synthesis of cheap PV devices and which allows for structure control on the mesoscale. Influences, which determine the phase separation behavior and respective morphological changes are further analyzed. Within this scope, a special focus is set upon decoupling the individual influences in a good-poor solvent pair system. Determining the function of each individual contribution to the combined phase separation process would allow for an improved custom tailoring of Ti-based nanostructures.

On the basis of an identical material system as introduced in chapter 5, compatibility of mesoporous Ti-based thin film formation with spray deposition is focused in chapter 6. Within this frame, key questions of time-dependent structure formation, the role of catalytic additives on the reaction dynamics of titania sol-gel processes and respective consequences for the efficiency of diblock copolymer templating are especially addressed through *in situ* measurements. Extracted results are aimed to lead to an improved understanding of Ti-based mesoporous structure formation dynamics. Obtained knowledge might particularly help in the development of large scale Ti-based deposition setups.

Diblock copolymer assisted sol-gel synthesis of mesoporous structures is fundamentally assumed to offer the advantage of a facile transition to different precursors and consequently different mesoporous materials with their unique properties. Chapter 7 targets a potential transition to a different precursor and ways to ensure similar control of mesoporous structures as demonstrated for the case of titania thin films via diblock copolymer templating. Therefore, new processing steps are developed and analyzed to meet the special demands of a novel precursor.

Advantages of a transition to a different precursor with optimized material properties for a potential application in the field of energy storage are treated in chapter 8. In this frame, key features of a mesoporous, foam-like nanostructure are compared to a rather compact morphology. Changes of performance are directly related to findings of altered composition and structure. Systematic manipulation towards achieving an ideal thin film composition and morphology is seen as a highly promising pathway for obtaining record device performances.

An introduction to relevant theoretical aspects is given in chapter 2, followed by a brief discussion of employed characterization methods in chapter 3 and sample preparation routines in chapter 4. Main results are discussed in chapter 5-8. The final chapter 9 summarizes major findings of the present thesis and utilizes the obtained knowledge to answer key questions raised in the present introduction.

2 Theoretical aspects

The present chapter introduces basic theoretical aspects relevant for topics discussed in this thesis. In the first section 2.1, the fabrication of mesoporous structures is discussed, followed by an explanation of the working principle of potential applications for mesoporous structures in section 2.2. Furthermore, the main characterization technique applied in the present thesis is X-ray scattering. Accordingly, basic concepts of X-ray scattering are addressed in the final section 2.3 of this chapter.

2.1 Synthesis of mesoporous materials

Mesoporous materials typically offer the advantage of increased surface-to-volume ratio, increased mechanical flexibility and altered properties as compared to their bulk counterpart [23]. Fabrication, structural control and understanding of mesoporous materials is one of the key objectives of the presented work. Novel techniques are introduced, which are inspired from diblock copolymer assisted sol-gel synthesis of mesoporous titania structures. Therefore, basics of diblock copolymer templates and phase separation are presented in section 2.1.1, followed by an overview in section 2.1.2 of properties of the two main elements used as a basis for the respectively formed mesoporous structures (Ge or Ti). Related reaction schemes for Ti- and Ge-based cross-linking and network formation are explained in section 2.1.3. In the final section 2.1.4, the combined process of diblock copolymer mediated structure control is further elaborated.

2.1.1 Diblock copolymers

Diblock copolymers are based on chains of two different monomeric building blocks, which are covalently bound and influence basic properties. The covalent bond prevents separation on a macroscopic scale and microphase separation can occur due to energy minimization. The mechanism of diblock copolymer mixing is a complex process. Models to describe the mixing behavior are usually based on simplifications as for example assuming the diblock copolymer system to be a blend of homopolymers.

A diblock copolymer consisting of homopolymer A and B is named polyA-block-polyB or in short PA-b-PB. The degree of polymerization N_A and N_B of each respective homopolymer reflects the number of monomeric repeating units. Diblock copolymer are commonly described via the block ratio f_A or f_B

$$f_A = \frac{N_A}{N_A + N_B}$$

$$f_B = \frac{N_B}{N_A + N_B} = 1 - f_A$$

Energetically, the mixing of two different types of homopolymers is usually not favored. To minimize the energy of the system, microphase separation with domains of homopolymer A and B occurs in the special case of covalently linked diblock copolymers. The dimension of the resulting phase separation is in the same order as the typical length of an individual homopolymer chain.

Major parameters influencing the phase separation behavior of a diblock copolymer in solution are the total degree of polymerization $N_{AB} = N_A + N_B$, the block ratio f_A and the Flory-Huggins interaction parameter χ describing the interaction between the two different homopolymers A and B [24, 25]

$$\chi = \chi_S + \frac{\chi_H}{k_B T} \tag{2.1}$$

where χ_S and χ_H represent the entropic and enthalpic part, T is the temperature and k_B is the Boltzmann constant. Conformation of the chains and chain end effects are key influences on the entropic part. A smaller value of the Flory-Huggins interaction parameter χ represents an increased likeliness of intermixing. An increased temperature usually has the effect of a decreased interaction parameter and, therefore, commonly enhances miscibility in a polymeric blend system. For diblock copolymers, the product of the Flory-Huggins interaction parameter χ and the total degree of polymerization N is a good measure for the phase separation behavior. For $\chi N \ll 10.5$ chains of homopolymer A and B intermix without microphase separation into a single phase. The weak segregation limit, where a transition between a disordered, single phase to a weakly ordered, mircophase-separated phase occurs, is typically in the order of $\chi N \approx 10.5$ [26]. Further increase of χN leads to an increase of energetic incompatibility of the respective diblock copolymer blocks. In the strong segregation regime at $\chi N \gg 10.5$, mircophase separation results in the formation of ordered and highly pure domains. Within the frame of the present thesis, transition to a strongly segregated regime is realized via addition of poor solvent (selective for only one of the two diblock copolymer blocks) to a diblock copolymer dissolved in a good solvent (dissolves both blocks). Thereby, the incompatibility between both diblock copolymer blocks is increased.

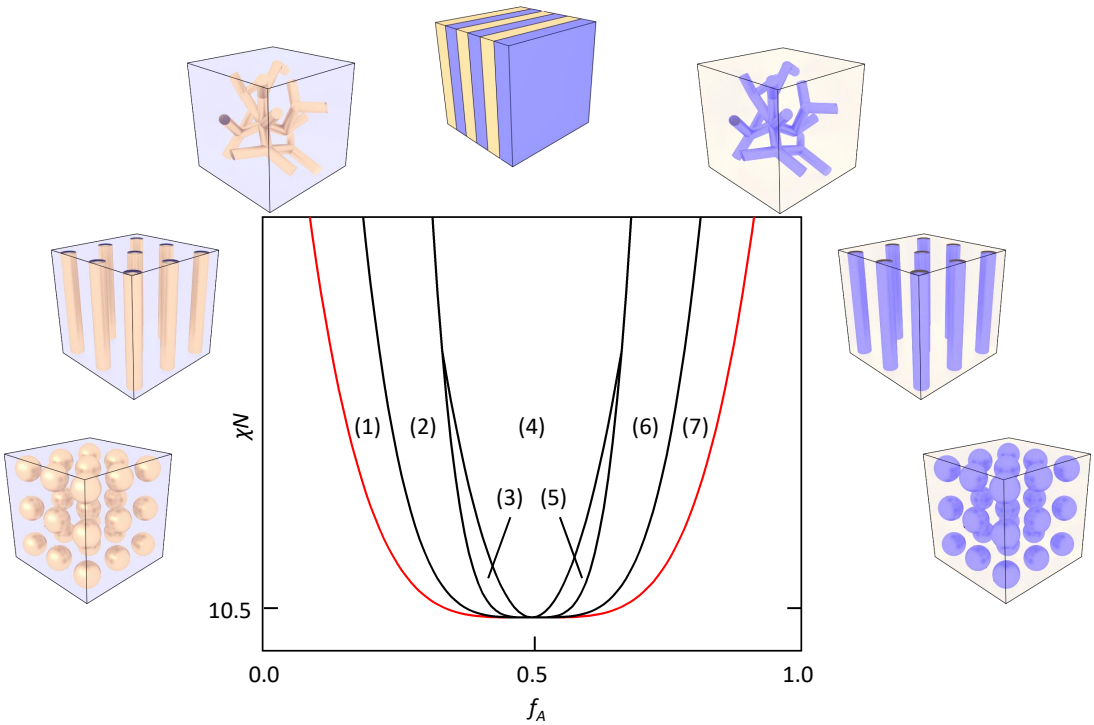

Figure 2.1: *Exemplary phase diagram of a diblock copolymer based on monomeric units A and B. The red line indicates the order-disorder transition. (1) At low ratio f_A, spheres made out of monomer A are embedded in matrix of monomer B. With increasing block ratio, (2) cylinder-, (3) gyroid- and (4) lamellar-type phase separation for symmetric blocks can be achieved. Upon further increase of the block ratio (5-7) phase distribution of block types is inverted for the before mentioned phase separation types. More information can be found in literature [27] (Figure redrawn/inspired from [27]).*

As stated in the previous section, the product of interaction parameter and degree of polymerization strongly influences the phase separation behavior of a diblock copolymer. Additionally, the block ratio of the employed diblock copolymer has a major impact on the type of morphological phase separation. The combined impact of all three influences (χ, N, f_A) on the type of phase separation can be summarized in a phase diagram. An example is shown in Figure 2.1. For $\chi N < 10.5$, a disordered, single phase is typically formed. In contrast, for $\chi N > 10.5$, phase separation leads to the formation of ordered morphologies. The type of phase separation morphology is influenced by the block ratio f_A. At low ratio f_A, spheres made out of monomer A are embedded in matrix of monomer B. With increasing block ratio, 2) cylinder-, 3) gyroid- and 4) lamellar-type phase separation for symmetric blocks can be achieved. Upon further increase of the block ratio, 5,6,7) phase distribution of block types is inverted for the before mentioned phase separation types. Note that phase diagrams in literature, which refer to measurements on

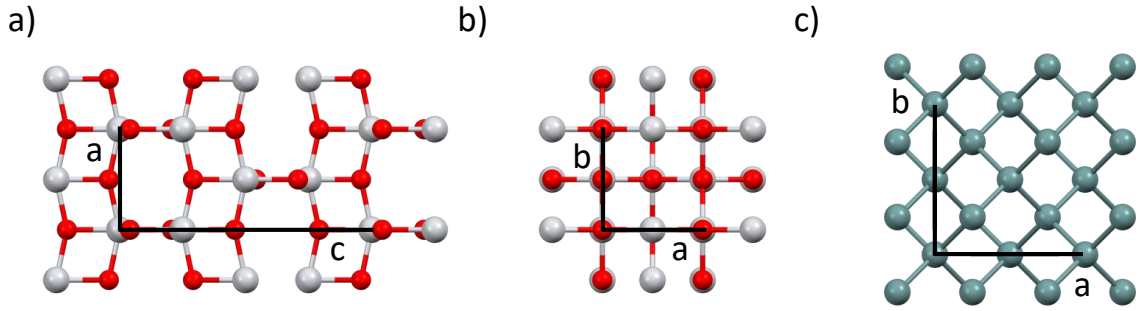

Figure 2.2: *Unit cell of anatase-type titania (a) with view along the b-axis, (b) with view along the c-axis [30] and (c) α-germanium with diamond-type symmetry independent of the view axis (same for a,b and c) [31].*

real systems, are asymmetric. The asymmetry is mainly caused by additional effects such as for example differences in the structure of monomeric building units [28]. Additionally, effects of confinement and interfaces come into play, which, especially for the case of thin films, influence possible morphologies formed according to Figure 2.1. Furthermore, methods for film fabrication of the present thesis are not performed in a state of thermodynamic equilibrium (non-equilibrium processes), which is why phase separation does not exclusively depend on the above mentioned parameters, but also on the time-dependent mobility of polymeric chains during the deposition process. Therefore, phase separation is described as an interplay between chain mobility and energetic incompatibility of the respective blocks.

2.1.2 Basic properties of titania and germanium

Within the frame of the present thesis, different methods are introduced to fabricate mesoporous thin films on the basis of germanium or titanium dioxide as a material. The common approach to fabricate those films is inspired from titania sol-gel [29]. From there on, different routines have been established to manufacture the above-mentioned mesoporous thin films. Mesoporous materials on the basis of different elements (Ti or Ge) come with all the inherent advantages of a mesoporous structure and add the characteristic physical properties of the respective element to form a new material with unique properties. Relevant basic properties of bulk germanium and bulk titanium are summarized in the next section.

Titania (TiO_2) is an indirect, wide band gap semiconductor with high electron mobility. The wide band gap of 3.2 eV comes with high absorption in the UV-regime around 388 nm.

The crystalline structures anatase and rutile are most commonly observed. Titania thin films fabricated in the frame of this thesis all indicate an anatase-type crystallization. If a rutile phase is desired, calcination temperatures typically have to be increased above 600 °C. An illustration of the unit cell of anatase-type titania is shown in Figure 2.2a and b with view along the b- and c-axis of the unit cell. Expected peak positions of anatase-type titania for X-ray diffraction measurements based on Cu k_α irradiation are listed in Table 2.2. More details on basic properties of anatase-type titania are listed in Table 2.1. The wide band gap in combination with the high electron mobility renders mesoporous, anatase-type titania an excellent candidate for application as electron-conducting material in photovoltaic applications [32, 33].

	band gap [eV]	density [g/cm^3]	electron mobility [cm^2 V^{-1} s^{-1}]
anatase TiO_2 [34]	3.20	3.83	10-30
α-Ge [22]	0.67	5.32	3900

Table 2.1: Summary of basic properties of bulk, anatase-type titania and α-germanium at room temperature [22, 34].

Germanium is a semiconductor with an indirect band gap of 0.67 eV and the highest known electron mobility of 3900 cm^2 V^{-1} s^{-1} for the crystalline α-Ge phase [22, 35]. The diamond-type, crystalline α-Ge phase is illustrated in Figure 2.2c with view along the c-axis of the unit cell. Basic properties of germanium are summarized in Table 2.1. The especially high electron mobility renders the material a highly attractive material for hybrid photovoltaic applications. Note that the indicated narrow band gap is referring to bulk material. Properties on a nanoscale are typically found to change as compared to their bulk value [36]. In addition to photovoltaic applications, the high specific capacity of 1385 mAhg^{-1} for $Li_{15}Ge_4$ and 1564 mAhg^{-1} for $Li_{17}Ge_4$ promises excellent performance as anode material in Li ion batteries. The high specific capacity furthermore comes with a Li ion diffusivity, which is approximately 400 times higher as compared to silicon [16, 17]. However, the main degradation mechanism of Ge-based anode materials in Li ion batteries is caused by the high volume expansion of germanium. Within the frame of the present thesis, this issue is aimed to be overcome through the fabrication of mechanically flexible, mesoporous Ge layers.

2.1.3 Titania reaction scheme

Titania sol-gel is a wet-chemical, bottom-up process on the basis of a titania precursor. Specifically for the frame of the present thesis, the metal alkoxide titanium (IV) isopropox-

ide (TTIP) is used. In solution, the precursor reacts and forms nanosized particles. This state is referred to as a sol. Cross-linking of nanosized particles leads to the formation of 3D interconnected networks, which naturally come with an increase of viscosity and are consequentially referred to as gel. Typical dimensions of those network structures lie in the order of sub-micrometer. As also demonstrated within the frame of the present thesis, one advantage of sol-gel synthesis is given by the flexibility of different available precursors to form thin films made out of different elements [37, 38].

The main reaction scheme for the conversion of the precursor TTIP to titania is based on hydrolysis and condensation. In presence of water (hydrolysis), the precursor $(RO)_4$-Ti (TTIP) reacts according to the following equation

$$(RO)_4 - Ti + H_2O \rightleftharpoons (RO)_3 - Ti - OH + R - OH \tag{2.2}$$

where a alkoxide group (RO) is replaced by a hydroxyl group (OH). This reaction can be repeated until all alkoxide groups are replaced (referred to as complete hydrolysis). Additionally, water and alcohol condensation leads to cross-linking of two partially hydrolyzed $(RO)_4$-Ti units via an oxygen bond (Ti-O-Ti) under release of H_2O or ROH and according to the following reaction scheme

$$(RO)_3 - Ti - OH + (RO)_3 - Ti - OH \rightleftharpoons (RO)_3 - Ti - O - Ti - (OR)_3 + H_2O \tag{2.3}$$

$$(RO)_4 - Ti + (RO)_3 - Ti - OH \rightleftharpoons (RO)_3 - Ti - O - Ti - (OR)_3 + R - OH \tag{2.4}$$

The final structure of the 3D network formed at the end of these hydrolysis and polycondensation reactions is typically determined by their reaction dynamics, which can be influenced by changing external parameters such as pH-value, temperature or type of catalyst. Especially important for the frame of the present thesis is the influence of the catalyst HCL. The presence of HCL typically promotes hydrolysis reactions over condensation reactions [39]. Through promoted hydrolysis (in the presence of HCL) linkage of chain ends occurs with an increased likeliness. This results in a natural tendency towards the formation of more elongated structures, which is especially beneficial for structure control of foam-like, mesoporous titania films templated through diblock copolymer usage [40]. In contrast, the absence of HCL is more likely to lead to the formation of more bulky, compact aggregates of titania. After complete hydrolysis and condensation reaction, typically amorphous titania is obtained, which can be transformed to a crystalline phase through heat treatment.

For the synthesis of mesoporous thin films on the basis of germanium, the Zintl precursor K_4Ge_9 is used and dissolved in the stable transfer solvent ethylenediamine (en) [41]. More information regarding the Zintl precursor and the solvent en can be found in section 4.1. Controlled removal of the solvent en triggers the oxidation of the Ge_9^{4-} Zintl anions and interconnected, amorphous Ge based structures are formed [41]. Through heat treatment, a crystalline α-Ge phase can be obtained. Note, that the process is extremely air-sensitive and only small amounts of air cause the formation of Ge oxides. Therefore, if metallic Ge is desired, temperature treatment was performed under vacuum conditions or under Ar-atmosphere.[1] Within the frame of the present thesis, no reaction scheme for Ge is developed.

2.1.4 Diblock copolymer mediated structure control

The aforementioned sol-gel process of titania only offers limited control for the synthesis of nanostructures. To tackle this limitation, the amphiphilic diblock copolymer polystyrene-block-polyethylene oxide (PS-b-PEO) is used as a structure directing agent and combined with core elements of titania sol-gel processes to allow for the synthesis of tunable, mesoporous structures on the basis of either germanium or titania.

In Figure 2.3, a schematic representation of a diblock copolymer templated synthesis routine is shown. The polymeric template PS-b-PEO is combined with the respective precursor. Within this scope, a good solvent (en or toluene) is used to initially dissolve both blocks of the diblock copolymer. Thereafter, addition of the respective precursor (K_4Ge_9 or TTIP) is carried out. It is essential for the fabrication of mesoporous material that the precursor is selectively incorporated in only one of the diblock copolymer blocks. For the case of titania based films, incorporation of TTIP into the PEO domain is proven [42]. Through a subsequent treatment including a poor solvent, strong phase separation as explained in section 2.1.1 can be induced. Accordingly, the selective nature of the poor solvent increases the energetic incompatibility of the two blocks. In solution, this typically leads to the formation of micelles with a PEO shell and a PS core for the applied solvent system [42]. In the case of TTIP, hydrolysis and condensation processes are simultaneously initiated and a interconnected 3D titania network with unique morphology starts to form. In the case of Ge-based thin film synthesis, oxidation and cross-linking of Ge atoms primarily occur during the evaporation of the transfer agent en. For both Ge- and Ti-based thin films, dynamic and non-equilibrium processes of film deposition have a major influence on the final morphology of the composite film. Additionally, change

[1] Temperature treatment for mesoporous, metallic Ge structures was performed at the chair of Prof. Fässler (Chemistry Department, TU München)

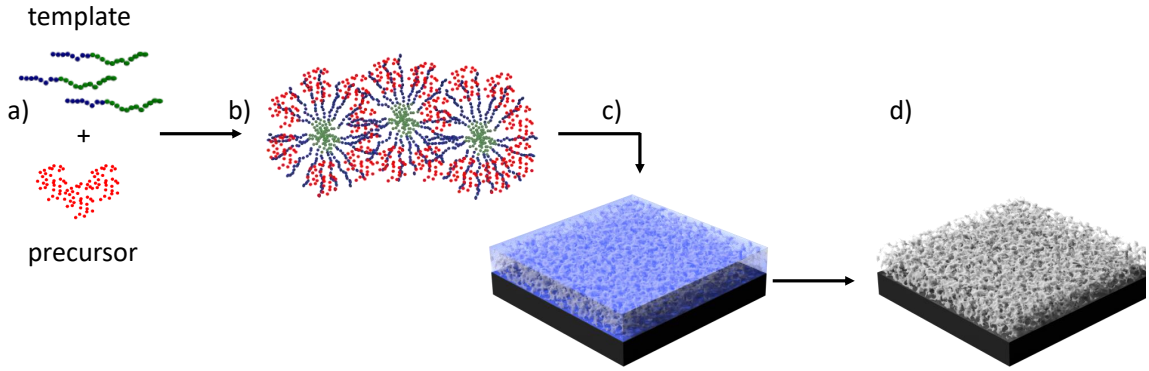

Figure 2.3: *Schematic representation of processing steps involved for the synthesis of mesoporous structures through diblock copolymer templating. (a) The diblock copolymer PS-b-PEO with PEO block (blue spheres) and PS block (green spheres) is employed as a template, while a respective precursor (TTIP or K_4Ge_9) is used for either Ti- or Ge-based films. (b) Phase separation of the diblock copolymer is induced and selective incorporation of the precursor into one diblock copolymer domain occurs. (c) A composite Ti/Ge:PS-b-PEO film is deposited and (d) a mesoporous film is obtained after template removal through temperature treatment.*

of the respective final morphology is especially targeted within the frame of the present thesis through controlling the mobility of the polymeric template, enhancing the energetic incompatibility through increase of poor solvent content, addition of the catalyst HCL to influence the cross-linking dynamics and step-wise increase of the precursor to template ratio for densification of structures. After deposition, temperature treatment can be applied to remove the polymeric template and to induce the formation of crystalline phases.

2.2 Applications

Within the frame of the present thesis, application of fabricated mesoporous thin films is especially envisioned in the field of hybrid photovoltaics (HPV) and Li ion batteries (LIB). Introduction of working principles for the field of HPV and LIB is provided in section 2.2.1 and 2.2.2, respectively.

For PV applications, the high surface-to-volume ratio of mesoporous thin films in the active layer is especially promising due to the increased amount of interface, which is expected to be beneficial for an enhanced splitting of excitons and a reduction of recombination losses. Mesopores ($\sim$ 40 nm) appear especially desirable as most exciton diffusion lengths of conjugated polymers commonly used for backfilling lie in the range $<$ 20 nm [13]. Within this context, pore sizes need to be precisely controlled to find

an optimal, characteristic pore size for the given system, which is on the one hand small enough do provide high amounts of interface and on the other hand large enough to ensure efficient backfilling. Titania as a material has already proven to be an attractive choice for hybrid, dye-sensitized and perovskite photovoltaics [33,43–45]. Nanostructuring additionally allows for flexible design approaches and to control optoelectronic properties, which is also desirable for PV applications [46, 47]. Through a transition to Ge-based mesoporous films, devices could profit from the outstanding electron mobility of germanium and new possibilities in terms of energy band alignment. In both cases, the potential of large scale deposition is maintained through a wet-chemical synthesis approach.

The exploitation of mesoporous Ge-based thin films is foreseen for the field of anode materials in LIB applications. Despite the high specific capacity of Ge and excellent Li ion diffusivity, device typically suffer from the high volume expansion of germanium, which results in device failure. Mesoporous materials promise to tackle this issue through improved mechanical flexibility. Additionally, the mesoporous nature is likely to facilitate Li ion intercalation.

In the following sections, the basic working principles of hybrid solar cells and LIBs are introduced to provide a basis for discussion of potential advantages of nanostructured materials in the respective fields. Since device fabrication was not the core objective of the present thesis, discussion of PV and LIB working principles is only provided in the form of a brief overview.

2.2.1 Hybrid photovoltaics

Solar cells are devices that convert sun light into electrical energy. Compared to purely inorganic solar cells, hybrid inorganic-organic photovoltaics (HPV) promises to enable all the advantages foreseen for organic solar cells (tunable optoelectronic properties, flexibility, large scale deposition / cost efficiency and semi-transparency) while maintaining high electron conductivity and chemical stability caused by employment of inorganic materials. Mesoporous Ge- or Ti-based thin films are envisioned to be especially attractive for HPV. Within this scope, controllable nanomorphologies are essential for efficient backfilling and correlated high exciton-energy conversion at interfaces.

An illustration of an exemplary hybrid solar cell in inverted geometry is shown in Figure 2.4a. Incoming light is absorbed in the active layer consisting of a mesoporous, inorganic layer (blue spheres) backfilled with an organic material (red). The active layer is sandwiched in between two blocking layers and is build upon a transparent conductive oxide (TCO) substrate. The top electrode is represented as gold-colored stripes. The

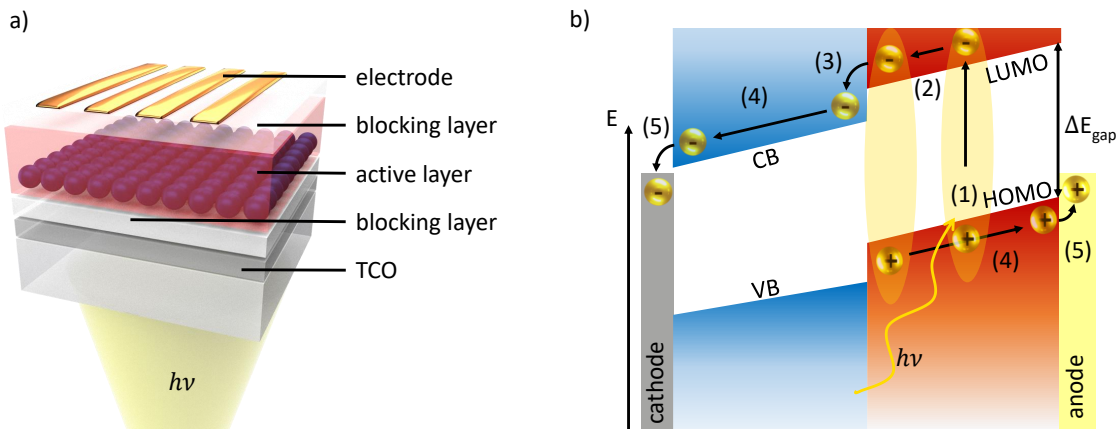

Figure 2.4: *Illustration of a solar cell in inverted geometry with respective schematic band diagram. (a) Incoming light is absorbed in the active layer consisting of an inorganic, electron conduction material (blue spheres) and an organic, hole-conducting material (red). The active layer is sandwiched in between two blocking layers. The transparent conductive oxide support allows for transmission of light. (b) Band diagram with absorption of light in the organic phase (1) and respective formation of a bound electron-hole pair (exciton; electron is excited to the LUMO level). In step (2) the exciton may diffuse to an interface, where exciton dissociation (3) occurs. Free charge carriers are transported through the respective layer (4) and extracted at the electrodes (5).*

band diagram in Figure 2.4b is depicted with the different steps (1-5) essential for energy conversion in a solar cell. In the following, each step is discussed in more detail for the example of a hybrid solar cell:

- (1) Absorption: Incoming sun light is commonly absorbed in the organic phase of the active layer according to the Lambert-Beer law

$$I(\lambda) = I_0(\lambda) \exp^{-\alpha(\lambda)d} \tag{2.5}$$

  where I is the transmitted intensity, I_0 the initial intensity, λ the wavelength of incoming light, α the absorption coefficient and d the thickness of the material. Thereby, the condition $\alpha > 0$ is only fulfilled, if the energy of the incident photon E_{photon} is sufficiently large to excite an electron from the highest occupied molecular orbital (HOMO) of the organic phase to the lowest unoccupied molecular orbital (LUMO)

$$E_{\text{photon}} = h\nu \geq E_{\text{gap}} = E_{\text{LUMO}} - E_{\text{HOMO}} \tag{2.6}$$

  If the condition is fulfilled, a strongly-bound electron-hole pair (Frenkel exciton) is formed. Compared to Si-based solar cells, the binding force of such an exciton is strong due to a lower dielectric constant for organic materials and dipoles tending

to weaken/screen the Coulomb attraction between electrons and holes. Therefore, thermal energy is not sufficient to separate excitons into free charges. Instead an interface is required.

- (2) Diffusion: Within the organic domain, the movement of the generated exciton can be described as a hopping process (random walk movement with no preferential direction). Short-range Förster transfer (dipole-dipole coupling) and long-range re-absorption processes are the underlying mechanisms [48]. The diffusion length l_d is a measure for the travel distance of an exciton before recombining

$$l_d \propto \sqrt{D\tau} \tag{2.7}$$

  where D is the diffusion coefficient in the respective material and τ the lifetime of the exciton. The lifetime in common conjugated, organic materials (like P3HT) is in the order of nanoseconds, which leads to diffusion lengths typically in the range < 20 nm [13]. If no interface is reached within this travel distance, the exciton recombines and the energy is not converted to electrical energy. Therefore, synthesis and control of inorganic structures with pores diameters d_p in the order of $2 * 20$ nm is focused in the present thesis. Recombination losses due to excitons not reaching an interface are assumed to be minimized via this approach. Devices would profit from increased generation of free charge carriers expressed through an enhanced short-circuit current.

- (3) Dissociation: Excitons reaching an interface between organic and inorganic material can be split into free charge carriers. One mechanism is based on the electron residing in the LUMO level of the organic phase to be transferred as a free charge carrier to the conduction band (CB) of the inorganic material, if the energetic difference of energy bands of donor and acceptor material is sufficient to overcome the exciton binding energy. Within this frame, the choice of materials plays a crucial role. In case of anatase-type titania with a large band gap of 3.2 eV and deep energy levels, suitable organic counterparts are typically not difficult to find (e.g. P3HT, PTB7-th). However, for the case of germanium, the narrow band gap of 0.67 eV imposes limitations for the choice of a suitable organic counterpart. One strategy to overcome this challenge lies in the fabrication of nanostructures, which typically also effects the band structure and band gap of a material [36]. Additionally, the band gap can be strongly increased through oxidation and the formation of germanium dioxide [49, 50].

- (4) Transport and (5) Extraction: Separated charge carriers are transported through the material to the respective electrodes. Particularly, low mobilities can lead to significant losses of separated charge carriers. Transported charge carriers reaching

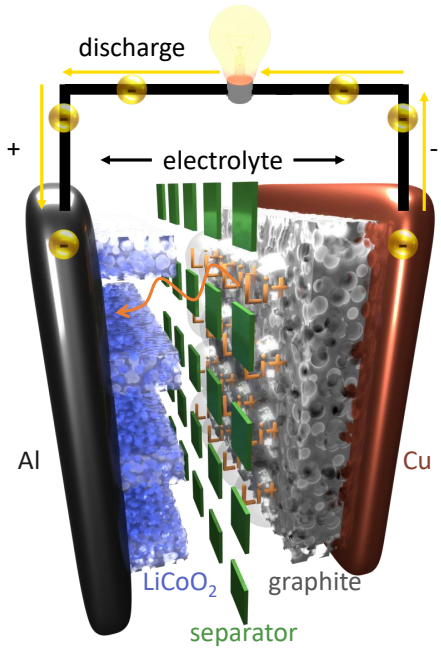

Figure 2.5: *Schematic illustration of the working principle of a lithium ion battery during discharge. Graphite is used an an anode material, while $LiCoO_2$ serves as cathode material. Both electrodes are separated through the separator. During discharge, lithium ions (orange) migrate from anode to cathode through the electrolyte releasing electrons to power a potential device.*

the electrodes are extracted. Within this scope, the employment of blocking layers is usually beneficial for the minimization of losses during charge extraction through preventing contact between active layer and electrodes.

2.2.2 Li ion batteries

Mesoporous Ge-based thin films are envisioned to be used as electrode material in lithium ion batteries (LIBs) due to high specific capacity and Li ion diffusivity. Additionally, the nanostructure is expected to reduce the typical degradation mechanism caused by the high volume expansion of germanium during alloying/de-alloying. As a basis for discussion, the working principle of a typical LIB is introduced in the following.

In Figure 2.5 the working principal of a typical LIB is illustrated. Core elements of a LIB are the positive and negative electrodes in combination with a liquid electrolyte in between. Different Li salts are typically added to an organic solvent mixture to yield an electrolyte with high ion conductivity [51]. Copper and aluminum current collectors are connected to the respective electrodes, which are separated via a separator. Most com-

monly, $LiCoO_2$ is exploited as cathode material, while graphite serves as anode material during the discharge cycle.

During charging, an external voltage is applied to the electrode and the following reactions occur

$$LiCoO_2 \rightharpoonup CoO_2 + Li^+ + e^- \tag{2.8}$$

$$C_6 + Li^+ + e^- \rightharpoonup LiC_6 \tag{2.9}$$

Li ions, released from the oxidation reaction at the cathode material ($LiCoO_2$) during charge, travel through the electrolyte and are reduced at the graphite cathode to form LiC_6. During discharge, the role of anode and cathode are reversed as well as the direction of the above given reactions. Li ions are oxidized at the LiC_6 anode and travel through the electrolyte to the cathode (CoO_2). As the electrolyte is electrically insulating (no electron conductivity, only ion conductivity), electrons are forced through a potential workload during discharge and, thereby, power a specific device. Li ions are oxidized at the CoO_2 cathode and $LiCoO_2$ is reversibly formed.

In the frame of the present thesis, mesoporous Ge-based thin films are exploited as electrode material. The material is used in a half-cell setup with $LiPF_6$ as Li salt and a Li foil as counter electrode. During charge, Li ions are presumably forming $Li_{15}Ge_4$ or $Li_{17}Ge_4$ with specific capacities of up to 1385 and 1564 mAh g^{-1}, respectively [16, 17]. Typical degradation processes due to Li intercalation and resulting high volume expansion of germanium is expected to be minimized through the porous nature of the employed material. Additionally, Ge is known for up to 400 times higher Li ion diffusivity as compared to silicon at room temperature. Residual carbon, potentially originating from the carbon-based template used for the synthesis of mesoporous structures, is foreseen to have a positive impact on the electron conductivity. Furthermore, pseudocapacitive processes have the ability to further boost the specific capacity for high surface-to-volume ratio materials. As a last influence, the presence of nanostructured germanium might enable reversible formation of LiO_2 in the conversion reaction of GeO_2. This would increase the number of available Li ions from 4.4 to 8.8 and accordingly enhance the theoretical specific capacity limit of bulk germanium even further up to 2152 $mAhg^{-1}$ [52].

2.3 X-ray scattering

Within the frame of the present thesis, elastic X-ray scattering techniques are applied to investigate the inner morphology and crystallinity with high statistical relevance. Data modeling is furthermore performed to extract quantitative information about lateral structures in probed mesoporous films. In the first section 2.3.1, basic principles of elastic X-ray

scattering are introduced. In the following sections 2.3.2 and 2.3.3, X-ray diffraction and grazing incidence small angle X-ray scattering with respectively applied approximations for data modeling are explained.

2.3.1 Basic principles

X-ray scattering refers to the interaction of an electromagnetic wave with electrons of a certain material present in the respective sample [53]. The electric field vector $\vec{E}(\vec{r})$ of a plane electromagnetic wave is described as a function of the position $\vec{r}$ as

$$\vec{E}(\vec{r}) = \vec{E_0} \exp(i\vec{k_i}\vec{r}) \tag{2.10}$$

where $\vec{E_0}$ reflects the polarization dependent amplitude and $\vec{k_i}$ is the wave vector. The modulus of the wave vector $|\vec{k_i}|$ is known as the wave number k, which is described by the wavelength λ as $|\vec{k_i}| = k = 2\pi/\lambda$. The following differential equation (Helmholtz equation) describes the propagation of such an electromagnetic wave through a medium with position dependent refractive index $n(\vec{r})$

$$\Delta\vec{E}(\vec{r}) + k^2 n^2(\vec{r})\vec{E}(\vec{r}) = 0. \tag{2.11}$$

The complex refractive index $n(\vec{r})$ is

$$n(\vec{r}) = 1 - \delta(\vec{r}) + i\beta(\vec{r}) \tag{2.12}$$

where the dispersion $\delta(\vec{r})$ and the absorption $\beta(\vec{r})$ are expressed by

$$\delta(\vec{r}) = \frac{\lambda^2}{2\pi} r_e \rho(\vec{r}) \sum_{j=1}^{N} \frac{f_j^0 + f_j'(E)}{Z} \tag{2.13}$$

and

$$\beta(\vec{r}) = \frac{\lambda^2}{2\pi} r_e \rho(\vec{r}) \sum_{j=1}^{N} \frac{f_j''(E)}{Z} = \frac{\lambda}{4\pi}\mu(\vec{r}) \tag{2.14}$$

with the classical electron radius $r_e = e^2/(4\pi\epsilon_0 m_e c^2)$, the position dependent electron density $\rho(\vec{r})$, the total number of electrons $Z = \sum_k Z_k$ with Z_k being the total number of electrons per species k and the linear absorption coefficient $\mu(\vec{r})$. The atomic form factor f_j, which describes the forced oscillator strength of the respective atom, is denoted as

$$f_j = f_j^0 + f_j'(E) + f_j''(E) \tag{2.15}$$

For small scattering vectors $\vec{q} = \vec{k_f} - \vec{k_i}$ (small momentum loss) with incident wave vector $\vec{k_i}$ and scattered wave vector $\vec{k_f}$, the first component f_j^0 can be written as $f_j^0 \approx Z_k$. In combination with the assumption of a homogeneous medium and the absence of absorption edges, the refractive index can be rewritten in a position independent form as

$$n = 1 - \frac{\lambda^2}{2\pi} r_e \rho + i\frac{\lambda}{4\pi}\mu = 1 - \frac{\lambda^2}{2\pi} Re(\mathrm{SLD}) + i\frac{\lambda^2}{2\pi} Im(\mathrm{SLD}) \tag{2.16}$$

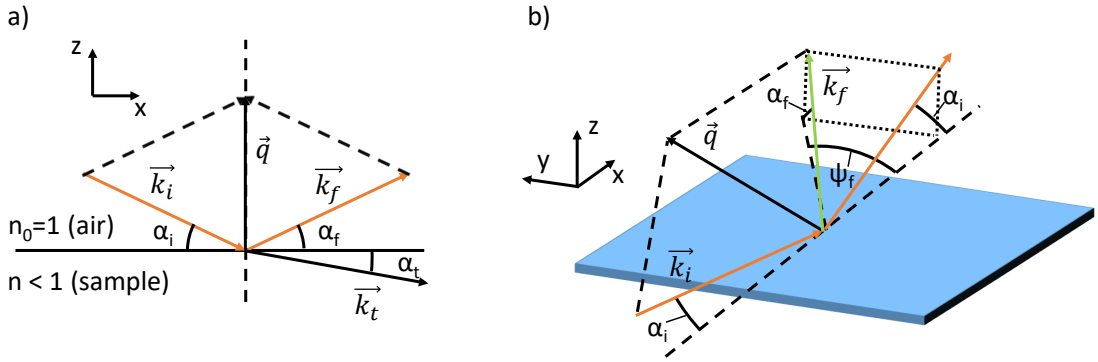

Figure 2.6: *Scattering geometry with (a) specular reflection projected onto the xz-plane and (b) off-specular, diffuse scattering in xyz representation. The incoming X-ray beam $\vec{k_i}$ impinges on the sample under a shallow angle α_i. The reflected beam (orange scattering line) in (a) and the scattered beam (green scattering line) in (b) are marked as $\vec{k_f}$. Respective angle and wave number for the transmitted beam are indexed with a "t". Note that the angle Ψ is measured between the projection of the scattered and specular reflected beam onto the substrate plane xy.*

where the product of classical electron radius and electron density $r_e\rho$ defines the real part of the scattering length density (SLD) and the absorption divided by two times the wavelength , $\mu\,(2\lambda)^{-1}$, defines the imaginary part of the SLD. Dispersion δ and absorption β for X-rays are commonly found in the order of 10^{-6} and 10^{-7}, respectively. Resulting refractive indexes are therefore typically slightly smaller than 1. The scattering contrast χ between two phases of different optical density is defined as

$$\chi = (\delta_1 - \delta_2)^2 + (\beta_1 - \beta_2)^2. \tag{2.17}$$

In Figure 2.6a the scattering geometry of a specular reflected beam in xz plane is depicted. The incoming X-ray beam $\vec{k_i}$ impinges on the sample under a shallow angle α_i. The reflected beam (orange scattering line) is marked with the wave vector $\vec{k_f}$ and the exit angle α_f. For the case of specular reflection, the condition $\alpha_i = \alpha_f$ is fulfilled. Within this frame, the xz plane is referred to as scattering plane, while the xy plane is referred to as substrate plane. In Figure 2.6b, the case of diffuse scattering is illustrated. In contrast to the specular reflection, the angle Ψ in the substrate plane is not zero for diffuse scattering out of the scattering plane. The difference between incident and scattered wave vector is defined as the scattering vector $\vec{q}$

$$\vec{q} = \vec{k_f} - \vec{k_i} \tag{2.18}$$

which represents the momentum transferred from incident beam to scattered beam. As only elastic scattering is considered within the frame of this thesis, the scattering vector $\vec{q}$ refers to a change of direction of the scattered beam in relation to the incident beam. The

modulus of scattered and incident beam is constant $|\vec{k_f}| = |\vec{k_i}| = k_0 = 2\pi/\lambda$ for elastic scattering.

The critical angle α_c of a specific material plays an important role in elastic scattering. Yoneda et al. first discovered a peak of increased intensity at the position of the critical angle (referred to as Yoneda peak) [54]. The increased intensity at this specific position can be explained through a maximum of the Fresnel coefficients. For thin films composed of multiple phases, material-sensitive analysis of the inner morphology can be carried out due to this effect.

In Figure 2.6a, also the case of a transmitted beam $\vec{k_t}$ is illustrated. For hard X-rays, the refractive index n of a material is smaller than unity. This means that the X-ray is refracted at the interface between a medium of higher density (air) to a medium of lower density (material). A refraction angle $\alpha_t = 0$ is the requirement for total external reflection and the definition of the critical angle α_c. The refraction itself is described by Snell's law

$$\cos(\alpha_i) = Re(n)\cos(\alpha_t) \tag{2.19}$$

which translates in the case of total external reflection ($\alpha_t = 0$, $\alpha_i = \alpha_c$) and small angle approximation in combination with the real part of Equation 2.16 to

$$\cos(\alpha_c) \approx 1 - \frac{\alpha_c^2}{2} = Re(n) = 1 - \frac{\lambda^2}{2\pi} Re(\mathrm{SLD}) \tag{2.20}$$

Resolving this equation to α_c leads to

$$\alpha_c = \lambda\sqrt{\frac{Re(\mathrm{SLD})}{\pi}} \tag{2.21}$$

For incident angles $\alpha_i < \alpha_c$, an evanescent wave with a small penetration depth in the range of a few nanometers is formed. In order to measure the scattering signal, the scattered beam also has to travel back through the medium, which is accounted for in the scattering depth Λ_c [55]

$$\frac{1}{\Lambda_c(\alpha_i)} = -2k_0 Im\sqrt{\alpha_i^2 - \alpha_c^2 - 2i\beta} \tag{2.22}$$

Typically, the scattering depth is approximately half of the penetration depth ($\sim$ 50 Å). For incident angles $\alpha_i = \alpha_c$, the scattering depth almost step-like increases with typical scattering depth in the order of micrometer for $\alpha_i > \alpha_c$.

2.3.2 X-ray diffraction

X-ray diffraction is a commonly employed technique to investigate the crystalline structure of respective materials. The principle is based on periodically arranged electron clouds, which act as scattering centers for an incoming X-ray beam. For a wavelength λ in the dimension of the respective periodic distance between electron clouds, the scenario can be described in form of a periodic grating with a characteristic lattice spacing d_{hkl}. Due to a difference of the path length, a characteristic interference pattern can be observed. Intensity peaks caused by constructive interference can accordingly be assigned to the crystal structure of different materials. Within the frame of the present thesis, special emphasis is put on crystalline α-Ge and anatase TiO_2. Information about the crystal order, peak position and the relative intensity for α-Ge or anatase TiO_2 phases can be extracted from Table 2.2.

	crystal order	2θ [°] at Cu K_α	rel. intensity
anatase TiO_2	(101)	25.28	100
	(103)	36.95	10
	(004)	37.80	20
	(112)	38.58	10
	(200)	48.05	35
	(105)	53.89	20
	(211)	55.06	20
α-Ge	(111)	27.28	100
	(220)	45.32	45
	(311)	53.70	28

Table 2.2: Bragg peaks of anatase TiO_2 and α-Ge in the range from 20 - 60°. Presented values are extracted from Crystallography Open Database [56, 57].

In order to derive an equation, which indicates the angle/position at which constructive interference occurs depending on the wavelength λ and the distance between crystal planes d_{hkl}, individual contributions to the total scattering intensity have to be considered. Within this frame, the atomic form factor F plays a key role and can be obtained via a Fourier transform of the electron density distribution ρ_e over the volume of the respective specimen

$$F(\vec{q}) = \int_V \rho_e(\vec{r}) \exp^{2\pi i \vec{q}\vec{r}} dV \tag{2.23}$$

In a simplified way, the atomic form factor can be seen as the geometrical shape of the electron cloud of the respective material. This property effects how an X-ray beam is scattered at the respective individual scattering center. For a crystal arrangement with multiple scattering centers N within a unit cell, the local arrangement in the respective crystal structure has to be additionally considered. This local arrangement is described through the structure factor S, which depends on the form factor of each individual scattering center of the unit cell

$$S(\vec{q}) = \sum_{k=1}^{N} F_k \exp^{2\pi i(hx_j+ky_j+lz_j)} \tag{2.24}$$

where the scattering vector $\vec{q}$ is described through a set of reciprocal unit vectors and respective values h, k, l. The structure factor S is zero, unless the Laue condition is fulfilled.

In a simplified case of specular, elastic scattering (only the modulus of $\vec{q}$ has to be considered), the Bragg equation describes the position of constructive maxima

$$2d_{hkl}\sin(\theta) = n\lambda \tag{2.25}$$

with the integer n for the respective order.

For elastic, specular scattering, the Bragg condition can be derived geometrically as depicted in Figure 2.7. The incoming X-ray beam $\vec{k_i}$ is scattered at the periodically arranged scattering centers represented as blue circles. Lattice planes with distance d_{hkl} are connected via a solid blue line. The path difference s (grey solid line) depends on the angle θ between beam and lattice plane. Note that certain intensity maxima can be oppressed due to the so-called extinction rule, which depends on the specific crystal structure, or due to orientation effects in solid thin films (texture effects).

2.3.3 Grazing incidence small angle X-ray scattering

Grazing incidence X-ray scattering geometrically has the advantage of an increased footprint at very shallow angles $\alpha_i < 1$ as compared to a transmission geometry. This is especially useful for the measurement of thin films with small amounts of deposited material. The schematic representation of the scattering geometry is depicted in Figure 2.6b. At a fixed incident angle α_i, a planar 2D detector is used to measure the scattering intensity. In this setup, the distance between sample and detector (SDD), the angle Ψ in the substrate plane and the exit angle α_f allow to define the position of every individual pixel

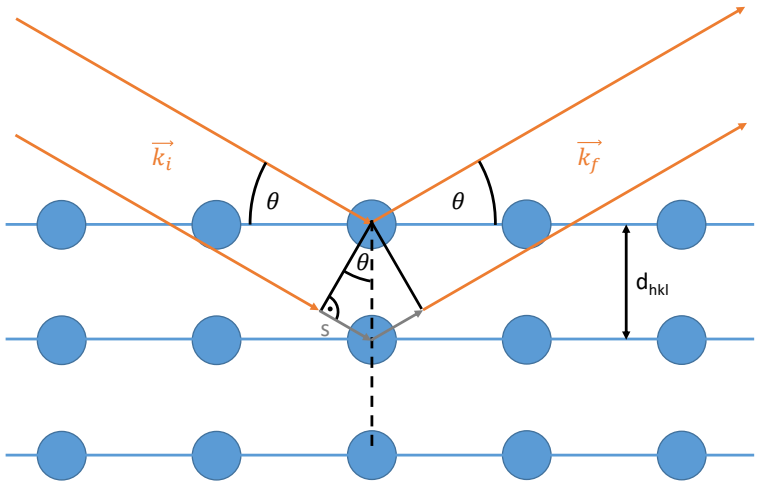

Figure 2.7: *Schematic representation of the Bragg condition. The incoming X-ray beam $\vec{k_i}$ is scattered at the periodically arranged scattering centers represented as blue circles. Lattice planes with distance d_{hkl} are connected via a solid blue line. The path difference s (grey solid line) depends on the angle θ between beam and lattice plane.*

of the detector. Together with the knowledge about the wavelength λ and the incident angle α_i, the scattering vector $\vec{q}$ can be calculated for each pixel of the detector as

$$\vec{q} = \frac{2\pi}{\lambda} \begin{pmatrix} \cos(\Psi_f)\cos(\alpha_f) - \cos(\alpha_i) \\ \sin(\Psi_f)\cos(\alpha_f) \\ \sin(\alpha_i) + \sin(\alpha_f) \end{pmatrix} \tag{2.26}$$

More information on the topic of grazing incidence small angle X-ray scattering (GISAXS) can be found in literature [54, 55, 58].

Within the frame of the present thesis, GISAXS measurements are performed to quantitatively determine length scales of the inner morphology in a respective thin film. Especially, the diffuse scattering signal is used to extract information about lateral structures. In the case of a non-ideal interface, roughness and lateral structures influence the diffuse scattering signal. These influences are accounted for in the Distorted Wave Born Approximation (DWBA) as first order perturbation theory. These perturbations cause multiple additional reflection events at the surface. A graphical illustration is shown in Figure 2.8. The differential cross section of diffuse scattering is denoted as

$$\frac{d\sigma}{d\Omega}|_{\text{diff}} = \frac{C\pi^2}{\lambda^4}(1-n^2)^2|T_i^F|^2|T_f^F|^2 P_{\text{diff}}(\vec{q}) \propto P_{\text{diff}}(\vec{q}) \tag{2.27}$$

with the illuminated area C, the Fresnel transmission coefficients T for incident and scattered beam and the diffuse scattering factor P_{diff}. Since $\frac{d\sigma}{d\Omega}|_{\text{diff}} \propto P_{\text{diff}}$, the diffuse scattering factor directly affects the scattered intensity [58]. Additionally, the Fresnel

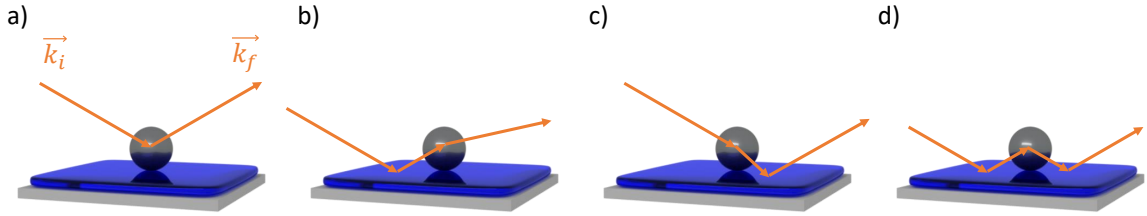

Figure 2.8: *Graphical illustration of four superimposed cases in the Distorted Wave Born Approximation. (a) The incoming X-ray beam is scattered with no additional reflection, (b) with a reflection before scattering, (c) with a reflection after scattering and (d) reflection before and after scattering.*

coefficients in Equation 2.27 have a maximum, if the incident or the scattered angle is equal to the critical angle α_c. As the critical angle in turn depends on the SLD of the respective material, the Fresnel coefficients give rise to a material characteristic peak (Yoneda peak). Performing horizontal line cuts at the Yoneda peak position allows to extract material characteristic information of lateral structures through modeling.

Data modeling presented in this thesis is based on the DWBA using the Effective Interface Approximation (EIA). In the EIA the scattering object is assumed to have only one specific surface, which allows to decouple the height and the radii of scattering objects. With N identical objects of a specific Gaussian distribution for form factor F (spherical or cylindrical) and structure factor S, the diffuse scattering factor is given by

$$P_{\text{diff}}(\vec{q}) \propto NS(\vec{q})F(\vec{q}) \tag{2.28}$$

Note that in the case of GISAXS, the form factor F is referring to the Fourier transform of the electron density distribution over a domain size from $\approx$ 1 nm up to 1 μm. The structure factor S is referring to the distance of objects described by the form factor F and placed on a periodic, 1D paracrystalline lattice. Up to three cylindrical / spherical form factors with respective structure factors are used for data modeling. Thereby, it is assumed that objects of different form factor and structure factor do not interact with each other (Local Monodisperse Approximation).

3 Methods

Within the frame of the present thesis, mesoporous thin films on the basis of TiO_2 and Ge were synthesized. To prove that the respective films are both surface- and bulk-tunable, real and reciprocal space characterization techniques were applied. Information about the composition, crystallinity and band structure was obtained through spectroscopic characterization for a potential application in the field of hybrid photovoltaics. Additionally, extracted information with respect to structure and composition was used to explain the outstanding performance of fabricated lithium ion batteries. The present chapter introduces methods utilized for structural characterization in section 3.1, while section 3.2 refers to applied spectroscopic characterization methods.

3.1 Structural characterization

Various novel approaches to manufacture size-tunable, mesoporous thin films are introduced in this thesis. To analyze their structure from a macroscopic to a mesoscopic scale, different characterization techniques in reciprocal and real space are exploited. Profilometry is applied to determine the thickness of synthesized thin films, while a macroscopic investigation of surface structures is carried out via optical microscopy (OM). Scanning electron microscopy (SEM) measurements serve to extract mesoscopic information about porous structures on the surface and in cross-section. Due to charging effects, surface characterization of composite thin films before calcination is carried out via atomic force microscopy (AFM) instead of SEM. X-ray diffraction (XRD) is applied to extract information about crystalline material phases. To prove that manufactured samples are not only surface-porous but also bulk-porous throughout the entire film, grazing incidence small angle X-ray scattering is performed. Moreover, quantitative information about the nanomorphology was extracted from GISAXS measurements.

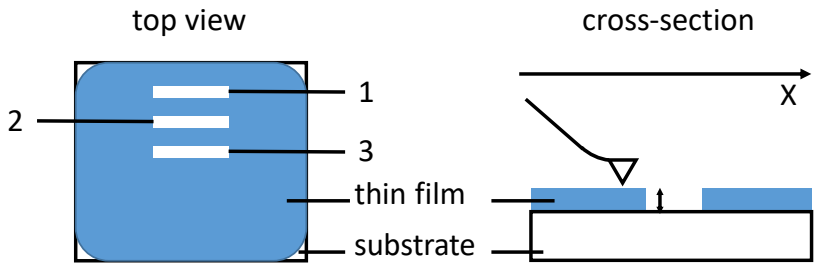

Figure 3.1: *Top view of a sample with multiple scratches for thickness determination via profilometry. The cross-section view shows the tip represented as a triangle scanning over the valley of a scratch. The difference between hill mean height and valley mean height is defined as the thin film thickness.*

3.1.1 Profilometry

A Stylus Profiler DektakXT fabricated by Bruker is used to determine the thickness of thin films. For this purpose, a tip with a curvature of 2 μm scans along the surface of the sample. The tip is pressed to the surface with a small vertical force (1-2 mg). Softer materials like polymers usually require a smaller stylus force to avoid tip-induced surface deformation. The z-position of the tip directly reflects the height profile of the sample. The scan speed is set to 40 μm s^{-1}. In order to derive the thickness, the films is scratched down to the surface of the substrate. The tip then scans perpendicularly over the scratch. By comparison of valley and hill mean height levels, the local thickness can be determined. The procedure is carried out several times over multiple scratches to exclude possible local differences in film thickness. Data acquisition and analysis are performed with the software Vision64 by Bruker. A sketch showing a sample with several scratches prepared for profilometry is depicted in Figure 3.1. The cross-section view shows the tip scanning over an exemplary scratch of the sample.

3.1.2 Optical microscopy

Optical microscopy can be used to obtain magnified real space images of a sample. Within this scope, structures in the micrometer range can be easily resolved. Optical microscopy is a easily-applicable technique to probe the homogeneity and the quality of a synthesized sample. A Carl Zeiss Axiolab A microscope with adjustable magnification in the range from 1.25x to 100x is used. A PixeLink USB Capture BE 2.6 charge couplet device camera enables digital image acquisition with a resolution of 1280x1024 pixel. Illumination is realized via a halogen Hal 100 lamp. Data analysis of acquired images can be performed with the software ImageJ [59].

The resolution of a conventional visible light microscope is given by the Rayleigh criterion

$$R = \frac{1.22\,\lambda}{2\,\mathrm{NA}} \tag{3.1}$$

where NA is the numerical aperture and λ the wavelength of the illumination source. With the largest magnification of 100x and an exemplary wavelength of 500 nm, a resolution of approximately 500 nm can be achieved. Parameters for different objectives are summarized in Table 3.1.

magnification	NA	pixel size [μm]	resolution [μm]
1.25 x	0.035	6.3	12.2
2.5 x	0.075	3.2	5.7
10 x	0.20	0.8	2.1
50 x	0.70	0.16	0.61
100 x	0.75	0.08	0.57

Table 3.1: Magnification, numerical aperture, pixel size and resolution for different objectives of the optical microscope Axiolab A from Carl Zeiss.

An illustration of the light path inside a microscope is shown in Figure 3.2[1]. Visible light is used as an illumination source and the object lens serves to generate a magnified real image. Utilization of the eye piece allows to observe a magnified virtual image.

3.1.3 Scanning electron microscopy

Scanning electron microscopy (SEM) is used to resolve structures of synthesized mesoporous thin films. Compared to visible light microscopy, higher resolution can be achieved and structures in the order of nanometer can be observed. The improved resolution is mainly attributed to the comparably smaller electron wavelength as compared to visible light microscopy. The wavelength of an electron follows the de Broglie relation

$$\lambda_e = \frac{h}{p_e(U_B)} \tag{3.2}$$

where λ_e is the wavelength of the electron, h the Planck's constant and $p_e(U_B)$ the momentum of the electron depending on the acceleration voltage U_B.

[1]Illustration redrawn on the basis of the Leica Mircosystems online-tutorial "Optical Microscopes - Some Basics" provided by H. Rühl, 2019 [online]. Available: https://www.leica-microsystems.com/

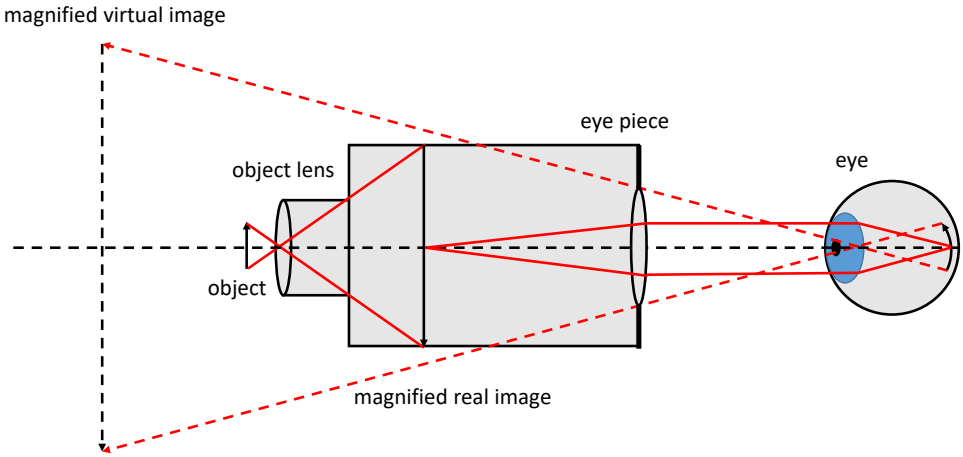

Figure 3.2: *Schematic overview of the light path inside a microscope. The object lens serves to generate a magnified real image of an object. Utilization of the eye piece allows to observe a magnified virtual image.*

A schematic overview of a SEM is shown in Figure 3.3. Electrons are either emitted thermally or through application of a field emission voltage. Subsequently, electrons are accelerated towards an anode by an acceleration voltage U_B in the range of several keV. The applied acceleration voltage especially defines the wavelength / energy of emitted electrons. Electromagnetic condenser lenses serve to shape the electron beam and to focus the beam onto the respective sample. Narrow-shaped beams typically allow for an improved resolution as compared to broader shaped beams. Scanning coils then control the beam deflection / line-by-line scanning movement. The incoming electron beam causes three main types of emission: secondary electrons with small escape depth due to low energy, backscattered electrons with large escape depth due to high energy and characteristic X-rays with the highest escape depth. Position of detector in combination with a de-acceleration bias voltage then allows to detect electrons of a certain energy. Image acquisition for structural analysis is usually performed through detection of secondary, low-energy electrons. The number / intensity of detected secondary electrons is plotted against the scanning position. Thereby, a grey scale image can be reconstructed. Among other parameters, the brightness value depends on the specific material, height and geometry of the scanned area. Edges typically appear especially bright. As these influences on brightness cannot easily be decoupled, SEM only gives a qualitative impression of the topography.

All SEM measurements presented in this thesis are obtained with a Zeiss Gemini NVi-

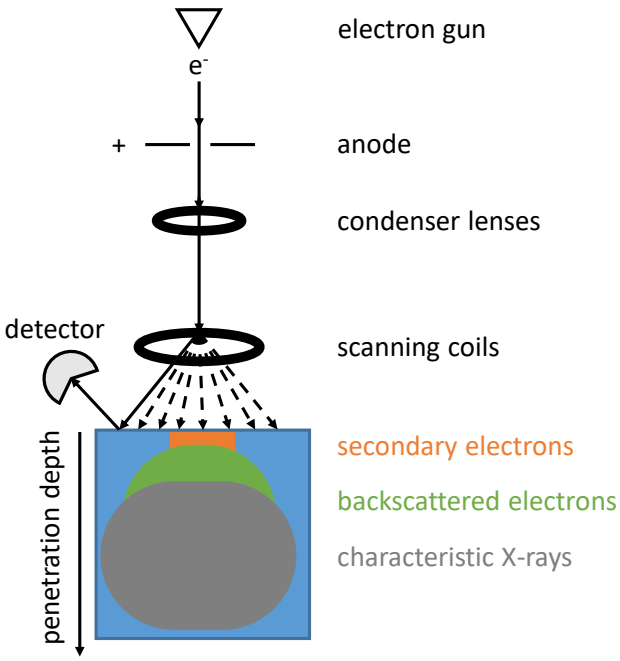

Figure 3.3: *Schematic overview of a scanning electron microscope setup. Electrons are emitted from the electron gun and accelerated towards the anode. Electromagnetic condenser lenses and scanning coils are used to shape and focus the e^--beam on the sample while scanning over the surface. Detectable secondary electrons are typically emitted from surface-near regions, while backscattered electrons and characteristic X-ray radiation steam from regions of increased penetration depth.*

sion 40[2] controlled by the software SmartSEM. Working distances and acceleration voltages were optimized in the range from 0.5 to 3.6 mm and 0.4 to 5 kV, respectively, to reduce local charging effects, while simultaneously maintaining high resolution. The In-Lens detector was primarily used for secondary electron detection.

Data analysis was performed via the software ImageJ. Within this frame, special focus was put on domain size analysis. Application of an Otsu algorithm is considered the best way to obtain a reasonable threshold value for binary image transformation from measured SEM images [60]. Neighboring pores were additionally separated via the noise reduction function and the so-called "erode" function. The ratio of black void area to the total area of the image is used as an estimation for the local surface porosity. As a last step the "analyze particle" function can be employed to extract the particle size distribution.

[2]Measurements with the Gemini NVision 40 were performed at the chair of Prof. A. Holleitner (Walter Schottky Institute, TU München)

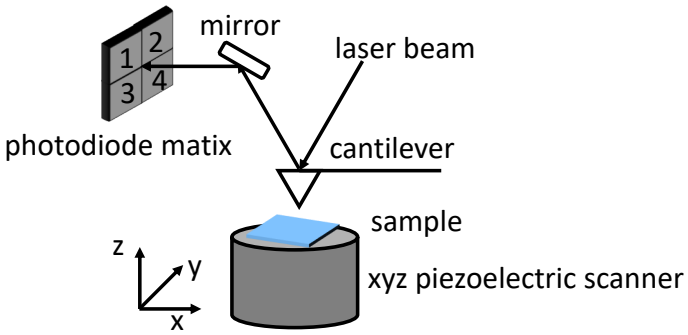

Figure 3.4: *Illustration of the working principle of an atomic force microscope. A laser beam is reflected from the backside of a cantilever to a mirror and photodetector matrix. Sample movement is realized via piezoelectric motors, which control the 3D-position of the sample stage.*

3.1.4 Atomic force microscopy

Atomic force microscopy (AFM) is a near-field technique, where the typical resolution limit $r \sim \lambda$ of diffraction-based microscopes (e.g. SEM, OM) does not apply. Spatial resolution on a molecular scale can be achieved and strongly depends on the diameter $d \ll \lambda$ of the employed tip. Unlike for optical or scanning electron microscopy, topographic information (e.g. height, roughness) can be extracted quantitatively. The working principle, invented by Bining, Quate and Gerger, is based on the interaction between a very sharp tip in close proximity to a sample and the sample itself [61]. The potential V as a function of distance r between sample and tip is described via the Lennard-Jones potential

$$V(r) = \frac{C_1}{r^{12}} - \frac{C_2}{r^6} \tag{3.3}$$

with constants C_1 and C_2, a term accounting for Pauli repulsion $C_1\, r^{-12}$ and a term accounting for attractive dipole-dipole interaction $-C_2\, r^{-6}$.

Core elements of an AFM are illustrated in Figure 3.4. A laser beam is initially focused onto the backside of a cantilever with the help of an optical microscope. The cantilever acts as a support for the tip and is part of the oscillator system composed of tip and cantilever. Any oscillation of the cantilever can be detected via a segmented photodiode via a change of deflection of the reflected laser beam. Piezoelectric motors control the scanning xy- and height z-movement of the sample.

The three main operation modes are contact, non-contact and tapping mode. Contact mode is based on operation in the Pauli repulsion regime (close distance between sample and tip). A feedback system usually controls the sample movement in a way that the deflection force on the cantilever is constant. This mode is usually used for fast scanning

and rigid samples only. Main reason for this are strong forces in this mode increasing the likeliness of measurement-induced sample damage. In contrast, non-contact and tapping mode are operated in a regime of increased sample-tip distance as compared to contact mode and attractive van der Waals forces become more dominant. An additional piezoelectric drive with frequency f forces the cantilever to oscillate. The resulting movement of the cantilever can be described by a differential equation including the driving force, the Pauli repulsion, the van der Waals attraction and the spring constant of the cantilever. As a result of the interaction, the amplitude, frequency and phase of the driving oscillation and the forced oscillation are different. Measurement of forced amplitude, frequency and phase allows to reconstruct the surface topography in combination with material contrast of the investigated sample. Usually, a feedback system in this operation mode is adjusted to keep the amplitude of the oscillation constant. Measurement-induced damage to a sample is less likely in this operation mode as compared to contact mode. Especially, the tip is less likely to break due to sharp and deep height variations in the thin film.

Surface topography investigation of uncalcined, composite films were carried out with a MFP-3D (Asylum Research) instrument.[3] Tapping mode was used at ambient conditions. Employed tips had a curvature radius of 7 nm and were mounted onto a cantilever (OMCL-AC240TS-R3, Asylum Research) with a spring constant of 2 N m^{-1}. Resonance frequencies were found around 70 kHz. Raw images were processed and analyzed using the software Gwyddion, which allows for tilt and polynomial background correction [62].

3.1.5 X-ray diffraction

X-ray diffraction (XRD) measurements were performed to extract information about the crystallinity of mesoporous Ti/Ge-based thin films. Exact positions of diffraction peaks were determined through fitting via Gaussian functions. Thereby, crystalline phases of Ge (α-Ge) or titania (anatase TiO_2) were identified.

A schematic overview of a typical setup used for XRD measurements is illustrated in Figure 3.5. For XRD measurements presented in the thesis, a Bruker D8 ADVANCE X-ray diffractometer was used. X-rays are generated via a copper anode at a voltage of 40 kV and a current of 40 mA. Characteristic Cu K_α radiation is emitted and shaped through a slit system. Measurements are performed in a coupled θ-2θ configuration. The X-ray beam impinges on the 2 x 2 cm^2-sized samples (Si or glass) under an angle θ while the detector is placed at an angle 2θ (specular position). Scans are typically performed in the range from 5° up to 80° with a step size of 0.04° for Ti-based films and up to

[3] AFM measurements were performed at the chair for semiconductor nanostructures and quantum systems (Prof. J. Finley, Walter Schottky Institute, TU München)

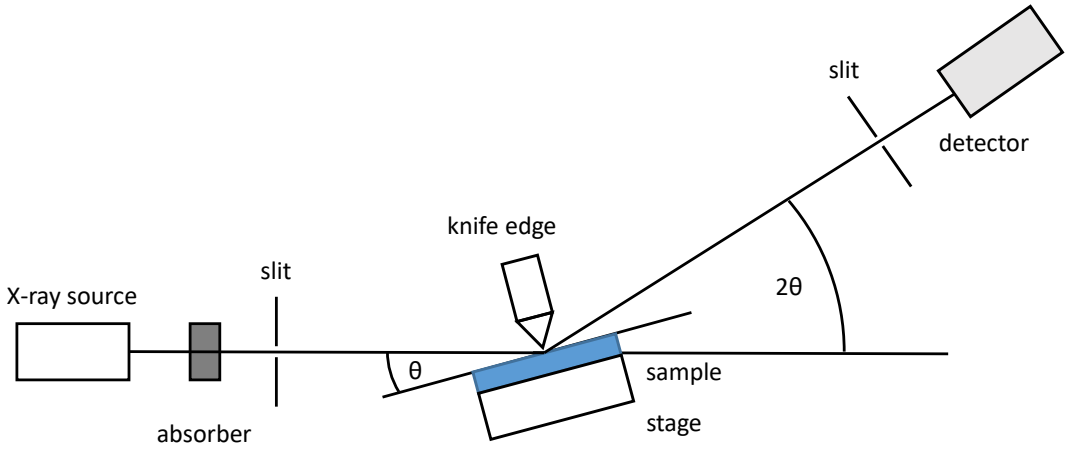

Figure 3.5: *Schematic overview of a typical setup used for X-ray diffraction measurements. A X-ray beam is guided through an absorber and slits before impinging at an angle θ on approximately 2 x 2 cm^2-sized samples. The angle-dependent diffraction pattern in a coupled θ-2θ configuration is measured via a point detector.*

0.01° for Ge-based thin films. Each data point was measured up to 50 s to improve the signal to noise ratio. While sample alignment was carried out with a 0.2 mm-, 0.05 mm- and 0.2 mm-sized slit system, the final data acquisition was performed with two 0.6 mm-sized slits. After background subtraction, the software Origin was used for Gaussian peak fitting. Peak positions were compared with literature cited in the respective chapter to identify crystalline phases of the material.[4]

3.1.6 Grazing incidence small angle X-ray scattering

Grazing incidence small angle X-ray scattering (GISAXS) is a technique to obtain information about the inner morphology of thin films. Within this scope, structure sizes and distances of repeating units can be quantitatively extracted through data modeling in a typical range from 1 nm to 1 μm, which is primarily defined by the sample detector distance (SDD). The applied model and the background of grazing incidence X-ray scattering is described in section 2.3.3. Further advantage of the applied technique is the extraction of properties over a large probing volume of the sample with high statistical relevance and in a non-destructive way. A schematic illustration[5] of a GISAXS setup in reflection geometry is depicted in Figure 3.6. The X-ray beam $\vec{k_i}$ impinges on the sample

[4]For the identification of metal-organic compound, Ge-based crystalline phases the website http://crystallography.net/ was especially useful. 2019 [online]

[5]Illustration was redrawn from [63] with "Blender", a free and open source 3D creation software.

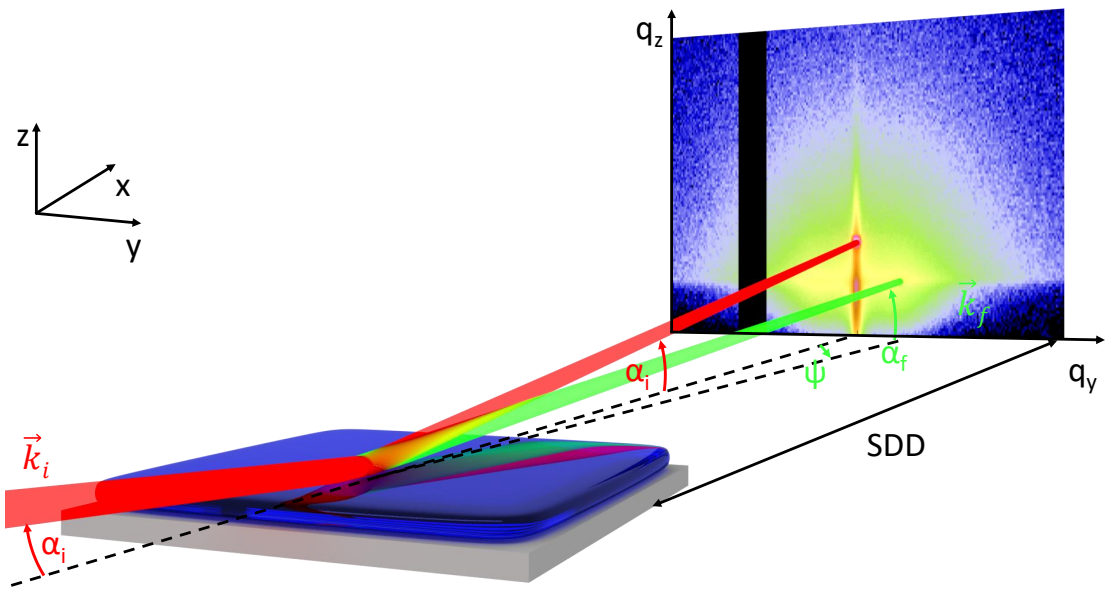

Figure 3.6: *Schematic overview of a typical setup used for grazing incidence small angle X-ray scattering. The X-ray beam $\vec{k_i}$ impinges on the sample surface under a shallow angle α_i. The scattered signal $\vec{k_f}$ is detected through a 2D detector and defined through the angle α_f (angle between horizon and scattered beam in the xz-plane) and Ψ (angle between incident beam and scattered beam in the xy-plane). The special case of the specular reflected beam ($\alpha_i = \alpha_f, \Psi = 0$) is indicated via the red beam. The 2D detector shows an exemplary GISAXS pattern of mesoporous TiO_2.*

surface under a shallow incident angle α_i. The scattered signal $\vec{k_f}$ is detected through a 2D detector and defined through the angle α_f (angle between horizon and scattered beam in the xz-plane) and Ψ (angle between incident beam and scattered beam in the xy-plane). The special case of the specular reflected beam ($\alpha_i = \alpha_f, \Psi = 0$) is indicated via the red beam in Figure 3.6. The 2D detector shows an exemplary GISAXS pattern of mesoporous TiO_2.

GISAXS measurements were carried out at the MiNaXS beamline P03 of the PETRAIII storage ring at DESY[6] with a high brilliance X-ray source and at the Chair for Functional Materials with a lab-scale Ganesha 300 XL SAXS-WAXS instrument. A summary of specifications used for the different GISAXS measurement setups is given in Table 3.2.

In the Ganesha instrument, Cu K_α radiation with a wavelength of $\lambda = 1.54$ Å was used as X-ray source. For each measurement, the sample detector distance was fixed to 1.056 m and an incident angle above the critical angle of the material was chosen. The

[6]DESY stands for Deutsches Elektronen-Synchrotron and is located in Hamburg, Germany

	Ganesha	P03 DESY
wavelength λ [Å]	1.54	0.94
incident angle α_i [°]	0.35-0.45	0.35-0.4
SDD [m]	1.056	3.166-4.337
detector size (h x v) [pixel]	619 x 487	1043 x 981
pixel size (h x v) [μm]	172 x 172	172 x 172
beam size (h x v) [μm]	200 x 100	24 x 12
footprint$_x$ [cm]	$\sim$ 1.6	$\sim$ 0.2

Table 3.2: Summary of specifications used for grazing incidence small angle X-ray measurements with the Ganesha SAXSLAB and at the beamline P03 at DESY. Note that "h x v" stands for "horizontal x vertical" and the footprint$_x$ refers to a direction along the x-axis (see Figure 3.6).

X-ray beam was vertically and horizontally shaped to 100 μm and 200 μm, respectively. Incident angles were chosen in the range from 0.35° to 0.45°. Exact values are given in the respective result chapters. Incident angle and vertical beam size combined result in a footprint in beam direction of approximately 1.6 cm. Data acquisition was realized via a Pilatus300K detector with a total of 619 x 487 pixels (single pixel size of 172 x 172 μm^2). The setup is evacuated to minimize air-induced scattering.

Synchrotron-based GISAXS measurements at DESY were performed with a wavelength of λ = 0.94 Å and an incident angle between 0.35° and 0.4°. The lower wavelength at the beamline results in a lower critical angle of the material, which was calculated prior to beamtime. The sample detector distance was varied in a range between 3.166 m and 4.377 m. An evacuated flight tube is installed in between sample and detector to minimize air-induced scattering. Due to the high brilliance, a significant smaller-shaped beam of 12 x 24 μm ($\sim$ 0.2 cm footprint in beam direction) was able to provide sufficient statistics in a shorter amount of time. Additionally, two different beamstops were needed to prevent the detector from oversaturation (direct and specular beamstop). Data acquisition was realized via a Pilatus1M with a total of 981 x 1043 pixel (single pixel size of 172 x 172 μm^2). Specific information concerning the individual measurement time and exact incident angle for different types of samples is provided in the respective result chapter.

Line cuts of 2D GISAXS images for analysis were performed with the software DPDAK [64]. An exemplary 2D GISAXS image of a mesoporous TiO_2 thin film obtained with the Ganesha instrument is depicted in Figure 3.7. Vertical line cuts (detector cut, red dotted line) were performed to determine the material characteristic Yoneda peak position (marked as $\alpha_f = \alpha_{\text{crit}}$) of the investigated thin film [54]. The position of the Yoneda peak especially depends on the density of the material and the respective elemen-

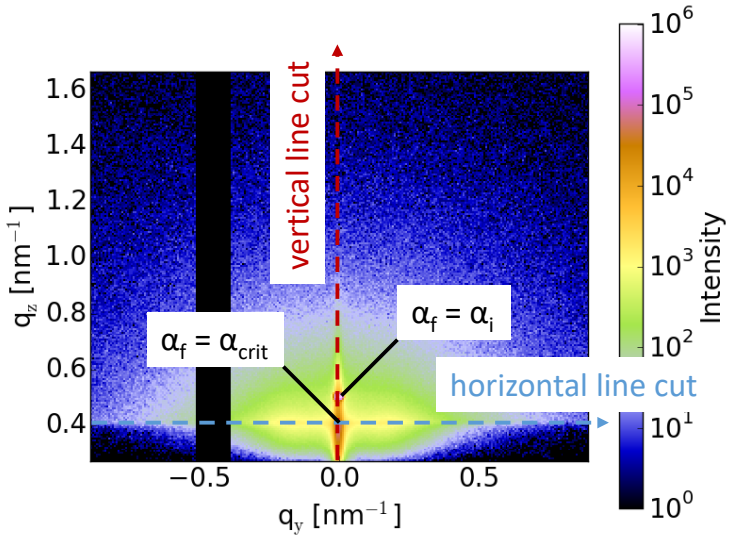

Figure 3.7: *Exemplary 2D grazing incidence small angle X-ray scattering image of a mesoporous TiO_2 thin film obtained with a Ganesha instrument. Vertical line cuts (detector cut, red dotted line) were performed to determine the Yoneda peak position (marked as $\alpha_f = \alpha_{\text{crit}}$). The specular reflection is marked as $\alpha_f = \alpha_i$. Horizontal line cuts (out-of-plane cuts, blue dotted line) at the q_z position of the Yoneda peak were performed to quantitatively determine lateral structures in the respective thin film.*

tal/chemical composition. The specular reflection is marked as $\alpha_f = \alpha_i$. Horizontal line cuts (out-of-plane cut, blue dotted line) at the identified q_z position of the Yoneda peak were performed to quantitatively extract information about structures perpendicular to the surface plane of the substrate (lateral structures). Data modeling of horizontal line cuts was realized via a custom-made and Python-based macro.[7] The employed model is based on the DWBA and EIA using up to three spherical or cylindrical form factors distributed on a respective 1D paracrystal lattice (translates into structure factor). Both structure and form factor are described through a Gaussian distribution [65]. The low q_y regime is modeled through an instrument-dependent, Lorentzian resolution function. Additional theoretical aspects are explained in section 2.3.3.

3.2 Spectroscopic characterization

One main objective of applied spectroscopic characterization within the frame of the present thesis consists in analysis of the material composition of mesoporous thin films fabricated via novel synthesis approaches. Additionally, insight into material character-

[7]The Python-based macro was developed in-house by C. Schaffer and D. Magerl (Physik-Department, TU München)

istic properties is obtained. Within this frame, UV/Vis spectroscopy is performed to reveal information about the specific absorption behavior especially relevant in the field of PV. Additionally, extraction of the optical band gap through UV/Vis spectroscopy is possible through extrapolation in a Tauc plot [66]. Furthermore, Fourier transform infrared spectroscopy (FTIR) is employed to analyze the molecular structure, while X-ray photoelectron spectroscopy (XPS) is measured to focus on the elemental composition in surface-near regions of respective samples.

3.2.1 UV/Vis spectroscopy

Light absorption properties of solid thin films are measured from ultraviolet to near-infrared via UV/Vis spectroscopy (UV/Vis). For this purpose two different instruments, namely a Lambda 35 (PerkinElmer) and a Lambda 900[8] (PerkinElmer), are used. Both instruments are controlled via the software Winlab (PerkinElmer). The Lambda 35 comes with a halogen lamp for near-infrared and visible light spectroscopy and a deuterium lamp used for spectroscopy in the ultraviolet region. An automatic lamp switch is carried out at 326 nm. In total, the Lambda 35 covers a probing range from 190 nm to 1100 nm. In contrast, the Lambda 900 is used to measure thin films with an extended probing range from 175 nm to 3300 nm, which is especially useful to determine the small band gap of Ge-based thin films (bulk Ge: 0.67 eV). A scan speed of 120 nm min^{-1} is chosen for the Lambda 35 and 100 nm min^{-1} for the Lambda 900. Both instruments are operated with a slit width of 1 nm.

In Figure 3.8[9] a schematic overview of the Lambda 35 is given. Initially, either a deuterium or a halogen lamp is used as a light source. Light is then guided through an optical system of mirrors and filters. Within this frame, the filter wheel functions as a pre-filter of the emitted light. The pre-filtered light enters and exits the monochromator unit (grating) through slits, which influence the spectral width of the selected wavelength λ by the monochromator. The light beam of wavelength λ is then split into reference and sample beam. While the reference beam is typically guided through a bare glass substrate, the sample beam hits the substrate covered with the respective thin film. Transmission intensities are measured via photodiodes. Logarithmic subtraction of reference transmission intensity $I_0(\lambda)$ from the sample transmission intensity $I(\lambda)$ allows to eliminate the glass substrate contribution from the measured data.

[8]Measurements with the Lambda 900 were carried out by David Müller and Hannah Schamoni at the Walter Schottky Institute (Stutzmann group, Lehrstuhl für experimentelle Halbleiterphysik, TU München)

[9]Schematic overview (Figure 3.8) was redrawn according to information obtained from PerkinElmer, "Lambda 25, 35, 45 user's guide", 2019 [online]. Available: http://people.bath.ac.uk

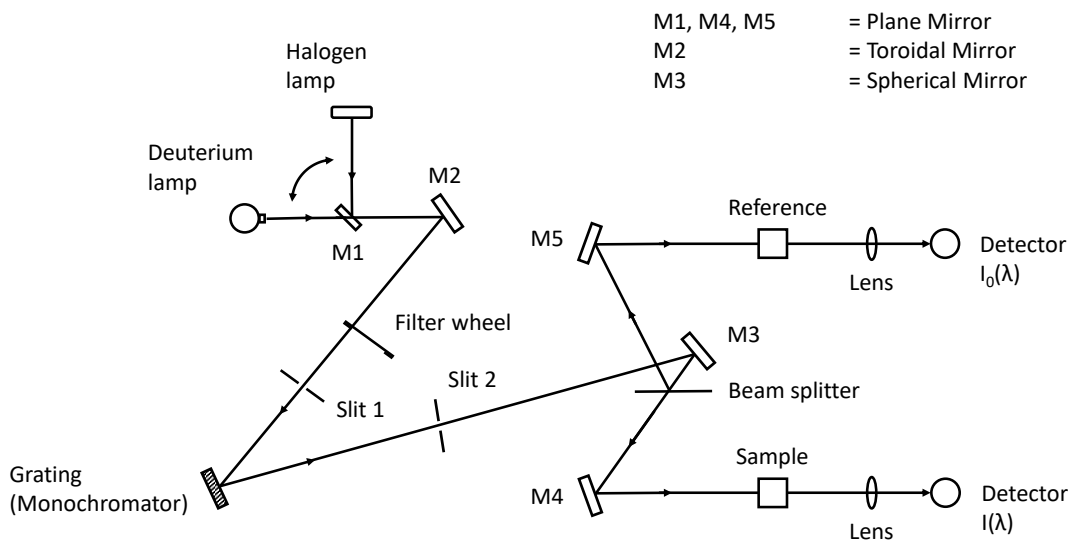

Figure 3.8: *Schematic overview of the light path inside a Lambda 35 UV/Vis spectrometer from PerkinElmer. Generated light is guided through an optical system and hits the sample. Transmission intensity is then detected via a photodiode. Respective mirror types are marked as M1-M5 in the legend.*

The absorbance A of the probed thin film is related to the absorption coefficient $\alpha(\lambda)$ of the respective material with thickness d by the Lambert-Beer law. The absorbance A can be obtained from the measured transmission intensity of the reference beam $I_0(\lambda)$ and sample beam $I(\lambda)$ as follows

$$A(\lambda) = -\log_{10}\left(\frac{I(\lambda)}{I_0(\lambda)}\right) = d\alpha(\lambda)\log_{10} e \tag{3.4}$$

To derive the absorption coefficient α, knowledge about the thickness d of the respective thin film is required.

A requirement for absorption is that the energy of the incoming photon is larger than the bandwidth in case of probing semiconductor material. Therefore, UV/Vis measurements also provide information about the band structure of the specific material. In turn, the band structure is strongly correlated to the crystallinity / structure of the probed material. In order to extract the band gap energy E_g of the probed film from UV/Vis transmission measurements, $(AE)^n$ is plotted against the photon energy $E = hc\,\lambda^{-1}$ with the Planck's constant h and the speed of light c. By linear extrapolation and determination of the intersection with the x-axis, the optical band gap energy can be extracted using the Tauc equation [66] as follows

$$(AE)^n = B(E - E_g) \tag{3.5}$$

The exponent n is reflecting the type of investigated band gap. Direct band gaps require $n = 2$ while indirect band gaps require $n = 1/2$. The Tauc equation was historically used to derive the indirect band gap of germanium. Similarly, the Tauc plot is used in the present thesis to derive the band gap of Ge-based, porous thin films. However, impact of the nanostructure on optical properties and increased scattering due to the porous nature of investigated thin films are not easily decoupled.

3.2.2 Fourier transform infrared spectroscopy

Fourier transform infrared spectroscopy (FTIR) is a technique to probe the molecular structure within the investigated material through excitation of vibrational states. In the current thesis, FTIR spectroscopy is primarily used to analyze Ge-based samples with special focus on polymeric template remains residing inside the thin film. Compared to standard infrared spectrometers, FTIR spectrometer typically have a larger range of excitation wavelengths. A non-monochromatic light source is used to generate an infrared spectrum (4000-700 cm^{-1}). Fourier transformation is then applied to reconstruct the typical wavelength vs. absorbance spectra. Key advantages of FTIR spectroscopy consist in good signal to noise ratio, a polychromatic light source and high excitation wavenumber precision.

A schematic overview of the light path inside a FTIR spectrometer is given in Figure 3.9. IR light is generated and guided to a Michelson interferometer. The beam in split into reflected beam R_1 and transmitted beam T_1 via a beamsplitter. The transmitted beam T_1 is reflected at a moving mirror. Thereby, the optical path difference between reflected beam and transmitted beam can be changed. The combined beam C_1 then passes through the sample and the intensity is measured as a function of the mirror position x (so called interferogram). The difference of the optical path goes along with the occurrence of constructive and destructive interference. At zero optical path difference, a maximum can be found. Since the IR source generates non-monochromatic light, the intensity of the interference pattern decreases with increasing optical path difference. The obtained interferogram is then translated into a single beam spectrum (intensity vs. wavenumber) through Fourier transformation. Absorbance peaks arise due to excitation of vibrational modes (bending or stretching) of a molecule.

Through comparison with literature, different peaks can be assigned to periodic motion (vibrations) between certain atoms of the molecule. An example of an FTIR spectrum for a composite PS-b-PEO/K_4Ge_9 thin film is given in Figure 3.10. The broad peak around 3500 cm^{-1} is typically caused by the presence of residual water, while polymer template based vibration peaks mainly arise in the region from 1000-1800 cm^{-1}. Spectra shown in

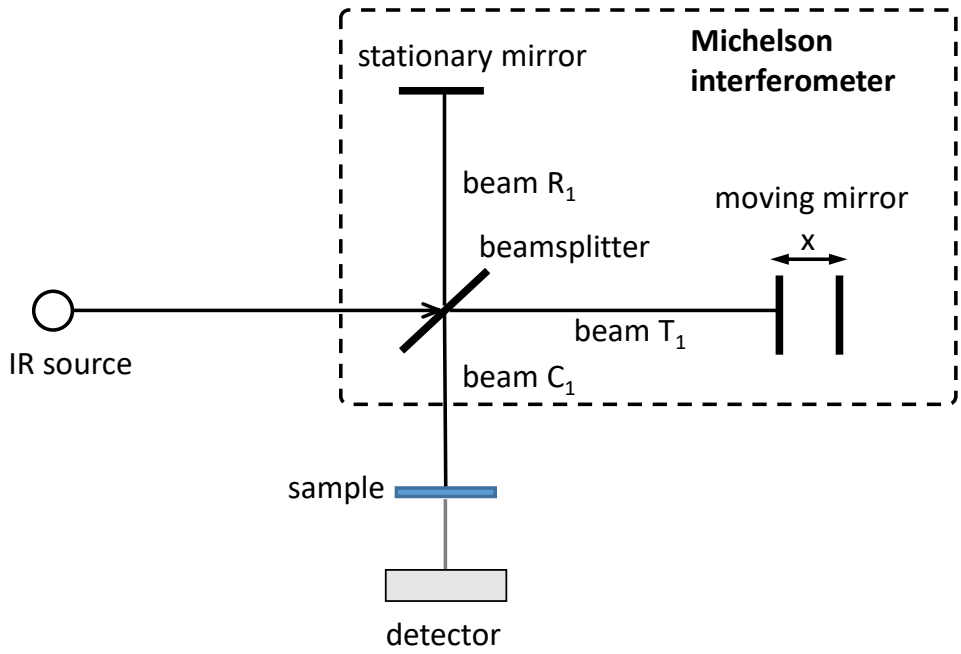

Figure 3.9: *Schematic overview of the light path inside a Fourier transform infrared spectrometer. An IR source is used to generate polychromatic light, which is split into reflected beam R_1 and transmitted beam T_1. A moving mirror serves to change the optical path difference between reflected and transmitted beam. The combined beam C_1 is then guided through the sample, where vibrational states can be excited. An IR detector is used to record the resulting interferogram.*

the present thesis are recorded with an Equinox 55 by Bruker and the instrument is operated with the software Opus v6.0. The standard procedure consists of the measurement of a background spectrum I_0 with the bare substrate, followed by the sample spectrum I with the actual sample installed in the spectrometer. The final absorbance A is calculated via

$$A = \log\left(\frac{I_0}{I}\right) \tag{3.6}$$

3.2.3 X-ray photoelectron spectroscopy

X-ray photoelectron spectroscopy (XPS) is a technique to investigate the elemental composition of a respective thin film. A schematic overview of a XPS setup is shown in Figure 3.11. X-rays with a photon energy $\hbar\omega$ are generated typically as Al K_α or Mg K_α radiation with photon energies of 1486.6 eV and 1253.5 eV, respectively. The photon energy $\hbar\omega$ can get completely absorbed by electrons inside the investigated sample. In order to

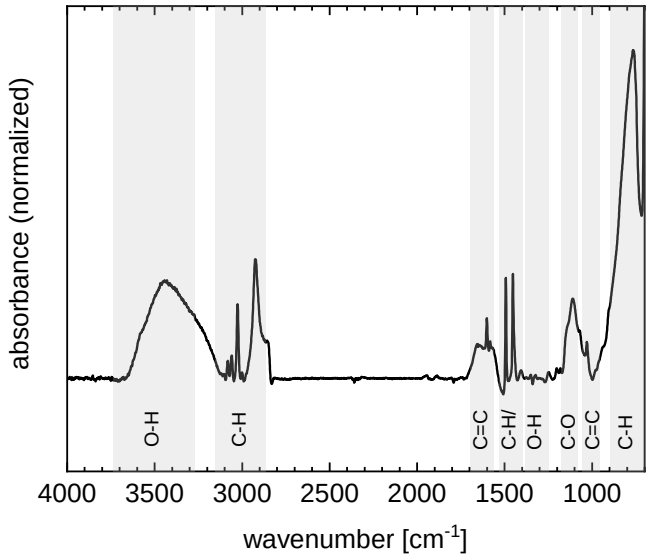

Figure 3.10: *Absorbance spectrum of a composite PS-b-PEO/K_4Ge_9 thin film measured via FTIR spectroscopy. Different vibration modes can be identified through comparison with literature databases. Grey areas with insets indicate spectral regions, where specific vibration modes commonly occur.*

be able to escape the surface of the sample, the electron requires a transferred energy larger than the sum of binding energy E_B and workfunction Ω_w. All additional energy is used to excite the electron to states of higher kinetic energy E_{kin} (movement). The relation can be written as

$$E_{kin} = \hbar\omega - E_B - \Omega_w \tag{3.7}$$

The number of electrons with a kinetic energy E_{kin} are measured through a hemispherical analyzer with an electron detector. In a typical XPS spectrum, E_B is plotted against the number of photoelectrons with this specific energy. As each chemical element has distinct and different core-level binding energies, the recorded spectrum can be used to reconstruct the elemental composition at the sample surface. Limitation to surface-near regions (∼10 nm) is caused by the typical strong interaction of electrons and solid matter [67]. As a result, the inelastic mean free path λ_e is very short. In addition to core-level emission, Auger emission lines can be be observed if the hole generated in the respective core-level is filled by an outer-shell electron. The energy difference is absorbed by an outer shell electron, which is consequently also emitted from the sample surface and detected. Auger transitions are commonly labeled with XYZ, where X indicates the shell of the initial core-level hole, while Y, Z represents the outer shell of the respective electrons.

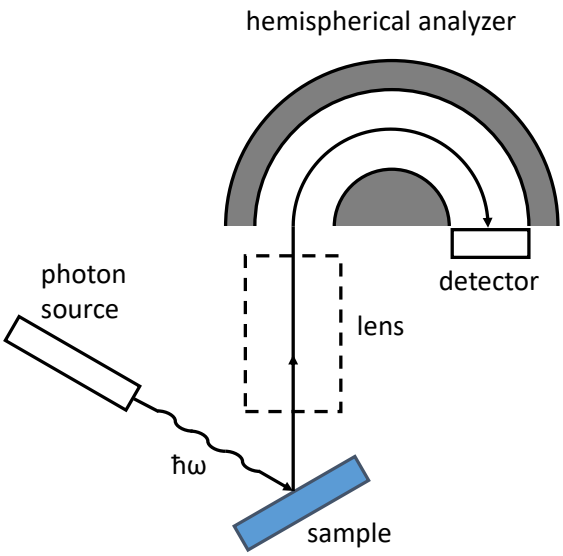

Figure 3.11: *Schematic overview of an X-ray photoelectron spectrometer used to determine the elemental composition of Ge-based thin films. Generated photons are used to emit core-level electrons from the surface of the respective sample. Electrons and their respective kinetic energy are detected via a hemispherical analyzer with an electron detector.*

In the present thesis, two different XPS instruments were used. Ge-based thin films synthesized via solution casting were measured with an Axis Ultra X-ray photoelectron spectrometer by Kratos[10]. Monochromatic Al K_α radiation was used as an X-ray source. The software CasaXPS 2.3.5 was used for data analysis. Calibration to C 1s (284.8 eV) was performed. For Ge-based thin films synthesized via spin coating[11] a conventional Leybold Heraeus X-ray source with non-monochromatized Al K_α radiation and a hemispherical analyzer (ES200 electron spectrometer, AEI Scientific Apparatus Ltd) for photoelectron detection were used. A grazing emission geometry with $\theta_e \sim 45°$ was set and calibration to Au 4f photoemission line was performed. Reference binding energies were taken from the X-ray Data Booklet [68].

[10]XPS measurements of solution cast, Ge-based samples were conducted during the ATUMS exchange in the Veinot group (Chemistry-Department, University of Alberta, CA) in collaboration with Haoyang Yu and Prof. Veinot

[11]XPS measurements of spin coated, Ge-based thin films were conducted at the Chair of Molecular Nanoscience and Chemical Physics of Interfaces (Barth group, E20, Physics-Department, TU München) within the frame of an TUM-internal ATUMS collaboration with Peter Deimel, Francesco Allegretti and Prof. Barth.

4 Sample preparation

Different novel approaches are introduced to synthesize mesoporous films on the basis of germanium or titanium. Materials and deposition techniques used within this frame are introduced in section 4.1 and section 4.2, respectively. In the final section 4.3, a detailed description of the sample preparation is provided for the synthesis of mesoporous thin films discussed within this thesis.

4.1 Materials

Exploited materials and solvents for the synthesis of mesoporous thin films are briefly introduced with regard to chemical structure, basic properties and supplier.

Polymer template

The amphiphilic diblock copolymer polystyrene-block-polyethylene oxide (PS-b-PEO) had a number average molecular weight of $M_n = 28.5$ kg mol^{-1} and a weight distribution of

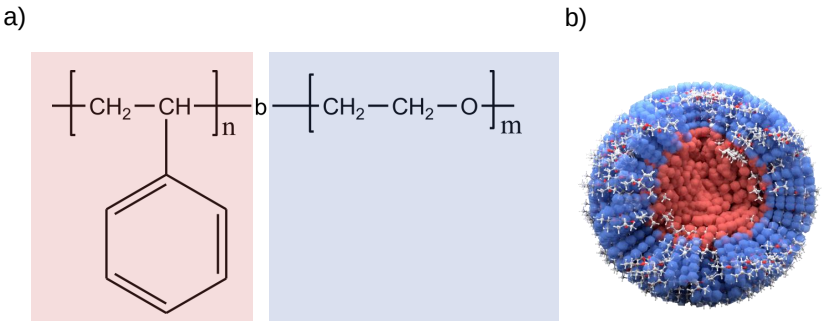

Figure 4.1: *(a) Chemical structure of the employed amphiphilic diblock copolymer polystyrene-block-polyethylene oxide (PS-b-PEO). PS-b-PEO with a number average molecular weight of 28.5 kg mol^{-1} was used as a template for the synthesis of all presented mesoporous thin films. (b) Illustration of micelle formation during phase separation with PEO (blue) and PS (red) blocks indicated in respective colors. The chemical structure of TTIP is additionally added to the PEO domain to illustrate selective incorporation of a precursor.*

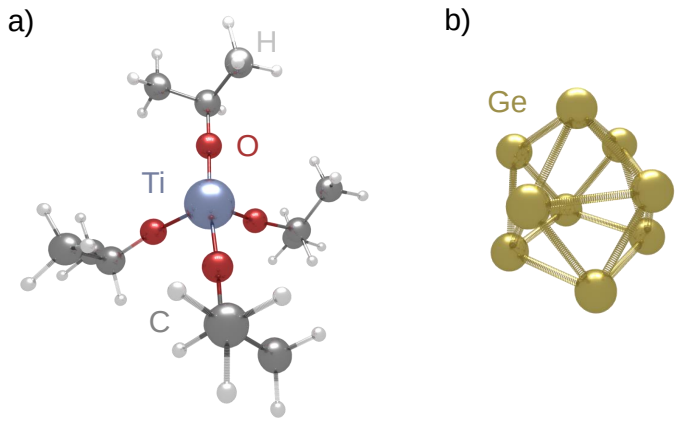

Figure 4.2: *Precursors for the fabrication of mesoporous films. (a) Illustration of the 3D spatial configuration of the employed precursor titanium (IV) isopropoxide (TTIP, $C_{12}H_{28}O_4Ti$). TTIP was used for the synthesis of all Ti-based thin films presented in this thesis. (b) Illustration of the 3D spatial configuration of the Zintl anion $[Ge_9]^{4-}$. K_4Ge_9 was used as a precursor for the fabrication of mesoporous, Ge-based films.*

M_n (PS) = 20.5 kg mol^{-1}; M_n (PEO) = 8 kg mol^{-1}. It was purchased from Polymer Source^{TM}. A sketch of the chemical structure is depicted in Figure 4.1a. Polar bindings to oxygen atoms render the PEO block hydrophilic, while the PS block is hydrophobic. The difference in polarity of the respective blocks is essential for a selective uptake of the precursors used within the frame of this thesis. The synthesis procedure of the diblock copolymer is based on living anionic polymerization and a polydispersity index of 1.02 was characterized by size exclusion chromatography. If not stated otherwise, the same batch and composition of this diblock copolymer was used for all presented results.

Titania precursor

Titanium (IV) isopropoxide (TTIP, $C_{12}H_{28}O_4Ti$) was used as a precursor to form TiO_2 nanostructures. A sketch of the 3D spatial configuration is depicted in Figure 4.2a. Each titanium atom is linked to four oxygen atoms. The polar binding to the oxygen atom makes the material hydrophilic. Therefore, TTIP is selectively incorporated into the also hydrophilic PEO domain of the employed diblock copolymer PS-b-PEO [42]. The transparent liquid TTIP was purchased from Carl Roth GmbH and no further treatment was applied before usage.

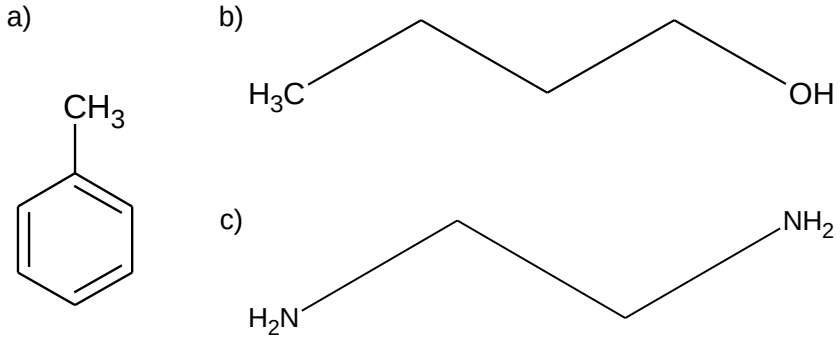

Figure 4.3: *Common organic solvents used within the frame of the present thesis. (a) Chemical structure of toluene used as good solvent in combination with the polymer template PS-b-PEO. (b) Chemical structure of 1-butanol used as poor solvent in combination with the polymer template PS-b-PEO. (c) Chemical structure of ethylenediamine used as stable transfer medium for the Ge-precursor* K_4Ge_9

Ge precursor

Zintl clusters are used as a precursor for the wet-chemical synthesis of tunable mesoporous Ge thin films. A Zintl phase is defined as an intermetallic compound between alkaline metal atoms and metal / semi-metal atoms of group 13-16 [69]. In the present thesis, K_4Ge_9 Zintl clusters were chosen with K as an alkaline metal and Ge as group 14 semi-metal. The material comes as a black powder with an indicated molar mass of $M_n = 0.81$ kg mol^{-1} and a solubility limit at a concentration of ~ 50 mg ml^{-1} in the solvent ethylenediamine. The material was synthesized by the Fässler group according to the synthesis routine described in literature [70]. An illustration of a $[Ge_9]^{4-}$-cluster is shown in Figure 4.2b. More information about the crystalline structure of the precursor K_4Ge_9 can be found in literature [71].

Solvents

Common organic solvents used within the frame of the present thesis are depicted in Figure 4.3. The apolar solvent toluene (C_7H_8, purity $\geq 99.8\%$, Figure 4.3a) was used as a good solvent to dissolve both blocks of the diblock copolymer PS-b-PEO, while the polar solvent 1-butanol ($C_4H_{10}O$, purity $\geq$ 99.5%, Figure 4.3b) was used as a poor/selective solvent during the synthesis of titania thin films. Additionally, an azeotrope solvent mixture of toluene and 1-butanol was used as post-treatment during the synthesis of mesoporous Ge thin films. Both solvents were purchased from Carl Roth GmbH and no further treatment was applied. For the synthesis of mesoporous Ge thin films, the solvent ethylenediamine (en, $C_2H_8N_2$, Figure 4.3c) was used as a stable transfer medium

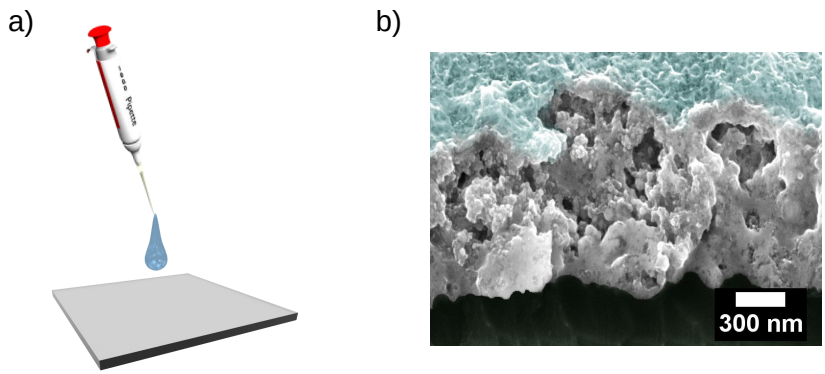

Figure 4.4: *(a) Illustration of drop casting as a deposition technique to fabricate films. 200-400 μl of a respective solution are pipetted onto a pre-cleaned substrate and drying is typically performed on a heating plate. (b) Exemplary scanning electron microscopy cross-section image of a thick Ge-based film fabricated via drop casting. The surface of the film is colored in light blue.*

/ solvent for the Ge precursor K_4Ge_9. To prevent oxidation of K_4Ge_9 Zintl cluster prior to deposition, it is of crucial importance that en is not exposed to water or oxygen. Even short exposure at small concentrations of air or water (∼10 ppm) can lead to unwanted oxidation of the precursor in en. As the Zintl clusters are extremely sensitive to air and water, en was additionally dried under reflux over CaH_2 before usage by the Fässler group.

4.2 Deposition techniques

Different deposition techniques were investigated within the frame of the thesis. Most common substrates used in combination with the respective deposition technique were either silicon substrates (525 μm thickness, Si-Mat, p-doped, (100)-orientation) or soda-lime glass substrates (1 mm thickness, Carl Roth). Substrates were cut into approximately 2 x 2 cm^2 sized pieces. Acid cleaning was applied to all substrates prior to deposition. More details about the applied acid treatment can be found in literature [72].

Drop casting

Drop casting was used as a deposition technique to obtain μm thick films with a rather rough/inhomogeneous surface. Typically, 200-400 μl of the respective solution were cast onto a pre-cleaned substrate via a pipette as illustrated in Figure 4.4a. Note that the amount of used solution plays a much more significant role for the final film thickness as compared to films fabricated via spin coating. Subsequent drying is performed on a

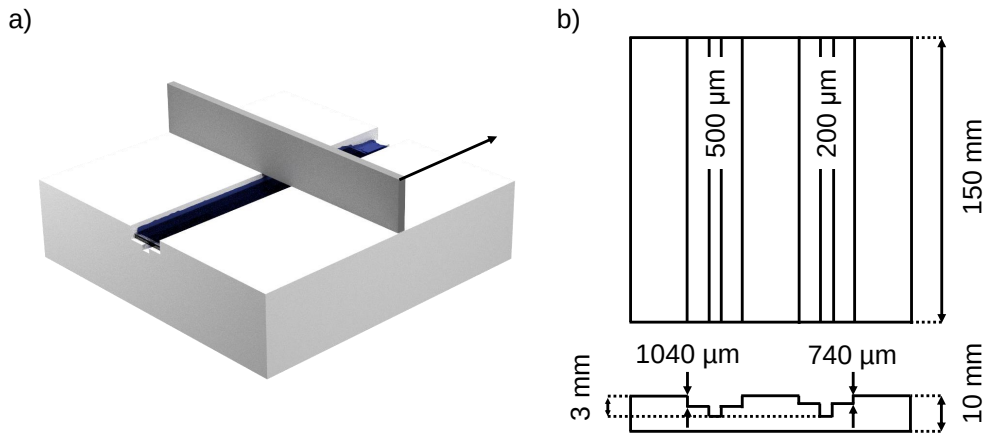

Figure 4.5: *(a) Illustration of blade coating as a deposition technique to fabricate titania films. 200 μl of solution are distributed along the substrate with a speed of 500 mm s^{-1} at a gate height of 200 μm. (b) Technical drawing of a spacer plate for substrate placement in the blade coating apparatus. 500 μm or 200 μm gate height can be chosen.*

pre-heated heating plate. An example of a rather thick, Ge-based film fabricated via drop casting can be seen in Figure 4.4b.

Blade coating

Blade coating is a deposition technique close to printing. An automatic film applicator 1137 (Sheen instruments) was used to fabricate homogeneous titania thin films. 200 μl of solution were deposited onto the glass or Si substrate and a speed of 500 mm s^{-1} was chosen to distribute the solution along the 200 μm channel of the spacer unit inside the device. An illustration and a technical drawing are depicted in Figure 4.5.

Spin coating

Most common deposition beside drop casting at a lab scale is spin coating (Figure 4.6a). Notable advantages of spin coating are typically high homogeneity and reproducibility. However, large amounts of material are flung off and lost during the deposition process. Furthermore, repeated spin coating steps to increase the film thickness are rather tedious and time consuming. Achieving films of increased thickness can even be impossible via this approach, as underlying layers might be redissolved. Therefore, the common thickness of spin coated thin films is found below 1 μm. An example SEM cross-section of a Ge-based thin film ($\sim$200 nm) fabricated via spin coating is shown in Figure 4.6b. A Delta 6 RC TT (Süss MicroTec Lithography GmbH) was used as a coating device. Cleaned substrates

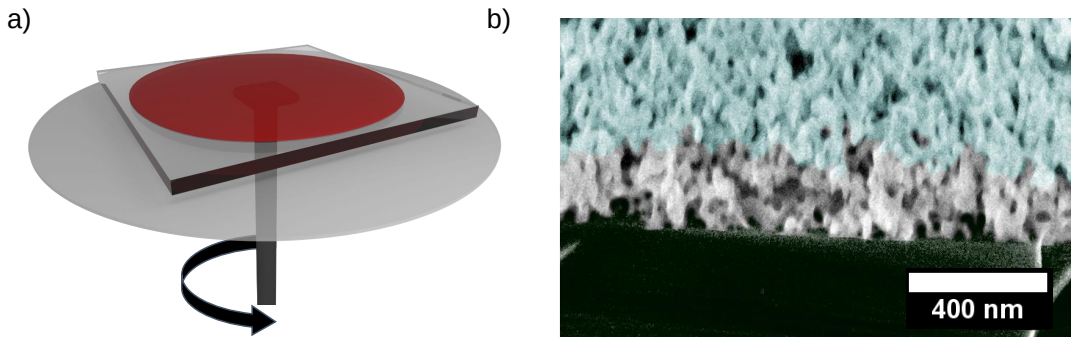

Figure 4.6: *(a) Illustration of spin coating as a deposition technique for highly reproducible/homogeneous thin films. The substrate is hold into position via application of a vacuum pump during the acceleration of rotation speed. (b) Exemplary cross-section scanning electron microscopy images of a mesoporous Ge-based thin film fabricated through spin coating. The surface of the thin film is colored in light blue.*

are fixed via a vacuum pump to the center of rotation of the instrument. Acceleration, rotation speed and time are chosen and typically 200 μl of solution are homogeneously pipetted onto the substrate. A three-stage-model can be used to describe the process of film formation. Solution is initially flung of the substrate through the acceleration of the rotation speed. Redistribution of material towards the edges is driven by convection in a second step. Finally, solvent evaporation dominates and a non-equilibrium, solid film is formed [73]. An estimation of final film thickness can be obtained via the Schubert equation [74]

$$d = A \cdot \left(\frac{1950\,\mathrm{min}^{-1}}{\omega}\right)^{\frac{1}{2}} \left(\frac{c_0}{20\,\mathrm{mg\,ml}^{-1}}\right) \left(\frac{M_\omega}{100\,\mathrm{kg\,mol}^{-1}}\right)^{\frac{1}{4}} \tag{4.1}$$

where A is an environmental and specific setup dependent constant, ω the rotational speed, M_ω the molecular weight and c_0 the initial concentration of the solution.

Spray coating

Spray coating is a technique with the potential to be used for large scale deposition. A typical setup with substrate, spray cone and spray device is depicted in Figure 4.7a. Small droplets are atomized from the stock solution through the N_2-carrier gas. Lateral pressure differences lead to the formation of a cone shaped beam with different lateral velocities. Consequently, droplet density decreases with distance to emission point (nozzle), while size of spray cone and homogeneity increase. Key parameters relevant for the final quality

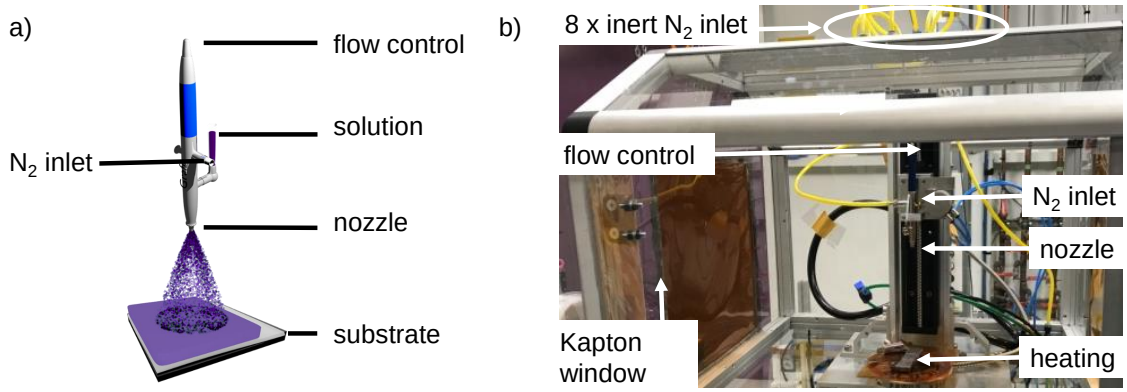

Figure 4.7: *(a) Illustration of spray coating setup for thin film deposition with substrate, spray cone and spray device. (b) Spray chamber used to perform in situ GISAXS measurements during spray coating.*

of the thin film are distance between nozzle and substrate, pressure/type of carrier gas, concentration of solution, viscosity, flow rate of the solution, spraying/drying sequencing, substrate temperature and geometry of the injector unit. Dry deposition is typically referred to as airbrushing, while wet deposition is referred to as spraying.

Within the frame of the present thesis, a special inert gas chamber was build in collaboration with the group of S. V. Roth to allow for *in situ* GISAXS measurements during spray deposition. Figure 4.7b depicts an image showing the chamber mounted at the beamline P03 at DESY, Hamburg. Eight different gas inlets at the top allow for constant N_2 flow and improved focus of the spray cone onto the substrate. The substrate itself is mounted on a heating plate and entrance/exit Kapton windows allow for efficient X-ray transmission. Note that the inert N_2 gas atmosphere inside the chamber does not only inhibit Ge-cluster oxidation, but additionally decreases the scattering background as compared to ambient conditions.

4.3 Fabrication of mesoporous thin films

In the following section, the sample preparation routine is described for the synthesis of mesoporous titania films via blade and spray coating as well as for the synthesis of mesoporous Ge films via spin coating and drop casting. For the convenience of the reader, a short and less detailed version of this description is repeated at the beginning of the respective result chapter.

4.3.1 Blade coating of titania

The diblock copolymer (0.2956 g) was dissolved in the good solvent toluene (1.792 ml) with a polymer concentration of 16.49 mg ml^{-1}. After 3 h of stirring at room temperature the titania precursor TTIP (0.87 ml) was added to the solution (weight ratio [polymer + solvent]:[TTIP] = 0.95:0.05). A homogeneous solution was obtained after 30 min of further stirring. The blade coating device automatic film applicator 1137 (Sheen instruments, speed = 500 mm s^{-1}, channel height = 200 μm) was used to homogeneously distribute a droplet of 200 μl along the 20 mm x 20 mm sized silicon substrates. A convenient feature of the setup consists in an easily controllable film thickness through a change of the channel height. All substrates were cleaned in an acid bath and exposed to an oxygen plasma treatment prior to the coating process [72]. Depending on, if either the evaporation time or the solvent bath impact was the subject of the studies, the preparation of the samples continued with one of the following two sections.

Evaporation time studies

After blade coating the solution onto the substrate, the drying process of the film sets in. A broad range of different evaporation times starting from 1 s up to 300 s was applied. Thereafter, the sample was immersed into a poor solvent bath of 1-butanol for 10 s. As a last step, the polymer template was removed via high temperature treatment in a tube furnace (3 h at 550 °C, heating rate = 80 °C h^{-1}, atmospheric conditions, Gero Hochtemperaturöfen GmbH) and anatase-type crystallization was induced.

Immersion bath composition studies

The evaporation time after blade coating was set to 50 s. The semi-dried samples were then treated with a solvent mixture of different compositions ranging from a 0.1:0.9 1-butanol (poor solvent)/toluene (good solvent) composition to a purely 1-butanol composition (10 vol% 1-butanol increment). 200 μl of the respective solution were therefore pipetted on the samples and, after an immersion time of 10 s, the samples were dried via a spin-drying process (500 rpm, 30 s, acceleration time = 4.5 s, Delta 6 RC TT, Süss MicroTec Lithography). The subsequent high temperature treatment protocol was identical to the one used for the evaporation time studies. Note that the coating, evaporation and immersion step are carried out under non-equilibrium conditions with ongoing kinetic processes.

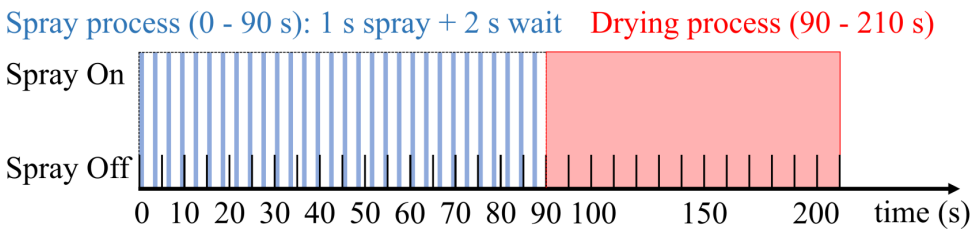

Figure 4.8: *Protocol for spray deposition of composite titania thin films for in situ GISAXS measurements. Alternating cycles of 1 s spraying and 2 s pause are performed within the first 90 s, adding up to a total of 30 spray shots. The drying process is further analyzed within the additional time from 90 s to 210 s.*

4.3.2 Spray deposition of titania

Solution preparation: 20 mg of PS-b-PEO were initially dissolved in toluene (6.700 ml, purity > 99.8%). Subsequently, 1-butanol (2.684 ml, purity > 99.8%) was added as a bad solvent. Due to the chosen weight percentages the resulting solution is considered a binary azeotrope. After further 10 min of stirring, the PEO-selective precursor TTIP (73.8 μl, purity > 97%) was pipetted into the solution. After 30 min, drop-wise addition of 121 μl of hydrochloric acid (6 M, diluted from 37% / 12 M) was carried out under constant stirring for the samples series referred to as WHCL. Both NHCl (no addition of HCL) and WHCl solutions are then stirred for further 20 h at 500 rpm under ambient conditions. All solvents were purchased from Sigma-Aldrich (Merck) and used without further processing.

Thin film deposition and calcination: Composite films were deposited onto silicon substrates, which were placed on a heating plate at 80 °C. The operated spray gun (Harder & Steenbeck GmbH & Co. KG, Grafo T3) was mounted on a height adjustable holding with a remote-controlled spray setup. Oil-free N_2 carrier gas was used under a pressure of 1.5 bar and a sample-to-nozzle distance of 17 cm was adjusted. Furthermore, the valve opening was calibrated to a flow rate of 33 μl s^{-1}. Additionally, the whole setup was placed into a custom-designed spray chamber with a dimension of approx. 60 x 60 x 60 cm^3, which allowed for enhanced control of the atmosphere as well as better focus of the spray cone onto the substrate (through 8 additional nitrogen inlets around the mounted spray device). Additionally, the closed N_2 environment in the chamber minimizes the risk of contamination through e.g. carbon sources during *in situ* measurements. The applied spray protocol is shown in Figure 4.8. A spray shot of 1 s was always followed by 2 s of drying to avoid liquid films. After 90 s, a final annealing period of 120 s was monitored via *in situ* GISAXS. After film deposition the polymer template was removed via high

molar ratio	PS-b-PEO conc. [mg ml^{-1}]	precursor conc. [mg ml^{-1}]
1/10	10	2.84
1/20	10	5.69
1/30	10	8.53
1/40	10	11.37
1/50	10	14.21
1/60	10	17.56
1/70	10	19.89
1/80	10	22.74

Table 4.1: *Molar ratios within mixed solution prior to spin-coating with respective concentrations (conc.) of the Ge precursor K_4Ge_9 and the polymer template PS-b-PEO dissolved in ethylenediamine*

temperature treatment (3 h at constant 550 °C after heating with a rate of 80 °C h^{-1}, atmospheric conditions, Gero Hochtemperaturöfen GmbH).

4.3.3 Spin coating of germanium

The structure directing polymer template PS-b-PEO was dissolved in dry ethylenediamine with a concentration of 20 mg ml^{-1}. Beforehand, ethylenediamine was dried under reflux over CaH_2. Subsequently, magnetic stirring of the solution was applied for 12 h at 1000 rpm. A second solution containing K_4Ge_9 dissolved in ethylenediamine was prepared with a concentration in the range between 5.6 and 45.5 mg ml^{-1} and stirred for 1 h at 1000 rpm. To investigate the impact of different molar mixing ratios, corresponding volume fractions (1:1) of the respective solutions were mixed together. The corresponding molar ratios with their respective concentrations can be found in Table 4.1. The mixed solution was stirred for additional 15 min at 1000 rpm before being spin-coated at 1500 rpm for 10 s onto acid cleaned substrates. Subsequently, an azeotrope solvent mixture of anhydrous toluene and 1-butanol was used to induce phase separation: 200 μl of the mixed solution had been pipetted onto the freshly coated and semi-dry composite thin film and soaked for 1 min, before the azeotrope solvent was removed by a second spinning process (same parameters). Sample annealing at 200 °C for 15 min was performed to remove residual solvent and allow for structural reorganization. Note that all steps were performed under inert gas conditions (N_2). As a last step, samples were calcined at 500 °C for 5 min in air.

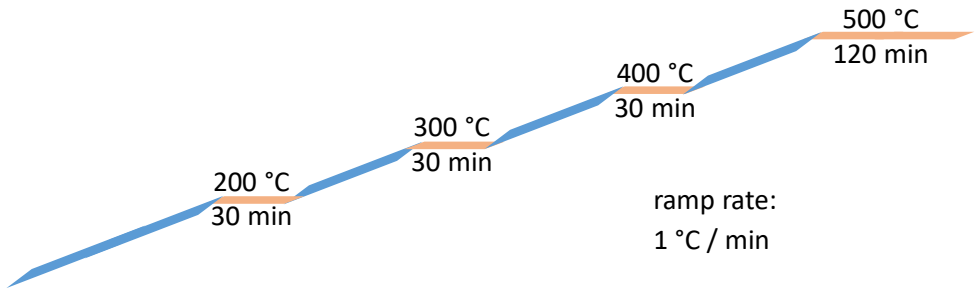

Figure 4.9: *Heat treatment protocol used to transform composite PS-b-PEO/K_4Ge_9 films into mesoporous α–Ge films. Tempering was performed under inert Ar atmosphere or in air. Each temperature plateau was reached with a ramp rate of 1 °C min^{-1}.*

4.3.4 Drop casting of germanium

Dry ethylenediamine (en) was used to dissolve PS-b-PEO with a concentration of 20 mg ml^{-1}. The solution was stirred for 12 h at 1000 rpm. Thereafter, the solution is mixed in a 1 : 1 volume ratio with a second solution of K_4Ge_9 dissolved in en (28.5 mg ml^{-1}, 1000 rpm, 1 h stirring) yielding a molar ratio of 50 (K_4Ge_9) : 1 (PS-b-PEO) in the mixed solution. The mixed solution was then stirred for further 15 min at 1000 rpm. 400 μl mixed solution were used for drop casting onto preheated substrates (200 °C). Special copper foil substrates for anode fabrication had a diameter of 13 mm. An additional post-treatment was applied to samples labeled "Ar; with PT", while no such treatment was applied for samples labeled "Ar; no PT". For the post-treatment, 200 μl of an azeotrope 1-butanol/toluene mixture were pipetted onto drop casted and semi-dry films. All samples were subsequently annealed for further 15 min at 200 °C. High temperature tempering (500 °C, 1 °C min^{-1}) was used to remove the polymer template. All steps prior to template removal were carried out under N_2 atmosphere. Template removal was performed under argon (Ar) atmosphere, if not stated otherwise. The applied temperature protocol for both air and Ar atmosphere is depicted in Figure 4.9. After calcination the sample was cooled naturally to room temperature.

The electrochemical performance of calcined samples on copper substrates was evaluated via half-cell tests using a lithium foil as the counter electrode and Celgard as the separator. Assembly of half-cells and measurement of cyclic performance was done by the group of Prof. Y. Cheng at the Ningbo Institute of Materials Technology and Engineering, China (Polymer and Composites Division). Electrolyte from Zhangjiagang Guotai-Huarong Chemical New Material Co., Ltd. was used, which was prepared by dissolving 1.0 M $LiPF_6$ in ethylene carbonate/dimethyl carbonate (EC/DMC) solvent mixture (1:1 v/v) with the addition of 5 wt% of fluoroethylene carbonate (FEC). Coin

cells were assembled in a glove box filled with high-purity argon. The cyclic performance was measured at the current density of 0.2 C in the voltage range between 3.0 V and 0.005 V (vs. Li/Li+) (1 C = 335 mAg^{-1}) for 300 cycles. The specific capacity was calculated against the mass loaded on the copper foil after calcination, which was measured using a balance with the resolution limit of 0.01 mg.

5 Morphological tunability of mesoporous TiO_2 thin films

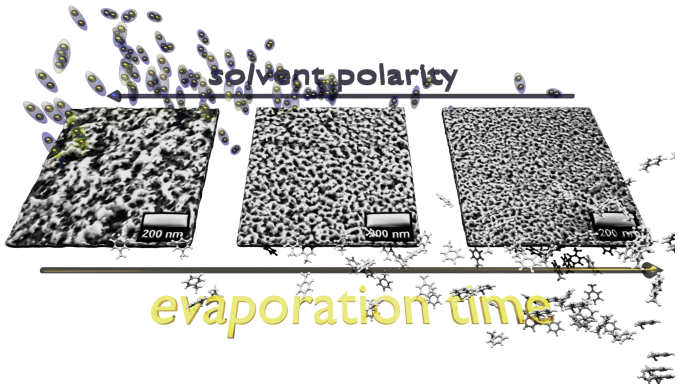

The following chapter is based on the published article: Readily available titania nanostructuring routines based on mobility and polarity controlled phase separation of an amphiphilic diblock copolymer [75] (Nuri Hohn et al., Nanoscale, 10, 5325-5334, 2018, DOI: 10.1039/C7NR09519H)[1].

High surface-to-volume ratio, mesoporous titania thin films play an important role in various fields of application. Therefore, novel and industrially compatible ways to control the mesoporous structure are of major importance. The following chapter first outlines the framework in terms of major scientific contributions in the scientific field of mesoporous titania thin film synthesis (section 5.1). Thereafter, the employed routine for mesoporous titania thin film synthesis is briefly introduced (section 5.2) and followed by a proof of principle in section 5.3. Influence of evaporation time and solvent bath composition on the surface and bulk morphology are investigated in the subsequent key sections 5.4 and 5.5 primarily via X-ray scattering and scanning electron microscopy.

[1]Reproduced/adapted by permission of The Royal Society of Chemistry. Results of the present chapter were obtained in close collaboration with the master's student Steffen J. Schlosser [76]

5.1 Preface

Over the past decades nanostructured metal oxides have attracted great interest within various fields of scientific research. Among those metal oxides, crystalline and nanostructured titania has been found especially useful due to its high electron mobility, compatibility with flexible device concepts and unique properties being a wide bandgap semiconductor [77–79]. One main branch of applications of nanostructured titania films is the development of energy harvesting devices such as solar cells [32, 33, 43–45, 80]. Among solar cells which make use of titania layers are dye-sensitized solar cells (DSSCs), solid-state DSSCs (ssDSSCs) and perovskite solar cells (PSCs), which demonstrate particular rapid progress and reached stabilized efficiencies over 21% recently [18–21]. All these devices can benefit from large effective surface areas for example in the form of mesoporous titania morphologies [81]. Apart from photovoltaic applications, nanostructured titania has as well become attractive within the field of gas sensing, photocatalysis, water purification, protein separation, Li ion batteries, metamaterials and supercapacitors [79, 82–90].

Due to the large variety of possible applications, huge efforts have been put into the synthesis of nanostructured titania layers. Promising techniques include deposition of pre-synthesized nanoparticle pastes, electrochemical deposition and, e.g. as shown by Martin and co-workers, a bottom-up approach using spinodal decomposition to obtain well-defined lamellar titania nanostructures [90–94]. Another approach consists in sol-gel synthesis which can be combined with organic macromolecule self-assembly and has emerged as a powerful tool to enable cheap and structured metal oxide layer deposition from a single solution [95, 96]. Furthermore, various types of nanostructures with unique properties can be obtained [97–104]. Periodic block copolymer structuring has been reported in many cases [105–108]. Using these block copolymers as a templating tool for titania nanostructures has been intensively studied. For example, Cheng and co-workers investigated the formation of different thin film morphologies like nanowires, clustered nanoparticles, collapsed vesicles and mesoscale network titania structures [42]. Within this frame, the process of film formation is based on the self-assembly of the structure-directing amphiphilic block copolymer polystyrene-b-polyethylene oxide (PS-b-PEO). A good-poor solvent pair induced microphase separation is used in combination with the PEO-selective precursor titanium (IV) isopropoxide (TTIP) to form micelles in solution. As a result of changing the precursor/poor solvent/good solvent ratio, the above-mentioned morphologies were obtained [42].

In case of hybrid photovoltaic applications exciton diffusion lengths of conjugated polymers used for backfilling into the titania matrix are typically found in the range < 20 nm [13]. As a result foam-like titania nanostructures with a pore diameter in the range of 40 nm

appear most promising for ensuring a high likeliness to the exciton of reaching an interface while not suffering from increased recombination losses in such a material system [18, 19, 21]. Consequently, in the present chapter foam-type, porous nanostructures with pores sizes in the above-mentioned range are focused. The amphiphilic diblock copolymer PS-b-PEO is used as a structure directing template. However, unlike used in common sol-gel approaches, the poor solvent, which initiates hydrolysis of the precursor, is not directly added to the solution of PS-b-PEO, good solvent and precursor [39, 109]. Instead, films are prepared out of PS-b-PEO, good solvent and precursor and the poor solvent is applied after a distinct evaporation time using an immersion bath as inspired from literature about porous polymer film preparation [105,108]. The aim of this approach consists in only having one master solution and analyzing the impact of the mobility and polarity on the phase separation behavior of an initially deposited film. Blade coating is used as film deposition method to ensure a potential upscale of the film preparation protocol for real world applications. Note that the dipping process into the immersion bath is as well potentially compatible with a large scale processing routine through upscaling of the employed solvent bath. Investigation of a morphological change due to a variation of the above-mentioned influences shows that titania nanomorphologies can be tuned in a wide range without changing the initial composition of the polymer/precursor mixture. Furthermore, the study described in this chapter is considered an approach to decouple the influence of good solvent and poor solvent on the phase separation behavior of the above-mentioned material system.

5.2 Experimental: Synthesis of mesoporous titania thin films via blade coating

To analyze the impact of the evaporation time and immersion bath composition on the phase separation behavior of PS-b-PEO, nanostructured thin films were synthesized according to following routine: Initially, the diblock copolymer was dissolved in the good solvent toluene (Figure 5.1a). After stirring at room temperature the titania precursor TTIP was added to the solution (Figure 5.1b). Subsequently, a homogeneous solution was obtained after further stirring. A blade coating device was used to homogeneously distribute the solution onto silicon substrates (Figure 5.1c). A convenient feature of the setup consists in an easily controllable film thickness through a change of the channel height. A more technical description including more details can be found in chapter 4.3.1. Depending on, if either the evaporation time or the solvent bath impact was the subject

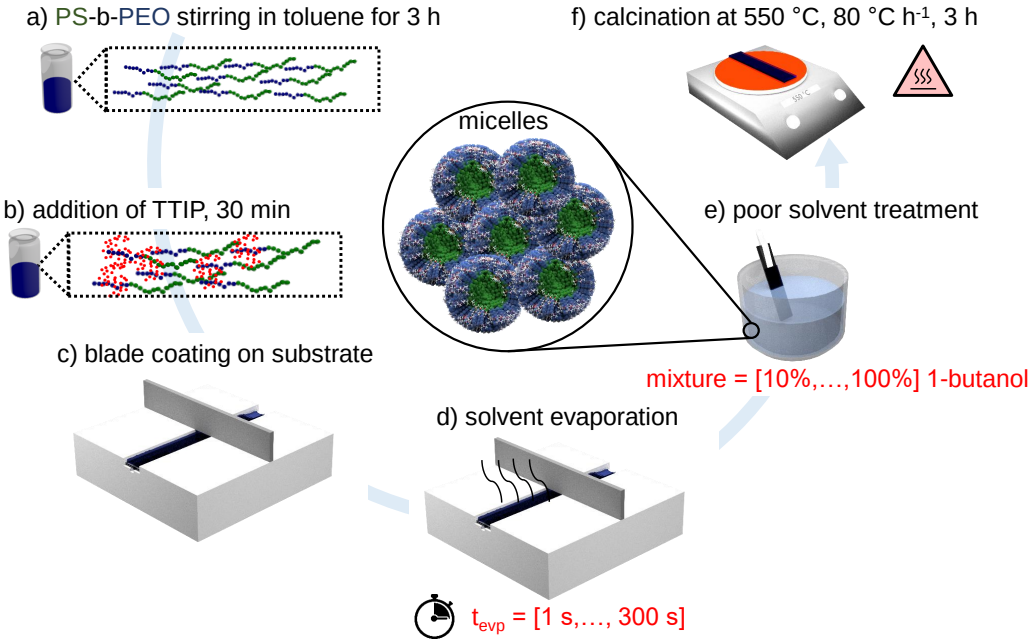

Figure 5.1: *Sample preparation steps for the synthesis of mesoporous titania via blade coating: (a) Stirring of structure-directing diblock copolymer PS-b-PEO in a good solvent for 3 h, (b) addition of the titania precursor, (c) subsequent blade coating on the silicon substrate, (d) waiting time before (e) exposure to an immersion bath with tunable 1-butanol/toluene ratio and (f) polymer template removal via calcination. Reproduced/adapted by permission of The Royal Society of Chemistry [75].*

of the studies, the preparation of the samples continued with one of the following two sections.

5.2.1 Evaporation time studies

After blade coating the solution onto the substrate the drying process of the film sets in. A broad range of different evaporation times starting from 1 s up to 300 s was applied to analyze the effect of the evaporation time on the phase separation behavior of the diblock copolymer (Figure 5.1d). Thereafter, the sample was immersed into a poor solvent bath of 1-butanol for 10 s (Figure 5.1e). As a last step, the polymer template was removed via high temperature treatment in a tube furnace and anatase-type crystallization was induced (Figure 5.1f).

5.2.2 Immersion bath composition studies

The evaporation time after blade coating was set to 50 s. The semi-dried samples were then treated with a solvent mixture of different compositions ranging from a 0.1:0.9 1-butanol (poor solvent)/toluene (good solvent) composition to a purely 1-butanol composition (10 vol% 1-butanol increment, Figure 5.1e). 200 μl of the respective solution were pipetted on the samples and, after an immersion time of 10 s, the samples were dried via a spin-drying process. The subsequent high temperature treatment protocol was identical as explained for the evaporation time studies.

5.3 Proof of principle: Influence of immersion bath

In previous studies it has been found that TTIP addition to a solution of PS-b-PEO leads to a selective incorporation of TTIP into the PEO domains [80]. Accordingly, changing the phase separation behavior of the diblock copolymer template directly translates into an altered nanomorphology of the final titania films. To prove this effect, a comparison is made between thin films, which have been manufactured according to the routine depicted in Figure 5.1. Part of the samples are exposed to a solvent treatment with 1-butanol (Figure 5.1e) after a drying time of 80 s (Figure 5.1d), while the other part of the samples are simply left to dry after blade coating (Figure 5.1c). After calcination (Figure 5.1f) the surface topography is analyzed via scanning electron microscopy (SEM), while the inner film morphology is investigated via grazing incidence small angle X-ray scattering (GISAXS) [63, 110]. As demonstrated in Figure 5.2a, titania films prepared without 1-butanol solvent treatment already exhibit nanopores to a small degree. Upon treatment with a poor solvent, a very distinct change in the surface morphology becomes visible. The overall degree of porosity is strongly enhanced and the average pore size is significantly increased (Figure 5.2c). One major advantage of an enhanced phase separation inducing larger pores is given by the facilitated backfilling of the resulting structures in solar cell applications. To quantify the effect of poor solvent treatment on the surface porosity, a Fast Fourier Transform (FFT) is performed and the radial power spectral density (PSD) function is extracted. A clear shift towards smaller reciprocal lengths is visible in the position of the intensity maximum (Figure 5.2e). The compact titania film of the untreated sample shows a broad intensity distribution with a maximum positioned at around 0.3 nm^{-1}. For the poor solvent treated samples, the distribution narrows and the peak shifts towards a value of 0.2 nm^{-1}. Thus, the PSD analysis quantifies the changes in pore sizes. Moreover, the decreased broadness of the distribution indicates a decrease in disorder of the surface structure of the films treated with poor solvent.

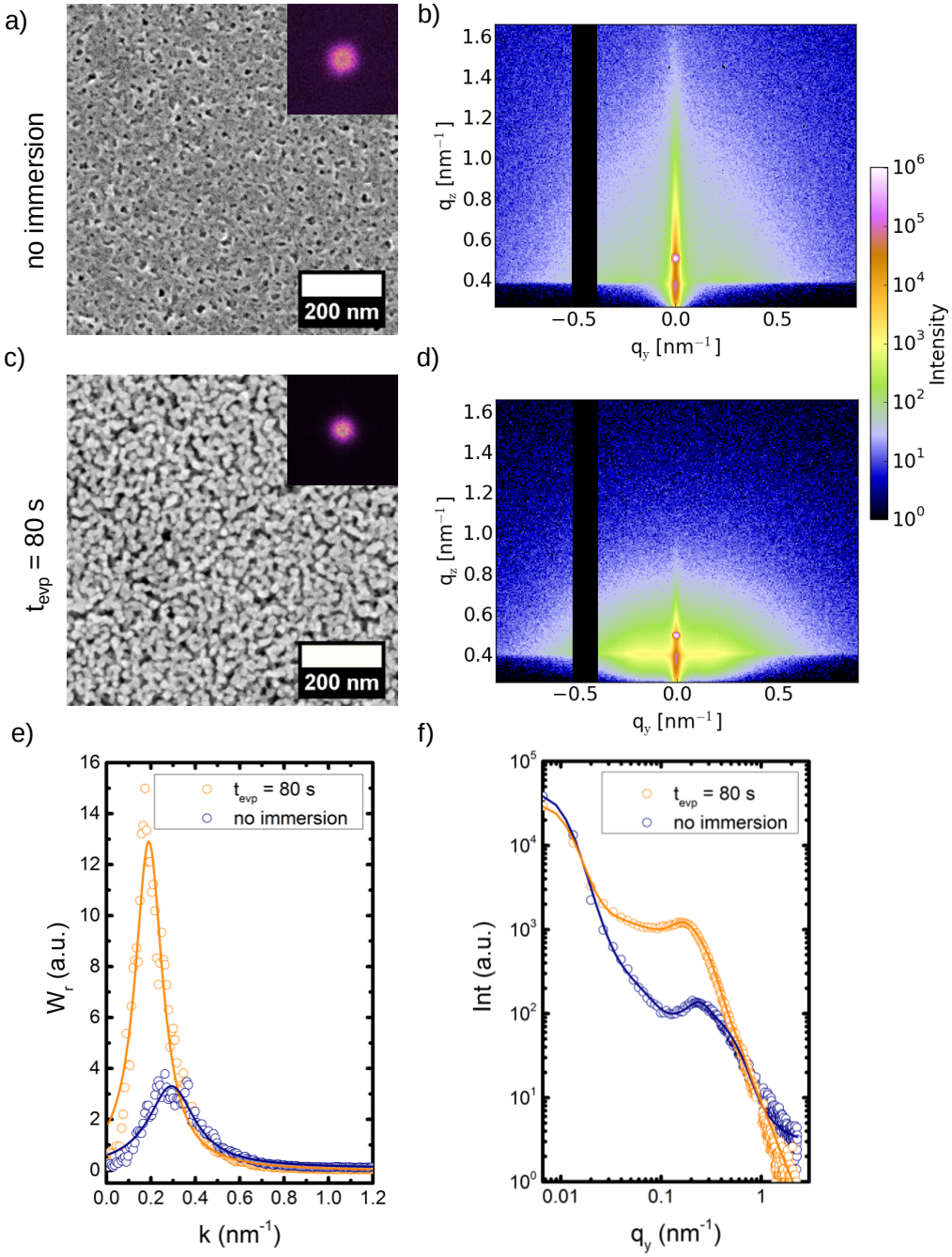

Figure 5.2: *Comparison of titania thin films immersed into a pure 1-butanol bath after 80 s evaporation time to titania films without 1-butanol treatment: (a) SEM and (b) 2D GISAXS data of the untreated samples are compared to (c) SEM and (d) 2D GISAXS data of the immersed samples. (e) PSD functions extracted from the SEM data and (f) horizontal line cuts of the 2D GISAXS data of the respective samples show a shift of the intensity peaks towards smaller reciprocal length scales for the immersed sample. Reproduced/adapted by permission of The Royal Society of Chemistry [75].*

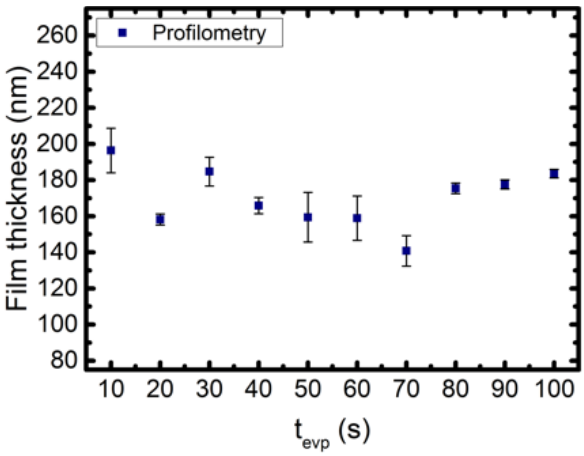

Figure 5.3: *Thickness estimation via profilometry for different evaporation times of mesoporous titania layers. Note that for every film 3 scratches (center, edge and intermediate position) with 5 lines have been measured. Reproduced/adapted by permission of The Royal Society of Chemistry [75].*

To access information of the buried morphology inside the titania films, GISAXS measurements are performed. Due to the large X-ray footprint at very low incident angles, the GISAXS observations exhibit high statistical relevance over macroscopic sample area. The 2D GISAXS data of the untreated (Figure 5.2b) and the treated (Figure 5.2d) samples show distinct and characteristic differences. With poor solvent treatment, the overall diffuse scattering is strongly increased, which confirms the assumption of an enhanced porosity in the entire film from the surface structures as seen by SEM. Furthermore, lateral intensity peaks at the material specific Yoneda peak position become more pronounced, which is a good indication for an improved formation of lateral nanostructures [54, 63]. Horizontal cuts are done at the expected Yoneda peak position of porous titania. A comparison of the horizontal cuts proves that lateral features appear at smaller scattering vectors q_y, if a solvent treatment is applied (Figure 5.2f). Together with the increased intensity (relative to the maximum intensity of the corresponding cut) this observation gives evidence that the phase separation process is not only enhanced at the surface but also extends into the bulk material, which is absolutely necessary, if the thin films are intended to be backfilled for use in photovoltaic applications.

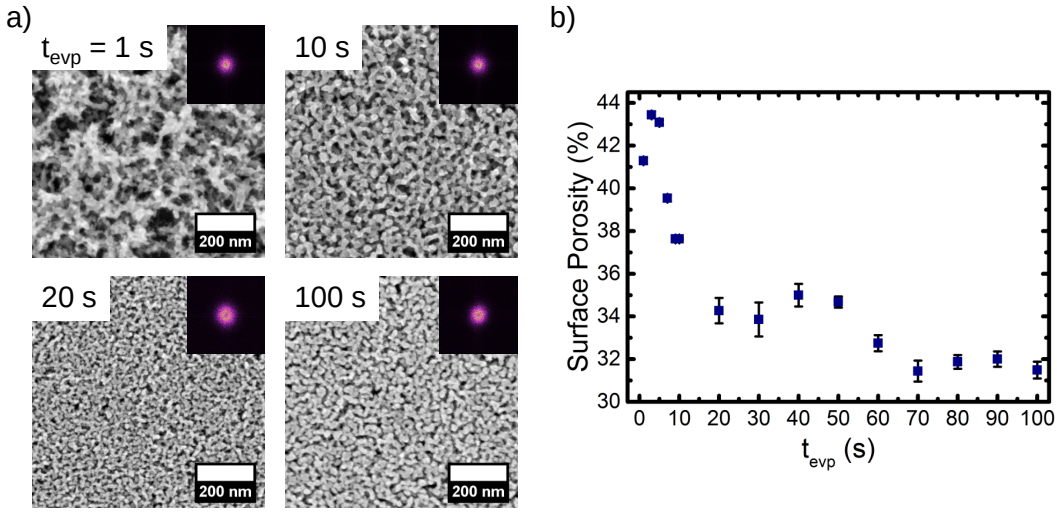

Figure 5.4: *(a) Scanning electron microscopy images of the surface topography of nanocomposite titania films after different evaporation times with FFT images (top right corners). With increasing evaporation times, the average structural distance is strongly decreased. (b) The evolution of surface porosity has been extracted for evaporation times ranging from 1 s to 100 s via binarization and application of an Otsu algorithm. Reproduced/adapted by permission of The Royal Society of Chemistry [75].*

5.4 Impact of evaporation time on phase separation behavior

As a precondition for comparability of different evaporation times, the thickness of all investigated samples is measured via profilometry. An approximately constant thickness of 170 nm is confirmed (Figure 5.3).

With the aim of determining the influence of the evaporation time on the phase separation behavior of the block copolymer template and, accordingly, on the final nanomorphology of the calcined titania films, samples with different evaporation times are studied. This corresponds to exclusively changing the parameter marked in red color in Figure 5.1d. Evaporation times from 1 s up to 300 s, representing a broad range of different dryness states, have been applied before the immersion into the poor solvent bath. Note that the phase separation behavior for the present material system is expected to be primarily affected by two dominant factors. First, an alternation of the relative good-to-poor solvent ratio within the immersion bath alters the energetic incompatibility between the PS block and the solvent mixture. Second, the dryness state of the film, which limits the mobility of the polymer chains to rearrange during the presence of a poor solvent. When

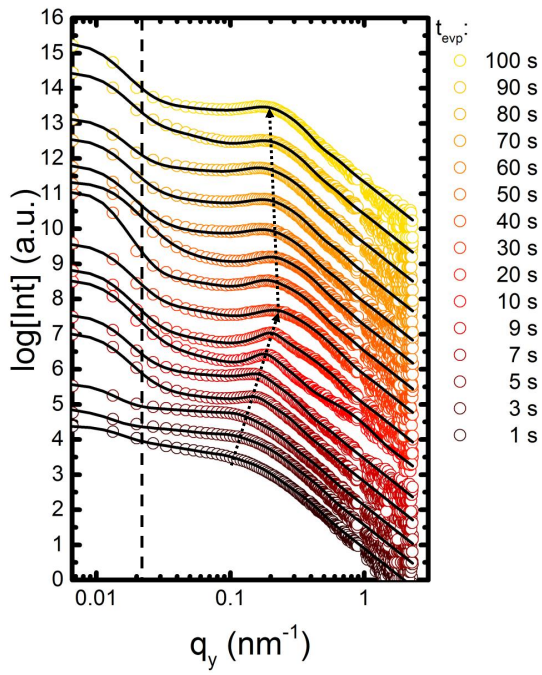

Figure 5.5: *Horizontal line cuts of the 2D GISAXS data at the material specific Yoneda peak position of mesoporous titania films after different evaporation times. As indicated by the dotted arrows a shift of the shoulder-like feature is visible for different evaporation times. The resolution limit is shown by the vertical dashed line. Data and modeling results (black lines between data points) are shifted along the y axis for clarity of the presentation. Reproduced/adapted by permission of The Royal Society of Chemistry [75].*

changing the evaporation time, the ratio of good-to-poor solvent in the immersion bath is highly dominated by the poor solvent. Therefore, small changes of the good-to-poor solvent ratio are not expected to have a large impact upon the final film morphology. On the contrary, changes of the dryness state and the correlated mobility of the polymer template are mainly responsible for an alteration of the observed morphologies.

The surface structure as seen by SEM is shown in Figure 5.4 for selected evaporation times of 1 s, 10 s, 20 s and 100 s. In the early stages up to 20 s, a decrease of the inter-domain spacing of titania nanostructures is clearly visible, which is mainly driven by a decrease in mobility of the polymer template. As a result, the polymer chains for low evaporation times exhibit an enhanced ability to phase separate in comparison to higher evaporation times, where the rearrangement of the polymer chains is limited. Exceeding evaporation times of 20 s, the inter-domain spacing of titania nanostructures appears to decrease more slowly, since the lower mobility limit for efficient rearrangement of the non-selective PS block is approached. Additionally, slight increase in the average radii of titania structures can be observed (Figure 5.4, 100 s). One possible reason for this finding

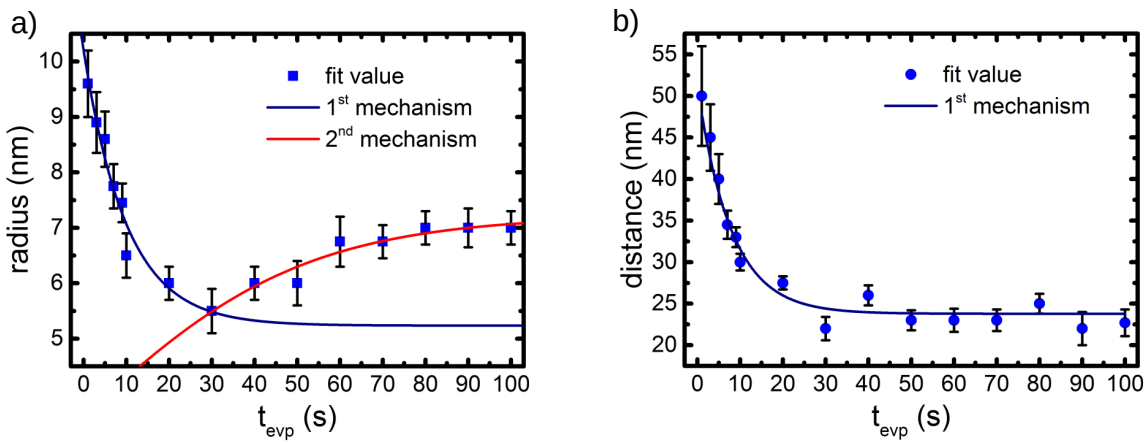

Figure 5.6: *(a) Radius and (b) lateral distance of titania nanostructures determined from modeling GISAXS data gathered for different evaporation times. Solid blue and red lines (guides to the eye) indicate two different mechanisms responsible for a change of the extracted radii. Note that lateral distances only seem to be affected by one mechanism leading to a decrease with increasing evaporation time. Reproduced/adapted by permission of The Royal Society of Chemistry [75].*

might be a simultaneous extraction of small amounts of the polar titania precursor TTIP by 1-butanol. As a result, a dry film state would reduce the amount of extracted TTIP and, thus, leading to an increase of titania structure sizes. Furthermore, from SEM image analysis, the surface porosity is estimated (Figure 5.4). A clear trend towards smaller pore sizes with increasing evaporation time is observed. For evaporation times of 1 s the extracted surface porosity is found to be approximately 43%, which is decreasing down to 31% for 100 s. Accordingly, the surface porosity can be readily tuned by 12% through a simple change in the evaporation time.

To further investigate if structures observed via SEM persist throughout the titania films and if the bulk behavior differs from the surface mechanisms, GISAXS measurements are performed for the same range of evaporation times. In order to identify lateral structures inside the titania films, line cuts are extracted from the 2D GISAXS data in horizontal direction (parallel to the sample surface) at the estimated critical angle of the porous titania (Figure 5.5). Accordingly, features appearing in these intensity distributions refer to lateral structures within the volume of the corresponding titania film. Apart from the resolution limit of the setup (black dashed line) for the low q_y region, a lateral structure related peak is visible for q_y values around 0.2 nm^{-1}. With increasing time, the position of the structural peak is shifting towards larger q_y values (dashed arrow), which is corresponding to a decrease in real space structure sizes (convolution of radii

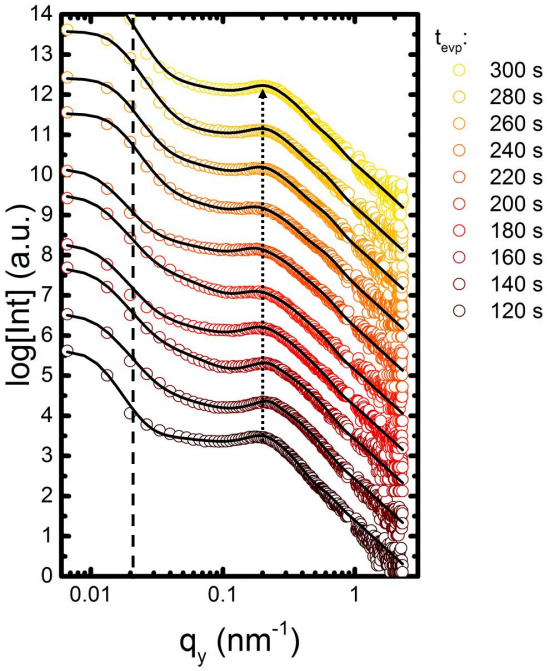

Figure 5.7: *Horizontal line cuts of 2D GISAXS data of mesoporous titania at the material specific Yoneda peak position after evaporation times ranging from 120 s to 300 s. As indicated by the dotted arrows no shift of the shoulder-like feature is visible for different evaporation times. Data points left to the dashed line originate from the laterally extended Yoneda region, the so-called resolution regime. The resolution limit is shown by the vertical dashed line. Data and modeling results (black solid lines) are shifted along the y axis for clarity of the presentation. Reproduced/adapted by permission of The Royal Society of Chemistry [75].*

and inter-domain distances). Reaching evaporation times above 30 s, the change of the peak position appears less prominent. Therefore, modeling of the horizontal cuts is done based on the Distorted Wave Born Approximation (DWBA) using the Effective Interface Approximation (EIA) [55]. The applied model in DWBA and EIA uses three different form factors with cylindrical geometry distributed over 1D paracrystal lattices [111] (see section 2.3.3). Whereas the lattice describes the center-to-center inter-domain distances (structure factors) of neighboring titania domains, the form factors refer to the Fourier transform of the electron density of titania objects residing inside the thin film.

The best achieved modeling results to the respective data are shown as solid black lines in Figure 5.5. Extracted inter-domain distances and radii of the cylindrical form factors of titania nanostructures are depicted in Figure 5.6. For short evaporation times up to 30 s, the radii are decreasing from 9.6 nm to 5.5 nm. For the same range of evaporation times, the inter-domain distances decrease from 50 nm to 22 nm due to the limited ability of the PS-b-PEO template to phase separate. This behavior is strongly supported by

the observations made for the surface of the investigated samples, where a similar trend is found (Figure 5.4). For evaporation times exceeding 30 s, slightly increased radii up to 7 nm are found, whereas the inter-domain distances of titania nanostructures remain constant. These evolutions are in accordance with observations at the surface, where the structures seem to slightly grow, while inter-domain distances are unaffected by a further increase of the evaporation time. Therefore, the inner film structures follow the same mechanisms as the surface structures. The decreasing mobility of PS-b-PEO leads to constraints in the ability to microscopically separate the two blocks of the polymer template (mechanism 1 shown by blue solid line in Figure 5.6). Thus, the average inter-domain distances of titania nanostructures are shrinking and the size of the structures is as well reduced due to the (mass) conservation of TTIP. Surprisingly, the second mechanism (red solid line in Figure 5.6) only seems to influence the radii of the titania. In general, the inner film structures show very similar mechanisms as found for the surface structures.

Since major changes only happen until 100 s, results for evaporation times > 100 s are depicted separately and can be found in Figure 5.7 and 5.8. To analyze the inner morphology of films with titania nanostructures for evaporation times exceeding 100 s, additional GISAXS measurements are performed. The same procedure, as done for shorter evaporation time studies, is carried out. Corresponding horizontal line cuts from the 2D GISAXS data are shown in Figure 5.7. Similar to evaporation times from 1 s to 100 s a shoulder like peak can be observed indicating the formation of a porous nanostructure. Nevertheless, there appears to be no further dependence on a change of evaporation time. As represented by the black dotted arrow, the peak positions remain almost constant for longer times.

Quantification is achieved via modeling of the horizontal line cuts with the same model as applied for shorter evaporation times. The extracted sizes and distances of titania nanostructures are shown in Figure 5.8. Obtained sizes (radii) are found around 6 nm, while distances are found around 22 nm. With increasing evaporation, no significant change is seen within the range of the errors. Consequently, it is assumed that the sample is already in a dry state meaning that the good solvent, in this case the toluene, is already completely evaporated. Therefore, no dependence could be found for a further increase of the discussed influence.

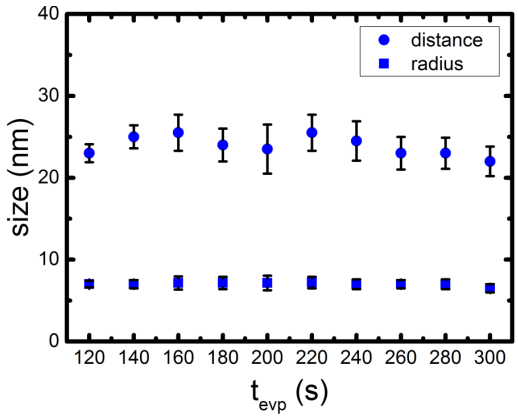

Figure 5.8: *Radius and lateral distance of titania nanostructures determined from the modeling to the corresponding GISAXS data gathered for different evaporation times > 100 s. Rectangle symbols are referring to the radii whereas circled symbols are referring to inter-domain distances. No significant change is observed within the range of the determined errors. Reproduced/adapted by permission of The Royal Society of Chemistry [75].*

5.5 Impact of immersion bath composition on phase separation behavior

In addition to the mobility of the polymer template, the solvent composition of the immersion bath has a major impact on the phase separation behavior. With the aim of quantifying this effect, samples are synthesized where exclusively the composition of the poor solvent mixture is changed (red parameter in Figure 5.1e). In contrast to the studies dedicated to analyzing the influence of the mobility, the evaporation time is fixed to 50 s. Note that an evaporation time of 50 s is chosen, since the mobility of the polymer is sufficiently high to show a good response to the immersion bath while still being adequately dry to allow for strong adhesion to the substrate. The compositions of the immersion bath with 1-butanol/toluene range from a volume ratio of 1:9 up to 9:1 in steps of 10 vol%. Consequently, the polarity of the solvent mixture is successively increased according to an effective medium approach with $P_{\text{total}} = \Phi_1 P_1 + \Phi_2 P_2$ where P_{total} is the polarity of the binary solvent system, Φ_i the volume fraction and P_i the polarity of solvent i. This change in polarity is expected to have a major influence on the phase separation behavior, since the selective solubility of the PEO block is enhanced. Furthermore, it should be noted that an increase in the 1-butanol content simultaneously leads to a reduction in toluene content, which in turn leads to a decreased mobility of the whole block copolymer complex. Accordingly, there are two major mechanisms to be considered for the final film formation: 1) The decrease in mobility of the polymer template with decreasing toluene

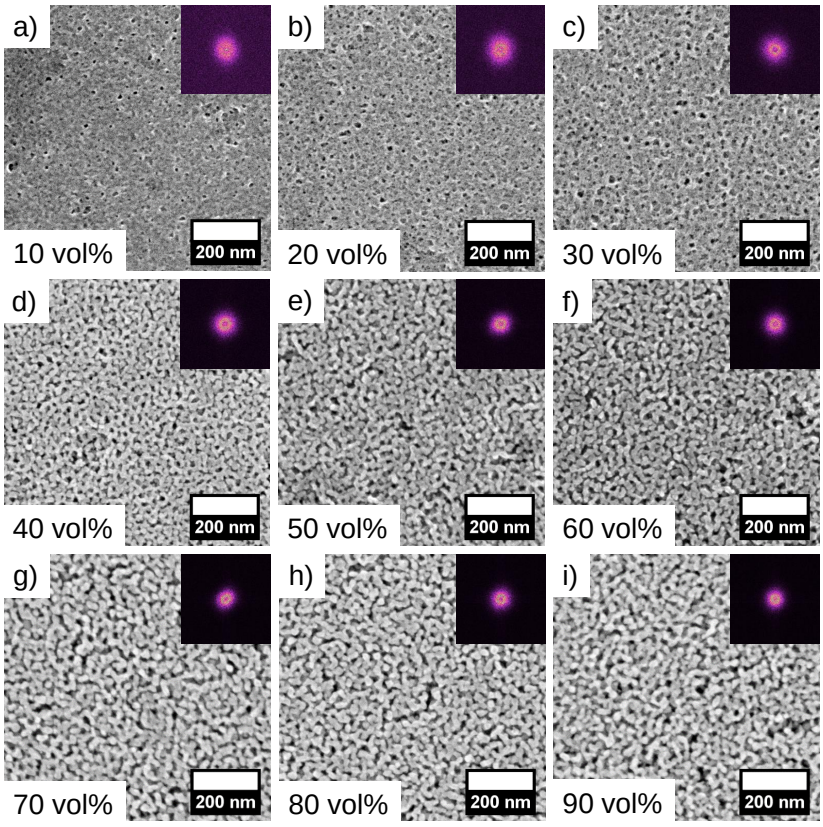

Figure 5.9: *SEM images of the surface morphology of mesoporous titania films exposed to different immersion baths with FFT images (top right corners). With increasing 1-butanol content from (a) to (i) the phase separation behavior is changed due to the increased polarity of the solvent mixture and the decreased mobility of the polymer template, which finally leads to an alteration of the surface structure. Reproduced/adapted by permission of The Royal Society of Chemistry [75].*

content and 2) the increased energetic incompatibility between 1-butanol and the PS domain, which is a driving force for phase separation.

The surface morphology is measured via SEM for all compositions. Obtained images are shown in Figure 5.9 with 1-butanol to toluene ratio increasing from top to bottom and from left to right. For 1-butanol concentrations of 10 vol% (Figure 5.9a), a rather compact structure is found. Due to the lack of poor solvent within the solvent mixture, phase separation of PS and PEO domains is decreased, even though the block copolymer disposes of a sufficient mobility provided by the high ratio of toluene. Therefore, only few and small pores are present in the titania films. With increasing the 1-butanol content up to 30 vol%, an increase in number and size of pores becomes visible, which is mainly attributed to the increase in polarity of the solvent mixture. At 1-butanol concentrations of 40 vol% the poor solvent has reached a sufficiently high ratio to obtain a very distinct

porous structure. For 1-butanol concentrations above 40 vol% the foam-like structure is maintained. Furthermore, the average pore size appears to slightly increase, which can be explained via the enhanced phase separation for higher 1-butanol ratios. Findings as described above might lead to the conclusion that exclusively the increase of poor solvent content is responsible for the phase separation process of the block copolymer template. The result would be the increase in number (from 10 vol% to 30 vol%) and size of pores, which are detected at the surface of the investigated titania films. Nevertheless, there appears to be a second influence upon the final titania structure. Comparison of SEM images and extracted FFT patterns for a 1-butanol content of 10 vol% and 30 vol%, not only indicates an increase in the number of pores, but, furthermore, shows a reduction of disorder. Additionally, the disorder of the foam-like structure increases again for concentrations above 40 vol% 1-butanol. This enhanced ordering is presumably caused by the interplay of poor solvent (driving phase separation) and good solvent (providing mobility) during the structure formation of the polymeric thin film. On the one hand, at low 1-butanol ratios the induced energetic incompatibility between PS and 1-butanol is not sufficient to result in a highly ordered structure formation. On the other hand, at high 1-butanol ratios the limited mobility suppresses a high order phase separation. Consequently, in between concentrations of 30 vol% to 40 vol% the most periodic titania structure is formed, where PS-b-PEO is able to energetically rearrange with higher long-range order.

GISAXS measurements are done to probe the influence of the good-poor solvent ratio on the inner film morphology. Shown in Figure 5.10 are the 2D GISAXS images for different solvent bath compositions, which have been measured at the MINAXS beamline P03 at DESY. Referring to Figure 5.10a, only weak lateral scattering is detected. With increasing the 1-butanol content the overall scattering is increasing (Figure 5.10b/c), while Bragg rods are as well starting to become more prominent. Since the formation of these rods is related to the formation of a periodic structure, an increase in 1-butanol is evidently beneficial to enhance the structuring process of titania. Exceeding 1-butanol concentrations of 40 vol% the lateral intensity peak becomes less pronounced and appears to have an increased FWHM. This observation is best seen when comparing Figure 5.10d with Figure 5.10i. Accordingly, the lateral peak at the q_z position of the Yoneda peak is easily visible for 40 vol%, while it is more difficult to identify a change of intensity along the same direction for 90 vol% from simply looking at the 2D GISAXS data. This increase in disorder is as well confirmed in SEM images and is attributed to the decreased content of good solvent. Finally, it can be stated that the most periodic structure is expected for 1-butanol concentration in between 30 vol% and 40 vol%.

Horizontal line cuts are performed at the material specific Yoneda peak position. Note

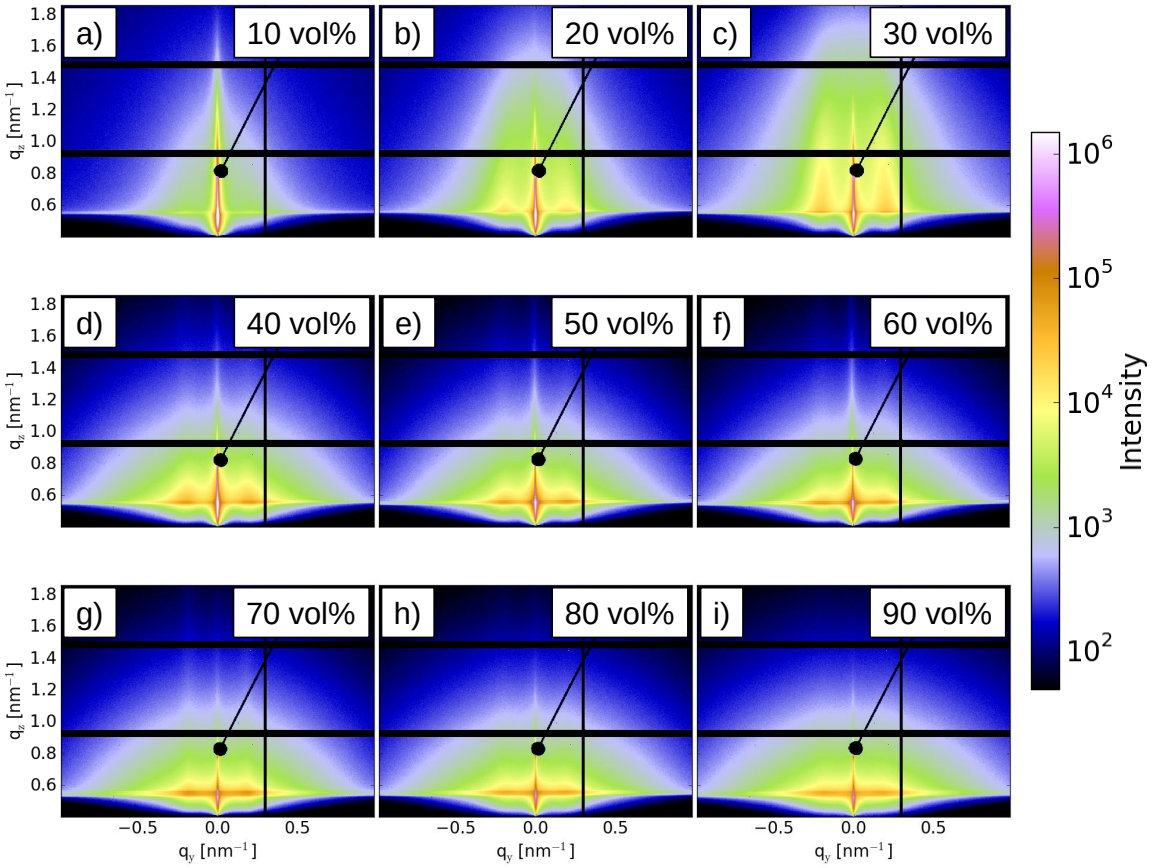

Figure 5.10: *2D GISAXS data of mesoporous titania exposed to different compositions of the immersion bath (as indicated in the insets). From top to bottom and left to right the 1-butanol content is successively increased. In (a) only weak lateral scattering is detected. With increasing the polarity, the lateral structures become more prominent and distinct. In (c) and (d) a maximum lateral scattering is reached, which decreases and smears out again with 1-butanol contents above 50 vol%. All data are shown with the same intensity scale bar as indicated on the right side. Reproduced/adapted by permission of The Royal Society of Chemistry [75].*

that the Yoneda peak position is found at smaller q_z values as expected for compact titania and, therefore, is further proof for a porous structure. However, to additionally confirm that the q_z shift of the Yoneda peak position relative to an expected value for compact titania is indeed related to the presence of a completely porous titania layer, cross section SEM measurements have as well been performed. An exemplary image for 90 vol% 1-butanol in the immersion bath is depicted in Figure 5.11 which confirms the conclusions drawn from the GISAXS measurements. Note that cross section SEM images have been taken for every sample and no significant changes between surface and bulk morphologies are found for evaporation times < 100 s.

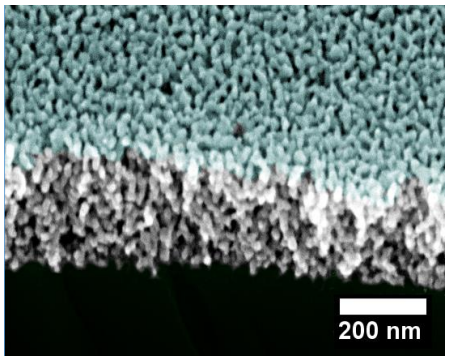

Figure 5.11: *Exemplary cross-section scanning electron microscopy image of a porous titania layer synthesized via immersion into a 90 vol% 1-butanol solvent bath. Clearly visible is that the whole film consists of porous titania and no significant differences are observed between surface and bulk morphology. The surface of the film is colored in light blue. Reproduced/adapted by permission of The Royal Society of Chemistry [75].*

For each investigated solvent mixture, the horizontal line cuts are shown in Figure 5.12. The black solid lines represent the respective modeling results done within the model as described in the evaporation time section 5.4. Accordingly, three structure and form factors are extracted from the regions marked with the solid, dashed and dotted vertical lines. For the first regime (marked via solid lines in Figure 5.12) in between q_y from 0.01 nm^{-1} to 0.1 nm^{-1}, an evolution of the shoulder-like peak position from higher to lower q_y values is visible as indicated by the dotted arrows. The transition from higher q_y regions to lower q_y regions is an indication for the growth of a lateral structure due to the change of the applied solvent treatment. Furthermore, a very pronounced peak can be found within the second regime (marked via dashed lines in Figure 5.12) between 0.1 nm^{-1} and 0.3 nm^{-1}. The position of the peak seems unaffected by the ratio of 1-butanol, whereas the relative intensity compared to the maximum intensity of the corresponding cut is changing. From 10 vol% to 30 vol%, the intensity of the peak is increasing, whereas the distribution is getting narrower. Within the frame of the applied model, this transition can be interpreted as an increase in periodically repeating titania nanostructures as well as an enhanced ordering upon the 1D para-crystal lattices. With 1-butanol concentrations over 40 vol% the intensity is again reduced and the second peak is getting broader again. The broadening is attributed to the enhanced disorder, which is confirmed via the SEM measurements. Within the third regime (marked via dotted lines in Figure 5.12) another shoulder-like feature is present showing no clear dependence on the 1-butanol content of the immersion bath. The three extracted structure and form factors of the titania nanostructure are shown in Figure 5.13. A change of titania radii is clearly visible for

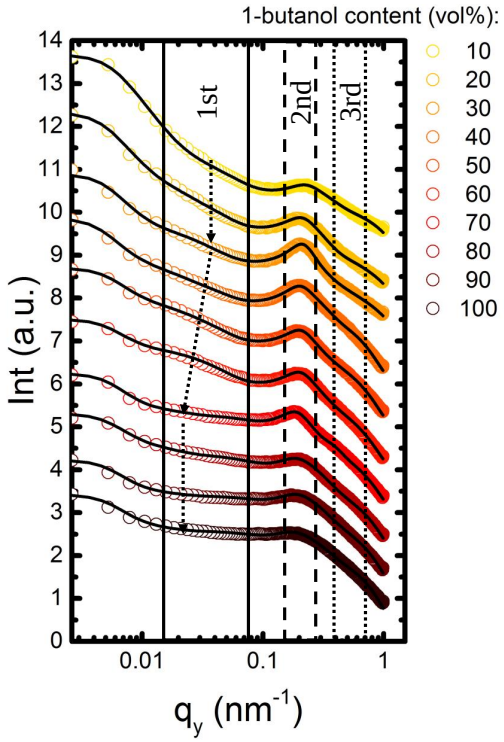

Figure 5.12: *Horizontal line cuts of the 2D GISAXS data at the material specific Yoneda position of mesoporous titania films after immersion into differently composed solvent baths. As indicated by the dotted arrows a shift towards smaller q_y values is evident for increasing 1-butanol within the 1st regime. Regimes denoted as 2nd and 3rd regime correspond to the respective modeling of radius and distance within the frame of the used model. Despite of not observing a shift of the q_y peak position within the 2nd regime, the intensity is especially enhanced for 1-butanol contents around 30 vol%, while the FWHM is reduced. The x-range with q_y values smaller than the 1st regime is the resolution limit. Data and modeling results (black lines between data points) are shifted along the y axis for clarity of the presentation. Reproduced/adapted by permission of The Royal Society of Chemistry [75].*

the area labelled as first regime. While radii for low 1-butanol content up to 20 vol% stay almost constant, an increase starts with 1-butanol concentrations of 30 vol%. Until 100 vol% the radii change from roughly 16 nm up to 20 nm. This behavior is in good agreement with the observations made via SEM, where an increase in the size of the foam-like nanostructures is as well found due to the enhanced phase separation with increasing polarity of the solvent. Furthermore, the absolute size of the radii matches the sizes of the structures observed via SEM. In contrast, within the second and third regime only minor changes of modeled structural sizes are extracted and no similarities to SEM images are found. Accordingly, it can be concluded that the extracted radii within this specific regime cannot be observed on the film surfaces, but are exclusively located inside the

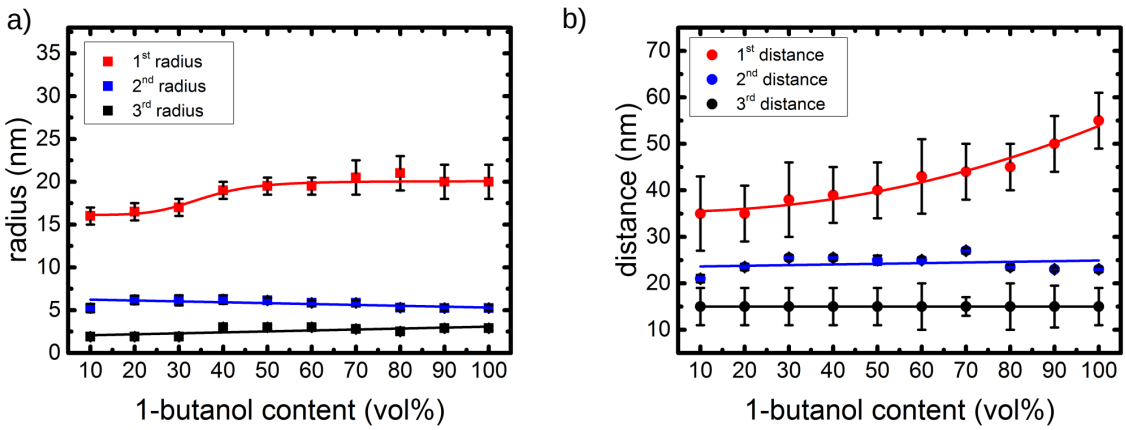

Figure 5.13: *(a) Radii and (b) lateral distances of titania nanostructures determined from the modeling to the GISAXS data gathered for different immersion bath compositions. Solid red, blue and black lines are guides to the eye. Within the 1st regime the radius and lateral distance are found to grow with increasing 1-butanol content of the immersion bath from 16 nm to 20 nm and 35 nm to 55 nm, respectively. No significant structural changes could be found within the 2nd and 3rd regime. Reproduced/adapted by permission of The Royal Society of Chemistry [75].*

films. The inter-domain distances of titania nanostructures increase from 35 nm to 55 nm in the first regime. This very significant change of distances is mainly attributed to the enhanced phase separation of PS-b-PEO. Comparison to the surface morphology of 40-90 vol% 1-butanol content in Figure 5.9, where a clear enlargement of pore sizes is visible, leads to the conclusion that the observed increase in inter-domain distances of titania nanostructures inside the films is closely correlated to the phase separation behavior at the surface.

5.6 Conclusion

In summary, the synthesis of easily tunable titania nanostructured thin films is realized via a block copolymer templating approach in combination with blade coating for film preparation. The effect of an alteration of evaporation time prior to poor solvent immersion is analyzed with respect to surface and inner film morphologies. Due to a change in mobility of the amphiphilic diblock copolymer template, the surface porosity can be tuned by 12%. Through GISAXS measurements with high statistical relevance it has been possible to monitor changes of the average predominant inter-domain distances and radii of titania structures from 50 nm to 22 nm and 9.6 nm to 5.5 nm, respectively. The dependence of surface and inner morphologies on the polarity of an applied solvent treatment is seen as well. With an increase in the ratio of 1-butanol to toluene inter-domain distances

are found to grow from 35 nm to 55 nm due to an enhanced phase separation, whereas the radii of the titania nanostructures are as well found to increase. In general, the presented studies show the interdependence of mobility and polarity upon the formation of porous titania thin films. An ideal mixing ratio around 4:6 of 1-butanol and toluene is found to yield the most periodic titania nanopores, which can be interpreted as an optimum interplay of mobility and polarity. The obtained knowledge provides fundamental new insights into the complex driving mechanisms of phase separation within an already precast wet hybrid film. It thereby paves the way for a more tailored fabrication of porous titania films with applications in DSSCs, ssDSSCs and perovskite solar cells making use of blade coating. The exposed processing routine is expected to be easily adaptable for different material systems with, for example, altered block lengths of the polymer template. Since blade coating enables an easy upscaling, new and readily accessible ways of tailoring the nanomorphology of titania thin films might be opened for a wide range of different real world applications.

6 Influence of HCl on spray-deposited mesoporous TiO_2 thin films

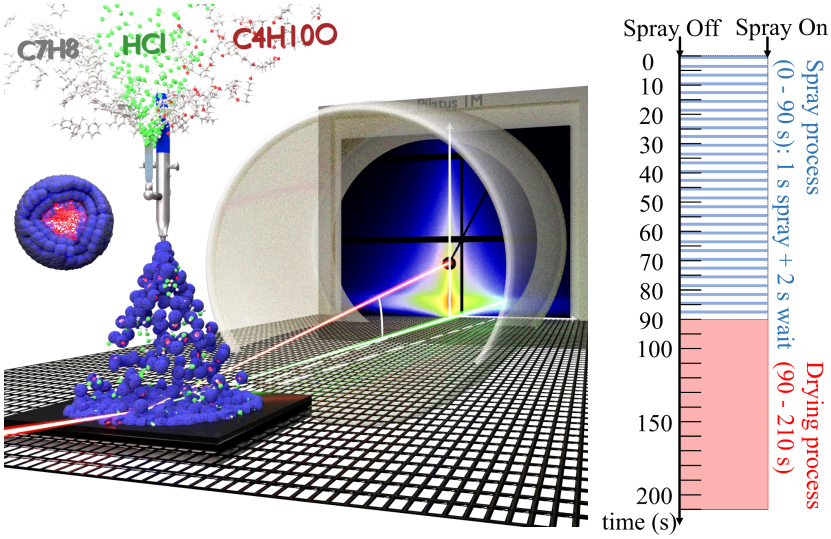

The following chapter is based on the published article: Impact of Catalytic Additive on Spray Deposited and Nanoporous Titania Thin Films Observed via in Situ X-ray Scattering: Implications for Enhanced Photovoltaics [40] (Nuri Hohn et al., ACS Applied Nano Materials, 1, 4227-4235, 2018, DOI: 10.1021/acsanm.8b00985)[1].

New approaches to control the surface and inner morphology of mesoporous titania thin films have been demonstrated in the precious chapter 5. Both evaporation time and composition of an immersion bath were found to be suitable parameters to alter the structure of the investigated titania thin film. While the chosen deposition technique

[1]Reprinted (adapted) with permission from [40]. Copyright (2018) American Chemical Society. Results of the present chapter were obtained in close collaboration with the master's student Steffen J. Schlosser [76]

of blade coating is likely to be easily upscalable to a large scale technique, the main focus was set upon the control of the mesoporous structure. In the following chapter, the focus upon large scale deposition and correlated potential for industrial applications is even further increased. Structure formation during spray deposition of mesoporous titania thin films is investigated through *in situ* GISAXS measurements and the special role of HCl for efficient diblock copolymer templating is analyzed. The initial preface of the chapter gives an orientation about key contribution in the field of mesoporous titania thin films deposition with focus on spraying (section 6.1). The section is followed by a short experimental section 6.2 to give an overview of the employed processing routine. The following two main sections primarily focus on structure formation and the role of catalytic HCl addition to the spray solution. This is realized through investigation of static samples (section 6.3) and *in situ* GISAXS measurements (section 6.4) during structure formation.

6.1 Preface

In chapter 5 advantages of high surface-to-volume ratio titania layers and respective applications have been outlined. Despite all advantages in the field of photovoltaics, today none of the titania based solar devices can compete with conventional crystalline Si-based solar cells in terms of photo-conversion efficiency or long-term stability, which demonstrates the need for more research in this area [112]. Besides efficiency and lifetime, the cost and energy effective fabrication of the PV devices is important in the realization of solar cells. Thus, large scale fabrication of alternative device technologies such as DSSCs, ssDSSCs or PSCs has started to gain significant interest, because it can be more cost- and energy-efficient as compared to conventional Si-based solar cells. In this regard, spray deposition has been found to be a very promising method to upscale the production of nanostructured titania films for use in DSSCs, ssDSSCs or PSCs.

Spray deposition is a wet chemical deposition technique that requires the use of an ink. Among the different wet chemical synthesis methods of titania nanostructures, sol-gel synthesis in combination with the self-assembly of an amphiphilic diblock copolymer such as polystyrene-b-polyethylene oxide (PS-b-PEO) has been proven to be a powerful tool. It allows to control the nanoscale morphology of the titania films, resulting in a variety of unique properties [75, 100, 101, 104, 107]. Spray coating has started to be used successfully to get nanostructured titania films for PV applications [113], but so far only a few reports focused on the kinetics of the structure formation processes during spraying. For example, Song et al. recently reported an *in situ* GISAXS observation of titania thin film formation during spray deposition in the airbrush regime [114]. Small-scale titania

nanostructures equilibrated as they reached the substrate surface and only for large titania nanostructures the evaporation of residual solvent caused a decrease of structure sizes and distances during the spray deposition. In contrast to this dry deposition, Su et al. studied the wet deposition in the spraying regime [115]. Having more solvent present, micelles were deposited and solvent evaporation occurred continuously. Consequently, titania nanostructures on all length scales showed a decrease in structure size and distance due to the transformation of the morphology towards equilibrium. In the present chapter the impact of hydrochloric acid (HCl) as a catalytic additive to the spray solution of titania in the air brush regime is focused. Being very powerful *in situ* GISAXS during the spray deposition is used to unwrap the underlying kinetics and get a deep understanding of the nanostructure formation process. The role of HCl in combining sol-gel synthesis and spray coating is outlined and its impact on the nanostructure formation in real-time is examined. Potential target applications of the obtained titania nanostructures are PV devices such as hybrid solar cells, DSSCs, ssDSSCs and PSCs.

6.2 Experimental: Synthesis of mesoporous titania thin films via spray deposition

A schematic overview of the steps involved in the mesoporous titania thin film synthesis is depicted in Figure 6.1. Typical porosity values of the mesoporous titania thin films are $(66 \pm 2)\%$. The amphiphilic diblock copolymer PS-b-PEO was used as a structure directing template and was initially dissolved in toluene. Addition of 1-butanol as a bad solvent was carried out to induce micelle formation and the titania precursor TTIP was selectively incorporated into the PEO phase [42]. A detailed experimental description with used amounts and suppliers can be found in the sample preparation section 4.3.2 along with the sequencing protocol during spray deposition. To analyze the role of HCl on the final nanostructure formation, two solutions were prepared. One solution contained HCl (called WHCl) and one solution was prepared without HCl (called NHCl). *In situ* GISAXS characterization was applied during spray deposition on a silicon substrate (80 °C) at the MiNaXS beamline P03 of the PETRA III storage ring at DESY, Hamburg ($\lambda = 0.94$ Å , SDD = 4377 mm, incident angle = 0.35°, vertical beam size = 12 μm, horizontal beam size = 24 μm) [116]. Data acquisition was realized via a Pilatus 1M (Dectris Ltd.) detector with a total of 981 $\times$ 1043 pixels (pixel size 172 μm $\times$ 172 μm) and with an acquisition time of 0.1 s. 2D GISAXS images were displayed and treated with the software DPDAK. For final static thin film characterization, the polymer template was removed via high temperature treatment in air.

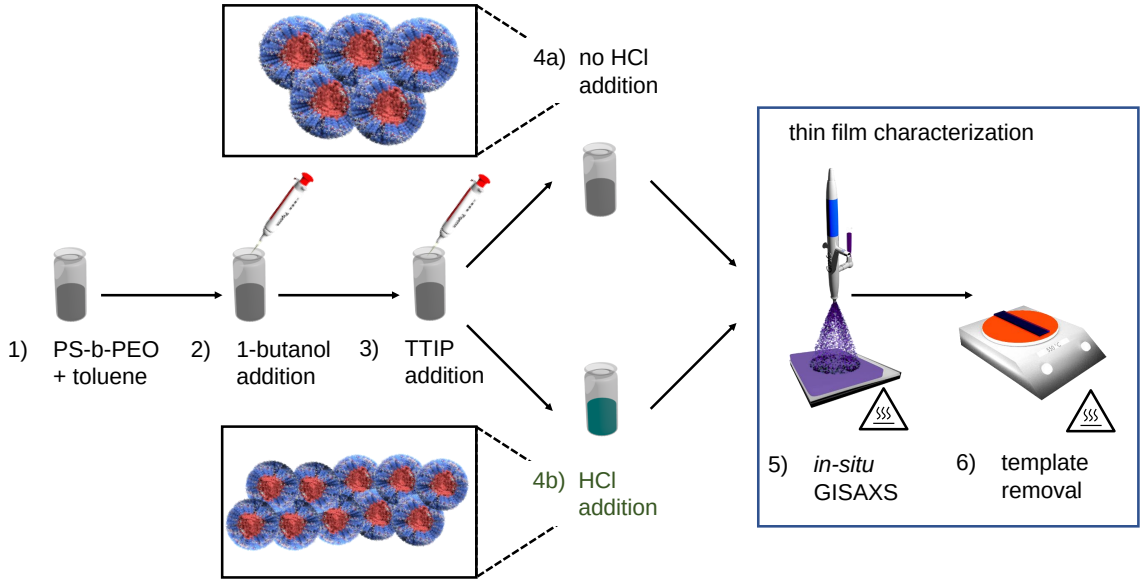

Figure 6.1: *Schematic overview of steps involved in the preparation of mesoporous titania thin films. (1) The initial solution is prepared based on the diblock copolymer PS-b-PEO in toluene and followed by (2) the addition of the bad solvent 1-butanol. (3) TTIP is selectively incorporated into the PEO domain of formed micelles. Unlike (4a), step (4b) consists in HCl addition to the solution. (5) in situ GISAXS measurements during spray deposition and (6) subsequent template removal through high temperature treatment. Reprinted (adapted) with permission from [40]. Copyright (2018) American Chemical Society.*

6.3 Characterization of static samples

The surface topography of the obtained titania films is shown in Figure 6.2 before and after the template removal via calcination. The AFM data show a smoother surface topography for the WHCl samples (rms roughness = 1.0 nm) as compared to the NHCl samples (rms roughness = 2.0 nm). Root mean square (rms) roughness has been extracted via the 2D statistics function of the software Gwyddion [62]. This difference in roughness can be explained by a suppressed agglomeration through electrostatic repulsion in the presence of HCl [39]. In case of the WHCl samples, only a few small circular pores (approx. 20 nm) are seen on the film surface before calcination, whereas the NHCl samples show a porous surface already. After the high temperature treatment induced removal of the block copolymer, both types of samples exhibit a porous morphology as seen with SEM. WHCl solutions yield films with relatively small and uniform pores and NHCl based films contain large nanopores which are rather polydisperse. This difference is attributed to altered reaction kinetics and cross-linking mechanisms, as the presence of HCl promotes hydrolysis reactions versus condensation reactions [39]. Accordingly, cross-linking of ti-

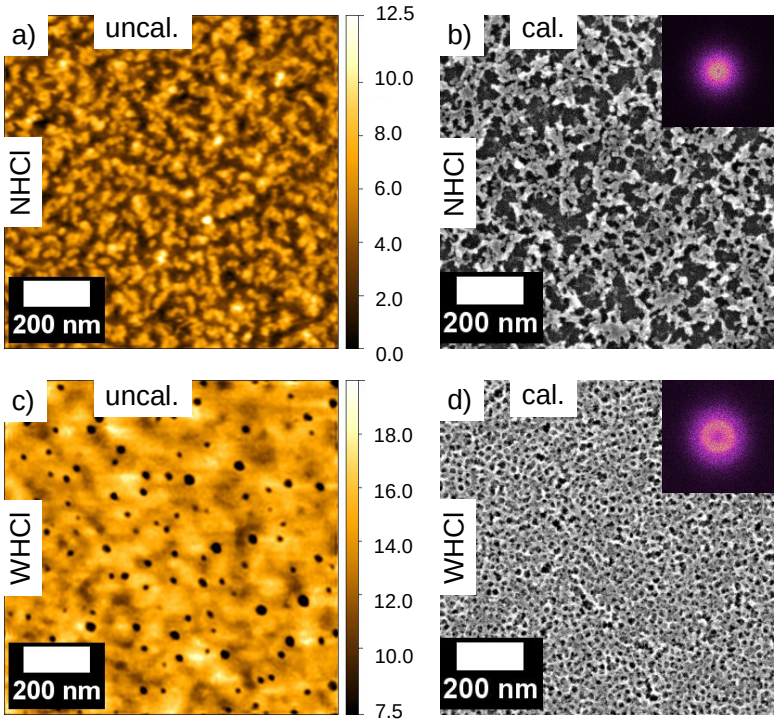

Figure 6.2: *Surface topography of sprayed titania thin films without (a,b) and with (c,d) HCl additive. (a,c) AFM topography images of the thin film before calcination (polymer template still inside the film) and (b,d) SEM images of the surface after polymer template removal. Reprinted (adapted) with permission from [40]. Copyright (2018) American Chemical Society.*

tania is more likely to connect chain ends. Thereby, cross-linking dynamics for titania nanostructure formation naturally favors a chain-like structure within the interconnected micellar PEO shells. Moreover, addition of HCl to the solution also leads to an increase of electrostatic repulsion, which further inhibits large TiO_2 cluster formation [117], and simultaneously increases the solution polarity, which further enhances the phase separation (micelle formation) of the block copolymer. In contrast, for NHCl solutions the cross-linking is more likely to occur near a center position as condensation reactions are less inhibited [39]. As a result, the cross-linking dynamics of NHCl solutions would rather favor the formation of a clustered titania morphology instead of following the structure of the polymeric template.

For both, WHCl and NHCl samples, a porous inner structure can be observed via cross-section SEM. An example is depicted in Figure 6.3b. Additionally, XRD measurements prove that an anatase titania phase was induced in both approaches (Figure 6.3a). However, under the influence of HCl the anatase (101) peak was found to broaden as compared to the acid-free sample. Application of the Scherrer equation [118] yields a

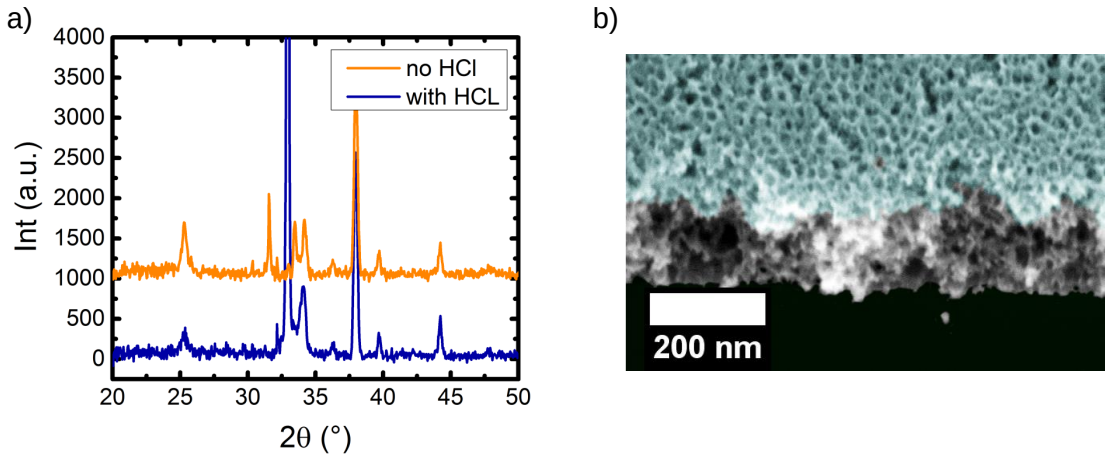

Figure 6.3: *(a) X-ray diffraction of sprayed mesoporous titania thin films. Both for NHCl and WHCl based solutions an anatase titania phase is observed after the calcination step. (b) Cross-section SEM image of sprayed mesoporous titania films from an WHCl based solution. Surface (colored in light blue) and bulk porosity appear to be very similar. Reprinted (adapted) with permission from [40]. Copyright (2018) American Chemical Society.*

relative reduction of crystallite sizes of approximately 32% through the influence of HCl. This trend is in accordance with observations made in literature [39].

For a statistical relevant investigation of the morphology inside the films, GISAXS measurements have been performed for both, as-prepared and calcined films. Respective 2D GISAXS images are depicted in Figure 6.4. Within the first column the initially sprayed (uncalcined) film state sprayed from NHCl solutions can be compared to thin films based on WHCl solutions. Clearly visible is the increased diffuse scattering for WHCl films, which is a strong indication for enhanced lateral structure formation. A similar behavior is found for calcined films in the second column. Again, WHCl films show an enhanced diffuse scattering as compared to the NHCl films. Furthermore, Bragg-rods start to emerge for the WHCl samples, which is another indication for an improved order of the nanostructures. Thus, 2D GISAXS data confirm the improved templating in the presence of HCl, since the diffuse scattering is strongly enhanced for films prepared out of WHCl solutions [63]. Furthermore, for both, WHCl and NHCl, calcination leads to an extension of diffuse scattering towards larger q_y regions (smaller structures) as compared to uncalcined films. This observation is in good agreement with the assumption that structures are shrinking, when the diblock copolymer template is removed.

Quantitative details of the titania nanostructures are extracted from modeling of horizontal line cuts of 2D GISAXS data. In Figure 6.5 vertical (a) and horizontal (b) line cuts of 2D GISAXS data of calcined titania films are shown. Horizontal cuts are taken at the

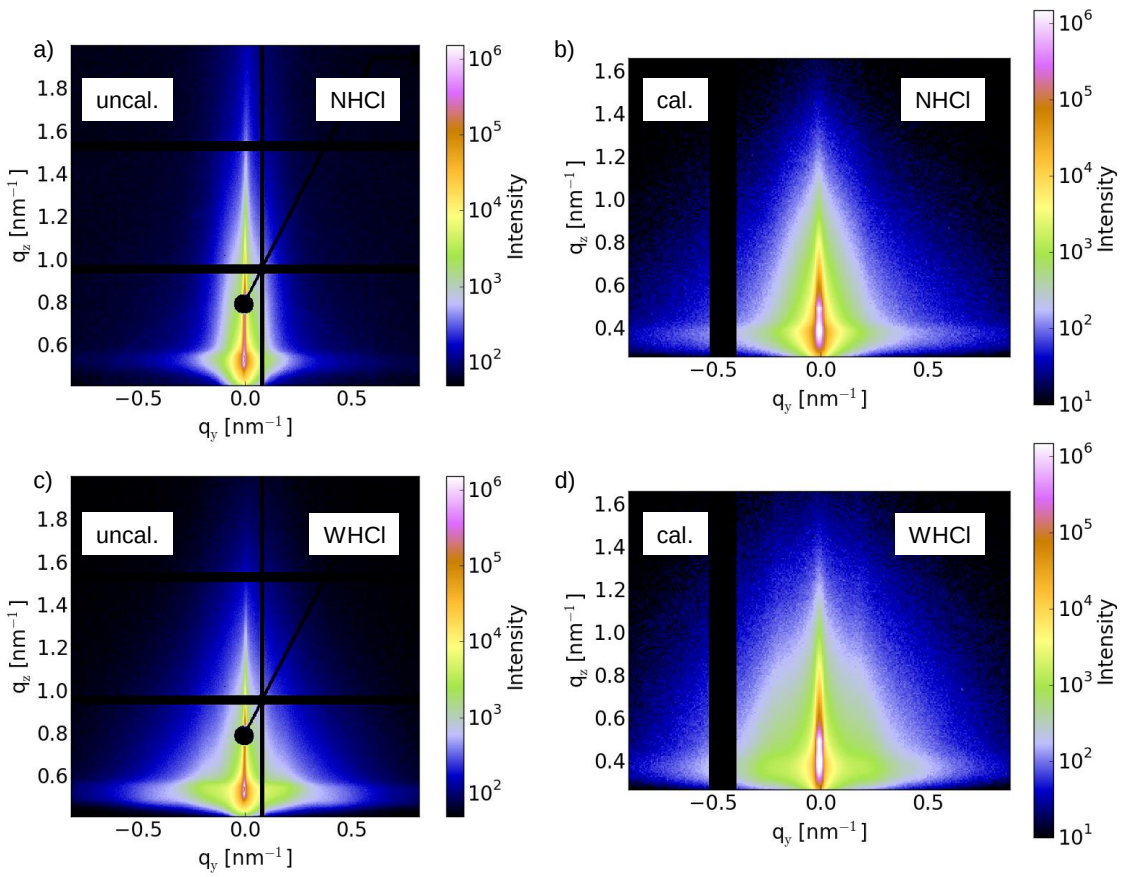

Figure 6.4: *2D GISAXS data of uncalcined (a,c) and calcined (b,d) titania thin films deposited via spraying. The top row is referring to films, which have been sprayed without HCl as an additive, while the bottom row refers to films made from solution with HCl as an additive. Note that data shown in the left column has been measured directly after deposition at the beamline P03, at DESY, while the right column shows data recorded with an inhouse SAXS instrument. Reprinted (adapted) with permission from [40]. Copyright (2018) American Chemical Society.*

material specific Yoneda peak position for porous titania ($q_z = (0.39 - 0.42)$ nm^{-1}, area between dashed lines in Figure 6.5a). The extracted horizontal line cuts for NHCl (orange points) and WHCl (blue points) based films are depicted in Figure 6.5b. Respective modeling results are shown as solid lines in the respective color. For NHCl the scattering is enhanced for regions of smaller q_y values, while for WHCl based films a feature for larger q_y values is strongly enhanced. This enhancement is a strong indication for an improved ordering of small structures through the influence of HCl as confirmed at the surface via SEM. Extracted values as obtained from horizontal line cut modeling before and after calcination can be found in Table 6.1. As expected, for both NHCl and WHCl samples, radii and distances tend to shirk after calcination, even though their base struc-

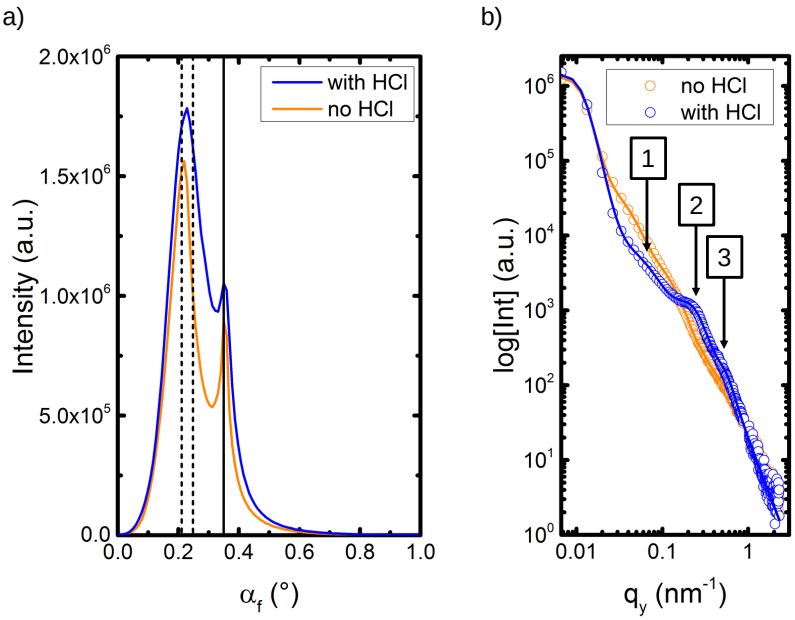

Figure 6.5: *Vertical (a) and horizontal (b) line cuts of 2D GISAXS data of calcined and mesoporous titania thin films deposited via spraying. The black dashed lines in (a) indicate the titania specific region where the horizontal line cuts have been performed. The black solid line refers to the specular reflection. Clearly visible in the horizontal line cut (b) is the strongly enhanced feature under the influence of HCl (blue data points). Modeling results are represented in the corresponding colored solid lines. Black boxes with numbers and arrows indicate different features, each originating from different lateral ordering in the probed sample. Reprinted (adapted) with permission from [40]. Copyright (2018) American Chemical Society.*

ture appears to be preserved. Furthermore, the overall size and distance of structures found for NHCl based films is found to be larger in the calcined and the uncalcined state as compared to their respective WHCl counterpart. The core findings can be summarized in the statement that 2D GISAXS modeling proves that pores appear smaller and more uniform through the addition of HCl to the spray solution.

6.4 *In situ* GISAXS investigation during spray deposition

With the aim to obtain a better understanding of how the different titania morphologies are formed, *in situ* GISAXS measurements are performed during the spray process. Due to the large X-ray footprint at very small incident angles and the high brilliance of the X-ray source combined with the fast readout system, inner morphological changes have been tracked with a high statistical relevance and a high time-resolution of 0.1 s.

	NHCl, uncal.	NHCl, cal.	WHCl, uncal.	WHCl, cal.
radius 1 [nm]	39 ± 3	17 ± 3	21 ± 2	11 ± 2
radius 2 [nm]	14 ± 1	9 ± 1	7 ± 1	5 ± 1
radius 3 [nm]	6 ± 3	2 ± 1	2 ± 1	3 ± 1
distance 1 [nm]	85 ± 10	85 ± 20	55 ± 10	55 ± 20
distance 2 [nm]	50 ± 15	50 ± 20	20 ± 3	18 ± 3
distance 3 [nm]	26 ± 6	19 ± 5	14 ± 4	9 ± 3

Table 6.1: *Radii and distances of sprayed and mesoporous titania structures as extracted from 2D GISAXS modeling.*

For a quantitative insight into the morphological evolution of dominant lateral structures residing inside the titania film, horizontal line cuts of the kinetic 2D GISAXS data are performed at the material specific Yoneda peak position [54]. Modeling is done based on the Distorted Wave Born Approximation (DWBA) using the Effective Interface Approximation (EIA) [55]. The applied model in DWBA and EIA is based on three different form factors with cylindrical geometry distributed over 1D paracrystal lattices [111]. Whereas the structure factors describe the center-to-center inter-domain distances of neighboring titania domains, the form factors refer to the Fourier transform of the electron density of titania objects residing inside the thin films. In the following part form factors are described by the radius of the cylindrical geometry used for modeling. Errors bars as indicated in the following figures are estimated by variation of modeling parameters until accordance to scattering data is lost. When possible, the data have been binned to a 1 s time resolution to further improve the signal to noise ratio for the data modeling after having checked the absence of faster kinetics. Note that a total of three different form factors have been used for data modeling since three distinct features have been identified in the horizontal line cuts at the Yoneda peak position (marked by arrows in Figure 6.5). Extracted distances and form factors (radii) are plotted as a function of time in Figure 6.6 within the first 90 s of the spraying period (1 s spraying, 2 s pause, 30 spray events in total). Exclusively for the first spray shot (first sec) modeling is done with the full time resolution of 0.1 s and intensities are upscaled to fit the integrated data. Additionally, morphological changes are tracked during a drying period after the last spray event (90 s – 210 s). Respective horizontal line cuts with corresponding modeling (solid lines) can be found in Figure 6.7 for the spray process (1 s – 90 s) and subsequent drying time (90 s – 210 s).

For NHCl based films, the best model fits are obtained with radii of (6 ± 3) nm, (15 ± 7) nm and (37 ± 7) nm during the first second of spraying. In contrast, WHCl based films

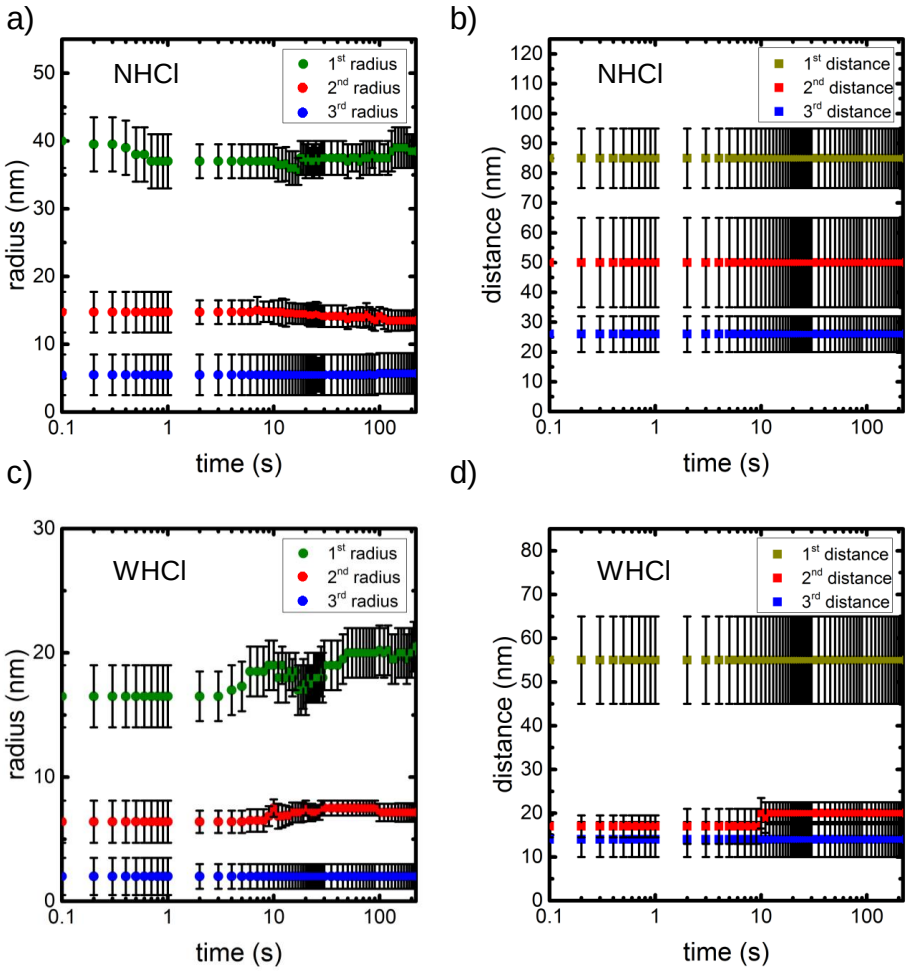

Figure 6.6: *Time evolution of (a,c) radii and (b,d) distances for the sprayed titania thin films obtained from modeling of in situ GISAXS data. (a,b) Modeling results for NHCl based solutions and (c,d) same parameters for WHCl solutions. In general, distances and radii are decreased for WHCl based thin films (better surface-to-volume ratio) and structural rearrangement is exclusively happening with the presence of HCl. Reprinted (adapted) with permission from [40]. Copyright (2018) American Chemical Society.*

exhibit smaller structures with radii of (2±1) nm, (6±2) nm and (17±3) nm in this time of the spray deposition. The significantly smaller sizes of the initially formed nanostructures for WHCl spraying are in good agreement with observations made for the final titania film morphologies. Both, larger inner structures and larger surface structures are observed for the final calcined NHCl films via GISAXS and SEM. Smaller distances and sizes for WHCl films in comparison to NHCl films imply smaller pores and, consequentially, a higher surface-to-volume ratio, which is fundamentally expected to enhance exciton splitting in hybrid photovoltaic devices. In fact, the temporal evolution of radii during the first

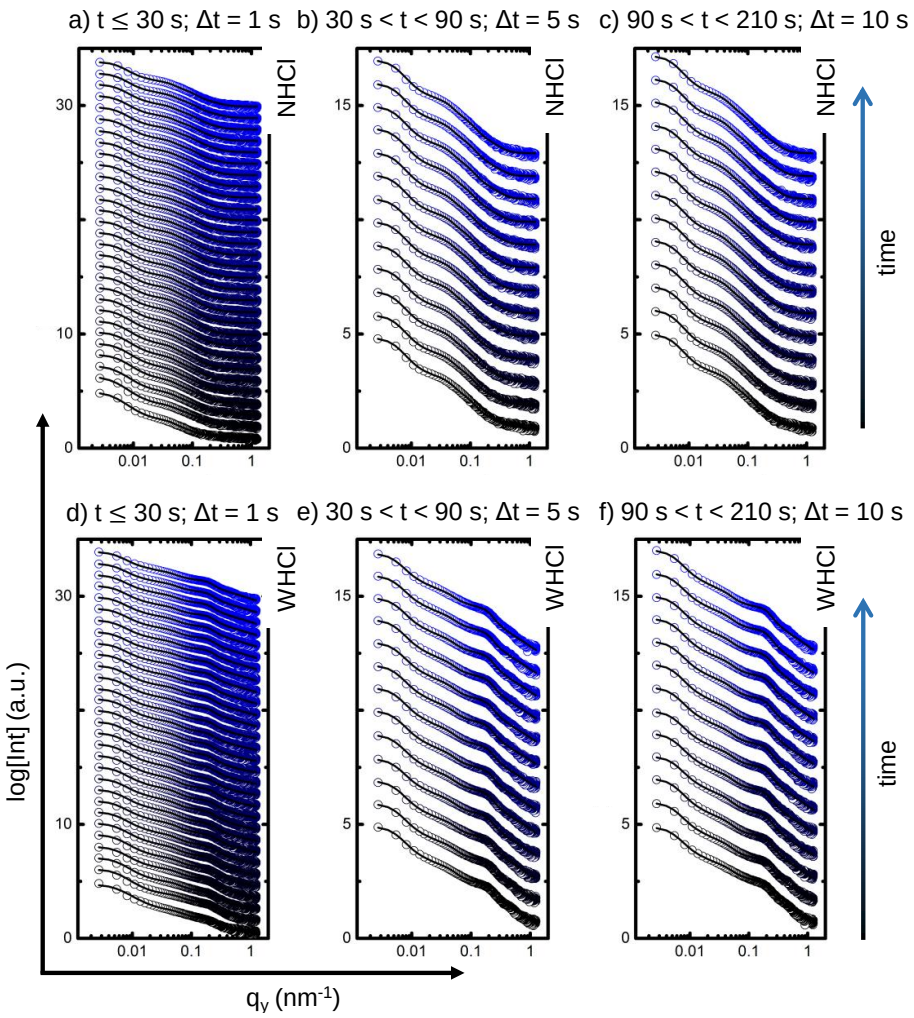

Figure 6.7: *Horizontal line cuts of in situ 2D GISAXS data during spray deposition of composite titania films. The modeling is depicted as the solid black line between data points. For clarity a vertical offset is used for different times. The top row (a-c) refers to data obtained from NHCl based solutions. Likewise, the bottom row (d-f) shows the results for WHCl based data. The same units in x- and y-direction are used for all graphs. Furthermore, the data is split into 3 different time regimes; 1 - 30 s (a,d), 30 – 90 s (b,e) and 90 – 210 s (c,f). Reprinted (adapted) with permission from [40]. Copyright (2018) American Chemical Society.*

second indicates that the nanostructure is not altered within the timeframe of the first spray shot. This leads to the conclusion that the observed nanostructures are formed before being deposited onto the substrate (either prior to spraying in the ink and/or in the time between emission from the nozzle and hitting the substrate). The same is seen, when looking to the horizontal line cuts belonging to the first second (Figure 6.8). In these cuts, no shift of the peak resembling the lateral structure is observed but rather an increase in intensity is found for both, NHCl and WHCl based thin films. Even after the

final 30th spray shot (t = 90 s) no significant change in the horizontal line cuts can be observed for the NHCl based films (Figure 6.7).

In contrast, a steady and small increase up to (20 ± 2) nm of the first radius is probed for the WHCl based structure formation, which appears to stop after 30 s (Figure 6.6). Under the assumption that the small increase is reflecting a structural change (as observed steadily for all measurements t > 3 s), no such behavior has been found for NHCl based film formation. This implies that the NHCl solution already favors cluster formation before being deposited (larger size of radii already for the first spray shot) and is less likely to follow the structure of the polymeric template due the difference in given reaction dynamics. Importantly, in both cases (NHCl and WHCl) no significant change of the radii could be observed during the final drying period (t > 90 s). Thereby, a stable morphology is already achieved after t = 90 s, which is attributed to an absence of residual solvents and, thus, airbrush conditions for spraying are indirectly confirmed. Advantages for potential industrial applications in terms of minimization of processing time are foreseen.

Apart from the radius, the modeling yields inter-domain distances (right column of Figure 6.6). For NHCl based film formation the best data modeling has been obtained with distances of (26 ± 6) nm, (50 ± 15) nm and (85 ± 10) nm in the early stages. Within the same time regime significantly smaller distances of (14 ± 4) nm, (17 ± 3) nm and (55 ± 10) nm are formed with the addition of HCl, which is in accordance with the observations made for the final film morphology via SEM and GISAXS. Note that from the three characteristic distances found in the *in situ* GISAXS modeling, only the two smaller ones match with observations in the SEM images of the film surfaces. The largest distance found in the GISAXS analysis is either not observed at the film surface due to the local character of the SEM measurements and/or is located inside the films and not at the surface. Similar to the time evolution of the radii, there is no apparent change of distances visible for NHCl based film formation. Only for WHCl based structure formation the medium sized distances slightly increases from (17 ± 3) nm up to (20 ± 3) nm. Under the same assumption that this observation is reflecting an actual morphological change (due to steady appearance for all later measurements), the most likely explanation would be a stretching/rearrangement of the polymer template. The constant solvent evaporation during the spray process can be understood as a solvent-vapor annealing and larger inter-domain distances between titania structures are formed due to bringing the morphology more towards equilibrium. Following the same logic introduced for the evolution of the radii, it is not surprising that this behavior only occurs under the influence of HCl, since the templating effect is strongly enhanced by the addition of HCl.

The overall smaller distances of scattering objects (smaller pores) / sizes of the WHCl samples as compared to the NHCl samples in conjunction with the increased number

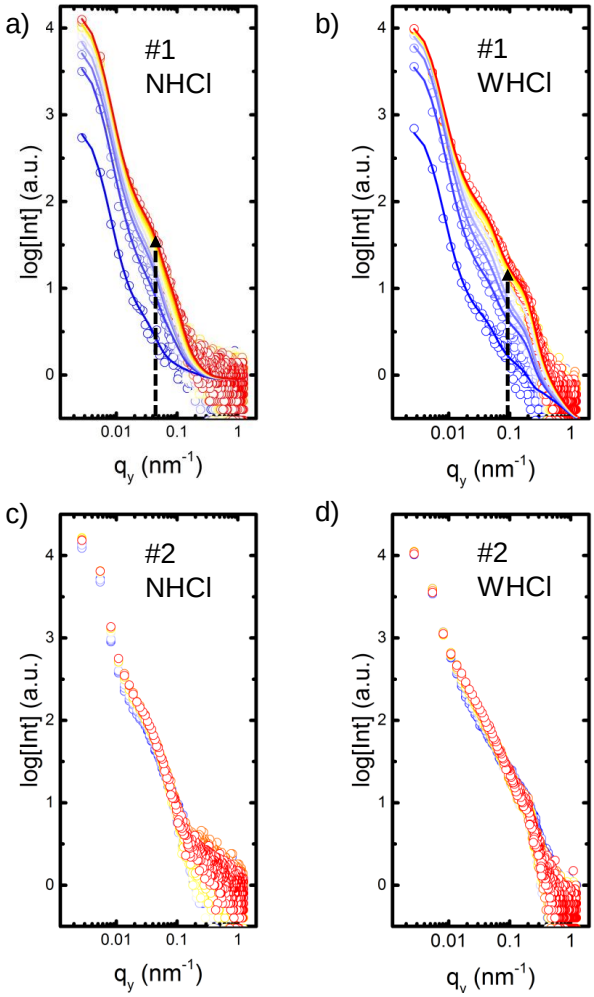

Figure 6.8: *Horizontal line cuts of in situ 2D GISAXS data during spray deposition of composite titania films. The top row (a,b) refers to the first spray shot, while the bottom row (c,d) shows the evolution of lateral structures for the second spray shot. Furthermore, the (a,c) refers to spray deposition without HCl. In contrast, the (b,d) shows data recorded from solution spraying with HCl. Color gradient from blue to red is following the time evolution with a total duration of 1 s (0.1 s steps). Reprinted (adapted) with permission from [40]. Copyright (2018) American Chemical Society.*

surface density of pores as seen via SEM are directly correlated to an increase in surface-to-volume ratio. In turn, an increased surface-to-volume ratio translates to a higher amount of interface between titania and air inside the pores. For hybrid photovoltaic application, the interface between two different materials is essential for efficient exciton splitting, which then effects the photo conversion efficiency of devices through an increase of charge-carriers. Thus, efficient backfilling of the structurally improved WHCl samples is fundamentally foreseen to yield enhanced device performance in comparison to backfilling of NHCl samples.

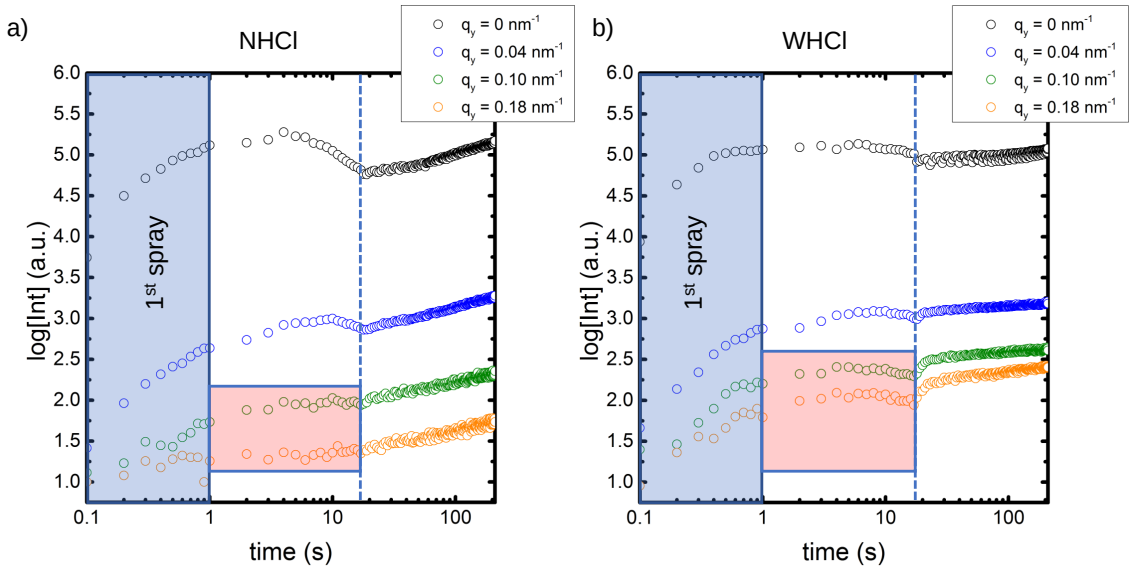

Figure 6.9: *In situ GISAXS time evolution of intensity during spray deposition of (a) NHCl and (b) WHCl based solutions and the subsequent drying process of hybrid Ti-based thin films. The intensities are shown for four different diffuse scattering regimes q_y as indicated. Reprinted (adapted) with permission from [40]. Copyright (2018) American Chemical Society.*

In order to have a closer look at the individual spray shots, the horizontal line cuts of the raw *in situ* 2D GISAXS data (0.1 s measurements, without integration) are displayed in Figure 6.8 for NHCl (left column) and WHCl (right column) based films within the period of the first (top row) and second (bottom row) spray shot. Comparison of NHCl and WHCl measurements exhibits the formation of a more pronounced lateral feature for WHCl based solutions already in the early stages of the first spray shot. No significant shift in q_y could be seen within these early stages (only intensity increases, not the peak positions). The assumption that most structures are already present within the spray solution is strongly supported by this observation. Overall, the intensity increase is more pronounced within the first spray shot as compared to the second spray shot.

In addition to modeling, the intensity for different q_y regimes is plotted for the time-frame of the *in situ* GISAXS measurement (Figure 6.9). Black and blue data points are extracted from a low q_y region ($q_y = 0$ nm^{-1} and $q_y = 0.04$ nm^{-1}). Green and orange points correspond to data extracted from a higher q_y region ($q_y = 0.10$ nm^{-1} and $q_y = 0.18$ nm^{-1}). For both, NHCl and WHCl solutions, the most evident intensity increase for all q_y regimes occurs during the first second of spraying. The initially deposited material causes a strongly enhanced diffuse scattering. Corresponding and stacked horizontal line cuts can be found in Figure 6.8. Another interesting feature is marked with the blue dashed line at the 18 s mark. This observed intensity drop is ascribed to a Volmer-Weber-

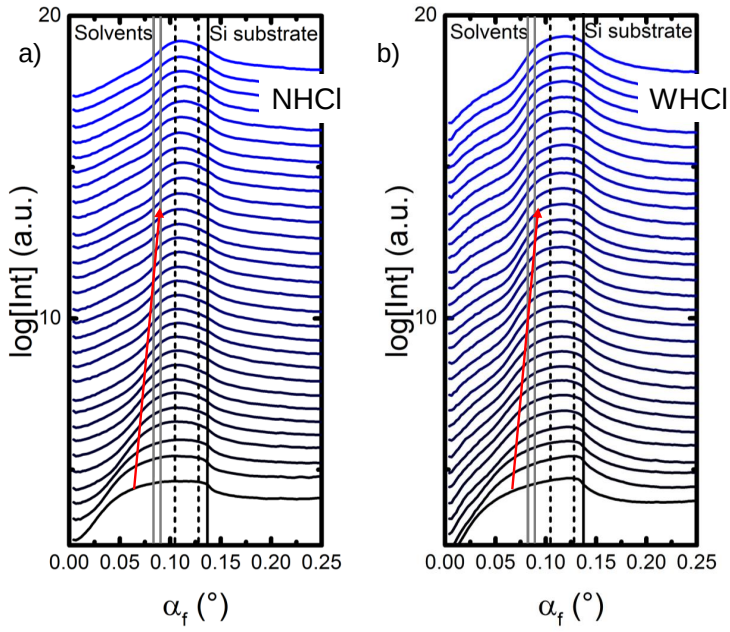

Figure 6.10: *Vertical line cuts of 2D GISAXS pattern for the initial 30 s of the in situ measurements of spray-deposited composite titania layers ((a) NHCl, (b) WHCl). Grey solid lines indicate areas, where solvent specific peaks are expected (toluene and 1-butanol) and dashed black lines mark the region for porous titania specific horizontal line cuts. The solid black line indicates the Yoneda peak position of the silicon substrate. For both cases (with and without the influence of HCl) an appearance of a shoulder-like feature (red arrow) can be observed until approximately 20 s after the initial spray event. Reprinted (adapted) with permission from [40]. Copyright (2018) American Chemical Society.*

like (island formation) macroscopic growth type. The most prominent difference between NHCl and WHCl appears within the red marked regions. The green and orange data points, which refer to higher q_y values (smaller structures), exhibit increased scattering intensities, especially for samples sprayed with HCl. The observation that WHCl sprayed samples resulted in smaller structures than NHCl based samples is consistent with the finding of overall lower intensities for NHCl based samples in the respective q_y region.

In Figure 6.10 vertical line cuts of 2D GISAXS patterns are stacked for the initial 30 s of the *in situ* measurement (left NHCl, right WHCl). Grey solid lines indicate areas, where solvent specific peaks are expected (toluene and 1-butanol) and dashed black lines mark the region for titania specific horizontal line cuts. For both NHCl and WHCl based film deposition a shoulder-like feature (red arrow, Figure 6.10) can be observed for the initial stages. This feature can be explained via two approaches. First, solvent remains might be present in the initial stages of the spray deposition and cause the appearance of the observed shoulder-like feature. Nevertheless, the shoulder-like feature

extends to q_z regions, which cannot solely be explained by the presence of solvent remains. Consequently, it is assumed that the initially present shoulder-like feature is related to regions of lower titania density. These low-density titania regions are probably caused by an island-growth type during spray deposition, which is as well suggested by the analysis of scattering intensity (Figure 6.9). This assumption appears even more likely as the shoulder-like feature is completely vanished after approximately 20 s. After these 20 s a closed titania layer is assumed to be formed, which is most-likely the reason, why the lateral scattering intensity of Figure 6.9 is reduced. Furthermore, this observation is found independent of the presence of HCl and is, therefore, attributed to the parameters chosen for the spray deposition process.

6.5 Conclusion

In summary, nanostructured titania thin films are successfully synthesized via polymer-template assisted sol-gel synthesis in combination with spray deposition for potential use in DSSCs, ssDSSCs or PSCs. The role of HCl as a catalytic additive to the sol-gel solution is analyzed with respect to surface and inner film morphologies. In AFM, SEM and GISAXS measurements prior to and after template removal, an overall smaller nanostructure with enhanced order is found due to the presence of HCl in the spray solution. The observed improved templating effect is ascribed to altered reaction dynamics and phase separation, which favor the formation of elongated structures and, thereby, allow titania nanostructures to be formed following the structure of a given block copolymer template. *In situ* GISAXS measurements reveal that while structure formation for no-HCl based templating is mostly guided through processes prior to deposition, the presence of HCl in the spray solution allows for a (small) further rearrangement of titania structures during deposition. Samples sprayed from solutions without HCl appear to lack this ability to rearrange, since following the rearrangement of the polymer template structure caused by the exposure to the inert solvent vapor is not favored due to different reaction dynamics. The obtained knowledge about the essential role of HCl in structure formation processes is expected to improve the development of large scale titania spray setups for industrial applications, which will be of particular importance in fabricating large scale DSSCs, ssDSSCs or PSCs.

7 Morphological tunability of mesoporous Ge-based thin films

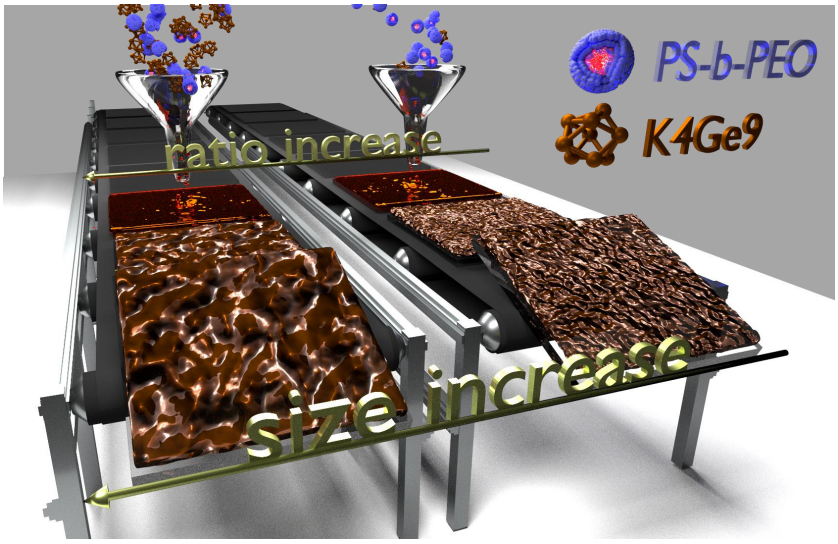

The following chapter is based on the published article: Amphiphilic diblock copolymer-mediated structure control in nanoporous germanium-based thin films [37] (Nuri Hohn et al., Nanoscale, 11, 2048-2055, 2019, DOI: 10.1039 / C8NR09427F)[1].

In chapter 5 it has been demonstrated that diblock copolymer templating can be successfully employed to control the nanomorphology of titania thin films. Similarly, spray deposition from a wet-chemical precursor was carried out to further approach potential industrial application (chapter 6). Within the present chapter, the employed material system is altered to allow for the synthesis of mesoporous Ge-based thin films. The element Ge offers advantages such as high electron mobility for photovoltaics and high

[1]Reproduced/adapted by permission of The Royal Society of Chemistry. Most results of the present chapter were obtained in close collaboration with the master's student Andreas E. Hetzenecker [119]

specific capacity for Li ion battery applications. The approach to achieve and control a mesoporous Ge-containing structure is based on similar diblock copolymer templating concepts as shown in previous chapters for the example of mesoporous titania and is assumed to offer all the inherent advantages, which have been demonstrated for the case of titania nanostructuring. The chapter begins with an orientation of major scientific contributions to the field of mesoporous Ge thin film synthesis (section 7.1). Thereafter, a short description is given on how to synthesize mesoporous Ge-based thin films (section 7.2). The following main sections report about basic properties of mesoporous Ge-based thin films (section 7.3) and structural control of surface and inner morphology as proven by SEM and GISAXS measurements (section 7.4). Additionally, the chemical composition analysis of synthesized thin films by XPS and XRD confirms that Ge is the core element of the observed mesoporous structure.

7.1 Preface

Nanostructuring porous semiconductors enables tuning of physical properties as compared to their solid, bulky counterparts [120, 121]. Applications typically profit from high surface-to-volume ratios as well as controllable optoelectronic behavior [46, 47, 122, 123]. A large variety of nanostructures has been realized via, for example, the block copolymer assisted sol-gel synthesis of metal oxides such as titanium dioxide [42, 75, 99, 101, 124–127]. In this approach a metal precursor is combined with an amphiphilic diblock copolymer acting as a structure directing template [128–130]. Numerous related studies have been conducted with respect to applications in diverse fields such as photovoltaics, energy storage, gas sensing, photocatalysis and metamaterials [79, 82–85, 87, 88, 90]. Further studies employing nanostructured Si or TiO_2 have shown great potential in energy storage applications [15, 131]. In comparison, studies on nanostructured group IV semiconductors such as Ge are scarce. In fact, energy storage applications based on nanostructured Ge could especially profit from the theoretically high specific capacity of 1385 mAh g^{-1} ($Li_{15}Ge_4$) and roughly 400 times higher Li ion diffusivity than Si at room temperature [17, 132–134]. Furthermore, with Ge being the semiconductor with the highest known electron mobility our approach to control the nanostructure of Ge-based thin films on the basis of wet-chemical processing bears the potential to set new benchmarks in photovoltaic applications [22].

Routines to synthesize Ge-based nanocrystals, nanosheets, nanowires and nanoparticles with highly tunable surfaces are well-established [135–137]. In contrast, reports on fabrication of nanoporous Ge-based thin films are less common. Within this frame, chemical and electrochemical etching have proven to be successful methods to manufacture porous

Ge-based layers [138, 139]. Despite the advantage of well-defined composition and crystallinity, the control of nanoscale structure is limited via these etching approaches. Consequently, a bottom-up synthesis routine based on organic macromolecule self-assembly combined with wet-chemical processing appears to be very interesting for synthesis of Ge-based nanostructures. Among those benefits, control of the pore sizes within the nanometer range while allowing for large scale production appears especially relevant for industrial usage [95, 96].

One requirement for the successful realization of sol-gel synthesis to fabricate nanoporous Ge-based thin films is the availability of a suitable precursor. Zintl clusters have been reported to be an attractive choice to enable wet-chemical solution processing for non-oxide thin film fabrication with tunable electronic properties [47, 140–142]. While through electrochemical approaches dense or macroporous Ge layers can be deposited, a combination of Zintl clusters with surfactants might enable the formation of nanoporous thin films [143–145]. Fässler and coworkers reported on successful usage of K_4Ge_9 Zintl clusters combined with polymethyl methacrylate (PMMA) nanosphere templating to fabricate periodic, inverse-opal Ge thin films with pore diameters larger than 200 nm [41]. Successful implementation of porous Ge films as anode material in Li ion batteries was demonstrated recently [16].

Herein, a new synthesis routine is introduced based on $[Ge_9]^{4-}$ Zintl clusters in combination with block copolymer assisted sol-gel synthesis to fabricate nanoporous, foam-like Ge-based thin films. Accordingly, K_4Ge_9 is used as a precursor, while controlled phase separation of the amphiphilic diblock copolymer polystyrene-b-polyethylene oxide (PS-b-PEO) serves as a structure directing mechanism. The following sections show for the first time the potential of diblock copolymer templating to manufacture size-controllable, nanoporous Ge-based thin films. The presented approach offers several advantages. Among those and most apparently, the exploitation of nanostructured Ge in the field of energy storage application would allow to profit from the high Li ion diffusivity and superior specific capacity in Ge-based thin films. Compared to bulk Ge, the nanoporous structure is expected to especially enhance capacity, cycle life and rate capacity as similar observations have been made for the case of nanostructured titanium oxide [15]. Furthermore, the size of pores in nanostructured Ge-based thin films is tunable within a range up to 40 nm, which matches the exciton diffusion length in most commonly employed polymeric material [13]. The introduced strategy is considered especially promising for hybrid (opto-)electronic applications as the polymeric material could be backfilled into the porous Ge-based matrix and, thereby, profit from the above-mentioned suitable pore size range for exciton splitting in hybrid devices. This specific range of pores sizes has not yet been accessible for nanoporous Ge-based thin films. Additionally, the potential for

large scale application through e.g. spray coating is ensured via wet-chemical processing. The formation of crystalline α–Ge phases can be achieved through annealing. Combining all advantages, the presented routine could boost future device performance in the field of energy storage and hybrid photovoltaics, as the substitution of commonly employed nanoporous titanium dioxide with Ge would strongly enhance the electron mobility within the device.

7.2 Experimental: Synthesis of mesoporous Ge-based thin films via spin coating

To obtain nanostructured Ge-based thin films, the precursor K_4Ge_9 is combined with the structure directing polymer template PS-b-PEO dissolved in the transfer medium ethylenediamine (Figure 7.1a). Under exclusion of water, different PS-b-PEO/K_4Ge_9 molar mixing ratios in the range between 1/10 up to 1/80 are made (Figure 7.1b). Note that referring to an increasing molar ratio always means that the amount of precursor (K_4Ge_9) is increased in relation to the polymer template (PS-b-PEO). More detailed information about the synthesis process can be found in section 4.3.3. Nanocomposite thin films are fabricated via spin-coating of the mixed solution onto a substrate (Figure 7.1c). A subsequent post-treatment based on an azeotrope solvent mixture of anhydrous toluene and 1-butanol is applied to enhance the phase separation of the diblock copolymer blocks (Figure 7.1d). Solvent removal and structural rearrangement is realized through a heat treatment at 200 °C for 15 min under inert gas conditions (N_2, Figure 7.1e). The template is removed by calcination at 500 °C for 5 min. Preparation steps shown in Figure 7.1a – d are performed under inert gas conditions (N_2). Unless otherwise stated, template removal is accomplished via heat treatment in air.

7.3 Basic properties of mesoporous Ge-based thin films

The most predictable consequence of an altered precursor to polymer template ratio is seen in an altered thickness of synthesized films after calcination. To probe the thickness of nanoporous Ge-based thin films quantitatively, profilometry measurements with a DektakXT™ apparatus by Bruker are carried out on films prepared from precursor solutions with molar ratios in the range from 1/10 to 1/80. Corresponding results are depicted in Figure 7.2a. The red dashed line serves as a guide-to-the-eye. Accordingly, the thickness increases up to an approx. molar ratio of 1/45. An increase of the K_4Ge_9

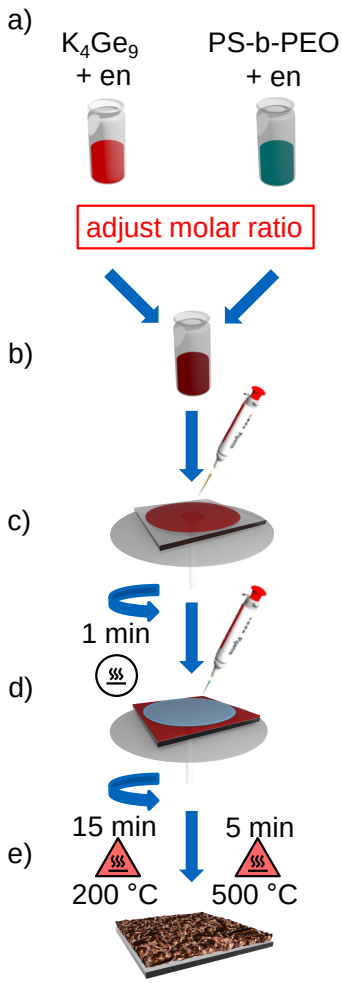

Figure 7.1: *Processing steps for the preparation of nanoporous Ge-based thin films. In (a) two separate ethylenediamine (en) solutions with the Ge precursor (K_4Ge_9) and the polymer template (PS-b-PEO) are prepared. Different molar ratios are mixed in (b) with subsequent spin-coating in (c). Post-treatment with an azeotrope solvent mixture of 1-butanol and toluene is carried out after 1 min drying in step (d). After a second spin-coating step, two successive heat treatment procedures are applied in (e) to allow for structural rearrangement and template removal. Reproduced/adapted by permission of The Royal Society of Chemistry [37].*

precursor content above this ratio leads to no further thickness increase as polymeric domains are over-saturated with the precursor K_4Ge_9.

Initial surface characterization of fabricated nanoporous Ge-based thin films is carried out via an Axiolab A microscope by Carl Zeiss, which is coupled to a CCD camera. Respective images shown in Figure 7.2b are obtained from a sample with an exemplary molar ratio of 1/50. At lower magnification a rather homogeneous film is observed with only few impurities. However, at higher magnification indications for a macroscopic foam-

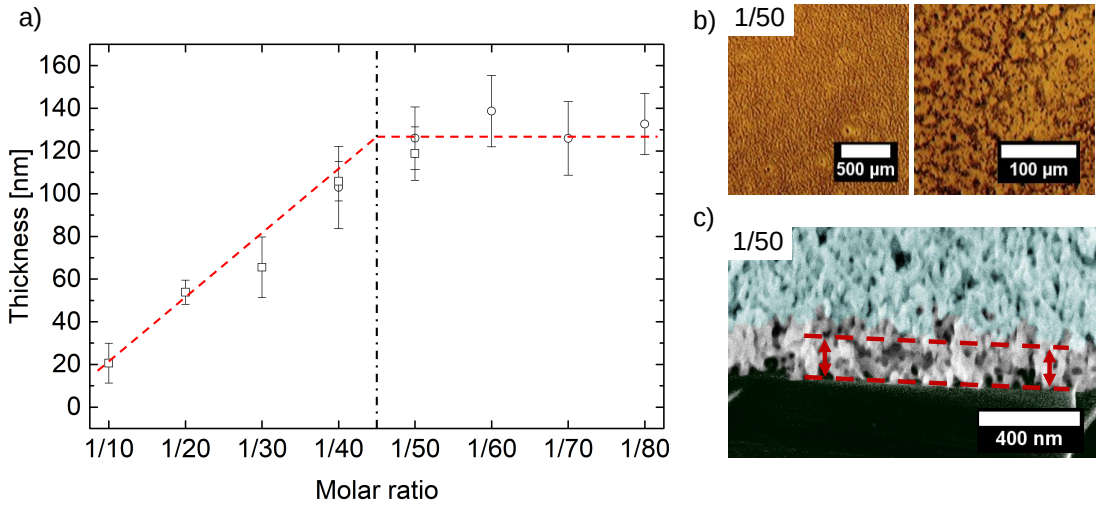

Figure 7.2: *(a) Thickness of nanoporous Ge-based thin films as obtained from profilometry measurements. Shown is the effect of different PS-b-PEO/K_4Ge_9 molar mixing ratios on the final thickness of the thin film. (b) Exemplary optical microscope images for a molar ratio of 1/50. (c) Cross-section SEM image for a molar ratio of 1/50 proves the existence of a fully nanoporous Ge-based thin film (from surface to substrate). The surface of the thin film is colored in light blue. An average thickness of approx. 120 nm is confirmed and is indicated between the red dashed lines. Reproduced/adapted by permission of The Royal Society of Chemistry [37].*

like surface with high surface roughness can be seen. In order to prove that the observed foam-like structure is also present at a mesoscopic range and that it is not only retained at the surface, cross-section SEM images are acquired (Figure 7.2c). As observed for an exemplary molar ratio of 1/50, the whole film consists of nanoporous Ge-based material with a thickness of approximately 120 nm. The measured thickness from cross-section SEM (dashed red lines) is consistent with results obtained from profilometry.

The chemical composition of the fabricated thin films is investigated via surface-sensitive X-ray photoelectron spectroscopy (XPS). For the XPS measurements, samples are spin-coated onto conductive FTO coated glass substrates. The probing depth of XPS in the set-up is assumed to be approximately 5 nm ($3\lambda\cos\theta$, with $\theta_e \sim 45°$ electron emission angle) [67]. A survey scan recorded with a pass energy of 20 eV is reported in Figure 7.3 and gives clear evidence for the presence of Ge, K, C, and O through the respective core-level lines. Additionally, the Ge LMM Auger transitions are observed in the spectrum. In the overview, the ratio I(O 1s) : I(Ge 3d) is about 4 : 1. Taking into account the ratio of photoionization cross-sections (0.04 : 0.02) at 1486.6 eV [146], the O : Ge concentration ratio is estimated to be 1.8-2.

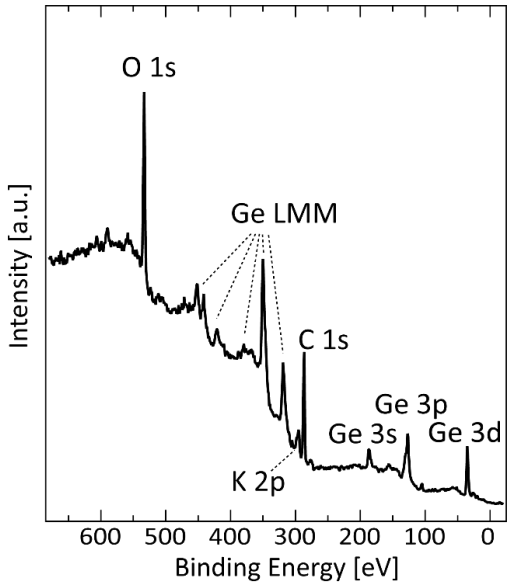

Figure 7.3: *Chemical characterization of nanoporous Ge-based thin films. X-ray photoelectron spectroscopy survey scan showing the presence of several Ge core-level peaks as well as Ge LMM Auger emission. Additionally, peaks attributed to the presence of carbon, oxygen and potassium remains are observed. Reproduced/adapted by permission of The Royal Society of Chemistry [37].*

Zoom-in spectra of the Ge 3d and Ge 3p core-level lines have been recorded with a pass energy of 10 eV. Figure 7.4a shows the Ge 3d core-level region. In the case of elemental Ge, the expected binding energy position of the spin-orbit split components is 29.8 eV ($3d_{3/2}$) and 29.2 eV ($3d_{5/2}$) [68, 147], respectively, which typically give rise to a single sharp, convoluted peak for a conventional (non-monochromatized) X-ray source. In the case of the measured Ge-based thin film, however, the Ge 3d emission appears as a rather broad peak, whose centroid is shifted to a binding energy of 35.6 eV. In Figure 7.4a, the Ge 3d spectrum has been fitted with a single Gaussian curve superimposed on a Shirley background (blue line) [148]. A binding energy of 35.6 eV is extracted through the fitting. In conjunction with surface charging effects in the order of 2 eV as confirmed by analysis of the C 1s emission line, this position matches the expected binding energy of GeO_2 (33.9 eV) [23, 149, 150]. Note that a 1.8-2 ratio of O : Ge as obtained from the intensity analysis in the overview might as well suggest traces of incomplete oxidation (GeO_x). Therefore, an alternative fitting with two Gaussian curves can be found in the next section to account for the possible presence of GeO_x and GeO_2. Analysis of the Ge 3p profile further confirms the existence of GeO_2 at the sample surface (Figure 7.4b). Here, the zoom-in of the Ge 3p emission line shows a similar shift towards higher binding energies. The expected binding energy position of the spin-orbit split components of elemental Ge is 124.9 eV ($3p_{1/2}$) and 120.8 eV ($3p_{3/2}$), respectively [147, 151]. According to the literature, for GeO_2, the Ge 3p emission shifts by about 4.5 eV towards higher binding energies compared to pristine Ge [152]. The Ge 3p spectrum in Figure 7.4b has been fitted via a Shirley background (blue line) and two Gaussian components (light and dark green) with the same FWHM, fixed spin-orbit splitting and fixed intensity ratios as

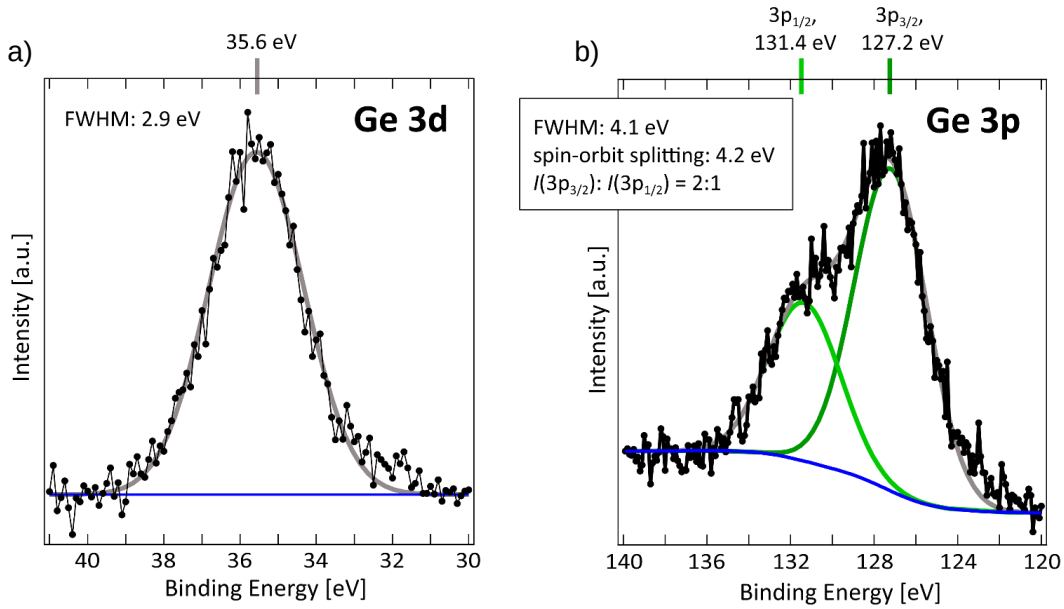

Figure 7.4: *Chemical characterization of nanoporous Ge-based thin films. Zoom-in X-ray photoelectron spectroscopy (XPS) showing (a) Ge 3d and (b) Ge 3p core-level lines. The corresponding peaks in the XPS spectra are fitted with Gaussian functions proving the presence of GeO_2. Reproduced/adapted by permission of The Royal Society of Chemistry [37].*

indicated in the inset. The obtained binding energies are 127.2 eV (Ge $3p_{3/2}$) and 131.4 eV (Ge $3p_{1/2}$), respectively. In conjunction with the above mentioned surface charging effects of approximately 2 eV, the extracted values match the typical expected binding energies of GeO_2 spin-orbit split components (125.6 eV and 129.5 eV) [152]. Note that the observed formation of Ge oxide layers at the surface is reasonably expected due to the applied calcination protocol in air. Removal of surface layers through, e.g., Ar^+ sputtering can yield an elemental Ge rich surface as demonstrated in literature [41, 143].

The minimum estimated concentration ratio of O : Ge of 1.8 as determined from the intensity ratio I(O 1s) : I(Ge 3d) of the survey scan (Figure 7.3) in conjunction with the respective photoionization cross-sections suggests the possible presence of incompletely oxidized Ge (GeO_x). Therefore, an alternative XPS fitting with components for GeO_x and GeO_2 can be found in Figure 7.5. Accordingly, for the Ge 3d core-level region two Gaussian curves with the same FWHM are fitted in Figure 7.5a. The fitting yields a FWHM of 2.5 eV, which is significantly larger than the neglected spin-orbit splitting of d levels (0.6 eV). Centroid positions of 34.3 eV and 35.8 eV are extracted for GeO_x and GeO_2, respectively. Positions of GeO_2 match the expectation of 33.9 eV when accounting for the observed charging effects in the order of 2 eV [23, 149, 150]. A binding energy difference of 1.5 eV between GeO_x and GeO_2 is determined, which is consistent with findings in

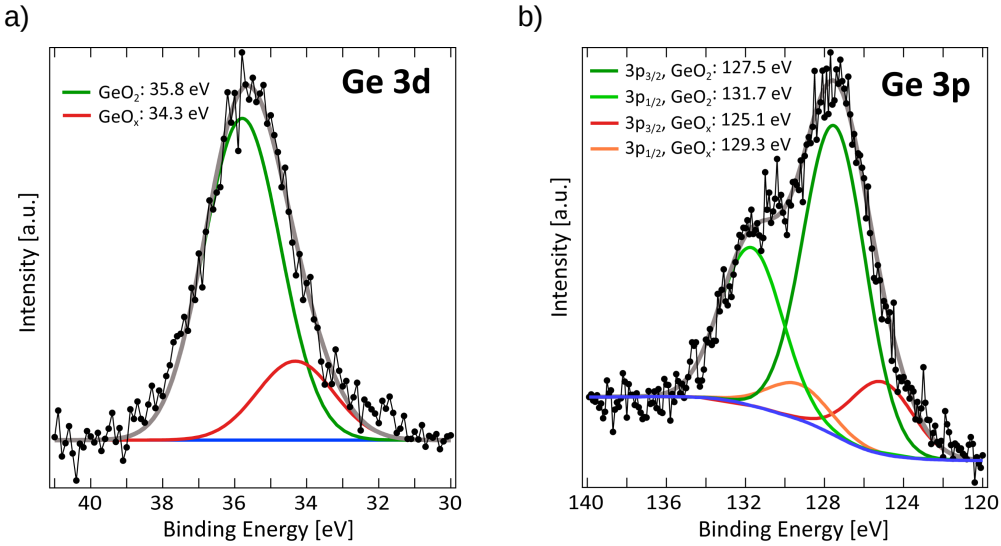

Figure 7.5: *XPS spectra of the Ge 3d and Ge 3p core-level regions with (a) two Gaussian curves and no spin-orbit split components and (b) four Gaussian curves with spin-orbit doublets used for fitting and to account for the possible presence of GeO_x (red and orange lines) and GeO_2 (dark and light green lines). For both fits a Shirley background is used (blue lines). Extracted positions of the respective Gaussian centroids are depicted in the legend. Reproduced/adapted by permission of The Royal Society of Chemistry [37].*

literature [153–156]. An intensity ratio I(GeO_x) : I(GeO_2) of approximately 1 : 4 is determined, which indicates that mainly GeO_2 is present as compared to GeO_x. This agrees with the estimation of concentration ratio from the survey scan in Figure 7.3. Ge 3p line analysis is performed using four Gaussian curves with the same FWHM (Figure 7.5b). A FWHM of 3.7 eV is determined, which is smaller than the fixed spin-orbit splitting of 4.2 eV. Therefore, spin-orbit doublets are accounted for through two additional Gaussian curves as compared to the Ge 3d analysis. Additionally, the intensity ratio of spin-orbit doublets is fixed to 2 : 1. For GeO_x, binding energies of 125.1 eV ($3p_{3/2}$) and 129.3 eV ($3p_{1/2}$) are extracted, which match theoretical values from literature (123.1 eV for Ge $3p_{3/2}$) when considering the above mentioned charging effects (∼2 eV). For GeO_2, binding energies of 127.5 eV ($3p_{3/2}$) and 131.7 eV ($3p_{1/2}$) are extracted, which again agrees with literature (>125.3 eV for $3p_{3/2}$) [152]. In conclusion, XPS proves that the surface of the measured films primarily consists of GeO_2; traces of incomplete oxidation (GeO_x) appear possible as well, but cannot be confirmed with complete certainty due to insufficient resolution (1-1.3 eV). The observed large FWHM values might be additionally broadened by the rough morphology of nanoporous thin films.

Further proof of successful fabrication of nanoporous Ge-based thin films using K_4Ge_9

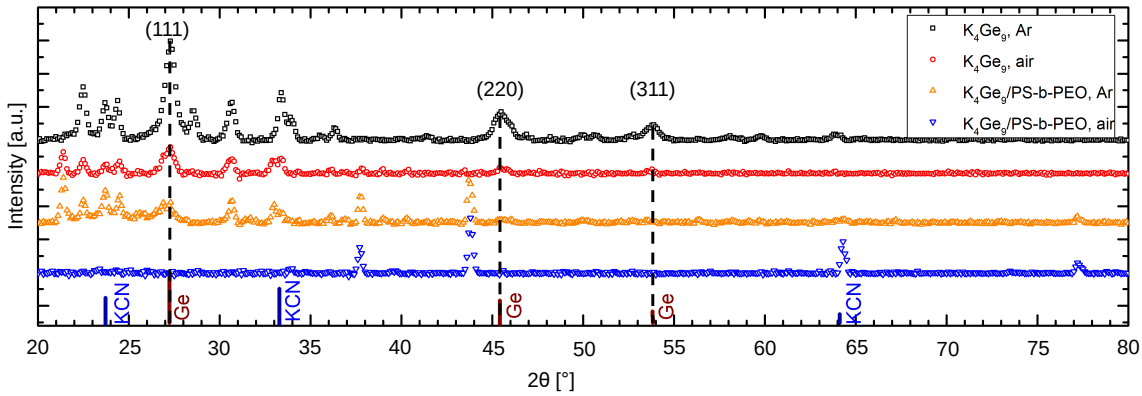

Figure 7.6: *Characterization of nanoporous Ge-based thin films. For an extended heat treatment protocol of 10 h the presence of crystalline α-Ge is found through X-ray diffraction measurements under different conditions as indicated in the legend. Reproduced/adapted by permission of The Royal Society of Chemistry [37].*

as a precursor is obtained from X-ray diffraction (XRD) measurements, which, in contrast to the XPS measurements, also provide information regarding the bulk material composition. For this purpose, solution casting is used to make thicker films. Additionally, the tempering is performed with an increased time of 10 h to obtain crystalline α-Ge. Highest peak intensities for a cubic, diamond Ge phase (α-Ge) are expected for the (111), (220) and (311) peaks [57]. Four different samples are probed to investigate the influence of oxygen and polymer template on the formation of crystalline phases: two samples are cast from a pristine K_4Ge_9 solution in ethylenediamine and two samples from a mixed K_4Ge_9/PS-b-PEO solution. One of each is afterwards tempered in air and the other in Ar atmosphere. Corresponding results are depicted in Figure 7.6. Under exclusion of oxygen during annealing, the polymer-free samples show clear evidence of α-Ge formation (black data points in Figure 7.6). The expected (111), (220) and (311) peak positions are marked with a black, dashed line. Comparison to the annealing protocol in air suggests a slight reduction of α–Ge formation in the latter case as can be seen by the decreased intensity of all three peaks (red data points in Figure 7.6). With additional polymer template PS-b-PEO in the solution, extra oxygen is added to the system (orange data points in Figure 7.6). Evidence for α-Ge is still present when films were annealed in Ar, even though its formation is mostly inhibited due to the oxygen incorporation. However, annealing the same sample in air (blue data points) does not yield any α-Ge peaks. This result is not surprising since the presence of air was already found to lead to the formation of GeO_x and GeO_2 [41]. In addition, the polymer not only adds oxygen to the system through its PEO block, but also induces a nanoporous structure with an increased surface area. Hence, the likeliness for surface oxidation is significantly increased and amorphous

Ge phases most likely mask any possible remains of α-Ge. Note that additional peaks (not α-Ge peaks) are observed through XRD, which could not be assigned with complete certainty due to texturing effects of thin film XRD measurements. However, it is assumed that these additional peaks in the range between 20-35° are mostly related to the formation of germanium carbide composites ($C_kH_lGe_mO_n$) during the calcination process, which typically are found to have crystalline peaks in that specific range [157–159]. Additionally, peaks are attributed to traces of KCN (blue markers in Figure 7.6). No other K-containing phases are found. Germanium carbide and KCN phases are assumed to be formed as a degradation product of K_4Ge_9 and ethylenediamine. Peaks found at 37.7° and 43.8° might be caused by a crystalline GeO_2 phase [160]. Furthermore, the formation of germanium carbide composites is found to be reduced if tempering is performed in air or for mesoporous structures which allow for an improved carbon-escape mechanism (CO_2 formation, pores). Thus, the XRD data in conjunction with XPS suggest the following scenario: air-tempered, nanoporous Ge-based thin films consist of GeO_x/GeO_2 surface layers and bulk GeO_x/GeO_2. Metallic α-Ge and Ge–C can be added to the composition through changing the tempering atmosphere to Ar instead of air. Note that no single crystalline Ge-based material was identified regardless of the applied annealing conditions.

7.4 Control of pore sizes in mesoporous Ge-based thin films

In the previous section exemplary results for samples with a constant PS-b-PEO/K_4Ge_9 molar mixing ratio of 1/50 were discussed (except for profilometry measurements). In the present section, control over polymer templated Ge-based nanostructures is achieved through changing the molar mixing ratio between PS-b-PEO and K_4Ge_9 in the range between 1/10 and 1/80. Characterization of the surface morphology is carried out by scanning electron microscopy (SEM) on Si substrates.

7.4.1 K_4Ge_9-unsaturated regime

SEM images of samples with molar mixing ratio in the range from 1/10 to 1/50, where most prominent changes occur, are depicted in the left column of Figure 7.7. For the lowest ratio of 1/10 (Figure 7.7a) rather thin, wormlike nanostructures with size in the order of 10 nm are present at the sample surface. With increasing molar ratio, additional K_4Ge_9 is introduced into the casting solution. As a result, the size of nanostructures increases while the average distance between structures remains constant (Figure 7.7a – e). This

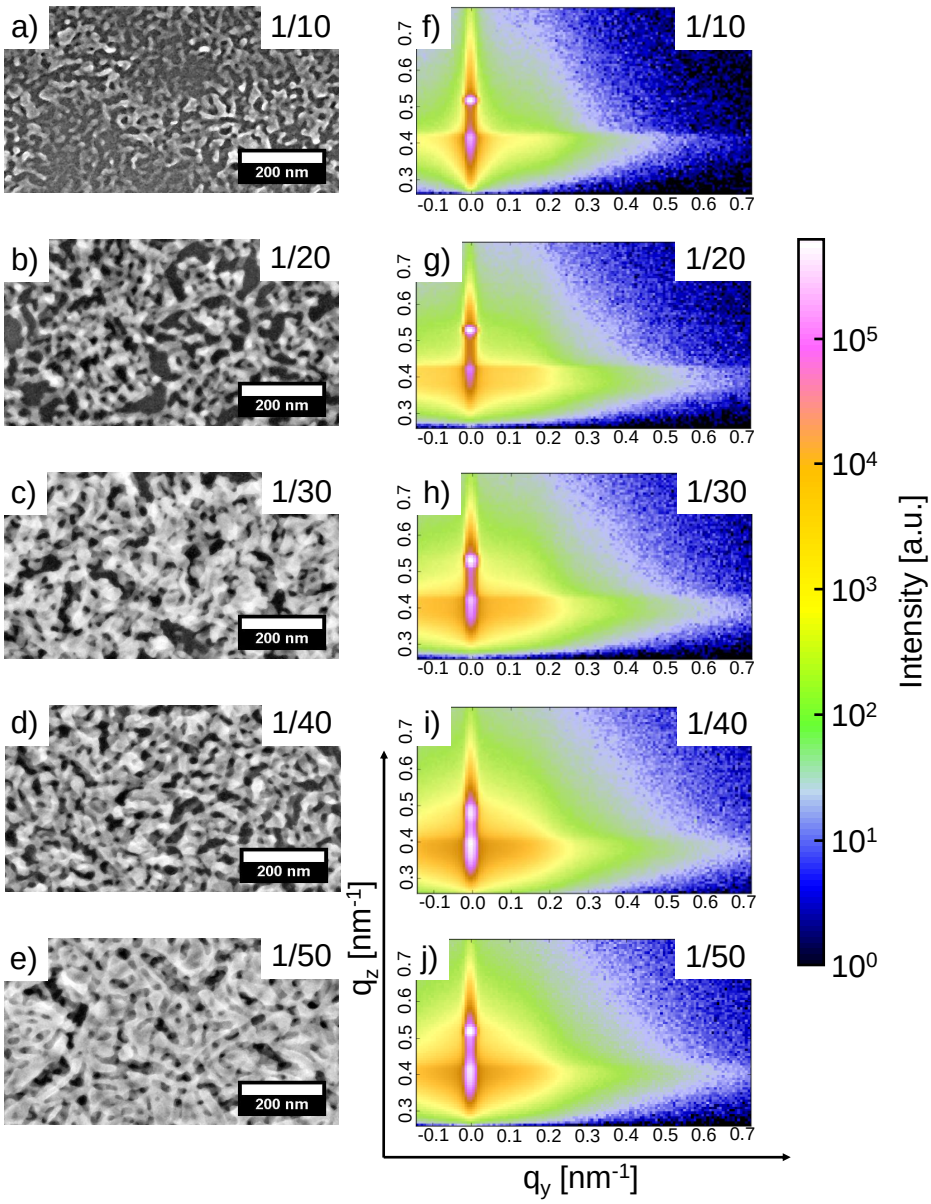

Figure 7.7: *(a)–(e) Scanning electron microscopy images of nanoporous Ge-based thin films with increasing molar mixing ratio (increasing amount of K_4Ge_9) from top to bottom as indicated in the inset. (f)–(j) Respective 2D GISAXS images showing an enhancement of diffuse scattering. The same units in x- and y-direction are used for all GISAXS images. Reproduced/adapted by permission of The Royal Society of Chemistry [37].*

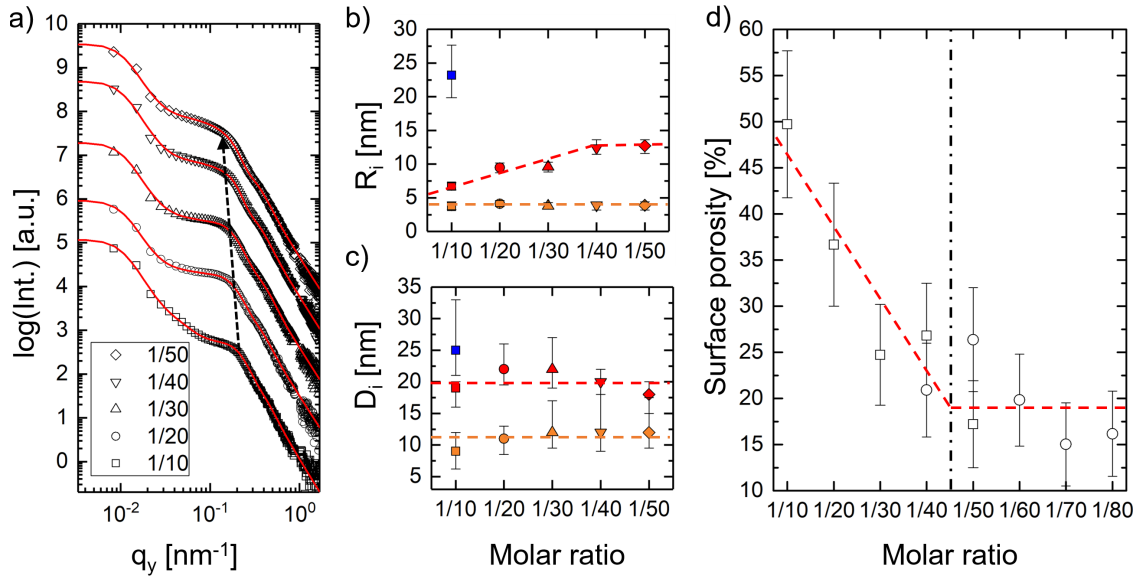

Figure 7.8: *(a) Horizontal line cuts of 2D GISAXS data at the materials specific Yoneda peak position of Ge. The dotted arrow indicates the shift towards smaller q_y values of the intensity shoulder with increasing molar ratio. (b) Radii and (c) lateral distances as extracted through the applied modeling (orange: R_1/D_1, red: R_2/D_2, blue: R_3/D_3). Guides to the eye are drawn as a dotted line in the respective color. Through SEM image treatment the (d) surface porosity is extracted for molar ratios up to 1/80. Reduction of surface porosity is explained as a result of structural growth of radius R_2 until a saturated regime is reached at a molar ratio of approximately 1/45 as marked by the vertical, black dash-dotted line in (d). Reproduced/adapted by permission of The Royal Society of Chemistry [37].*

behavior can be summarized in general as densification with increasing precursor content. Profilometry measurements confirm that the film thickness is increasing with molar ratio (Figure 7.2a) until saturation is reached for ratios of approximately 1/45. Combining the knowledge obtained from profilometry and SEM images, we conclude that nanostructures grow vertically into a densified 3D nanostructure with increasing K_4Ge_9 content.

Inner film morphology characterization is carried out by grazing incidence small angle X-ray scattering (GISAXS) measurements [63, 110]. Corresponding 2D GISAXS data within a range of molar ratios from 1/10 to 1/50 are presented in the right column of Figure 7.7. The most prominent difference between the 2D GISAXS images is the higher amount of diffuse scattering intensity with increasing molar ratio due to the formation of a 3D porous network of higher thickness as proven by profilometry. As a result, more scattering centers contribute to the final observed diffuse scattering intensity.

For a quantitative analysis of the 2D GISAXS data, horizontal line cuts are performed

at the material specific Yoneda peak position of Ge [54]. The cuts are modeled based on the Distorted Wave Born Approximation (DWBA) using the Effective Interface Approximation (EIA) [55]. Accordingly, cylindrical and spherical form factors distributed over 1D-paracrystal lattices are employed for data modeling [111]. Within this frame, the form factors R_i relate to the Fourier transform of the electron density of Ge scattering centers. Center-to-center inter-domain distances D_i (structure factors) of neighboring Ge domains are mapped through the 1D-paracrystal lattices. In Figure 7.8a, the best obtained modeling to the horizontal line cuts is shown as a red solid line for molar ratios up to 1/50. As labeled by the black dashed line, the position of the first shoulder (in between 0.08 nm^{-1} and 0.2 nm^{-1}) shifts towards smaller q_y values for increasing molar ratios. Converting this reciprocal space behavior into a real space interpretation, a first indication is found that lateral structures within the buried bulk of the thin films are growing in size with increasing molar ratio [54]. Thus, structural changes of surface and bulk appear to follow the same trend. At closer look, an additional shoulder appears for all molar ratios for the higher q_y region in between 0.2 nm^{-1} and 0.4 nm^{-1}. This shoulder is modeled through the smallest size R_1 and distance D_1 (orange data points in Figure 7.8b and c). Within that frame, no significant structural change as function of molar ratio is visible. The size R_1 and distance D_1 stay constant at approx. 3.7 nm and 11.9 nm, respectively. However, referring to the larger size R_2 and distance D_2 (red data points in Figure 7.8b and c), which are related to the shoulder in the lower q_y region (dashed line in Figure 7.8a), an increase in the size of scattering centers is quantified through the applied model. For the smallest molar ratio of 1/10, a size R_2 of (6.7 ± 0.2) nm is found. Up to a molar ratio of 1/40, the size R_2 further increases and finally stays constant at an almost doubled size of (12.7 ± 0.5) nm for a molar ratio of 1/50. Again, the corresponding distance D_2 is found unaltered (approx. 20 nm) within the accuracy of the applied model. Note that an additional feature for the lowest molar ratio can be found in a smaller q_y region between 0.05 nm^{-1} and 0.07 nm^{-1}, which is identified through the less steep decay of scattering intensity right after the resolution area (Figure 7.8a). This feature originates from an additional larger structure (blue data points in Figure 7.8b and c), which could not be observed with SEM.

Through binarization of SEM images and application of an Otsu algorithm [60], an estimation for the local surface porosity is extracted (Figure 7.8d). For a molar ratio of 1/10, the estimation yields a surface porosity of approximately 50%. Further increase of the molar ratio leads to a reduced surface porosity of approximately 19%, which is first reached in between 1/40 and 1/50. For higher molar ratios no significant change is observed and the polymer template is assumed to be K_4Ge_9-saturated. This observation is in agreement with the behavior of size increase and saturation as extracted from GISAXS

modeling as well as with the stagnation of thickness increase via profilometry for molar ratios exceeding 1/40.

7.4.2 K_4Ge_9-saturated regime

For molar ratios higher than 1/50, the basic worm-like morphology does not appear to significantly change anymore. Respective surface characterization via SEM for a molar ratio range from 1/40 till 1/80 is depicted in Figure 7.9a - e. The foam-like nanostructure is retained for all molar ratios. However, the formation of sphere-like aggregates can be observed for the highest molar ratio of 1/80. A possible explanation is that the polymer domain is saturated with the precursor K_4Ge_9. Consequently, the polymer has no templating effect on the excess amount of precursor and an aggregate layer is formed on top of the nanostructured bottom layer.

For the same molar ratio range, samples are investigated via GISAXS at the MiNaXS beamline P03 of the PETRA III storage ring at DESY, Hamburg (λ = 0.94 Å, sample-detector distance = 4.377 m, incident angle = 0.35°, vertical beam size 12 μm, horizontal beam size 24 μm). A Pilatus1M by Dectris Ltd. with a total of 981 x 1043 pixels (172 μm x 172 μm) is used for data acquisition. Specular and direct beam are blocked by two beamstops to prevent oversaturation of the detector. Acquired 2D GISAXS images are shown in the right column of Figure 7.9. At first sight, no apparent change in the 2D GISAXS images could be observed for different molar ratios.

For a quantitative analysis, horizontal line cuts are taken at the material specific Yoneda peak position of Ge (Figure 7.10a). As described in section 7.4.1, data modeling is performed and average radii and distances of scattering centers are extracted. In contrast to the low molar ratio regime in between 1/10 – 1/40, no indication for a significant change of radii and distances is found for the molar ratio range between 1/40 – 1/80 (Figure 7.10b – c). Consequently, the polymeric domain is assumed to be saturated with the precursor K_4Ge_9 and additional precursor either leads to the formation of a spherical aggregate layer on top of the nanostructured bottom layer or is simply flung of the substrate during the spin-coating process, since there is no further thickness increase detected. Note that the horizontal line cut for the molar ratio of 1/50 exhibits a slightly more pronounced shoulder-like feature, which might be an indication for an improved periodic structure inside the thin film. Nevertheless, the q_y position is not significantly altered.

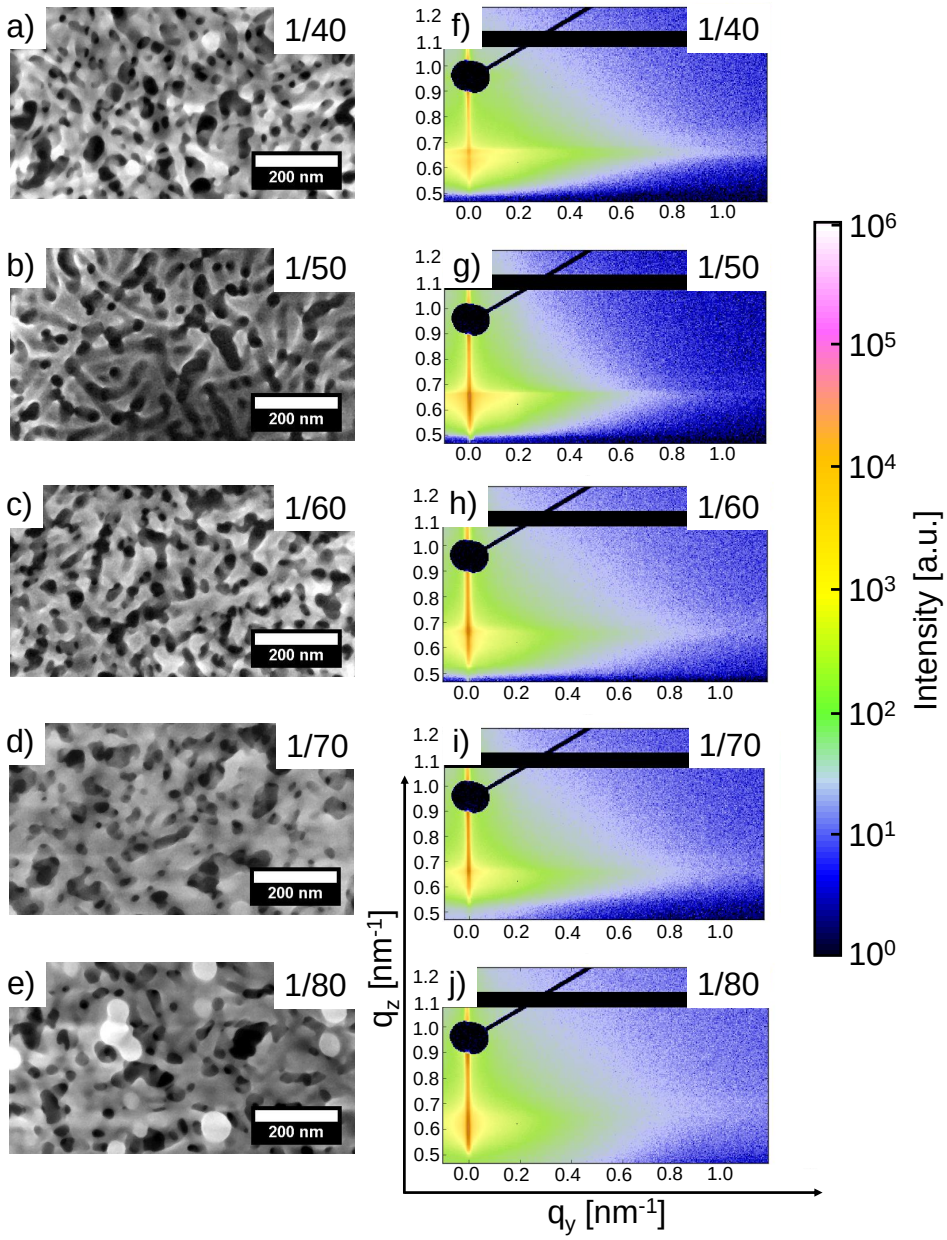

Figure 7.9: *(a)–(e) Scanning electron microscopy images of nanoporous Ge-based thin films with increasing molar mixing ratio from top to bottom as indicated in the inset. (f)–(j) Respective 2D GISAXS data as obtained at the MiNaXS beamline P03 at the PETRA III storage ring at DESY, Hamburg, is depicted on the right side showing no significant change for different molar ratios. The same units in x- and y-direction are used for all GISAXS images. Reproduced/adapted by permission of The Royal Society of Chemistry [37].*

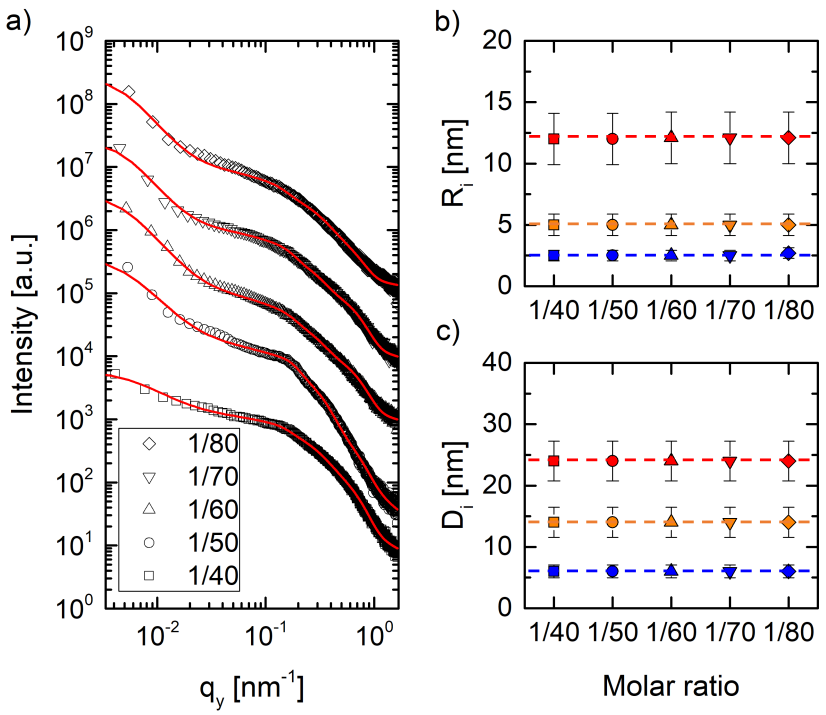

Figure 7.10: *(a) Horizontal line cuts obtained from 2D GISAXS images of nanoporous Ge-based thin films at the material specific Yoneda peak position for different molar ratios as indicated in the axis label. Through data modeling average predominant (b) radii and (c) distances of scattering centers are derived. The system appears precursor-saturated and no further indication for structural change is found. Reproduced/adapted by permission of The Royal Society of Chemistry [37].*

7.4.3 Summary

Based on the above described observations, Ge-based structure formation is expected to follow a decoupled interplay of PS-b-PEO microphase separation and PEO block infiltration with the precursor K_4Ge_9. Due to the exposure to the azeotrope solvent post-treatment with toluene and 1-butanol, the diblock copolymer phase-separates and micelles are formed [42]. Since the extracted inter-domain distances are constant for all prepared samples regardless of the molar ratio, this phase separation is probably only weakly influenced by the amount of K_4Ge_9 inside the casting solution. As the PEO block typically forms the shell of micelles for the used material system of PS-b-PEO, toluene and 1-butanol and as a nanoporous Ge-based network is obtained, the strongly polar precursor K_4Ge_9 is assumed to be preferentially incorporated into the more polar PEO block of the polymer template. Depending on the amount of K_4Ge_9 precursor, the mixing ratio of Ge and PEO increases up to a saturation at a molar ratio of approximately 1/40 (or

over-saturation for molar ratios larger than 1/40) without changing the distance between neighboring PS cores. As a result, different structure sizes and porosities of Ge-based thin films can be achieved through changing the precursor to polymer ratio in the reported novel block copolymer assisted sol-gel synthesis route.

7.5 Conclusion

For the first time, wet-chemical synthesis of high surface-to-volume ratio, nanostructured Ge-based thin films is achieved via exploitation of the Zintl precursor K_4Ge_9 and the diblock copolymer template PS-b-PEO. Through sol-gel synthesis, structural control is realized with respect to both surface and bulk morphology. Increasing the precursor-to-polymer molar ratio allows to approximately double the size of predominant, foam-like structure sizes inside the Ge-based thin film from an average radius of 6.7 nm up to 12.7 nm as proven by GISAXS measurements. Additionally, the inter-domain distance of neighboring structures is kept constant, resulting in the respective reduction of the surface porosity from up to 50% down to 19% with typical pore sizes smaller than 40 nm. Combined with the insights from XRD measurements that crystalline α-Ge phases are as well accessible, the presented preparation routine introduces novel pathways for nanoporous Ge-based thin film fabrication. Future-oriented applications like hybrid photovoltaics or batteries could tremendously profit from the outstanding properties of nanostructured Ge.

8 Mesoporous Ge-based films as anode material in Li ion batteries

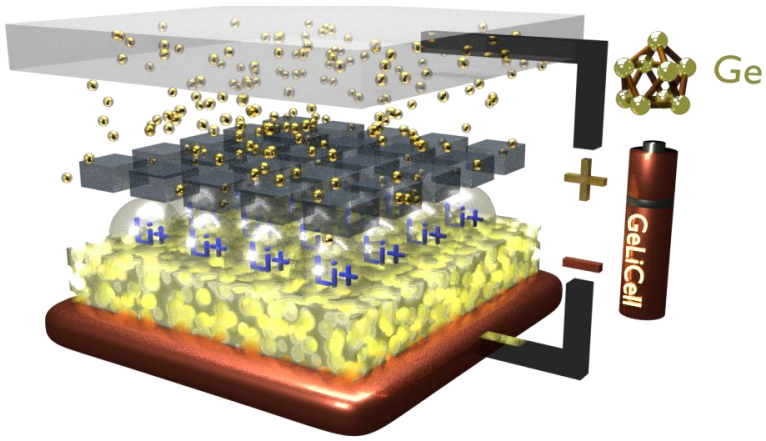

The following chapter is based on the manuscript[1]: Mesoporous GeO_2/Ge/C as Highly Reversible Anode Material with High Specific Capacity for Lithium Ion Batteries. Submission to the journal "Nature Materials" is in preparation [162].

In chapter 7 the morphological tunability of spin-coated, mesoporous Ge-based thin films was discussed. Within the present chapter mesoporous Ge-containing film synthesis based on drop-casting as a deposition technique is presented. The change of the applied deposition technique results in significantly thicker films which can be directly applied as anode material in Li ion batteries. Morphological and compositional analysis of drop-casted, mesoporous Ge-based films is carried out and the performance as anode material is tested in half-cells. Furthermore, the impact of an azeotrope solvent post-treatment

[1]Parts of the results of the present chapter were obtained within the frame of a Bachelor's and Master's thesis of David Müller and Andreas Hetzenecker [119, 161].

on film morphology and composition is investigated. A correlation to the performance of respective mesoporous Ge-based anodes in Li ion batteries is found. Through alteration of the polymer template removal conditions from Ar atmosphere to ambient atmosphere it was additionally found that C residues in the case of Ar tempering are still present in the mesoporous structure. Those C residues are assumed to have a beneficial impact on the performance of Li ion batteries due to improved conductivity.

The present chapter starts with a summary of major scientific contributions in the field of Li ion batteries and the respective employment of Ge-based nanostructures (section 8.1). In the following, a short description of mesoporous Ge-based film synthesis via drop-casting is given (section 8.2). In the first main section 8.3, the impact of an azeotrope solvent post-treatment is investigated morphologically via SEM and GISAXS and compositionally via EDX, XPS, XRD and FTIR. Respective correlation to the performance of Li ion batteries is tested in half-cells. In the second main section 8.4, different template removal atmospheres are investigated and consequential changes of morphology and composition are analyzed via similar techniques as introduced for section 8.3.

8.1 Preface

Nowadays, the development of efficient energy storage devices is one of the key challenges in modern power generation, automotive industry and mobile phone technology. Group IV semiconductors such as Si and Ge are promising anode materials for efficient energy storage in Li ion batteries [15, 163–167]. Main advantages of Ge anodes are a high specific capacity of 1385 $mAhg^{-1}$ for $Li_{15}Ge_4$ and 1564 $mAhg^{-1}$ for $Li_{17}Ge_4$, 400 times higher Li ion diffusivity than Si at room temperature and the highest known electron mobility [16, 17]. However, devices typically suffer from capacity fading caused by high volume expansion during lithiation and delithiation [168–170]. Tailoring of mechanically flexible and structurally stable nanostructures is found to efficiently counteract negative impacts of volume expansion [14, 171–173]. Additionally, nanostructured materials typically result in high surface-to-volume ratios with the advantage of an enhanced surface capacity [174–178].

Pioneering work in the field of nanostructured group IV anode semiconductors for Li ion batteries was primarily achieved on the basis of Si. Porous and nanostructured morphologies of Si thin films have proven to significantly reduce capacity fading as induced by the large volume expansion upon lithiation [179]. Most prominent morphologies are nanoparticles, nanowires or porous thin films with pore sizes in the range from nano to micrometers [180–183]. However, the above-mentioned advantages of Ge have led to

an increased interest in similar Ge-based nanostructures. Within this frame, successful fabrication of Ge-nanosheets, wires and particles has been reported [135, 137, 184]. While methods based on chemical and electrochemical etching to obtain porous Ge thin films are well-established, reports on synthesis of high surface-to-volume ratio, porous Ge thin films through bottom-up approaches are rather scarce [138, 139]. For example, Armatas and coworkers successfully investigated the formation of mesoporous Ge through self-polymerization of Ge clusters [46]. Bentlohner et al. demonstrated the usage of PMMA spheres and K_4Ge_9 Zintl clusters to manufacture inverse-opal structured, microporous Ge thin films [41]. Also based on Zintl clusters, the macromolecular assisted self-assembly of these precursors to fabricate mesoporous, size-tunable and oxidized Ge thin films was recently demonstrated [37].

Due to the advantages of high surface-to-volume ratio thin films, various types of nanostructured Ge were investigated with respect to their application as anode material in Li ion batteries. For example, Cui et al. reported Ge nanospheres encapsulated in a C matrix with a reversible specific capacity of 900 $mAhg^{-1}$ after 50 cycles [185]. Good performance was mainly ascribed to an improved Li intercalation due to the unique nanostructure in conjunction with an improved electrical contact trough the C matrix. Similarly, solution-grown Ge nanowires have proven to yield excellent reversible capacities of up to 1248 $mAhg^{-1}$ after 100 cycles [186]. Highly porous, inverse-opal structured Ge thin films as fabricated by Fässler and coworkers exhibited capacities larger than 1300 $mAhg^{-1}$ after 100 cycles. Good cycle stability and capacity are likely to be caused by the porous and nanostructured nature of the exploited materials [16]. Apart from elemental Ge, employment of GeO_2/Ge/C composite structures has recently demonstrated capacities larger than 1800 $mAhg^{-1}$ after 50 cycles [52]. Again, good performance was explained through an increased surface-to-volume ratio resulting in shorter Li reaction pathways and enhanced reversibility of the conversion reaction of GeO_2 in the presence of elemental Ge nanostructures. The latter is assumed to lead to an increase of theoretically available Li ions from 4.4 to 8.4 per GeO_2. Thereby, an increased theoretical capacity limit for Li storage of 2152 $mAhg^{-1}$ is deduced [52, 187].

In the present chapter the fabrication of mesoporous GeO_2/Ge/O films via drop casting on the basis of polystyrene-block-polyethylene oxide (PS-b-PEO) templating of K_4Ge_9 Zintl clusters used as Ge precursor is reported. The employment of K_4Ge_9 enables the wet-chemical processing routine for the synthesis of mesoporous Ge thin films, which appears especially interesting for potential large scale deposition techniques commonly used in industry (e.g. spray coating or printing) [40, 188]. Application of an azeotrope solvent mixture based on 1-butanol and toluene leads to an enhanced control over predominant structures and overall smaller pores with higher number area density. A morphological

and compositional comparison between samples with and without the above-mentioned post-treatment is presented. As compared to the work presented in chapter 7, material purity and crystallinity are improved through the novel fabrication routine used in the present chapter. Excellent specific capacities of larger than 2000 $mAhg^{-1}$ are observed for post-treated, mesoporous Ge-based samples after 300 cycles. The high cycle stability in conjunction with the outstanding specific capacity of larger than 2000 $mAhg^{-1}$ is found to be a new record in the field of Ge-based anode employment for Li ion batteries.

8.2 Experimental: Synthesis of mesoporous Ge thin films via drop casting

A schematic representation of the fabrication process of mesoporous Ge-based films is depicted in Figure 8.1. Initially, the polymer template (PS-b-PEO) and the Ge precursor (K_4Ge_9) are separately dissolved in ethylenediamine (en). After stirring, a homogeneous mixed solution with a molar mixing ratio of 50 (K_4Ge_9) : 1 (PS-b-PEO) is used for solution casting. A post-treatment (PT) with an azeotrope solvent mixture of 1-butanol and toluene is applied for samples referred to as "Ar; with PT" (right branch of Figure 8.1). No such PT was applied for samples referred to as "Ar; no PT" (left branch of Figure 8.1). Subsequently, both types of samples are annealed, and high-temperature template removal is performed under Ar atmosphere. Note that all steps prior to template removal are performed under N_2 atmosphere. Additional information can be found in section 4.3.4.

8.3 Influence of azeotrope solvent treatment

Proof of a successful fabrication of foam-like Ge-based nanostructures is provided through surface characterization via scanning electron microscopy (SEM) for samples with PT (Figure 8.2a) and without PT (Figure 8.2b). Average pore sizes are found to significantly shrink from ∼200 nm to ∼40 nm through application of the PT. Additionally, the number area density of pores and homogeneity increase. This observation is ascribed to improved phase separation of the diblock copolymer as induced by treatment with the poor-good solvent pair.

With grazing incidence small angle X-ray scattering (GISAXS) measurements the inner morphology of respective samples can be accessed [189, 190]. In Figure 8.3a and Figure 8.3b 2D GISAXS data are shown for mesoporous Ge-based samples with and without application of post-treatment and tempered under Ar atmosphere. Most significantly the

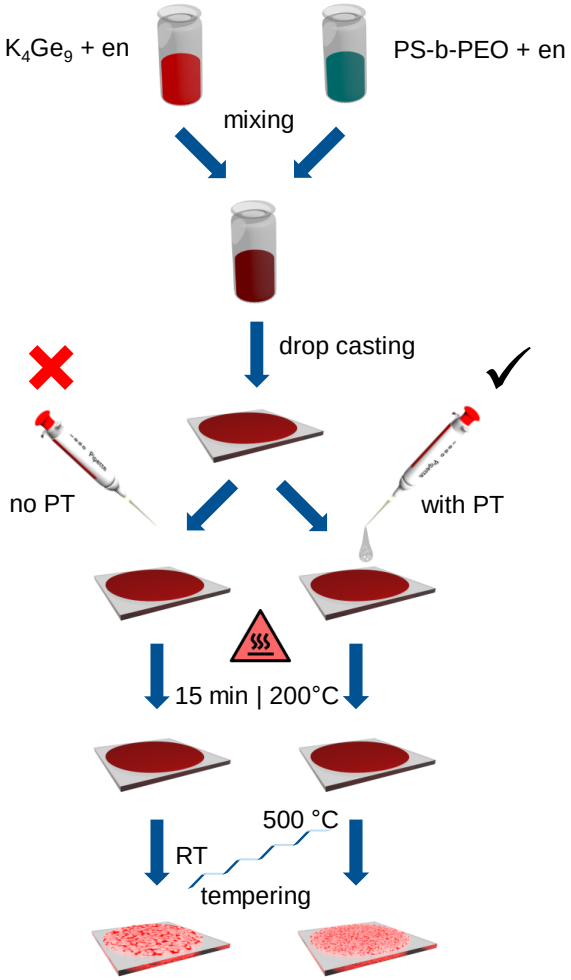

Figure 8.1: *Schematic representation of the synthesis process of mesoporous Ge-based films using PS-b-PEO templating in combination with K_4Ge_9 as a precursor. The left branch is referred to as "Ar; no PT", while the right branch is referred to as "Ar; with PT". The only difference is the additionally applied post-treatment with 1-butanol/toluene for samples denoted "Ar; with PT".*

overall scattering intensity is increased for post-treated samples, which is likely to be the result of increased porosity as induced by the post-treatment. Vertical line cuts from 2D GISAXS data as reported in Figure 8.3c indicate a single Yoneda peak at an angle of 0.19° [54]. However, for post-treated samples two different Yoneda peaks are identified at 0.1° and 0.27°. The appearance of two different Yoneda peaks is caused by two layers with different density. It is assumed that the post-treatment mainly affects the surface-near layer, which leads to an increased porosity (lower density) with a Yoneda peak at lower angles. However, a layer closer to the substrate appears not to be affected by the

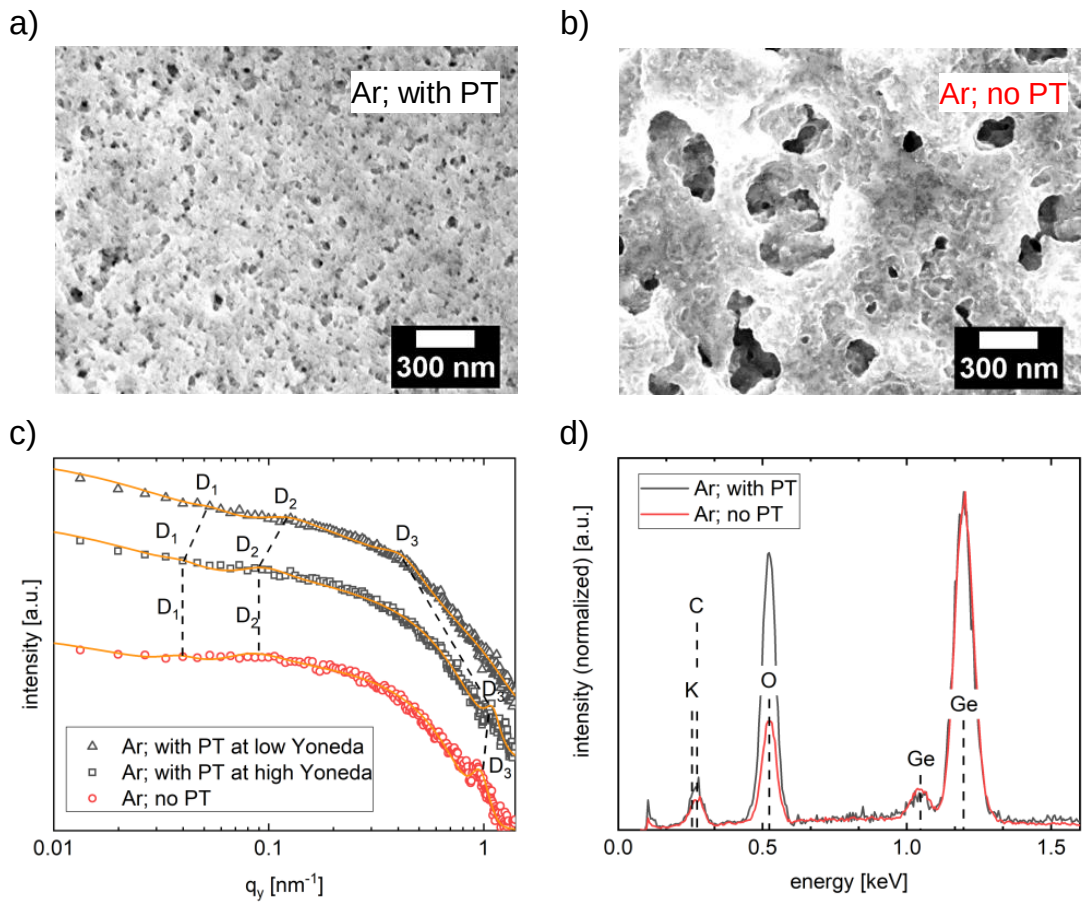

Figure 8.2: *Morphological and compositional analysis of mesoporous Ge-based films. Scanning electron microscopy images of (a) "Ar; with PT" (black) and (b) "Ar; no PT" (red) samples. (c) Respective horizontal line cuts of 2D GISAXS data with data modeling (orange line) and respective distances D_1-D_3 (dashed, black lines). (d) Energy-dispersive X-ray spectroscopy confirms the presence of germanium.*

post-treatment, which is why a second Yoneda peak appears at higher angles (higher density).

Figure 8.2c shows horizontal line cuts as extracted from 2D GISAXS data at the material specific Yoneda peak position. Data modeling is performed based on the Distorted Wave Born Approximation (DWBA) using the Effective Interface Approximation (EIA) [55, 58]. Thereby, average center-to-center distances and cylindrical structure sizes of scattering centers are determined [111]. Note that for the PT sample two specific Yoneda peaks are identified, which is why in total three horizontal line cuts are depicted in Figure 8.2c. Qualitatively it can be seen that the peak labeled with D_1 is shifting towards larger q_y values for "Ar, with PT" samples, which is an indication for smaller

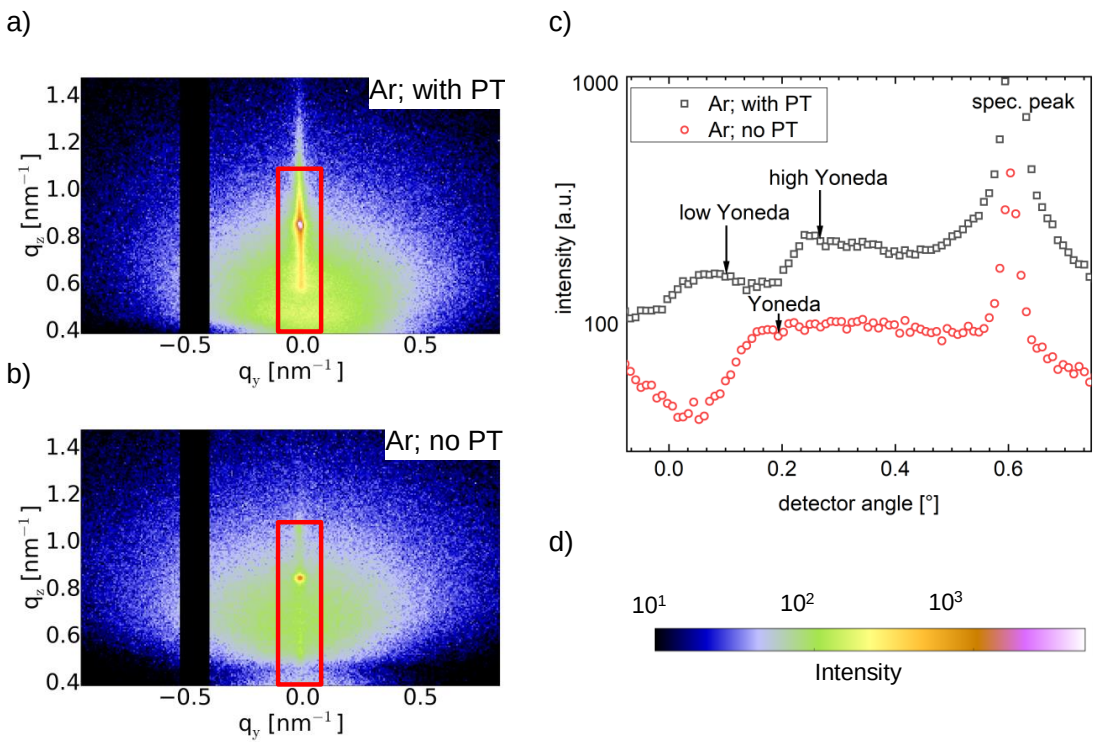

Figure 8.3: *2D GISAXS data of mesoporous Ge-based films tempered under Ar atmosphere with (a) post-treatment and (b) without post-treatment. The range used for vertical line cuts is indicated as red squares. (c) Extracted vertical line cuts for post-treated samples (black squares) and not post-treated samples (red spheres). Yoneda peak positions are marked by respective black arrows. (d) Intensity scale bar for (a) and (b).*

sizes/distances in the low Yoneda region as compared to the high Yoneda region. Similarly, the peak labeled D_3 is found at smaller q_y. Quantification is obtained in the following section through data modeling.

Data modeling gives proof that large (D_1) and medium (D_2) extracted distances are shrinking from (145 ± 5) nm and (50 ± 2) nm to (105 ± 5) nm and (35 ± 2) nm in the low-density (highly porous) domains, respectively. This shrinkage is found in good agreement with observations made via SEM. The smallest (D_3) distance is found to slightly increase from (6 ± 1) nm to (14 ± 1) nm. Thereby, the total spread of the smallest distance D_3 compared to the large distance D_1 and medium distance D_2 is reduced upon PT. Thus, the distribution of distances is narrower for PT samples at lower density surface-near regions of the sample confirming the effect of improved control over predominant nanostructures in PT samples. An overview of all extracted sizes/distances can be found in Table 8.1

The following scenario is concluded: Through application of the PT the phase separation of near-surface areas is improved. As a result, the overall porosity is enhanced

	S_1	S_2	S_3	D_1	D_2	D_3
no PT	13.5 ± 2.1	3.5 ± 1.1	1.7 ± 0.3	145 ± 5	50 ± 2	6.4 ± 0.3
with PT; high Yoneda	13.5 ± 2.1	2.9 ± 0.9	2.0 ± 0.2	145 ± 5	50 ± 2	5.6 ± 0.2
with PT; low Yoneda	13.5 ± 1.2	4.1 ± 0.9	2.0 ± 0.3	105 ± 5	35 ± 2	13.5 ± 0.6

Table 8.1: *Extracted sizes S_x [nm] and distances D_x [nm] as obtained from 2D GISAXS modeling of drop-casted, mesoporous Ge-based films with and without the application of an azeotrope solvent post-treatment.*

through the PT, while the distribution of pores sizes is better controlled as proven by GISAXS and SEM. The following section gives attention to the chemical composition of the observed nanostructures.

Figure 8.2d reports the results of EDX measurements on foam-like nanostructures. For samples without PT clear evidence for the presence of Ge and O is given (red line). Additionally, traces of K from the precursor and C from the polymer template are found. The most significant difference for the PT samples (black line) is seen in the increased ratio O : Ge.

Through XRD measurements the presence of crystalline α-Ge (black vertical lines) is furthermore confirmed for both types of samples (Figure 8.4a, PT samples: black line, no PT samples: red line). Notably, for PT samples additional peaks are found as marked by the vertical orange lines at the bottom of Figure 8.4a, which are ascribed to the formation of $C_xH_yK_{z1}O_{z2}$ compounds [191]. Additionally, a survey scan and the Ge 3p core level region as obtained from XPS measurements for both types of samples on FTO substrates are depicted in Figure 8.4b and c. Regardless of the applied PT, measurements are in good agreement with EDX measurements and confirm the presence of Ge, O, C and K. Note that traces of Sn and Si are as well detected, which are likely to originate from the used FTO substrate. In the zoom-in spectrum shown in Figure 8.4c, four Gaussians curves superimposed on a Shirley background are used to fit Ge 3p core level emission. According to literature, Ge 3p core level emission is expected around 124.9 eV ($3p_{1/2}$) and 120.9 eV ($3p_{3/2}$) [147]. Best fits to the data yield 125.6 eV and 121.2 eV as Gaussian centroid position and are determined independent of the applied PT. Likewise, peaks ascribed to GeO_x are found at 127.8 eV and 123.6 eV [151]. Note that the ratio GeO_x : Ge is significantly increased under the influence of PT. This observation is in accordance with observations made via EDX and leads to the conclusion that the PT is promoting the Ge oxidation. Further evidence for C residues as well as for a promoted oxidation through the PT can been seen in FTIR data (Figure 8.4d), as the doublet ascribed to GeO_x at 765 cm^{-1} and 825 cm^{-1} is found to be more pronounced for PT samples [192].

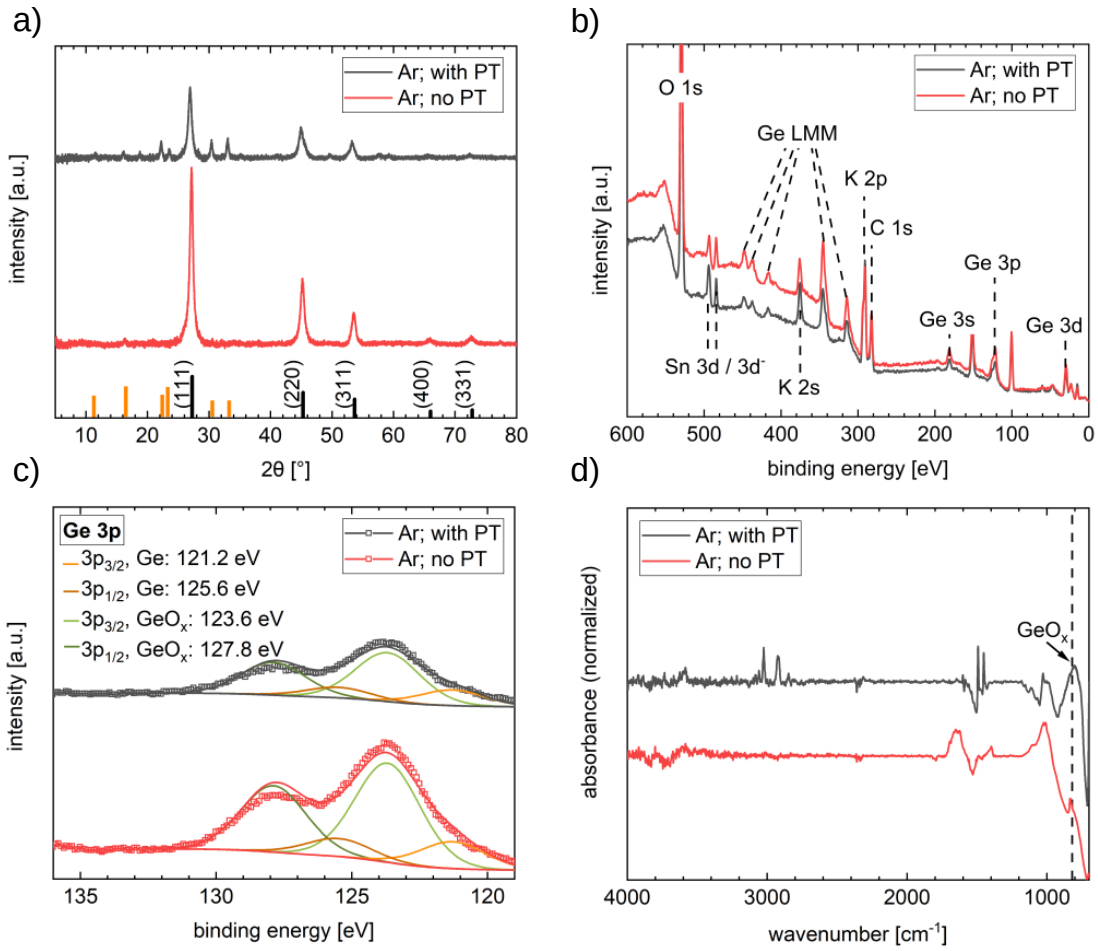

Figure 8.4: *Morphological and compositional analysis of mesoporous Ge-based films. (a) X-ray diffraction measurements confirm the presence of crystalline α-Ge for both "Ar; with PT" (black line) and "Ar; no PT" (red line) samples. Theoretical peak positions of α-Ge [31] and $C_xH_yK_{z1}O_{z2}$ compounds [191] are indicated by black and orange vertical lines, respectively. Partial oxidation of germanium is confirmed through (b)-(c) X-ray photoelectron spectroscopy with respective fits (black and red line) and (d) Fourier transform infrared spectroscopy data of "Ar; with PT" (black) and "Ar; no PT" (red) samples.*

Thus, we find foam-like Ge-based nanostructures with enhanced porosity and higher surface-to-volume ratio through the applied PT. Additionally, the applied PT promotes Ge oxidation. High temperature treatment under Ar atmosphere cannot completely remove the polymer template as C residues are detected in EDX, FTIR and XPS.

The above characterized mesoporous Ge-based films can be directly applied as anode material for Li ion batteries through deposition on copper substrates without any further need for binder materials or carbon black. Figure 8.5 reports the cycle stability of PT (black circles) and no PT (red squares) based Ge anodes at a rate of 0.2 C. Comparison of

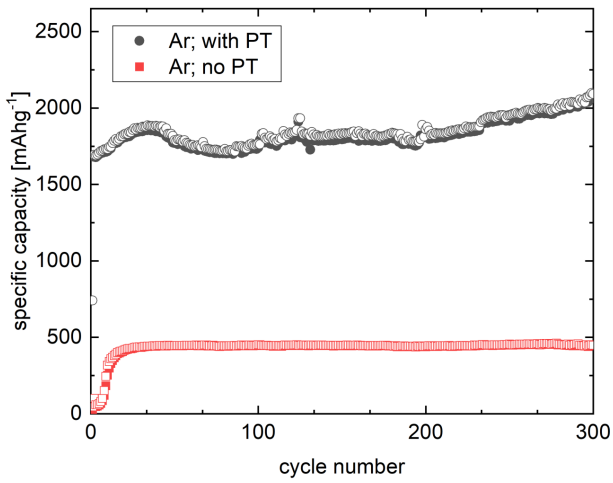

Figure 8.5: *Performance of Li ion half-cells with mesoporous Ge-based anode material. The specific capacity is plotted against the cycle number for "Ar; no PT" (red spheres) and for "Ar; with PT" (black spheres) anodes during discharge (hollow symbols) and charge (solid symbols).*

the delithiation capacity of 447.5 mAhg^{-1} in the 100th cycle to the 300th cycle yields an excellent capacity retention as high as 99.5% for no PT samples. Unlike for bulk material, high volume expansion of Ge upon lithiation is not found to significantly decrease the performance of the anode material, which is reasonably considered to be the result of an increased mechanical flexibility in mesoporous Ge-based structures. For PT samples the delithiation capacity in the 100th cycle of 1766.6 mAhg^{-1} is even further increased up to 2091.9 mAhg^{-1} in the 300th cycle. This gradual capacity increase is ascribed to surface adsorption type lithiation processes in conjunction with a gradual collapse of the nanostructure upon lithiation. Notably, the measured specific capacity outperforms reported literature champion values of 1564 mAhg^{-1} for the Li-richest phase $Li_{17}Ge_4$ in bulk Ge anodes, which proofs the advantage of nanostructuring.

Findings from the morphological and compositional characterization give strong indication that the excellent specific capacity of over 2000 mAhg^{-1} is primarily cause by two different influences: the enhanced mesoporous structure of Ge-based samples and the increased oxidation induced through the applied PT. The mesoporous nature of the samples immensely boosts the surface-to-volume ratio as compared to bulk materials. Beside the typical lithiation through alloy reactions of Ge and Li, so called pseudocapacitive processes at the surface have a significantly increased influence on the amount of stored lithium for mesoporous samples as compared to low surface-to-volume, bulk samples. From this point of view, it appears reasonable that the PT samples with enhanced porosity and smaller pore size (increased surface-to-volume ratio) significantly outperform the samples without PT. Additionally, Seng et al. recently reported that the presence of elemental Ge nanoparticles in GeO_2/Ge/C based anodes allows to overcome the typically irreversible formation of LiO_2 in the conversion reaction of GeO_2 through catalytic activity of nanostructured Ge [52]. Rendering the formation of LiO_2 reversible would allow for

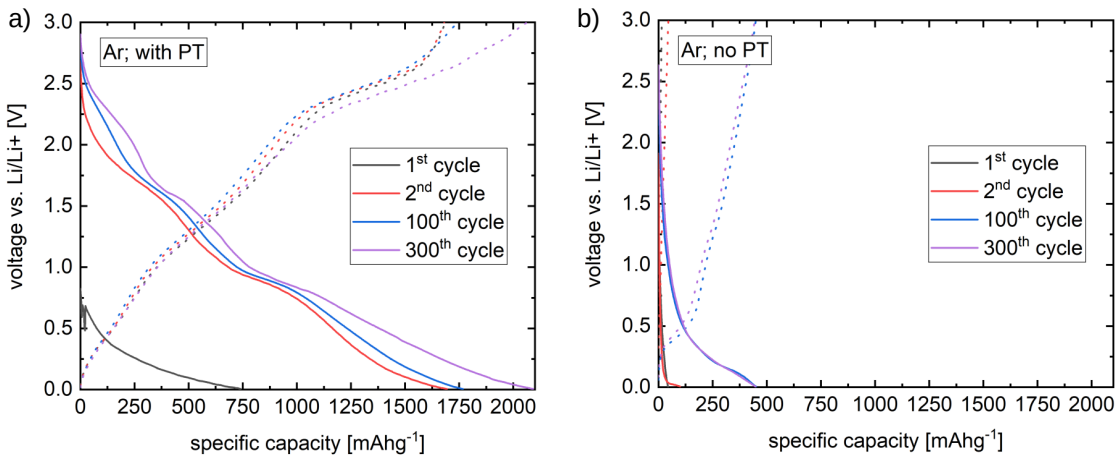

Figure 8.6: *Performance of Li ion half-cells with mesoporous Ge-based anode material. Charge (dashed lines) and discharge (solid lines) characteristics are plotted for the 1st, 2nd 100th and 300th cycle of (a) "Ar; with PT" and (b) "Ar; no PT" anodes.*

increasing the number of storable Li^+ ions from 4.4 to 8.8 and thus boosting the capacity limit up to 2152 $mAhg^{-1}$. For both PT and no PT samples, strong indications from the morphological and compositional characterization suggest that similar processes take place in the here presented anodes. For all samples Ge, GeO_x/GeO_2 and C are found as well as the formation of a mesoporous foam-like nanostructure. One major compositional difference between PT samples with high specific capacity and no PT samples with lower specific capacity is the decreased ratio of GeO_2/GeO_x to Ge. Thus, the explanation appears likely that the increased relative amount of GeO_2/GeO_x as compared to Ge is beneficial for the reversible conversion reaction of GeO_2 as reported by Seng et al. Note that the residual C found after template removal has a beneficial impact on the cycle stability, specific capacity, and accelerated electrochemical kinetics due to its good electron conductivity [15].

Figure 8.6a and 8.6b show the voltage profiles for discharge (solid lines) and charge (dashed lines) of the 1st, 2nd, 100th and 300th cycle as obtained from galvanostatic testing at room temperature and between 0 V and 3 V versus Li/Li+ for PT samples and no PT samples, respectively. For PT samples two small plateaus are most clearly identified in the discharge curve of the 100th cycle occurring at a voltage of 0.9 V and 1.6 V, respectively. These plateaus are ascribed to delithiation reactions. However, for no PT samples only one small plateau at 0.2 V can be clearly identified in the 100th cycle. The reduced number of pronounced plateaus is considered as additional indication for altered delithiation reactions of no PT samples in comparison to PT samples and reversible LiO_2 reaction behavior.

Ar; with PT	Ar; no PT	air; with PT	air; no PT	none; with PT	none; no PT
7.0 ± 0.3	2.2 ± 0.1	4.3 ± 1.0	6.9 ± 1.6	4.4 ± 0.4	9.7 ± 0.2

Table 8.2: *Thickness [μm] as determined through profilometry measurements of PS-b-PEO/K_4Ge_9 composite ("none") and mesoporous Ge-based films tempered under Ar atmosphere ("Ar") and in air ("air"). Samples treated with a post-treatment are labeled "with PT", while "no PT" indicates samples not treated with a post-treatment.*

8.4 Influence of tempering atmosphere

In addition to samples described in section 8.3, which have exclusively been tempered under Ar atmosphere (labeled as "Ar"), the present section covers samples, which have been tempered in air (labeled as "air") with an identical tempering protocol. Furthermore, composite PS-b-PEO/K_4Ge_9 samples at a state prior to the high temperature template removal are investigated (labeled as "none"). Determined thicknesses as extracted via profilometry are summarized in Table 8.2 for all investigated samples.

Optical microscopy images for Ar-tempered Ge-based films (Ar), air-tempered Ge-based films (air) and not-tempered films (none) are depicted in Figure 8.7. Optical microscopy images of samples with post-treatment (second column, with PT) appear more homoge-

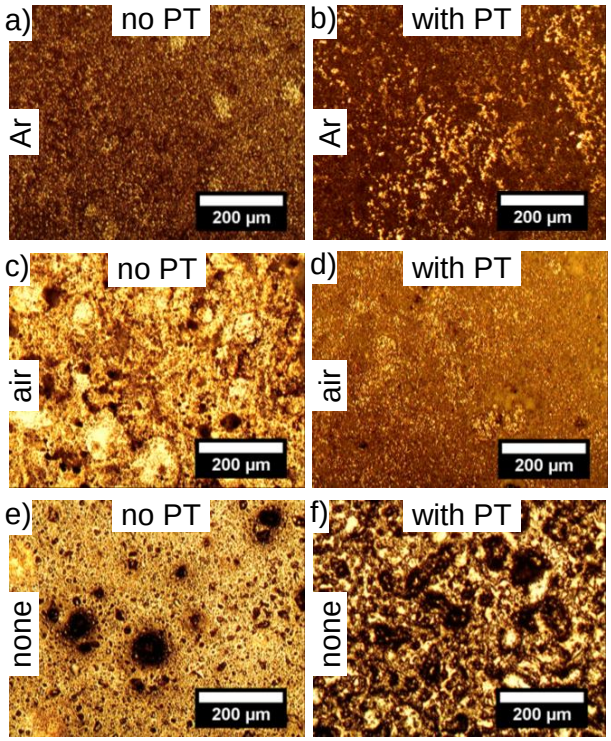

Figure 8.7: *Optical microscopy images of Ar-tempered Ge-based films (a,b), air-tempered Ge-based films (c,d) and not-tempered composite films (e,f). The first column (a,c,e) refers to samples not treated with any post-treatment (no PT), while the second column (b,d,f) refers to samples, which have been post-treated (with PT). Within this scope, post-treated films appear more homogeneous.*

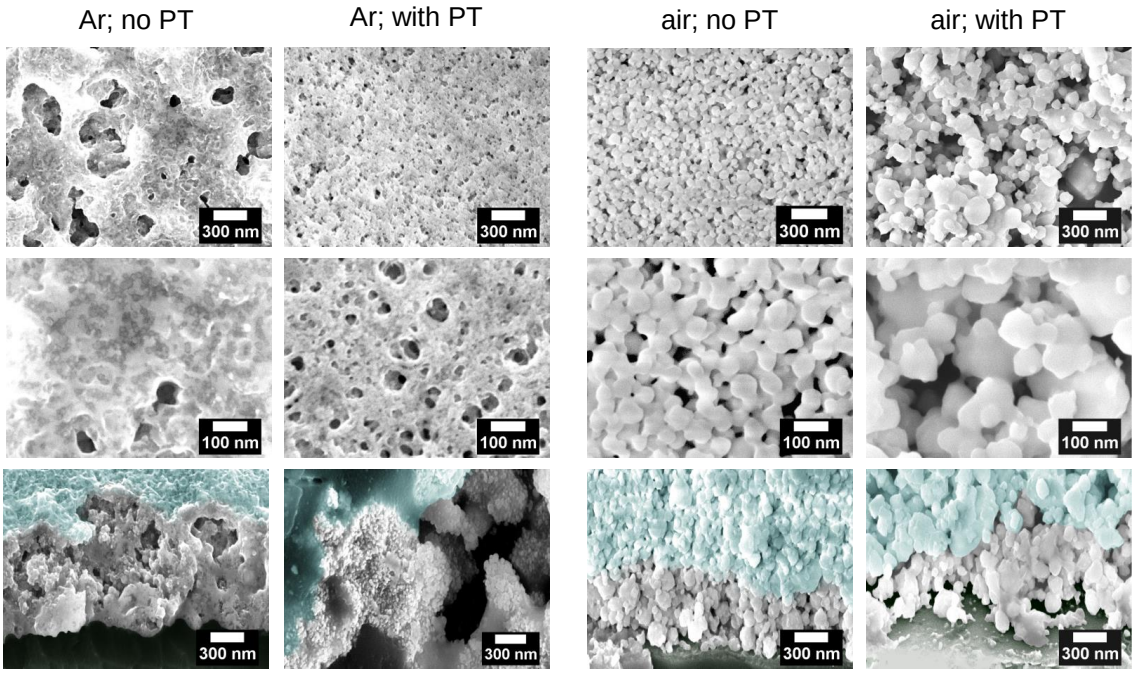

Figure 8.8: *Surface and cross-section scanning electron microscopy images of mesoporous Ge-based samples tempered in Ar atmosphere or air as indicated in the respective insets. Comparison between the column labeled "Ar; no PT" and "Ar; with PT" yields that the PT enhances porosity. Overall, the porosity appears increased for tempering in air (columns labeled "air; no PT" and "air; with PT"). Cross-section images confirm bulk porosity of all samples. The surface in cross-section images is marked in light blue.*

neous as compared to images of samples without post-treatment (first column, no PT). This finding is interesting because the applied post-treatment not only appears to enhance mesoscopic phase-separation as discussed in section 8.3, but also improves the homogeneity on a more macroscopic scale.

SEM surface and cross-section images of Ge-based films after tempering in Ar atmosphere or air are reported in Figure 8.8. The surface in cross-section images is marked in light blue. Notably, the mesoporous structure is found throughout the whole cross-section of all investigated samples. Furthermore, improved homogeneity of pores and smaller pore sizes / higher surface-to-volume ratios are achieved at the surface and in the bulk for Ar tempered samples upon post-treatment. In comparison, air tempered mesoporous Ge-based films, which have been exposed to the post-treatment, appear to have increased pore sizes. This can be best seen trough comparison of the column labeled "air; with PT" to the column labeled "Ar; with PT" in Figure 8.8. A reasonable explanation consists in the incomplete template removal as found for Ar tempered samples through EDX, FTIR and XPS shown in section 8.3. In case of air tempering, it is not surprising

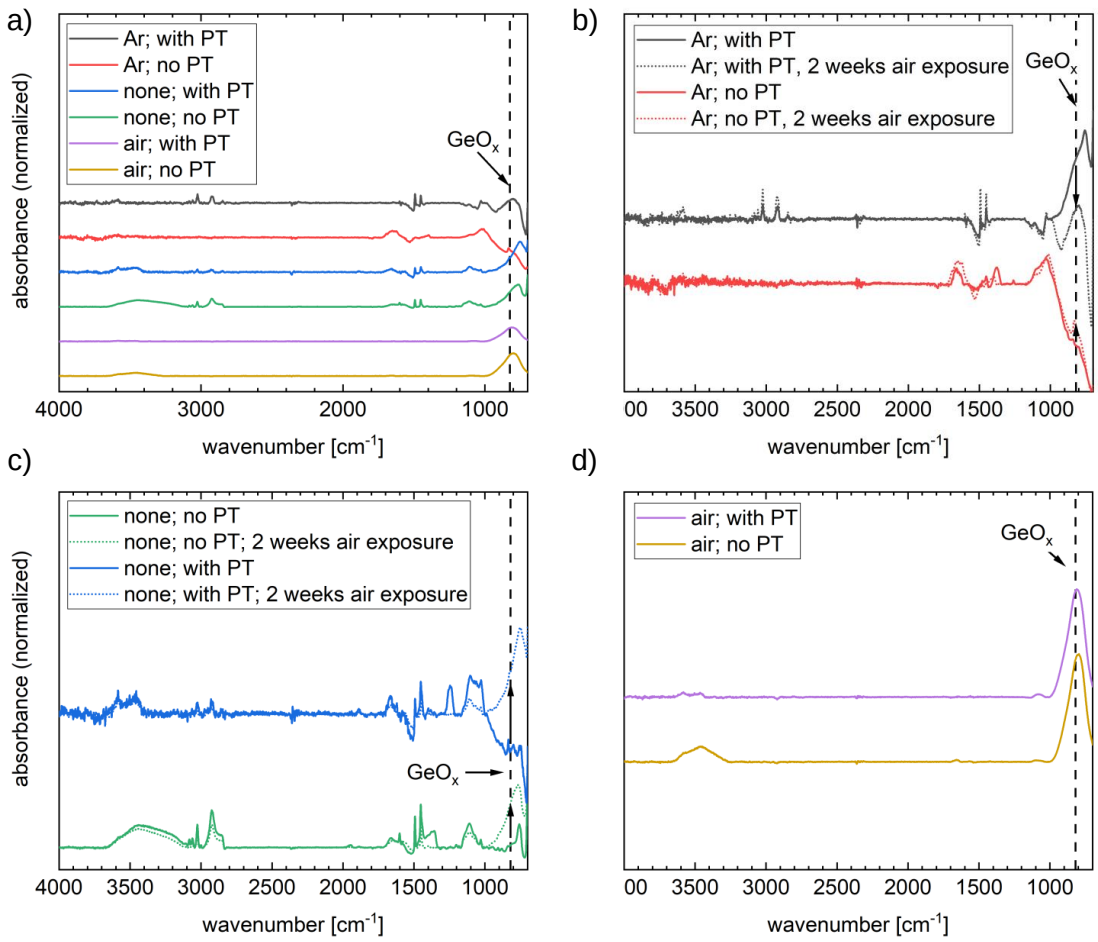

Figure 8.9: *Normalized FTIR spectra of mesoporous Ge-based films. (a) An overview of all samples. (b) Mesoporous films tempered in Ar atmosphere directly after synthesis (Ar, solid lines) and after 2 weeks of exposure to air (Ar, dotted lines). (c) Not tempered composite PS-b-PEO / K_4Ge_9 films directly after synthesis (solid lines) and after 2 weeks of exposure to air (dotted lines). (d) Mesoporous Ge-based films tempered in air directly after synthesis (solid lines).*

that pores appear bigger, if the polymer template is completely removed. The hypothesis of improved template removal is confirmed in the next section including FTIR analysis of air tempered samples.

FTIR absorption spectra are depicted in Figure 8.9. An overview of all measured samples can be seen in Figure 8.9a with the position of GeO_x related absorption indicated via a vertical, black dashed line. Ge oxidation behavior of mesoporous Ge-based samples tempered under Ar atmosphere was studied in Figure 8.9b. Peaks assigned to GeO_x are found more pronounced after two weeks exposure to air. A similar behavior of Ge oxidation can be observed for not tempered samples (Figure 8.9c). For air tempered

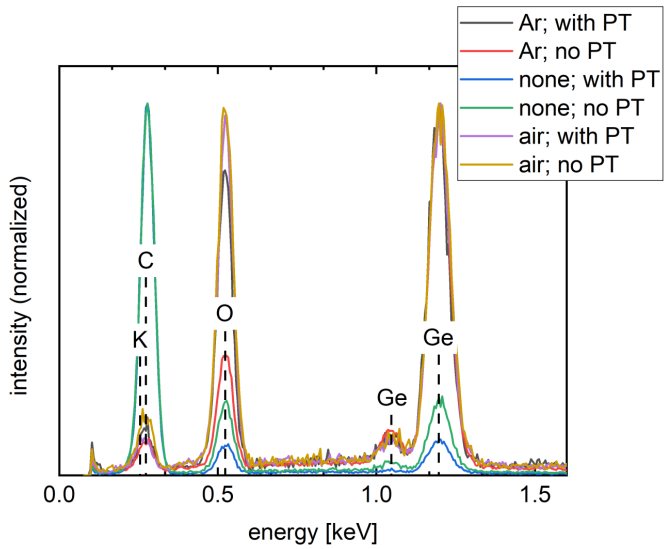

Figure 8.10: *Normalized EDX spectra of mesoporous Ge-based films tempered in Ar atmosphere (Ar), air (air) and composite PS-b-PEO / K_4Ge_9 films not tempered (none). Additionally, the effect of post-treatment (labeled as "with PT") was analyzed and compared to samples without post-treatment ("no PT"). Particularly, the presence of air and post-treatment clearly promotes oxidation.*

samples the GeO_x peak is most apparent (Figure 8.9d). Notably and in agreement with the hypothesis of improved template removal for air tempered samples, almost no traces of C can be identified in the typical range from 1100 to 2500 cm^{-1} for air tempered samples.

Normalized EDX spectra are shown in Figure 8.10 for Ar tempered, air tempered and not tempered samples. The intensity ratio O : Ge is higher for air samples as compared to Ar samples. Additionally, the post-treatment appears to promote oxidation (comparison between "Ar; with PT" and "Ar; no PT"). The highest peak for not tempered samples (none) is found in the energy range assigned to the polymer template (carbon atoms). This is not surprising since the polymer template has not yet been exposed to high temperature treatment and is therefore still residing inside the film for samples labeled as "none". Additionally, a small shoulder to the left side of the carbon (C) peak might be originating from potassium (K) residues of the K_4Ge_9 precursor.

Results of XPS survey scans for all samples are depicted in Figure 8.11a. Unlike for Ar tempered samples, no contribution of the FTO substrate can be seen in the case of not tempered samples (green and blue lines). However, air tempered samples (purple and yellow lines) show peaks attributed to Sn and Si. This is not surprising as air tempered samples also have a mesoporous structure and the likeliness of measuring the substrate underneath the mesoporous Ge layer is increased as compared to a compact composite film (none). Comparison of zoom-in spectra of Ar and air tempered samples in Figure 8.11b reveals a more pronounced shoulder for Ar tempered samples near the literature value of elemental Ge $3p_{3/2}$ emission. Calculated intensity ratios as obtained from fitting indicated an increased ratio GeO_x : Ge of 6.4 for air tempered samples as compared to 3.1 for Ar tempered samples. Figure 8.11d shows that the post-treatment only has a major impact on the degree of oxidation if tempering is performed in air. This finding appears reasonable

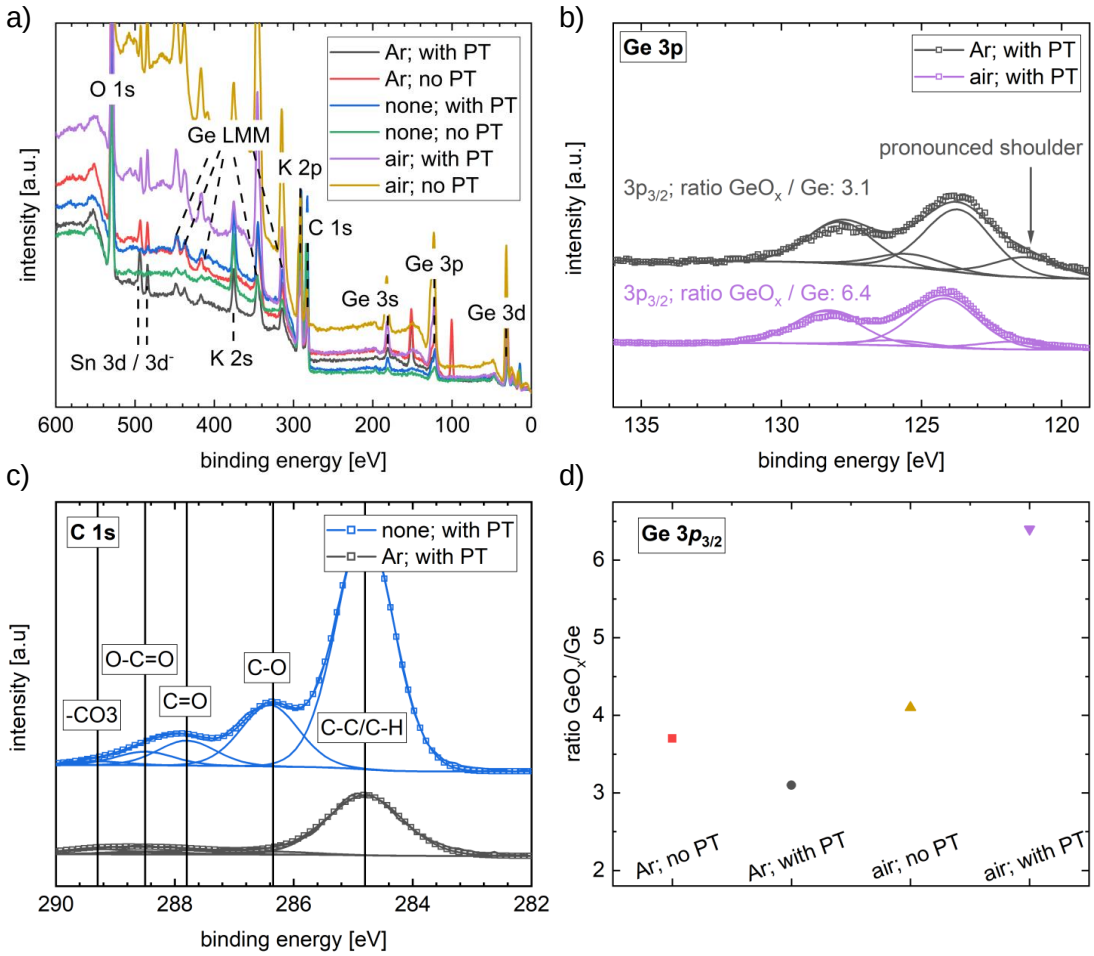

Figure 8.11: *X-ray photoelectron spectroscopy measurements of mesoprous and composite Ge films. (a) Survey scans of mesoporous Ge-based films tempered in air (yellow and purple lines), under Ar atmosphere (red and black lines) and composite, not tempered films (blue and green lines). (b) Zoom-in spectra of Ge 3p core level emission of air (purple squares) and Ar (black squares) tempered samples with respective GeO_x / Ge intensity ratios as indicated in the insets. (c) Example of C 1s calibration for not tempered samples (blue squares) and Ar tempered samples (black squares). (d) Comparison of GeO_x / Ge intensity ratios for all tempered samples.*

as the post-treatment enhances phase separation and, thus, leads to increased surface-to-volume ratios which in turn implies increased surface oxidation of Ge layers. An example of calibration to C 1s emission is shown in Figure 8.11c. Notably, peaks in the case of not tempered composite films could be attributed to C double bonds. For Ar tempered samples these peaks are significantly reduced in intensity but still detectable.

UV/Vis absorption measurements are reported in Figure 8.12a. A comparison of air tempered (Figure 8.12b), Ar tempered (Figure 8.12d) and not tempered (Figure 8.12e) shows an increased scattering for all samples which have been post-treated with a mixture

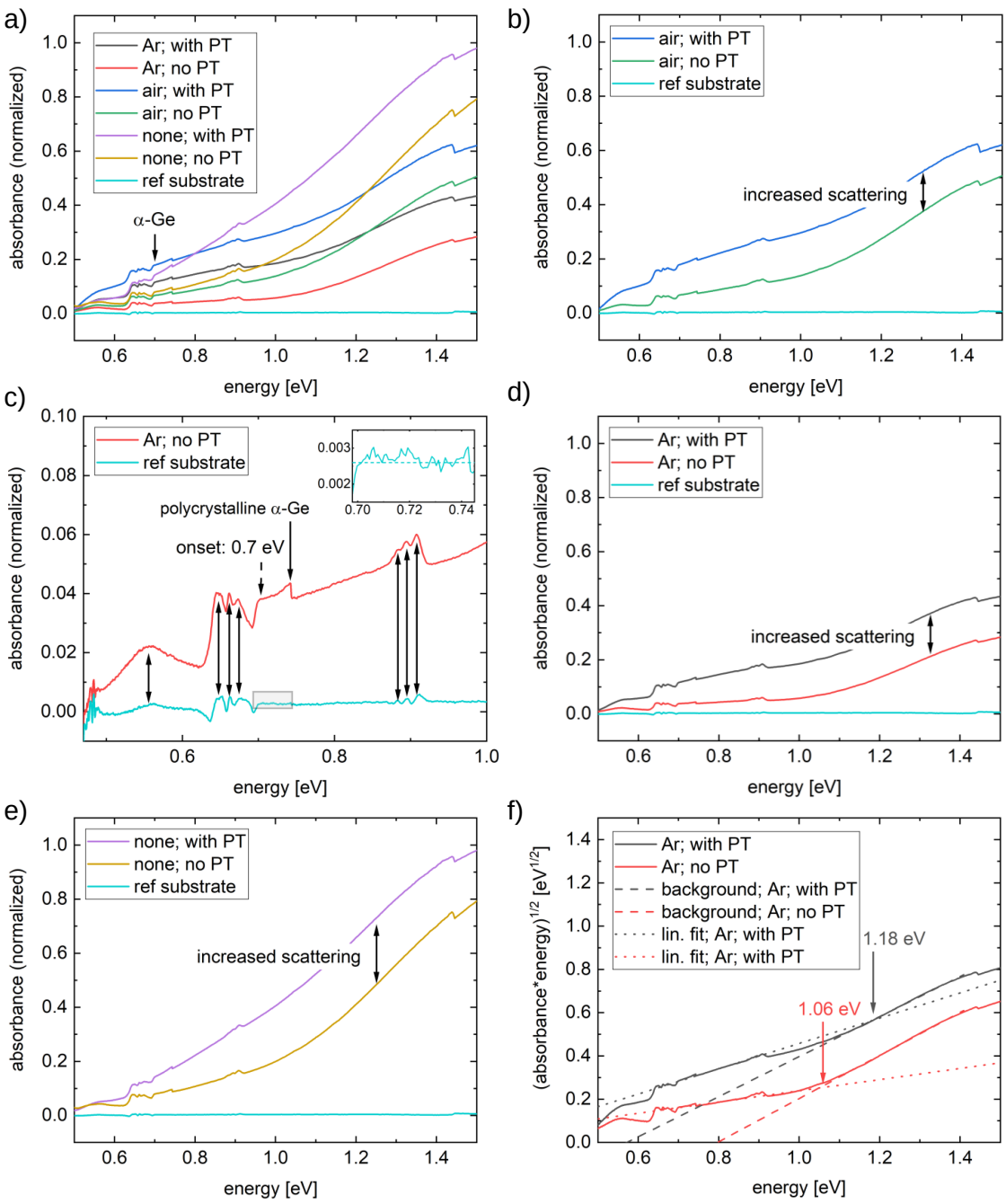

Figure 8.12: *UV/Vis absorption measurements of mesoporous and composite Ge films. (a) Overview of Ar (black and red lines), air (blue and green lines) and not tempered (purple and yellow lines) samples. (b), (d), (e) Impact of post-treatment on absorption behavior for Ar, air and not tempered samples. (c) Comparison of Ar tempered sample to a reference measurement of a glass substrate shows that on onset of absorption can be clearly seen around 0.7 eV. (f) Tauc plots for Ar tempered mesoporous Ge-based films with background (dashed lines), data (solid lines) and linear fitting (dotted lines).*

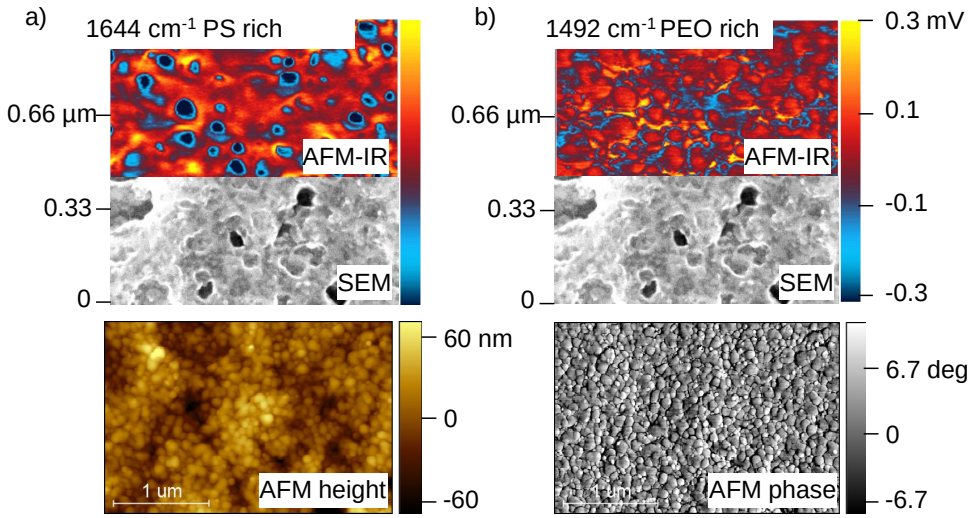

Figure 8.13: *Atomic force microscopy combined with local infrared absorption (AFM-IR) measurements of composite PS-b-PEO / K_4Ge_9 films (none; no PT) at (a) 1644 cm^{-1} and (b) 1492 cm^{-1}, two times SEM image of Ar tempered mesoporous Ge-based samples (Ar; no PT) and standard AFM microscopy images (none, no PT). Comparison of AFM-IR to SEM gives the impression that Ge-based structures are preferentially formed in PS-rich domains. AFM-IR measurements were performed at Physical Electronics GmbH (see footnote 2).*

of 1-butanol/toluene. The increased scattering is seen as direct consequence of enhanced phase separation and the resulting increased porosity. Furthermore, an absorption edge is detected around 0.7 eV which is best seen in Figure 8.12c and roughly matches literature values for polycrystalline α-Ge. Note that dynamic effects inside the film layer might as well be a possible explanation for increased absorption in this range. Contributions of the underlying glass substrate are excluded as shown in the zoom-in graph of the substrate measurement in Figure 8.12c. Examples of Tauc plots to determine the optical bandgap are reported in Figure 8.12f. A linear baseline (dashed line) is used to account for the high scattering contributions of mesoporous samples and the intersection of baseline and linear Tauc fit is defined as optical bandgap. Within this scope, a slightly increased optical bandgap of 1.18 eV is extracted for post-treated, Ar tempered samples. Ar tempered samples without post-treatment indicate a decreased bandgap of 1.06 eV. The increased value of optical bandgap for post-treated Ge-based films might be correlated to a decreased structure/pore size as observed for post-treated samples. According to literature smaller nanostructures tend to result in larger optical bandgaps [193]. Note that the linear baseline might not be sufficient to fully account for the increased scattering of mesoporous samples and that the range used for the linear Tauc fit was not well-defined especially due to the high amount of scattering.

A comparison is depicted in Figure 8.13 which shows atomic force microscopy combined with infrared absorption (AFM-IR)[2] measurements of composite PS-b-PEO/K_4Ge_9 films ("none, no PT") prior to polymer template removal and SEM images as obtained from samples after PS-b-PEO template removal through Ar tempering. For the AFM-IR measurements, detection of two different wavenumbers is selected for selective chemical mapping of PS and PEO rich domains over a total AFM scan size of 1 μm x 1 μm. Chemical mapping at 1644 cm^{-1} (PS sensitive, Figure 8.13a) exhibits an approximately inverse structure as compared to chemical mapping performed at an excitation of 1492 cm^{-1} (PEO sensitive, Figure 8.13b). Thereby, the mesoscopic phase separation behavior of PS and PEO is demonstrated. Comparison to simultaneously recorded standard AFM height images at the bottom of Figure 8.13a illustrates the additional information as obtained through AFM-IR. While through standard AFM no contrast between the two blocks of the PS-b-PEO template is observed, AFM-IR clearly allows to identify two different material phases, which are ascribed to PS and PEO. Moreover, SEM images as obtained from samples after template removal (Ar; no PT) indicate through comparison with AFM-IR measurements that Ge-based structures tend to be formed/remain in areas where PS was detected prior to removal. Rather than observing an agglomeration of sphere-like structures, which appears likely if the precursor K_4Ge_9 would be incorporated into the PEO structure of Figure 8.13b, an interconnected, slightly porous structure similar to the PS structure in Figure 8.13a is observed. Thus, selective K_4Ge_9 incorporation into PS domains of the diblock copolymer template PS-b-PEO appears also possible. Additionally, moderate phase separation of the polymeric template even without the application of a post-treatment is confirmed, which is in agreement with results as obtained from SEM for "no PT" samples. Consequentially, the post-treatment is not exclusively responsible for the phase separation of the polymer template but rather acts as an instrument to strongly enhance phase separation, which also occurs without the post-treatment in a weakened form. This information would not have been accessible through standard AFM as demonstrated in the phase image in Figure 8.13b, where no significant difference between PS and PEO was observed.

[2]Atomic force microscopy infrared absorption measurements of composite PS-b-PEO/K_4Ge_9 films were performed by Miriam Unger within the frame of a demonstration series at Physical Electronics GmbH (Ismaning, Germany). A nanoIR2 by Anasys Instruments was used to locally measure mid-infrared absorption (MIR) in the range from 3600 – 1000 cm^{-1} (optical parametric oscillator (OPO)-laser excitation). Chemical mapping at excitation wavelengths of 1644 cm^{-1} (PS sensitive) and 1492 cm^{-1} (PEO sensitive) was conducted over an AFM scan area of 1 μm x 1 μm.

8.5 Conclusion

Mesoporous $GeO_2/GeO_x/Ge/C$ films with crystalline α-Ge phases are synthesized based on K_4Ge_9 Zintl clusters as a Ge precursor in combination with diblock copolymer templating. Notably, the simple and wet-chemical nature of the synthesis procedure appears compatible with large scale deposition through e.g. spray-coating or printing. AFM-IR measurements suggest that the K_4Ge_9 precursor might be incorporated into the PS domain of the polymer template prior to tempering. SEM and GISAXS measurements give strong indication that the applied post-treatment with a poor-good azeotrope solvent mixture of 1-butanol and toluene yields enhanced porosity and significantly increased surface-to-volume ratios as compared to reference samples without post-treatment. Indirect evidence of increased porosity/surface-to-volume ratio is provided through UV/Vis measurements, where a decreased transmission intensity is ascribed to increased scattering losses for samples with post-treatment. Through EDX, XPS and FTIR measurements the applied post-treatment is found to additionally promote Ge oxidation. Assembly of half-cells demonstrates the promising potential of mesoporous Ge-based films as anode material in Li ion batteries. The achieved outstanding specific capacity of larger than 2000 $mAhg^{-1}$ is close to the expected theoretical limit of 2152 $mAhg^{-1}$. Moreover, almost 100% capacity retention is reached over 300 cycles. The high specific capacity results from an increased amount of pseudocapacitive processes in high surface-to-volume ratio mesoporous Ge-based films and reversible LiO_2 formation reactions due to the presence of catalytically active Ge nanostructures.

9 Conclusion and outlook

In the present thesis, novel nanostructuring routines on the basis of titanium and germanium with potential application in hybrid photovoltaics and lithium ion batteries are introduced. Within this scope, the focus was set upon understanding morphological changes, which were induced by altered processing conditions. Identified influences on the structure formation process were exploited to systematically control the surface and inner morphology of nanostructured and mesoporous thin films. Implications for performance in photovoltaic devices were discussed and the advantages of nanostructured material were directly proven in lithium ion battery half cells. In the following, key questions raised in the introduction are addressed for each chapter.

In the first result chapter, a novel and readily available processing routine is introduced to fabricate foam-like and mesoporous titania thin films. For this purpose, the amphiphilic diblock copolymer template polystyrene-block-polyethylene oxide was combined with sol-gel concepts and blade coating as a deposition technique. The introduced routine is potentially up-scalable, as wet-chemical processing requirements are fulfilled during all stages. For hybrid photovoltaic applications, precise control of pore sizes in the range < 40 nm was achieved on the basis of titania nanostructures to especially tackle the challenge of optimization between good backfilling conditions with an organic material (larger pores with decreased number density) and reduction of recombination losses through higher amounts of inorganic-organic interface (smaller pores with increased number density). As deduced from studies targeting altered good solvent and poor solvent conditions, the mobility of the polymer template and the energetic incompatibility of both polymer blocks were determined as key influences on the final film morphology. Additionally, a respective interplay of those influences is primarily found responsible for the degree of order in formed structures. In general, the introduced routine is envisioned to strongly boost the development of next generation solar devices through enabling precise custom tailoring of titania nanostructures.

On the basis of an identical material system as mentioned above, spray deposition was successfully proven to allow for large scale deposition of mesoporous titania thin films. The role of the catalytic additive HCl was investigated *in situ* via X-ray scattering. Thereby,

the presence of HCl was found to significantly alter the structure formation dynamics and reactions. As a result, improved control over foam-like structures was obtained. Note that especially under dry airbrush conditions, only small structural changes were found to occur during the deposition process and post-deposition annealing. Major structure-determining processes were deduced to be happening prior to deposition. Moreover and through the obtained knowledge, potential industrial routines for photovoltaic device production could be optimized in terms of processing time.

Beyond the proven potential of large scale deposition, the full versatility of diblock copolymer templating is demonstrated via the transition to and introduction of a novel germanium nanostructuring routine. Again, the identical fundamental idea of diblock copolymer templating combined with a good-poor solvent pair was exploited to form foam-like and size-controllable mesoporous Ge-based nanostructures via a Ge-Zintl precursor. To meet the special demands of the novel precursor, meticulous exclusion of air and water during the processing steps had to be ensured and a different organic solvent (ethylenediamine) as a stable transfer agent was required to prevent precursor oxidation prior to deposition. A successive increase of the precursor to polymer template ratio was found to enable precise structural control on a mesoscale. The development of the presented wet-chemical processing routine for controllable, Ge-based mesoporous structures allows for all potential advantages of Ge-nanostructures to be combined with wet-chemical manufacturing concepts of photovoltaic devices. New possibilities for the design of hybrid solar cells are generated in terms of energy band level alignment, reduction of recombination losses through record electron mobilities and unique properties of germanium.

In the last result chapter, mesoporous Ge-based films were synthesized via drop casting on the basis of an identical material system as described in the previous section. Fabricated nanostructured films were applied as anode material in Li ion battery half cells. Thereby, record specific capacities of over 2000 mAh g^{-1} were measured with high cycle lifetimes (> 300), which was attributed to the inherent properties of germanium as an element combined with a mesoporous structure. In detail, the nanostructure was found to mainly increase the specific capacity through pseudocapacitive processes. Additionally, high cycle lifetimes were achieved, as nanostructuring counteracts negative effects of high volume expansion. Particularly, films with higher degree of porosity were found to heavily outperform films with lower degree of porosity. Additionally and under specific annealing conditions, the diblock copolymer approach was found to leave traces of carbon inside the films, which is furthermore seen as beneficial for electrochemical kinetics.

In general, the immense versatility of diblock copolymer templating was proven in terms of precise mesoscale structure control, compatibility with large scale deposition techniques, availability of different suitable precursors and outstanding potential and performance of

synthesized thin films in applications. Recommended future projects in the field of photovoltaics are the quantification of backfilling efficiencies in dependence on foam-like pore sizes and correlation to the power conversion efficiency of photovoltaic devices. However and due to the success in the field of battery application, future projects should primarily focus on compositional and structural optimization of thin films for Li ion batteries. Within this frame, *in situ* observation of structural changes during operation could allow to obtain additional information, which might further explain the structural origins of the excellent cycle lifetime and specific capacity of manufactured devices. Notably, a transition to mixed Ge/Si-Zintl precursors appears also promising due to several reasons. Despite the porous structure of Ge-based thin films and an inherently reduced quantity of needed material, introduction of abundant silicon with also excellent properties for Li ion battery application would negate any concerns in terms of material availability. Similarly as observed for nanostructured Ge-based films, mixed Ge/Si films would profit from nanostructuring in terms of expected cycle lifetime and specific capacity. The introduced diblock copolymer structuring routine has already proven to be compatible with different precursors. Therefore, the introduction of a chemically similar mixed Ge/Si-Zintl precursor also appears feasible. Last but not least, transition to a new precursor might also enable the usage of a less toxic organic transfer agent as compared to the employed ethylenediamine. In addition, investigation of alternative battery concepts such as sodium ion batteries appears furthermore promising for Ge-based nanostructures to reduce fabrication costs and to minimize supply risks.

Bibliography

[1] C. K. Chiang, C. R. Fincher, Y. W. Park, A. J. Heeger, H. Shirakawa, E. J. Louis, S. C. Gau, and A. G. MacDiarmid, "Electrical conductivity in doped polyacetylene," *Physical Review Letters*, vol. 39, no. 17, pp. 1098–1101, 1977.

[2] L. Meng, Y. Zhang, X. Wan, C. Li, X. Zhang, Y. Wang, X. Ke, Z. Xiao, L. Ding, R. Xia, H.-L. Yip, Y. Cao, and Y. Chen, "Organic and solution-processed tandem solar cells with 17.3% efficiency," *Science*, vol. 361, no. 6407, pp. 1094–1098, 2018.

[3] C. J. Schaffer, C. M. Palumbiny, M. A. Niedermeier, C. Jendrzejewski, G. Santoro, S. V. Roth, and P. Müller-Buschbaum, "A direct evidence of morphological degradation on a nanometer scale in polymer solar cells," *Advanced Materials*, vol. 25, no. 46, pp. 6760–6764, 2013.

[4] P. Müller-Buschbaum, M. Thelakkat, T. F. Fässler, and M. Stutzmann, "Hybrid photovoltaics - from fundamentals towards application," *Advanced Energy Materials*, vol. 7, no. 16, p. 1700248, 2017.

[5] M. Graetzel, R. A. J. Janssen, D. B. Mitzi, and E. H. Sargent, "Materials interface engineering for solution-processed photovoltaics," *Nature*, vol. 488, no. 7411, pp. 304–312, 2012.

[6] S. Pröller, F. Liu, C. Zhu, C. Wang, T. P. Russell, A. Hexemer, P. Müller-Buschbaum, and E. M. Herzig, "Following the morphology formation in situ in printed active layers for organic solar cells," *Advanced Energy Materials*, vol. 6, no. 1, p. 1501580, 2016.

[7] R. Green, A. Morfa, A. J. Ferguson, N. Kopidakis, G. Rumbles, and S. E. Shaheen, "Performance of bulk heterojunction photovoltaic devices prepared by airbrush spray deposition," *Applied Physics Letters*, vol. 92, no. 3, p. 033301, 2008.

[8] M. Knupfer, "Exciton binding energies in organic semiconductors," *Applied Physics A*, vol. 77, no. 5, pp. 623–626, 2003.

[9] B. Kippelen and J.-L. Brédas, "Organic photovoltaics," *Energy & Environmental Science*, vol. 2, no. 3, p. 251, 2009.

[10] M. Grätzel, "Photoelectrochemical cells," *Nature*, vol. 414, no. 6861, pp. 338–344, 2001.

[11] L. Schmidt-Mende and M. Grätzel, "Tio2 pore-filling and its effect on the efficiency of solid-state dye-sensitized solar cells," *Thin Solid Films*, vol. 500, no. 1-2, pp. 296–301, 2006.

[12] I.-K. Ding, N. Tétreault, J. Brillet, B. E. Hardin, E. H. Smith, S. J. Rosenthal, F. Sauvage, M. Grätzel, and M. D. McGehee, "Pore-filling of spiro-ometad in solid-state dye sensitized solar cells: Quantification, mechanism, and consequences for device performance," *Advanced Functional Materials*, vol. 19, no. 15, pp. 2431–2436, 2009.

[13] Y. Tamai, H. Ohkita, H. Benten, and S. Ito, "Exciton diffusion in conjugated polymers: From fundamental understanding to improvement in photovoltaic conversion efficiency," *The Journal of Physical Chemistry Letters*, vol. 6, no. 17, pp. 3417–3428, 2015.

[14] M. G. Kim and J. Cho, "Reversible and high-capacity nanostructured electrode materials for li-ion batteries," *Advanced Functional Materials*, vol. 19, no. 10, pp. 1497–1514, 2009.

[15] S. Goriparti, E. Miele, F. de Angelis, E. Di Fabrizio, R. Proietti Zaccaria, and C. Capiglia, "Review on recent progress of nanostructured anode materials for li-ion batteries," *Journal of Power Sources*, vol. 257, pp. 421–443, 2014.

[16] S. Geier, R. Jung, K. Peters, H. A. Gasteiger, D. Fattakhova-Rohlfing, and T. F. Fässler, "A wet-chemical route for macroporous inverse opal ge anodes for lithium ion batteries with high capacity retention," *Sustainable Energy & Fuels*, vol. 2, no. 1, pp. 85–90, 2018.

[17] M.-H. Park, K. Kim, J. Kim, and J. Cho, "Flexible dimensional control of high-capacity li-ion-battery anodes: From 0d hollow to 3d porous germanium nanoparticle assemblies," *Advanced Materials*, vol. 22, no. 3, pp. 415–418, 2010.

[18] B. O'Regan and M. Grätzel, "A low-cost, high-efficiency solar cell based on dye-sensitized colloidal tio2 films," *Nature*, vol. 353, no. 6346, pp. 737–740, 1991.

[19] M. Saliba, T. Matsui, K. Domanski, J.-Y. Seo, A. Ummadisingu, S. M. Zakeeruddin, J.-P. Correa-Baena, W. R. Tress, A. Abate, A. Hagfeldt, and M. Grätzel, "Incorporation of rubidium cations into perovskite solar cells improves photovoltaic performance," *Science*, vol. 354, no. 6309, pp. 206–209, 2016.

[20] M. Saliba, T. Matsui, J.-Y. Seo, K. Domanski, J.-P. Correa-Baena, M. K. Nazeeruddin, S. M. Zakeeruddin, W. Tress, A. Abate, A. Hagfeldt, and M. Grätzel, "Cesium-containing triple cation perovskite solar cells: Improved stability, reproducibility and high efficiency," *Energy & Environmental Science*, vol. 9, no. 6, pp. 1989–1997, 2016.

[21] Y. Cao, Y. Saygili, A. Ummadisingu, J. Teuscher, J. Luo, N. Pellet, F. Giordano, S. M. Zakeeruddin, J.-E. Moser, M. Freitag, A. Hagfeldt, and M. Grätzel, "11% efficiency solid-state dye-sensitized solar cells with copper(ii/i) hole transport materials," *Nature Communications*, vol. 8, p. 15390, 2017.

[22] R. Pillarisetty, "Academic and industry research progress in germanium nanodevices," *Nature*, vol. 479, no. 7373, p. 324, 2011.

[23] G. S. Armatas and M. G. Kanatzidis, "Hexagonal mesoporous germanium," *Science*, vol. 313, no. 5788, pp. 817–820, 2006.

[24] P. J. Flory, "Thermodynamics of high polymer solutions," *The Journal of Chemical Physics*, vol. 10, no. 1, pp. 51–61, 1942.

[25] M. L. Huggins, "Thermodynamic properties of solutions of long-chain compounds," *Annals of the New York Academy of Sciences*, vol. 43, no. 1, pp. 1–32, 1942.

[26] F. S. Bates and G. H. Fredrickson, "Block copolymer thermodynamics: theory and experiment," *Annual Review of Physical Chemistry*, vol. 41, pp. 525–557, 1990.

[27] G. R. Strobl, *The physics of polymers: Concepts for understanding their structures and behavior*. Berlin, Heidelberg: Springer, 3., rev. and expanded ed. ed., 2007.

[28] Y. Mai and A. Eisenberg, "Self-assembly of block copolymers," *Chemical Society Reviews*, vol. 41, no. 18, pp. 5969–5985, 2012.

[29] U. Schubert, "Chemical modification of titanium alkoxides for sol–gel processing," *Journal of Materials Chemistry*, vol. 15, no. 35-36, p. 3701, 2005.

[30] M. Horn, C. F. Schwebdtfeger, and E. P. Meagher, "Refinement of the structure of anatase at several temperatures," *Zeitschrift für Kristallographie - Crystalline Materials*, vol. 136, no. 1-6, 1972.

[31] A. S. Cooper, "Precise lattice constants of germanium, aluminum, gallium arsenide, uranium, sulphur, quartz and sapphire," *Acta Crystallographica*, vol. 15, no. 6, pp. 578–582, 1962.

[32] J. Weickert, R. B. Dunbar, H. C. Hesse, W. Wiedemann, and L. Schmidt-Mende, "Nanostructured organic and hybrid solar cells," *Advanced Materials*, vol. 23, no. 16, pp. 1810–1828, 2011.

[33] S.-Q. Fan, C. Kim, B. Fang, K.-X. Liao, G.-J. Yang, C.-J. Li, J.-J. Kim, and J. Ko, "Improved efficiency of over 10% in dye-sensitized solar cells with a ruthenium complex and an organic dye heterogeneously positioning on a single tio2 electrode," *The Journal of Physical Chemistry C*, vol. 115, no. 15, pp. 7747–7754, 2011.

[34] T. Tachikawa, M. Minohara, Y. Nakanishi, Y. Hikita, M. Yoshita, H. Akiyama, C. Bell, and H. Y. Hwang, "Metal-to-insulator transition in anatase tio2 thin films induced by growth rate modulation," *Applied Physics Letters*, vol. 101, no. 2, p. 022104, 2012.

[35] F. Kiefer, A. J. Karttunen, M. Döblinger, and T. F. Fässler, "Bulk synthesis and structure of a microcrystalline allotrope of germanium (m-allo-ge)," *Chemistry of Materials*, vol. 23, no. 20, pp. 4578–4586, 2011.

[36] D. A. Ruddy, J. C. Johnson, E. R. Smith, and N. R. Neale, "Size and bandgap control in the solution-phase synthesis of near-infrared-emitting germanium nanocrystals," *ACS Nano*, vol. 4, no. 12, pp. 7459–7466, 2010.

[37] N. Hohn, A. E. Hetzenecker, M. A. Giebel, S. Geier, L. Bießmann, V. Körstgens, N. Saxena, J. Schlipf, W. Ohm, P. S. Deimel, F. Allegretti, J. V. Barth, S. V. Roth, T. F. Fässler, and P. Müller-Buschbaum, "Amphiphilic diblock copolymer-mediated structure control in nanoporous germanium-based thin films," *Nanoscale*, vol. 11, no. 4, pp. 2048–2055, 2019.

[38] L. L. Hench and J. K. West, "The sol-gel process," *Chemical Reviews*, vol. 90, no. 1, pp. 33–72, 1990.

[39] C.-C. Wang and J. Y. Ying, "Sol−gel synthesis and hydrothermal processing of anatase and rutile titania nanocrystals," *Chemistry of Materials*, vol. 11, no. 11, pp. 3113–3120, 1999.

[40] N. Hohn, S. J. Schlosser, L. Bießmann, L. Song, S. Grott, S. Xia, K. Wang, M. Schwartzkopf, S. V. Roth, and P. Müller-Buschbaum, "Impact of catalytic additive on spray deposited and nanoporous titania thin films observed via in situ x-ray scattering: Implications for enhanced photovoltaics," *ACS Applied Nano Materials*, vol. 1, no. 8, pp. 4227–4235, 2018.

[41] M. M. Bentlohner, M. Waibel, P. Zeller, K. Sarkar, P. Müller-Buschbaum, D. Fattakhova-Rohlfing, and T. F. Fässler, "Zintl clusters as wet-chemical precursors for germanium nanomorphologies with tunable composition," *Angewandte Chemie International Edition*, vol. 55, no. 7, pp. 2441–2445, 2016.

[42] Y.-J. Cheng and J. S. Gutmann, "Morphology phase diagram of ultrathin anatase tio2 films templated by a single ps-b-peo block copolymer," *Journal of the American Chemical Society*, vol. 128, no. 14, pp. 4658–4674, 2006.

[43] M. Grätzel, U. Bach, D. Lupo, P. Comte, J. E. Moser, F. Weissörtel, J. Salbeck, and H. Spreitzer, "Solid-state dye-sensitized mesoporous tio2 solar cells with high photon-to-electron conversion efficiencies," *Nature*, vol. 395, no. 6702, pp. 583–585, 1998.

[44] B. E. Hardin, H. J. Snaith, and M. D. McGehee, "The renaissance of dye-sensitized solar cells," *Nature Photonics*, vol. 6, no. 3, pp. 162–169, 2012.

[45] J. M. Szeifert, D. Fattakhova-Rohlfing, D. Georgiadou, V. Kalousek, J. Rathouský, D. Kuang, S. Wenger, S. M. Zakeeruddin, M. Grätzel, and T. Bein, ""brick and mortar" strategy for the formation of highly crystalline mesoporous titania films from nanocrystalline building blocks," *Chemistry of Materials*, vol. 21, no. 7, pp. 1260–1265, 2009.

[46] G. S. Armatas and M. G. Kanatzidis, "High-surface-area mesoporous germanium from oxidative polymerization of the deltahedral [ge9]4– cluster: Electronic structure modulation with donor and acceptor molecules," *Advanced Materials*, vol. 20, no. 3, pp. 546–550, 2008.

[47] D. Sun, A. E. Riley, A. J. Cadby, E. K. Richman, S. D. Korlann, and S. H. Tolbert, "Hexagonal nanoporous germanium through surfactant-driven self-assembly of zintl clusters," *Nature*, vol. 441, no. 7097, pp. 1126–1130, 2006.

[48] W. J. D. Beenken, "Excitons in conjugated polymers: Do we need a paradigma change?," *Physica Status Solidi A: Applications and Materials Science*, vol. 112, pp. NA–NA, 2009.

[49] V. V. Atuchin, V. V. Kaichev, I. V. Korolkov, A. A. Saraev, I. B. Troitskaia, T. V. Perevalov, and V. A. Gritsenko, "Electronic structure of noncentrosymmetric alpha-geo2 with oxygen vacancy: Ab initio calculations and comparison with experiment," *The Journal of Physical Chemistry C*, vol. 118, no. 7, pp. 3644–3650, 2014.

[50] M. Zacharias and P. M. Fauchet, "Blue luminescence in films containing ge and geo2 nanocrystals: The role of defects," *Applied Physics Letters*, vol. 71, no. 3, pp. 380–382, 1997.

[51] J. T. Dudley, D. P. Wilkinson, G. Thomas, R. LeVae, S. Woo, H. Blom, C. Horvath, M. W. Juzkow, B. Denis, P. Juric, P. Aghakian, and J. R. Dahn, "Conductivity of electrolytes for rechargeable lithium batteries," *Journal of Power Sources*, vol. 35, no. 1, pp. 59–82, 1991.

[52] K. H. Seng, M.-H. Park, Z. P. Guo, H. K. Liu, and J. Cho, "Catalytic role of ge in highly reversible geo2/ge/c nanocomposite anode material for lithium batteries," *Nano Letters*, vol. 13, no. 3, pp. 1230–1236, 2013.

[53] M. Tolan, *X-Ray Scattering from Soft-Matter Thin Films: Materials Science and Basic Research*, vol. 148 of *Springer Tracts in Modern Physics*. Berlin and Heidelberg: Springer, 1999.

[54] Y. Yoneda, "Anomalous surface reflection of x rays," *Physical Review*, vol. 131, no. 5, pp. 2010–2013, 1963.

[55] R. Lazzari, "Isgisaxs: A program for grazing-incidence small-angle x-ray scattering analysis of supported islands," *Journal of Applied Crystallography*, vol. 35, no. 4, pp. 406–421, 2002.

[56] S. Gražulis, A. Daškevič, A. Merkys, D. Chateigner, L. Lutterotti, M. Quirós, N. R. Serebryanaya, P. Moeck, R. T. Downs, and A. Le Bail, "Crystallography open database (cod): an open-access collection of crystal structures and platform for world-wide collaboration," *Nucleic Acids Research*, vol. 40, no. D1, pp. D420–D427, 2012.

[57] M. E. Straumanis and E. Z. Aka, "Lattice parameters, coefficients of thermal expansion, and atomic weights of purest silicon and germanium," *Journal of Applied Physics*, vol. 23, no. 3, pp. 330–334, 1952.

[58] P. Müller-Buschbaum, "A basic introduction to grazing incidence small-angle x-ray scattering," in *Applications of synchrotron light to scattering and diffraction in materials and life sciences* (T. A. Ezquerra, ed.), Lecture notes in physics, pp. 61–89, Berlin: Springer, 2009.

[59] C. T. Rueden, J. Schindelin, M. C. Hiner, B. E. DeZonia, A. E. Walter, E. T. Arena, and K. W. Eliceiri, "Imagej2: Imagej for the next generation of scientific image data," *BMC Bioinformatics*, vol. 18, no. 1, p. 529, 2017.

[60] N. Otsu, "A threshold selection method from gray-level histograms," *IEEE Transactions on Systems, Man, and Cybernetics*, vol. 9, no. 1, pp. 62–66, 1979.

[61] Binnig, Quate, and Gerber, "Atomic force microscope," *Physical review letters*, vol. 56, no. 9, pp. 930–933, 1986.

[62] D. Nečas and P. Klapetek, "Gwyddion: An open-source software for spm data analysis," *Open Physics*, vol. 10, no. 1, p. 99, 2012.

[63] A. Hexemer and P. Müller-Buschbaum, "Advanced grazing-incidence techniques for modern soft-matter materials analysis," *International Union of Crystallography Journal*, vol. 2, no. Pt 1, pp. 106–125, 2015.

[64] G. Benecke, W. Wagermaier, C. Li, M. Schwartzkopf, G. Flucke, R. Hoerth, I. Zizak, M. Burghammer, E. Metwalli, P. Müller-Buschbaum, M. Trebbin, S. Förster, O. Paris, S. V. Roth, and P. Fratzl, "A customizable software for fast reduction and analysis of large x-ray scattering data sets: applications of the new dpdak package to small-angle x-ray scattering and grazing-incidence small-angle x-ray scattering," *Journal of Applied Crystallography*, vol. 47, no. Pt 5, pp. 1797–1803, 2014.

[65] Q. Zhong, L. Mi, E. Metwalli, L. Bießmann, M. Philipp, A. Miasnikova, A. Laschewsky, C. M. Papadakis, R. Cubitt, M. Schwartzkopf, S. V. Roth, J. Wang, and P. Müller-Buschbaum, "Effect of chain architecture on the swelling and thermal response of star-shaped thermo-responsive (poly(methoxy diethylene glycol acrylate)-block-polystyrene)3 block copolymer films," *Soft Matter*, vol. 14, no. 31, pp. 6582–6594, 2018.

[66] J. Tauc, R. Grigorovici, and A. Vancu, "Optical properties and electronic structure of amorphous germanium," *Physica Status Solidi B: Basic Solid State Physics*, vol. 15, no. 2, pp. 627–637, 1966.

[67] S. Tanuma, C. J. Powell, and D. R. Penn, "Calculations of electron inelastic mean free paths. v. data for 14 organic compounds over the 50-2000 ev range," *Surface and Interface Analysis*, vol. 21, no. 3, pp. 165–176, 1994.

[68] Lawrence Berkeley National Laboratory, University of California, ed., *X-ray Data Booklet*. 3rd ed. ed., 2009.

[69] E. Zintl, "Intermetallische verbindungen," *Angewandte Chemie*, vol. 52, no. 1, pp. 1–6, 1939.

[70] T. F. Fässler, "The renaissance of homoatomic nine-atom polyhedra of the heavier carbon-group elements si–pb," *Coordination Chemistry Reviews*, vol. 215, no. 1, pp. 347–377, 2001.

[71] S. Ponou and T. F. Fässler, "Crystal growth and structure refinement of k4ge9," *Zeitschrift fuer Anorganische und Allgemeine Chemie*, vol. 633, no. 3, pp. 393–397, 2007.

[72] P. Müller-Buschbaum, "Influence of surface cleaning on dewetting of thin polystyrene films," *The European Physical Journal. E, Soft Matter*, vol. 12, no. 3, pp. 443–8; discussion 448, 2003.

[73] C. J. Lawrence, "The mechanics of spin coating of polymer films," *Physics of Fluids*, vol. 31, no. 10, p. 2786, 1988.

[74] D. W. Schubert and T. Dunkel, "Spin coating from a molecular point of view: its concentration regimes, influence of molar mass and distribution," *Materials Research Innovations*, vol. 7, no. 5, pp. 314–321, 2003.

[75] N. Hohn, S. J. Schlosser, L. Bießmann, S. Grott, S. Xia, K. Wang, M. Schwartzkopf, S. V. Roth, and P. Müller-Buschbaum, "Readily available titania nanostructuring routines based on mobility and polarity controlled phase separation of an amphiphilic diblock copolymer," *Nanoscale*, vol. 10, no. 11, pp. 5325–5334, 2018.

[76] S. J. Schlosser, *Investigation and characterization of diblock copolymer controlled titania morphologies.* Master's thesis, Technische Universität München, München, 09.11.2017.

[77] D. Cahen, G. Hodes, M. Grätzel, J. F. Guillemoles, and I. Riess, "Nature of photovoltaic action in dye-sensitized solar cells," *The Journal of Physical Chemistry B*, vol. 104, no. 9, pp. 2053–2059, 2000.

[78] L. Kavan, M. Grätzel, S. E. Gilbert, C. Klemenz, and H. J. Scheel, "Electrochemical and photoelectrochemical investigation of single-crystal anatase," *Journal of the American Chemical Society*, vol. 118, no. 28, pp. 6716–6723, 1996.

[79] M. Yu, Y. Zeng, C. Zhang, X. Lu, C. Zeng, C. Yao, Y. Yang, and Y. Tong, "Titanium dioxide@polypyrrole core-shell nanowires for all solid-state flexible supercapacitors," *Nanoscale*, vol. 5, no. 22, pp. 10806–10810, 2013.

[80] Y.-J. Cheng, P. Müller-Buschbaum, and J. S. Gutmann, "Ultrathin anatase tio2 films with stable vesicle morphology templated by pmma-b-peo," *Small*, vol. 3, no. 8, pp. 1379–1382, 2007.

[81] E. J. W. Crossland, M. Nedelcu, C. Ducati, S. Ludwigs, M. A. Hillmyer, U. Steiner, and H. J. Snaith, "Block copolymer morphologies in dye-sensitized solar cells: Probing the photovoltaic structure-function relation," *Nano Letters*, vol. 9, no. 8, pp. 2813–2819, 2009.

[82] L. D. Birkefeld, A. M. Azad, and S. A. Akbar, "Carbon monoxide and hydrogen detection by anatase modification of titanium dioxide," *Journal of the American Chemical Society*, vol. 75, no. 11, pp. 2964–2968, 1992.

[83] R. Terzian, "Photocatalyzed mineralization of cresols in aqueous media with irradiated titania*1," *Journal of Catalysis*, vol. 128, no. 2, pp. 352–365, 1991.

[84] C. Stegelmeier, A. Exner, S. Hauschild, V. Filiz, J. Perlich, S. V. Roth, V. Abetz, and S. Förster, "Evaporation-induced block copolymer self-assembly into membranes studied by in situ synchrotron saxs," *Macromolecules*, vol. 48, no. 5, pp. 1524–1530, 2015.

[85] J. M. Macak, M. Zlamal, J. Krysa, and P. Schmuki, "Self-organized tio2 nanotube layers as highly efficient photocatalysts," *Small*, vol. 3, no. 2, pp. 300–304, 2007.

[86] M. Wang, S.-J. Moon, M. Xu, K. Chittibabu, P. Wang, N.-L. Cevey-Ha, R. Humphry-Baker, S. M. Zakeeruddin, and M. Grätzel, "Efficient and stable solid-state dye-sensitized solar cells based on a high-molar-extinction-coefficient sensitizer," *Small*, vol. 6, no. 2, pp. 319–324, 2010.

[87] M. Wagemaker, A. P. M. Kentgens, and F. M. Mulder, "Equilibrium lithium transport between nanocrystalline phases in intercalated tio(2) anatase," *Nature*, vol. 418, no. 6896, pp. 397–399, 2002.

[88] L. Ren, Y. Liu, X. Qi, K. S. Hui, K. N. Hui, Z. Huang, J. Li, K. Huang, and J. Zhong, "An architectured tio2 nanosheet with discrete integrated nanocrystalline subunits and its application in lithium batteries," *Journal of Materials Chemistry*, vol. 22, no. 40, p. 21513, 2012.

[89] H. B. Wu, J. S. Chen, H. H. Hng, and X. W. D. Lou, "Nanostructured metal oxide-based materials as advanced anodes for lithium-ion batteries," *Nanoscale*, vol. 4, no. 8, pp. 2526–2542, 2012.

[90] Z. Chen, X. Wang, Y. Qi, S. Yang, J. A. N. T. Soares, B. A. Apgar, R. Gao, R. Xu, Y. Lee, X. Zhang, J. Yao, and L. W. Martin, "Self-assembled, nanostructured, tunable metamaterials via spinodal decomposition," *ACS Nano*, vol. 10, no. 11, pp. 10237–10244, 2016.

[91] L. de Marco, M. Manca, R. Buonsanti, R. Giannuzzi, F. Malara, P. Pareo, L. Martiradonna, N. M. Giancaspro, P. D. Cozzoli, and G. Gigli, "High-quality photoelectrodes based on shape-tailored tio2 nanocrystals for dye-sensitized solar cells," *Journal of Materials Chemistry*, vol. 21, no. 35, p. 13371, 2011.

[92] P. Hoyer, "Semiconductor nanotube formation by a two-step template process," *Advanced Materials*, vol. 8, no. 10, pp. 857–859, 1996.

[93] E. J. W. Crossland, M. Kamperman, M. Nedelcu, C. Ducati, U. Wiesner, D.-M. Smilgies, G. E. S. Toombes, M. A. Hillmyer, S. Ludwigs, U. Steiner, and H. J. Snaith, "A bicontinuous double gyroid hybrid solar cell," *Nano Letters*, vol. 9, no. 8, pp. 2807–2812, 2009.

[94] K. M. Coakley, Y. Liu, M. D. McGehee, K. L. Frindell, and G. D. Stucky, "Infiltrating semiconducting polymers into self-assembled mesoporous titania films for photovoltaic applications," *Advanced Functional Materials*, vol. 13, no. 4, pp. 301–306, 2003.

[95] P. F. W. Simon, R. Ulrich, H. W. Spiess, and U. Wiesner, "Block copolymer−ceramic hybrid materials from organically modified ceramic precursors," *Chemistry of Materials*, vol. 13, no. 10, pp. 3464–3486, 2001.

[96] N. Haberkorn, M. C. Lechmann, B. H. Sohn, K. Char, J. S. Gutmann, and P. Theato, "Templated organic and hybrid materials for optoelectronic applications," *Macromolecular Rapid Communications*, vol. 30, no. 14, pp. 1146–1166, 2009.

[97] Zhao, Feng, Huo, Melosh, Fredrickson, Chmelka, and Stucky, "Triblock copolymer syntheses of mesoporous silica with periodic 50 to 300 angstrom pores," *Science*, vol. 279, no. 5350, pp. 548–552, 1998.

[98] C. T. Kresge, M. E. Leonowicz, W. J. Roth, J. C. Vartuli, and J. S. Beck, "Ordered mesoporous molecular sieves synthesized by a liquid-crystal template mechanism," *Nature*, vol. 359, no. 6397, pp. 710–712, 1992.

[99] G. D. Stucky, P. Yang, D. Zhao, D. I. Margolese, and B. F. Chmelka, "Generalized syntheses of large-pore mesoporous metal oxides with semicrystalline frameworks," *Nature*, vol. 396, no. 6707, pp. 152–155, 1998.

[100] S. H. Joo, S. J. Choi, I. Oh, J. Kwak, Z. Liu, O. Terasaki, and R. Ryoo, "Ordered nanoporous arrays of carbon supporting high dispersions of platinum nanoparticles," *Nature*, vol. 412, no. 6843, pp. 169–172, 2001.

[101] S. C. Warren, L. C. Messina, L. S. Slaughter, M. Kamperman, Q. Zhou, S. M. Gruner, F. J. DiSalvo, and U. Wiesner, "Ordered mesoporous materials from metal nanoparticle-block copolymer self-assembly," *Science*, vol. 320, no. 5884, pp. 1748–1752, 2008.

[102] J. Lee, M. C. Orilall, S. C. Warren, M. Kamperman, F. J. DiSalvo, and U. Wiesner, "Direct access to thermally stable and highly crystalline mesoporous transition-metal oxides with uniform pores," *Nature Materials*, vol. 7, no. 3, pp. 222–228, 2008.

[103] G. Kaune, M. Memesa, R. Meier, M. A. Ruderer, A. Diethert, S. V. Roth, M. D'Acunzi, J. S. Gutmann, and P. Müller-Buschbaum, "Hierarchically structured titania films prepared by polymer/colloidal templating," *ACS Applied Materials & Interfaces*, vol. 1, no. 12, pp. 2862–2869, 2009.

[104] S. V. Roth, G. Santoro, J. F. H. Risch, S. Yu, M. Schwartzkopf, T. Boese, R. Döhrmann, P. Zhang, B. Besner, P. Bremer, D. Rukser, M. A. Rübhausen, N. J. Terrill, P. A. Staniec, Y. Yao, E. Metwalli, and P. Müller-Buschbaum, "Patterned diblock co-polymer thin films as templates for advanced anisotropic metal nanos-

tructures," *ACS Applied Materials & Interfaces*, vol. 7, no. 23, pp. 12470–12477, 2015.

[105] M. Karunakaran, S. P. Nunes, X. Qiu, H. Yu, and K.-V. Peinemann, "Isoporous ps-b-peo ultrafiltration membranes via self-assembly and water-induced phase separation," *Journal of Membrane Science*, vol. 453, pp. 471–477, 2014.

[106] J. Hahn, V. Filiz, S. Rangou, J. Clodt, A. Jung, K. Buhr, C. Abetz, and V. Abetz, "Structure formation of integral-asymmetric membranes of polystyrene -block -pol y (ethylene oxide)," *Journal of Polymer Science Part B: Polymer Physics*, vol. 51, no. 4, pp. 281–290, 2013.

[107] K.-V. Peinemann, V. Abetz, and P. F. W. Simon, "Asymmetric superstructure formed in a block copolymer via phase separation," *Nature Materials*, vol. 6, no. 12, pp. 992–996, 2007.

[108] V. Abetz, "Isoporous block copolymer membranes," *Macromolecular Rapid Communications*, vol. 36, no. 1, pp. 10–22, 2015.

[109] B. B. Lakshmi, C. J. Patrissi, and C. R. Martin, "Sol−gel template synthesis of semiconductor oxide micro- and nanostructures," *Chemistry of Materials*, vol. 9, no. 11, pp. 2544–2550, 1997.

[110] K. Sarkar, E. V. Braden, T. Fröschl, N. Hüsing, and P. Müller-Buschbaum, "Spray-deposited zinc titanate films obtained via sol–gel synthesis for application in dye-sensitized solar cells," *Journal of Materials Chemistry A*, vol. 2, no. 36, pp. 15008–15014, 2014.

[111] R. Hosemann and S. N. Bagchi, "The interference theory of ideal paracrystals," *Acta Crystallographica*, vol. 5, no. 5, pp. 612–614, 1952.

[112] M. A. Green, Y. Hishikawa, W. Warta, E. D. Dunlop, D. H. Levi, J. Hohl-Ebinger, and A. W. Ho-Baillie, "Solar cell efficiency tables (version 50)," *Progress in Photovoltaics: Research and Applications*, vol. 25, no. 7, pp. 668–676, 2017.

[113] L. Song, W. Wang, V. Körstgens, D. M. González, Y. Yao, N. K. Minar, J. M. Feckl, K. Peters, T. Bein, D. Fattakhova-Rohlfing, G. Santoro, S. V. Roth, and P. Müller-Buschbaum, "Spray deposition of titania films with incorporated crystalline nanoparticles for all-solid-state dye-sensitized solar cells using p3ht," *Advanced Functional Materials*, vol. 26, no. 10, pp. 1498–1506, 2016.

[114] L. Song, W. Wang, V. Körstgens, D. Moseguí González, F. C. Löhrer, C. J. Schaffer, J. Schlipf, K. Peters, T. Bein, D. Fattakhova-Rohlfing, S. V. Roth, and P. Müller-Buschbaum, "In situ study of spray deposited titania photoanodes for scalable fabrication of solid-state dye-sensitized solar cells," *Nano Energy*, vol. 40, pp. 317–326, 2017.

[115] B. Su, H. A. Caller-Guzman, V. Körstgens, Y. Rui, Y. Yao, N. Saxena, G. Santoro, S. V. Roth, and P. Müller-Buschbaum, "Macroscale and nanoscale morphology evolution during in situ spray coating of titania films for perovskite solar cells," *ACS Applied Materials & Interfaces*, vol. 9, no. 50, pp. 43724–43732, 2017.

[116] A. Buffet, A. Rothkirch, R. Döhrmann, V. Körstgens, M. M. Abul Kashem, J. Perlich, G. Herzog, M. Schwartzkopf, R. Gehrke, P. Müller-Buschbaum, and S. V. Roth, "P03, the microfocus and nanofocus x-ray scattering (minaxs) beamline of the petra iii storage ring: the microfocus endstation," *Journal of Synchrotron Radiation*, vol. 19, no. Pt 4, pp. 647–653, 2012.

[117] J. Y. Ying, J. B. Benziger, and A. Navrotsky, "Structural evolution of alkoxide silica gels to glass: Effect of catalyst ph," *Journal of the American Chemical Society*, vol. 76, no. 10, pp. 2571–2582, 1993.

[118] A. L. Patterson, "The scherrer formula for x-ray particle size determination," *Physical Review*, vol. 56, no. 10, pp. 978–982, 1939.

[119] A. E. Hetzenecker, *Hybrid photovoltaics based on diblock copolymer structured, mesoporous germanium thin films*. Master's thesis, Technische Universität München, München, 28.08.2017.

[120] A. Stein, "Materials science: Germanium takes holey orders," *Nature*, vol. 441, no. 7097, pp. 1055–1056, 2006.

[121] A. P. Alivisatos, "Semiconductor clusters, nanocrystals, and quantum dots," *Science*, vol. 271, no. 5251, pp. 933–937, 1996.

[122] T. Waitz, T. Wagner, T. Sauerwald, C.-D. Kohl, and M. Tiemann, "Ordered mesoporous in2o3: Synthesis by structure replication and application as a methane gas sensor," *Advanced Functional Materials*, vol. 19, no. 4, pp. 653–661, 2009.

[123] T. F. Fässler, "Germanium(cf136): A new crystalline modification of germanium with the porous clathrate-ii structure," *Angewandte Chemie International Edition*, vol. 46, no. 15, pp. 2572–2575, 2007.

[124] S. C. Warren, F. J. DiSalvo, and U. Wiesner, "Nanoparticle-tuned assembly and disassembly of mesostructured silica hybrids," *Nature Materials*, vol. 6, no. 2, pp. 156–161, 2007.

[125] T. Gerfin, M. Grätzel, and L. Walder, "Molecular and supramolecular surface modification of nanocrystalline tio2 films: Charge-separating and charge-injecting devices," in *Molecular level artificial photosynthetic materials* (G. J. Meyer, ed.), vol. 109 of *Progress in Inorganic Chemistry*, pp. 345–393, New York: John Wiley & Sons, 1997.

[126] E. L. Crepaldi, G. J. d. A. A. Soler-Illia, D. Grosso, F. Cagnol, F. Ribot, and C. Sanchez, "Controlled formation of highly organized mesoporous titania thin films: from mesostructured hybrids to mesoporous nanoanatase tio2," *Journal of the American Chemical Society*, vol. 125, no. 32, pp. 9770–9786, 2003.

[127] A. C. Finnefrock, R. Ulrich, A. Du Chesne, C. C. Honeker, K. Schumacher, K. K. Unger, S. M. Gruner, and U. Wiesner, "Metal oxide containing mesoporous silica with bicontinuous "plumber's nightmare" morphology from a block copolymer-hybrid mesophase," *Angewandte Chemie International Edition*, vol. 40, no. 7, pp. 1207–1211, 2001.

[128] M. C. Orilall and U. Wiesner, "Block copolymer based composition and morphology control in nanostructured hybrid materials for energy conversion and storage: solar cells, batteries, and fuel cells," *Chemical Society Reviews*, vol. 40, no. 2, pp. 520–535, 2011.

[129] R. Shenhar, T. B. Norsten, and V. M. Rotello, "Polymer-mediated nanoparticle assembly: Structural control and applications," *Advanced Materials*, vol. 17, no. 6, pp. 657–669, 2005.

[130] M. Rawolle, M. A. Niedermeier, G. Kaune, J. Perlich, P. Lellig, M. Memesa, Y.-J. Cheng, J. S. Gutmann, and P. Müller-Buschbaum, "Fabrication and characterization of nanostructured titania films with integrated function from inorganic-organic hybrid materials," *Chemical Society Reviews*, vol. 41, no. 15, pp. 5131–5142, 2012.

[131] Y. Wang, K. Xie, X. Guo, W. Zhou, G. Song, and S. Cheng, "Mesoporous silica nanoparticles as high performance anode materials for lithium-ion batteries," *New Journal of Chemistry*, vol. 40, no. 10, pp. 8202–8205, 2016.

[132] H. Jung, P. K. Allan, Y.-Y. Hu, O. J. Borkiewicz, X.-L. Wang, W.-Q. Han, L.-S. Du, C. J. Pickard, P. J. Chupas, K. W. Chapman, A. J. Morris, and C. P. Grey, "Elucidation of the local and long-range structural changes that occur in germanium anodes in lithium-ion batteries," *Chemistry of Materials*, vol. 27, no. 3, pp. 1031–1041, 2015.

[133] C. S. Fuller and J. C. Severiens, "Mobility of impurity ions in germanium and silicon," *Physical Review*, vol. 96, no. 1, pp. 21–24, 1954.

[134] M. Zeilinger and T. F. Fässler, "Structural and thermodynamic similarities of phases in the li-tt (tt = si, ge) systems: redetermination of the lithium-rich side of the li-ge phase diagram and crystal structures of li17si4.0-xgex for x = 2.3, 3.1, 3.5, and 4 as well as li4.1ge," *Dalton transactions*, vol. 43, no. 40, pp. 14959–14970, 2014.

[135] T. K. Purkait, A. K. Swarnakar, G. B. de Los Reyes, F. A. Hegmann, E. Rivard, and J. G. C. Veinot, "One-pot synthesis of functionalized germanium nanocrystals from a single source precursor," *Nanoscale*, vol. 7, no. 6, pp. 2241–2244, 2015.

[136] A. Dowd, R. G. Elliman, and B. Luther-Davies, "Linear optical properties of ge nanocrystals in silica," *Applied Physics Letters*, vol. 79, no. 15, pp. 2327–2329, 2001.

[137] M. Amato, M. Palummo, R. Rurali, and S. Ossicini, "Silicon-germanium nanowires: Chemistry and physics in play, from basic principles to advanced applications," *Chemical Reviews*, vol. 114, no. 2, pp. 1371–1412, 2014.

[138] H. C. Choi and J. M. Buriak, "Preparation and functionalization of hydride terminated porous germanium," *Chemical Communications*, no. 17, pp. 1669–1670, 2000.

[139] C. Fang, H. Föll, and J. Carstensen, "Electrochemical pore etching in germanium," *Journal of Electroanalytical Chemistry*, vol. 589, no. 2, pp. 259–288, 2006.

[140] S. Scharfe, F. Kraus, S. Stegmaier, A. Schier, and T. F. Fässler, "Zintl ions, cage compounds, and intermetalloid clusters of group 14 and group 15 elements," *Angewandte Chemie International Edition*, vol. 50, no. 16, pp. 3630–3670, 2011.

[141] G. S. Armatas and M. G. Kanatzidis, "Mesostructured germanium with cubic pore symmetry," *Nature*, vol. 441, no. 7097, pp. 1122–1125, 2006.

[142] P. N. Trikalitis, K. K. Rangan, T. Bakas, and M. G. Kanatzidis, "Varied pore organization in mesostructured semiconductors based on the snse4(4-) anion," *Nature*, vol. 410, no. 6829, pp. 671–675, 2001.

[143] N. Chandrasekharan and S. C. Sevov, "Anodic electrodeposition of germanium films from ethylenediamine solutions of deltahedral ge9 4 − zintl ions," *Journal of The Electrochemical Society*, vol. 157, no. 4, pp. C140–C145, 2010.

[144] S. D. Korlann, A. E. Riley, B. S. Mun, and S. H. Tolbert, "Chemical tuning of the electronic properties of nanostructured semiconductor films formed through surfactant templating of zintl cluster," *The Journal of Physical Chemistry C*, vol. 113, no. 18, pp. 7697–7705, 2009.

[145] X. Meng, R. Al-Salman, J. Zhao, N. Borissenko, Y. Li, and F. Endres, "Electrodeposition of 3d ordered macroporous germanium from ionic liquids: a feasible method to make photonic crystals with a high dielectric constant," *Angewandte Chemie International Edition*, vol. 48, no. 15, pp. 2703–2707, 2009.

[146] J. J. Yeh and I. Lindau, "Atomic subshell photoionization cross sections and asymmetry parameters: $1 \leq z \leq 103$," *Atomic Data and Nuclear Data Tables*, vol. 32, no. 1, pp. 1–155, 1985.

[147] C. O. Chui, D.-I. Lee, A. A. Singh, P. A. Pianetta, and K. C. Saraswat, "Zirconia-germanium interface photoemission spectroscopy using synchrotron radiation," *Journal of Applied Physics*, vol. 97, no. 11, p. 113518, 2005.

[148] D. A. Shirley, "High-resolution x-ray photoemission spectrum of the valence bands of gold," *Physical Review B*, vol. 5, no. 12, pp. 4709–4714, 1972.

[149] G. Hollinger, P. Kumurdjian, J. M. Mackowski, P. Pertosa, L. Porte, and T. M. Duc, "Esca study of molecular ges3-x tex as2 glasses," *Journal of Electron Spectroscopy and Related Phenomena*, vol. 5, no. 1, pp. 237–245, 1974.

[150] M. F. Ebel and H. Ebel, "About the charging effect in x-ray photoelectron spectrometry," *Journal of Electron Spectroscopy and Related Phenomena*, vol. 3, no. 3, pp. 169–180, 1974.

[151] D. Chi, C. O. Chui, K. C. Saraswat, B. B. Triplett, and P. C. McIntyre, "Zirconia grown by ultraviolet ozone oxidation on germanium (100) substrates," *Journal of Applied Physics*, vol. 96, no. 1, pp. 813–819, 2004.

[152] W. E. Morgan and J. R. van Wazer, "Binding energy shifts in the x-ray photoelectron spectra of a series of related group iva compounds," *The Journal of Physical Chemistry*, vol. 77, no. 7, pp. 964–969, 1973.

[153] K. Prabhakaran and T. Ogino, "Oxidation of ge(100) and ge(111) surfaces: an ups and xps study," *Surface Science*, vol. 325, no. 3, pp. 263–271, 1995.

[154] N. M. Bom, G. V. Soares, S. Hartmann, A. Bordin, and C. Radtke, "Geo 2 /ge structure submitted to annealing in deuterium: Incorporation pathways and associated oxide modifications," *Applied Physics Letters*, vol. 105, no. 14, p. 141605, 2014.

[155] D. Wang, Y.-L. Chang, Q. Wang, J. Cao, D. B. Farmer, R. G. Gordon, and H. Dai, "Surface chemistry and electrical properties of germanium nanowires," *Journal of the American Chemical Society*, vol. 126, no. 37, pp. 11602–11611, 2004.

[156] Z. C. Lei, K. H. Goh, N. I. Zainal Abidin, and Y. H. Wong, "Effect of oxidation temperature on physical and electrical properties of zro 2 thin-film gate oxide on ge substrate," *Thin Solid Films*, vol. 642, pp. 352–358, 2017.

[157] S. Ech-Cherif El Kettani, M. Lazraq, H. Ranaivonjatovo, J. Escudié, H. Gornitzka, and F. Ouhsaine, "Versatile reactivity of the germene mes2ge=cr2 toward esters and related carbonyl derivatives," *Organometallics*, vol. 26, no. 15, pp. 3729–3734, 2007.

[158] L. Li, T. Fukawa, T. Matsuo, D. Hashizume, H. Fueno, K. Tanaka, and K. Tamao, "A stable germanone as the first isolated heavy ketone with a terminal oxygen atom," *Nature Chemistry*, vol. 4, no. 5, p. 361, 2012.

[159] Z. X. Xie, S. Z. Hu, Z. H. Chen, S. A. Li, and W. P. Shi, "Redetermination of the structure of polymeric carboxyethylgermanium sesquioxide," *Acta Crystallographica Section C Crystal Structure Communications*, vol. 49, no. 6, pp. 1154–1156, 1993.

[160] T. Yamanaka and K. Ogata, "Structure refinement of geo2 polymorphs at high pressures and temperatures by energy-dispersive spectra of powder diffraction," *Journal of Applied Crystallography*, vol. 24, no. 2, pp. 111–118, 1991.

[161] D. S. Müller, *Synthesis and Characterization of Novel, Mesoporous Ge Thin Films for Li-Ion Battery Applications*. Bachelor's thesis, Technische Universität München, München, 18.09.2018.

[162] N. Hohn, X. Wang, M. A. Giebel, D. S. Müller, A. E. Hetzenecker, L. Bießmann, L. P. Kreuzer, G. E. Möhl, H. Yu, J. G. C. Veinot, T. F. Fässler, Y.-J. Cheng, and P. Müller-Buschbaum, "Mesoporous geo2/ge/c as highly reversible anode material with high specific capacity for lithium ion batteries," *Nat. Mater. (in preparation)*, 2019.

[163] X. Zuo, J. Zhu, P. Müller-Buschbaum, and Y.-J. Cheng, "Silicon based lithium-ion battery anodes: A chronicle perspective review," *Nano Energy*, vol. 31, pp. 113–143, 2017.

[164] J. F. M. Oudenhoven, L. Baggetto, and P. H. L. Notten, "All-solid-state lithium-ion microbatteries: A review of various three-dimensional concepts," *Advanced Energy Materials*, vol. 1, no. 1, pp. 10–33, 2011.

[165] T. Kennedy, M. Brandon, and K. M. Ryan, "Advances in the application of silicon and germanium nanowires for high-performance lithium-ion batteries," *Advanced Materials*, vol. 28, no. 27, pp. 5696–5704, 2016.

[166] M.-H. Park, Y. Cho, K. Kim, J. Kim, M. Liu, and J. Cho, "Germanium nanotubes prepared by using the kirkendall effect as anodes for high-rate lithium batteries," *Angewandte Chemie International Edition*, vol. 50, no. 41, pp. 9647–9650, 2011.

[167] S. Wu, C. Han, J. Iocozzia, M. Lu, R. Ge, R. Xu, and Z. Lin, "Germanium-based nanomaterials for rechargeable batteries," *Angewandte Chemie International Edition*, vol. 55, no. 28, pp. 7898–7922, 2016.

[168] L. Ji, Z. Lin, M. Alcoutlabi, and X. Zhang, "Recent developments in nanostructured anode materials for rechargeable lithium-ion batteries," *Energy & Environmental Science*, vol. 4, no. 8, p. 2682, 2011.

[169] M.-H. Park, M. G. Kim, J. Joo, K. Kim, J. Kim, S. Ahn, Y. Cui, and J. Cho, "Silicon nanotube battery anodes," *Nano Letters*, vol. 9, no. 11, pp. 3844–3847, 2009.

[170] M. Aghajamali, H. Xie, M. Javadi, W. P. Kalisvaart, J. M. Buriak, and J. G. C. Veinot, "Size and surface effects of silicon nanocrystals in graphene aerogel composite anodes for lithium ion batteries," *Chemistry of Materials*, vol. 30, no. 21, pp. 7782–7792, 2018.

[171] C. P. Grey and J. M. Tarascon, "Sustainability and in situ monitoring in battery development," *Nature Materials*, vol. 16, no. 1, pp. 45–56, 2016.

[172] Y.-K. Sun, Z. Chen, H.-J. Noh, D.-J. Lee, H.-G. Jung, Y. Ren, S. Wang, C. S. Yoon, S.-T. Myung, and K. Amine, "Nanostructured high-energy cathode materials for advanced lithium batteries," *Nature Materials*, vol. 11, no. 11, pp. 942–947, 2012.

[173] A. R. Armstrong, G. Armstrong, J. Canales, R. García, and P. G. Bruce, "Lithium-ion intercalation into tio2-b nanowires," *Advanced Materials*, vol. 17, no. 7, pp. 862–865, 2005.

[174] S. Yin, D. Zhao, Q. Ji, Y. Xia, S. Xia, X. Wang, M. Wang, J. Ban, Y. Zhang, E. Metwalli, X. Wang, Y. Xiao, X. Zuo, S. Xie, K. Fang, S. Liang, L. Zheng, B. Qiu, Z. Yang, Y. Lin, L. Chen, C. Wang, Z. Liu, J. Zhu, P. Müller-Buschbaum, and Y.-J. Cheng, "Si/ag/c nanohybrids with in situ incorporation of super-small silver nanoparticles: Tiny amount, huge impact," *ACS Nano*, vol. 12, no. 1, pp. 861–875, 2018.

[175] X. Zuo, X. Wang, Y. Xia, S. Yin, Q. Ji, Z. Yang, M. Wang, X. Zheng, B. Qiu, Z. Liu, J. Zhu, P. Müller-Buschbaum, and Y.-J. Cheng, "Silicon/carbon lithium-ion battery anode with 3d hierarchical macro-/mesoporous silicon network: Self-templating synthesis via magnesiothermic reduction of silica/carbon composite," *Journal of Power Sources*, vol. 412, pp. 93–104, 2019.

[176] Y. Wang and G. Cao, "Developments in nanostructured cathode materials for high-performance lithium-ion batteries," *Advanced Materials*, vol. 20, no. 12, pp. 2251–2269, 2008.

[177] X. Ji, K. T. Lee, and L. F. Nazar, "A highly ordered nanostructured carbon-sulphur cathode for lithium-sulphur batteries," *Nature Materials*, vol. 8, no. 6, pp. 500–506, 2009.

[178] N. Yan, F. Wang, H. Zhong, Y. Li, Y. Wang, L. Hu, and Q. Chen, "Hollow porous sio2 nanocubes towards high-performance anodes for lithium-ion batteries," *Scientific Reports*, vol. 3, p. 1568, 2013.

[179] L. Y. Beaulieu, K. W. Eberman, R. L. Turner, L. J. Krause, and J. R. Dahn, "Colossal reversible volume changes in lithium alloys," *Electrochemical and Solid-State Letters*, vol. 4, no. 9, p. A137, 2001.

[180] H. Ma, F. Cheng, J.-Y. Chen, J.-Z. Zhao, C.-S. Li, Z.-L. Tao, and J. Liang, "Nest-like silicon nanospheres for high-capacity lithium storage," *Advanced Materials*, vol. 19, no. 22, pp. 4067–4070, 2007.

[181] C. K. Chang, H. Peng, G. Liu, K. McIlwrath, X. F. Zhang, R. A. Huggins, and Y. Cui, "High-performance lithium battery anodes using silicon nanowires," *Nature Nanotechnology*, vol. 3, no. 1, p. 31, 2008.

[182] A. Esmanski and G. A. Ozin, "Silicon inverse-opal-based macroporous materials as negative electrodes for lithium ion batteries," *Advanced Functional Materials*, vol. 19, no. 12, pp. 1999–2010, 2009.

[183] H. Jia, P. Gao, J. Yang, J. Wang, Y. Nuli, and Z. Yang, "Novel three-dimensional mesoporous silicon for high power lithium-ion battery anode material," *Advanced Energy Materials*, vol. 1, no. 6, pp. 1036–1039, 2011.

[184] Z. Ni, Q. Liu, K. Tang, J. Zheng, J. Zhou, R. Qin, Z. Gao, D. Yu, and J. Lu, "Tunable bandgap in silicene and germanene," *Nano Letters*, vol. 12, no. 1, pp. 113–118, 2012.

[185] G. Cui, L. Gu, L. Zhi, N. Kaskhedikar, P. A. van Aken, K. Müllen, and J. Maier, "A germanium-carbon nanocomposite material for lithium batteries," *Advanced Materials*, vol. 20, no. 16, pp. 3079–3083, 2008.

[186] A. M. Chockla, K. C. Klavetter, C. B. Mullins, and B. A. Korgel, "Solution-grown germanium nanowire anodes for lithium-ion batteries," *ACS Applied Materials & Interfaces*, vol. 4, no. 9, pp. 4658–4664, 2012.

[187] J. S. Peña, I. Sandu, O. Joubert, F. S. Pascual, C. O. Areán, and T. Brousse, "Electrochemical reaction between lithium and beta-quartz geo2," *Electrochemical and Solid-State Letters*, vol. 7, no. 9, p. A278, 2004.

[188] S. D. Lacey, D. J. Kirsch, Y. Li, J. T. Morgenstern, B. C. Zarket, Y. Yao, J. Dai, L. Q. Garcia, B. Liu, T. Gao, S. Xu, S. R. Raghavan, J. W. Connell, Y. Lin, and L. Hu, "Extrusion-based 3d printing of hierarchically porous advanced battery electrodes," *Advanced Materials*, vol. 30, no. 12, p. e1705651, 2018.

[189] P. Müller-Buschbaum, "Grazing incidence small-angle x-ray scattering: an advanced scattering technique for the investigation of nanostructured polymer films," *Analytical and bioanalytical chemistry*, vol. 376, no. 1, pp. 3–10, 2003.

[190] D.-M. Smilgies, P. Busch, C. M. Papadakis, and D. Posselt, "Characterization of polymer thin films with small–angle x–ray scattering under grazing incidence (gisaxs)," *Synchrotron Radiation News*, vol. 15, no. 5, pp. 35–42, 2002.

[191] E. Patyk-Kaźmierczak, M. R. Warren, D. R. Allan, and A. Katrusiak, "Pressure inverse solubility and polymorphism of an edible gamma-cyclodextrin-based metal-organic framework," *Physical Chemistry Chemical Physics*, vol. 19, no. 13, pp. 9086–9091, 2017.

[192] G. Lucovsky, S. S. Chao, J. Yang, J. E. Tyler, R. C. Ross, and W. Czubatyj, "Chemical bonding of hydrogen and oxygen in glow-discharge–deposited thin films of a-ge:h and a-ge:(h,o)," *Physical Review B*, vol. 31, no. 4, p. 2190, 1985.

[193] G. Guisbiers, O. van Overschelde, and M. Wautelet, "Theoretical investigation of size and shape effects on the melting temperature and energy bandgap of tio2 nanostructures," *Applied Physics Letters*, vol. 92, no. 10, p. 103121, 2008.

[194] F. Guelle, *Novel structuring routine of germanium films for application in photovoltaics*. Master's thesis, Technische Universität München and Faculté des sciences de Montpellier, München and Montpellier, 03.07.2017.

[195] J. Schmitt, *Fundamental Characterization of Thin Films Based on a Novel Heavy Element Containing Small Molecule for Photovoltaic Applications*. Bachelor's thesis, Technische Universität München, München, 01.08.2018.

[196] R. Märkl, *Next generation hybrid solar cells based on heavy element containing small molecule and high-performance polymer PTB7-th (working title)*. Master's thesis (in preparation), Technische Universität München, München, 2019.

List of publications

Publications related to the dissertation

- N. Hohn, S. J. Schlosser, L. Bießmann, S. Grott, S. Xia, K. Wang, M. Schwartzkopf, S. V. Roth, P. Müller-Buschbaum, "Readily available titania nanostructuring routines based on mobility and polarity controlled phase separation of an amphiphilic diblock copolymer", *Nanoscale*, 10(11), 5325-5334, 2018.
- N. Hohn, S. J. Schlosser, L. Bießmann, L. Song, S. Grott, S. Xia, K. Wang, M. Schwartzkopf, S. V. Roth, P. Müller-Buschbaum, "Impact of Catalytic Additive on Spray Deposited and Nanoporous Titania Thin Films Observed via in Situ X-ray Scattering: Implications for Enhanced Photovoltaics", *ACS Appl. Nano Mater.*, 1(8), 4227-4235, 2018.
- N. Hohn, A. E. Hetzenecker, M. A. Giebel, S. Geier, L. Bießmann, V. Körstgens, N. Saxena J. Schlipf, W. Ohm, P. S. Deimel, F. Allegretti, J. V. Barth, S. V. Roth, T. F. Fässler, P. Müller-Buschbaum, "Amphiphilic diblock copolymer-mediated structure control in nanoporous germanium-based thin films", *Nanoscale*, 11, 2048-2055, 2019.
- N. Hohn, X. Wang, M. A. Giebel, D. Müller, A. E. Hetzenecker, L. Bießmann, L. P. Kreuzer, G. E. Möhl, H. Yu, J. G. C. Veinot, T. F. Fässler, Y. Cheng, P. Müller-Buschbaum, "Mesoporous GeO_2/Ge/C as Highly Reversible Anode Material with High Specific Capacity for Lithium Ion Batteries", *Nat. Mater.*, in preparation, 2019.

Further publications

- L. Song, M. Rawolle, N. Hohn, J. S. Gutmann, H. Frielinghaus, P. Müller-Buschbaum, "Deformation of Mesoporous Titania Nanostructures in Contact with D2O Vapor", *Small*, 14(30), 1801461, 2018.

- K. Wang, S. Xia, W. Cao, N. Hohn, S. Grott, L. P. Kreuzer, M. Schwartzkopf, S. V. Roth, P. Müller-Buschbaum, "Comparison of UV Irradiation and Sintering on Mesoporous Spongelike ZnO Films Prepared from PS-b-P4VP Templated Sol–Gel Synthesis", *ACS Appl. Nano Mater.*, 1(12), 7139-7148, 2018.
- K. Wang, V. Körstgens, D. Yang, N. Hohn, S. V. Roth, P. Müller-Buschbaum, "Morphology control of low temperature fabricated ZnO nanostructures for transparent active layers in all solid-state dye-sensitized solar cells", *J. Mater. Chem. A*, 6(10), 4405-4415, 2018.
- L. Bießmann, L. P. Kreuzer, T. Widmann, N. Hohn, J. F. Moulin, P. Müller-Buschbaum, "Monitoring the Swelling Behavior of PEDOT: PSS Electrodes under High Humidity Conditions", *ACS Appl. Mat. & Int.*, 10(11), 9865-9872, 2018.
- L. Bießmann, N. Saxena, N. Hohn, Md A. Hossain, J. G. C. Veinot, P. Müller-Buschbaum, "Highly Conducting, Transparent PEDOT: PSS Polymer Electrodes from Post-Treatment with Weak and Strong Acids", *Adv. Electron. Mater.*, 1800654, 2019.
- J. Schlipf, Y. Hu, S. Pratap, L. Bießmann, N. Hohn, L. Porcar, T. Bein, P. Docampo, P. Müller-Buschbaum, "Shedding Light on the Moisture Stability of 3D/2D Hybrid Perovskite Heterojunction Thin Films", *ACS Appl. Energy Mater.*, accepted, 2019, doi: 10.1021 / acsaem.9b00005.
- S. Xia, L. Song, N. Hohn, K. Wang, S. Grott, M. Opel, M. Schwartzkopf, S. V. Roth, P. Müller-Buschbaum, "Spray-Coating Magnetic Thin Hybrid Films of PS-b-PNIPAM and Magnetite Nanoparticles", *Adv. Funct. Mater.*, accepted, 2019, doi: 10.1002 / adfm.201808427.

Scientific reports, cover pictures and certificates

- N. Hohn, W. Ohm, M. Boone, E. Rivard, S. V. Roth, P. Müller-Buschbaum, "Investigation of novel materials for hybrid photovoltaic applications using sol-gel chemistry for mesoscale-structural control", *Lehrstuhl für Funktionelle Materialien, Annual Report*, 2016.
- N. Hohn, "Chapter cover picture", *Lehrstuhl für Funktionelle Materialien, Annual Report*, 2016.
- N. Hohn, "Certificate of Recognition for ACS Reviewing Activities", *ACS Publications*, 2016.

- N. Hohn, S. J. Schlosser, P. Müller-Buschbaum, "Impact of precursor concentration on crystallinity and nanostructure of titanium dioxide in diblock copolymer templated sol-gel processes", *Lehrstuhl für Funktionelle Materialien, Annual Report*, 2017.
- N. Hohn, "Cover picture", *Lehrstuhl für Funktionelle Materialien, Annual Report*, 2017.
- N. Hohn, S. Grott, S. Xia, K. Wang, P. Müller-Buschbaum, "Experimental report for DESY beamtime: In-situ spray coating of novel Germanium nano-structures for photovoltaic applications", *DESY*, 2017.
- N. Hohn, T. Widmann, L. P. Kreuzer, K. Wang, M. Haese, J. F. Moulin, P. Müller-Buschbaum, "Experimental report to proposal no. 11287: Inorganic-organic hybrid photovoltaic solar cells using hybrid materials", *Heinz Maier-Leibnitz Zentrum*, 2017.
- N. Hohn, P. Müller-Buschbaum, "ATUMS individual report by doctoral researcher: Tuning the interface of hybrid solar cells through structural investigation of novel materials", *ATUMS, DFG*, 2018.
- N. Hohn, P. Müller-Buschbaum, "ATUMS 1.2 report for DFG: Inorganic-organic hybrid photovoltaic solar cells using novel hybrid materials", *ATUMS, DFG*, 2018.
- N. Hohn, P. Müller-Buschbaum "ATUMS renewal application; project 1-2: Investigation of novel inorganic-organic hybrid materials for application in next generation solar cells", *ATUMS, DFG*, 2018.
- N. Hohn, T. Widmann, L. P. Kreuzer, M. Pomm, M. Haese, P. Müller-Buschbaum, "Experimental report to proposal no. 13682: Size-effect of Te core small molecules on the efficiency of backfilling titania nanostructures", *Heinz Maier-Leibnitz Zentrum*, 2018.
- N. Hohn, S. J. Schlosser, L. Bießmann, L. Song, S. Grott, S. Xia, K. Wang, M. Schwartzkopf, S. V. Roth, P. Müller-Buschbaum, "Impact of catalytic additive on spray deposited and nanoporous titania thin films observed via *in situ* X-ray scattering: implications for enhanced photovoltaics", *Lehrstuhl für Funktionelle Materialien, Annual Report*, 2018.

Talks

- N. Hohn, M. A. Giebel, M. Boone, E. Rivard, T. F. Fässler, P. Müller-Buschbaum, "Novel materials and structuring routines for hybrid solar cells" *Semi-Annual Meet-*

ing of Alberta/Technical University of Munich International Graduate School, Chemistry Department, TU München, Germany, April 2016.

- N. Hohn, "Novel Materials for Hybrid Solar Cells", *Seminar talk*, Chair for Functional Materials, Physics-Department, TU München, Germany, June 2016.
- N. Hohn, F. Löhrer, M. Čorić, "Organic Solar Cells", *Polymer Physics Summer School 2016*, Obertauern, Austria, June 2016.
- N. Hohn, P. Müller-Buschbaum, "Novel Materials for Hybrid Solar Cells" *Annual Meeting of Alberta/Technical University of Munich International Graduate School*, Raitenhaslach, Germany, November 2016.
- N. Hohn, M. Boone, E. Rivard, P. Müeller-Buschbaum, "Investigation of novel material systems for hybrid photovoltaics - alternatives for the paradigm", *DPG-Frühjahrstagung*, Dresden, Germany, March 2017.
- N. Hohn, S. Schlosser, L. Bießmann, S. Xia, P. Müller-Buschbaum, "Readily accessible structuring routines for hybrid materials", *3rd Internal Biennial Science Meeting of the MLZ*, Grainau, Germany, June 2017.
- N. Hohn, P. Müller-Buschbaum, "Amphiphilic diblock copolymer templating for mesoporous thin film structuring investigated via GISAXS", *Annual Meeting of Alberta/Technical University of Munich International Graduate School*, Jasper, Canada, November 2017.
- N. Hohn, "From physics to chemistry – Investigation of nanostructured materials and introduction to synthesis of pi-extended Te-based molecules" *Seminar Talk in Rivard Group*, UofA, Edmonton, Canada, December 2017.
- N. Hohn, S. J. Schlosser, L. Bießmann, S. Grott, S. Xia, K. Wang, M. Schwartzkopf, S. V. Roth, P. Müller-Buschbaum, "Investigation of mobility controlled amphiphilic diblock copolymer templating for hybrid photovoltaic applications", *DPG-Frühjahrstagung*, Berlin, Germany, March 2018.
- N. Hohn, "Inorganic-organic hybrid photovoltaic solar cells using novel hybrid materials", *Seminar talk*, Chair for Functional Materials, Physics-Department, TU München, Germany, Mai 2018.
- N. Hohn, M. Giebel, S. J. Schlosser, A. E. Hetzenecker, L. Bießmann, S. Grott, S. Xia, K. Wang, M. Schwartzkopf, S. V. Roth, T. F. Fässler, P. Müller-Buschbaum, "Approaching photovoltaic industry - Morphological tuning of inorganic thin films through amphiphilic diblock copolymer templating on the basis of large scale coating techniques", *Novel Concepts in Hybrid Structures*, Tutzing, Germany, Mai 2018.

- J. Heger, D. Yang, N. Hohn, "GISAXS/GIWAXS and GISANS/GIWANS", *Polymer Physics Summer School 2018*, Obertauern, Austria, June 2018.
- N. Hohn, P. Müller-Buschbaum, "Diblock Copolymer Templating – A Powerful Tool for Versatile Nanostructure Fabrication", *Annual Meeting of Alberta/Technical University of Munich International Graduate School*, Garching, Germany, November 2018.
- N. Hohn, P. Müller-Buschbaum, "Diblock Copolymer Templated Mesoporous TiO2/Ge Thin Films for Hybrid Photovoltaics and Energy Storage Applications", *Evaluation of IRTG 2022 ATUMS*, TU München, Garching, Germany, January 2019.

Poster presentations

- N. Hohn, L. Song, M. Boone, E. Rivard, P. Müller-Buschbaum, "Tuning the interface of hybrid thin films for photovoltaic applications", *DPG-Frühjahrstagung*, Regensburg, Germany, March 2016.
- N. Hohn, L. Bießmann, M. A. Giebel, M. Boone, E. Rivard, T. F. Fässler, P. Müller-Buschbaum, "Novel materials and structuring routines for HPV applications", *4th International SolTech Conference in Munich*, Munich, Germany, April 2016.
- N. Hohn, M. A. Giebel, M. Boone, E. Rivard, T. F. Fässler, P. Müller-Buschbaum, "Developing alternative material systems for energy conversion through hybrid photovoltaics", *6th Colloquium of the Munich School of Engineering*, TU München, Garching, Germany, July 2016.
- N. Hohn, M. A. Giebel, M. M. Bentlohner, D. Fattakhova-Rohlfing, T. F. Fässler, P. Müller-Buschbaum, "Ge_9-Zintl Clusters as Wet Chemical Precursors for macro- and mesoporous Ge-Films in Hybrid Solar Cells", *10th International Graduate School of Science and Engineering Forum*, Raitenhaslach, Germany, June 2016.
- N. Hohn, "Renewable Energies", *TUM Kick-off Seminar*, Raitenhaslach, Germany, May 2017.
- N. Hohn, M. A. Giebel, T. F. Fässler, P. Müller-Buschbaum, "Silylated Ge_9Si-Zintl Clusters as Wet Chemical Precursors for mesoporous Films in Hybrid Solar Cells", *11th International Graduate School of Science and Engineering Forum*, Raitenhaslach, Germany, May 2017.

- N. Hohn, F. Guelle, M. A. Giebel, M. Schwartzkopf, S. V. Roth, T. F. Fässler, P. Müller-Buschbaum, "Controlling the nano-morphology of inorganic thin films for efficient solar energy conversion", *7th Colloquium of the Munich School of Engineering*, Garching, Germany, July 2017.
- M. A. Giebel and N. Hohn, H. Schamoni, A. Lyuleeva, C. Ott, K. Rodewald, M. Narreto, C. Jensen, Md. A. Hossain, H. Yu, C. Braun, R. Kisslinger, D. Yang, M. Stutzmann, M. Becherer, T. Nilges, B. Rieger, F. Hegmann, J. Veinot, E. Rivard, K. Shankar, J. Buriak, T. F. Fässler, P. Müller-Buschbaum, "Investigation of novel inorganic-organic hybrid materials for application in next generation solar cells", *Evaluation of IRTG 2022 ATUMS*, TU München, Garching, Germany, January 2019.

Acknowledgments

I would like to start thanking Prof. Dr. Peter Müller-Buschbaum for entrusting me with the position of a PhD student at his chair. He gave me the possibility to work in diverse and exciting fields such as photovoltaics, lithium ion batteries, semiconductors, softmatter, X-ray and neutron scattering with special focus on nanostructures. Additionally, I am extremely grateful that Peter gave me the opportunity to experience many different conferences, highly intense beamtimes and a six months stay abroad at an international institution (UofA, Edmonton, Canada) to work in the field of chemistry. Many collaborations have led to colleagues becoming invaluable friends. Furthermore, I was responsible for advising a total of six students during my PhD period. So at some point I was advising a small group of young scientists. As a result, I was able to especially strengthen team-leadership, presentation skills and handling responsibility. I would like to express my gratitude, because I learned about my personal and professional strengths and I was able to further develop them. It is difficult to include all the unique experiences here which I made during my PhD thesis. During the whole period Peter gave me continuous feedback, which was invaluable for the success of the science coming out of the present thesis. I honestly had a great time with a lot of moments to positively remember. Thank you for this Peter.

I would like to thank many different persons in the following. Each of them was contributing to the success of the present thesis in their own individual way. Within this scope, no specific order is retained.

I am grateful to have worked with the now alumni Dr. Martin Niedermeier, Dr. Daniel Moseguí González, Dr. Claudia Maria Palumbiny, Dr. Christoph J. Schaffer, Dr. Bo Su, Dr. Konstantinos N. Raftopoulos, Dr. Lin Song, Dr. Johannes Schlipf and Dr. Nitin Saxena. I looked up to them and they were a constant source of scientific inspiration and motivation during discussions. Within this frame, Martin even continued to help me throughout my PhD student period as my mentor.

Mentoring a small group of students was one of the core elements to the success of the present thesis. Therefore, a big thank you goes to Andreas Erich Hetzenecker [119], Stef-

fen Johannes Schlosser [76], Fabien Guelle [194], David Müller [161], Jonas Schmitt [195] and Raphael Märkl [196]. All of you did an excellent job and I wish you all the best.

Many passionate and constructive discussions with Dr. Volker Körstgens, Lorenz Bießmann, Sebastian Grott, Lucas Kreuzer, Franziska Löhrer, Shambhavi Pratap, Simon J. Schaper, Kun Wang, Christian Weindl, Tobias Widmann, Senlin Xia, Dan Yang, Wei Chen, Wei Cao, Bart-Jan Niebuur and Florian Jung have led to new scientific perspectives to improve my knowledge in a certain field. I would like to thank all of you for helping me with obtaining new insights and for the wonderful time I had with you.

Thank you Peter S. Deimel, Dr. Francesco Allegretti and Prof. Dr. Johannes V. Barth for the joint X-ray photoelectron spectroscopy measurements and our efficient collaboration within the frame of nanostructuring Ge-based thin films.

Together with Michael A. Giebel, Dr. Sebastian Geier and Prof. Dr. Thomas F. Fässler I experienced my first and longest (∼3 years) collaboration. I am very grateful that a friendly and extremely constructive atmosphere was always maintained. Additionally, I am especially thankful for receiving almost inexhaustible amounts of the germanium precursor K_4Ge_9 and for the support during the publication process of germanium-related papers.

I want to thank Xiaoyan Wang and Prof. Yajun Cheng for testing of Ge-based Li ion half-cells and their continuous discussion of related affairs. Within this frame, a high efficiency email correspondence was maintained despite the long distance between China and Germany and due to the remarkable scientific commitment of Yajun.

I would like to thank Prof. Dr. Christine Papadakis for a good working climate at the Chair for Functional Materials and access to her labs. Her commitment with respect to motivating young scientists like my young cousin Leo Höhne are especially appreciated.

One main pillar of the success of the present thesis is the access to large scale scattering facilities. With no doubt the present thesis would not have been possible without the contribution of motivated beamline scientists like Dr. Matthias Schwartzkopf and Dr. Wiebke Ohm at DESY. Within this frame, special thanks go out to Marc Gensch, Calvin J. Brett and Jan Rubeck for their help in the design process of an *in situ* spray setup. Prof. Dr. Stephan V. Roth's invaluable contribution in both affairs (spray chamber design and beamtimes) is very much appreciated. His deep understanding of scattering physics combined with his approachable nature will always be positively remembered.

I enjoyed working with Dr. Jean-Francois Moulin, Dr. Gaetano Mangiapia, Martin Haese, Matthias Pomm and Dr. Sebastian Busch during time-of-flight grazing incidence small angle neutron scattering experiments at the RefSans instrument (FRMII). Friendly introduction sessions by Jean-Francois were especially helpful to approach the physics of

neutron scattering. The work of the local contact Dr. Lionel Porcar ensuring the success of a beamtime at the Institut Laue-Langevin (ILL) is also well-appreciated.

I am tremendously grateful for the opportunities provided by the Alberta/Technical University of Munich International Graduate School "Functional Hybrid Materials" (IRTG 2022), or in short the ATUMS program. I would like to thank Prof. Dr. Bernhard Rieger for having initiated the program together with Prof. Dr. Jonathan G. C. Veinot. Thanks to ATUMS coordinators Dr. Carsten Troll, Dr. Sergei Vagin and Leah Veinot for organizing conferences, seminars and their help with planning the stay abroad. Thanks to the ATUMS program, many inter-disciplinary collaborations with various groups were easily enabled. I am grateful for each of the following collaborations: Nanostructuring Ge-based thin films with Prof. Thomas F. Fässler and Michael A. Giebel, Investigation of SnIP with Prof. Dr. Tom Nilges and Dr. Claudia Ott, UV/Vis analysis of Ge-based thin films with Prof. Dr. Martin Stutzmann and Hannah Schamoni, XPS surface analysis of Ge-based thin films with Dr. Anna Cattani-Scholz and Dr. Reka Csiki, FET mobility measurements and investigation of SiNS-P3HT via scattering with Prof. Markus Becherer, Prof. Paolo Lugli and Dr. Alina Lyuleeva. I am furthermore grateful for the constant scientific feedback with respect to given talks during conferences and meetings especially by Prof. Dr. Tom Nilges, Prof. Dr. Vladimir Michaelis and Prof. Dr. Job Boekhoven in a relaxed atmosphere.

I enjoyed collaborating with and learning from Prof. Dr. Jonathan G. C. Veinot during my stay abroad at the University of Alberta (UofA). Due to his expertise and chemical analysis performed at his chair with the help of Haoyang Yu (Emmett) and Md Asjad Hossain, two publications have been enabled within this joint project. Thank you, Jon. I especially appreciate your approachable and uncomplicated, friendly nature. Additionally, I am grateful to Prof. Dr. Eric Rivard for hosting me at his chair at the UofA. I had an excellent time during my stay learning a lot about chemistry and how complex the synthesis of novel materials can be. This was a totally new experience to me. Special thanks go to Dr. Emanuel Hupf and Christina Braun for their patience and given introductions to the synthesis of tellurophenes at the Rivard group. I would like to additionally thank Prof. Dr. Frank Hegmann and Charles Jensen for enabling and teaching THz spectroscopy measurements. I also want to thank Prof. Dr. Karthik Shankar and Ryan Kisslinger for entrusting me with the GIWAXS measurements on TiO_2 nanotube samples and related discussions. In general, I feel very lucky that all of my many collaboration partners were dedicated, friendly and approachable people.

For an especially enjoyable time in Canada and during ATUMS annual meetings I would like to thank Christina Braun, Matthew Roy, Alvaro Omana, Jocelyn Sinclair, Ian Watson, Patrick Moon, Kevin Hooton, Bruno Luppi, Sarah Parke, Dr. Paul Lummis,

Charles Jensen, Dr. Felix Kaiser, Michael Giebel, Dr. Claudia Ott, Hannah Schamoni, Ebru A. Uezer, Raphael Grötsch, Josef Mock and Marc Kloberg.

Good science is difficult to achieve without constructive discussions with friendly colleagues during coffee breaks. Within this frame, I would like to additionally thank Christina Geiger, Julian Heger, Xinyu Jiang, Anna-Lena Oechsle, Lennart Reb and many other people, who have already been named and therefore won't get double credits. However, special credits for their relentless effort in terms of constructive scientific feedback on talks, discussions or just having a good time together is cordially awarded to the Herzig group with Dr. Jenny Lebert, Oliver Filonik, Mihael Coric, Dr. Stephan Pröller and Prof. Dr. Eva Maria Herzig.

For their contribution to an excellent atmosphere during annual summer BBQ celebrations or other events, the Polymer Music Band (PMB) with Dr. Johannes Schlipf, Dr. Jenny Lebert, Dr. Nitin Saxena, Chia-Hsin Ko, Lucas Kreuzer, Gilles Möhl, Julian Heger, Christina Geiger, Prof. Dr. Eva Maria Herzig, Dr. Claudia Maria Palumbiny and Dr. Christoph J. Schaffer is highly appreciated.

Furthermore, I would like to express my gratitude to Dr. Miriam Unger for NANO-IR demonstration measurements at the company Physical Electronics GmbH. It was interesting to see the power of AFM and IR spectroscopy combined in a single technique. Thank you Prof. Alexander Holleitner for granting access to the very essential SEM instrument at your chair.

The help of Marion Waletzki, Carola Kappauf and Susanna Fink with organizing many lively events such as summer schools, conferences, Wiesn visits or simply for helping getting travel expenses back is deeply appreciated. The technical support and the friendly breaks with Reinhold Funer will always be positively remembered. Thank you Dieter Müller for your support with software issues of all types.

A big thank you goes to the International Graduate School of Science and Engineering (IGSSE)-team Dr. Michael Klimke, Dr. Marco Barden, Dr. Tobias Bidon and Jo-Anna Küster for their help with all the organization.

I would like to further thank the funding agencies Deutsche Forschungsgemeinschaft (DFG), IGSSE, ATUMS and SolarTechnologiesGoHybrid (SolTech) for their trust and support. Furthermore, the Deutsche Physikalische Gesellschaft (DPG) is acknowledged for organizing the annual spring meeting, which I always enjoyed attending.

I would also like to thank the people, who helped me to scientifically arrive at the stage of being a PhD student. My physics school teacher Bernd Cremer highly contributed with his excellent teaching and encouragement to maintain a child-like curiosity for all things in life. To Prof. Dr. Martin Erdmann I would like to give my personal award for

the best and most structured lecture series I had experienced during my Bachelor studies. Thank you Dr. Ilhan Engin and Prof. Dr. Detlev Gotta for being inspiring people with a remarkable cool attitude working in the field of physics. Thanks again to Dr. Daniel Moseguí González for being the most awesome mentor I could have imagined during my master thesis. And last but not least, thank you Prof. Dr. Peter Müller-Buschbaum for entrusting me with the position of a PhD student, lots of constructive feedback and for the overall success of this path in my life. You are all awesome!

Finally and most importantly, I would like to express my unlimited gratitude to my mother Dr. Christiane Hohn and my sister Yasmin Hohn for their support and simply for being the best family I could have wished for. An immense thank you is also dedicated to my grandmothers Dr. Marlene Hohn and Anni Hohn for encouraging, caring and being admirable persons. And for his smart advice all the time and for sharing and caring, P. V. Charles is granted my personal thank you award.

At the very end, I would like to express my deepest gratitude to my precious Christine Conrad, the person who endured with me the last seven years, the person who was always most concerned about cheering me up when I was down, the person who appreciates me despite all my flaws, the person who cared the most and the person I love.